A REVIEW OF THE PILLAR DESIGN METHODOLOGY FOR MANGANESE MINING OPERATIONS IN SOUTH AFRICA

DANÉL GEORGINA WESSELS

Presented as partial fullfilment for the degree

M.Eng (Mining Engineering)

IN THE FACULTY OF ENGINEERING, BUILT ENVIRONMENT AND INFORMATION TECHNOLOGY

DEPARTMENT OF MINING ENGINEERING

UNIVERSITY OF PRETORIA

2022/06/27

DECLARATION OF ORIGINALITY

I hereby declare that this dissertation is my own unaided work. It is being submitted for the degree M. Eng (Mining Engineering) at the University of Pretoria, Pretoria. It has not been submitted before for any degree or examination in any other University. This document represents my own opinion and interpretation of information received from the mine or people on the mine.

_____

Danél Georgina Wessels
15066097
27 June 2022

UNIVERSITY OF PRETORIA

FACULTY OF ENGINEERING, BUILT ENVIRONMENT AND INFORMATION TECHNOLOGY

DEPARTMENT OF MINING ENGINEERING

The Department of Mining Engineering places great emphasis upon integrity and ethical conduct in the preparation of all written work submitted for academic evaluation. While academic staff teaches you about systems of referring and how to avoid plagiarism, you too have a responsibility in this regard. If you are at any stage uncertain as to what is required, you should speak to your lecturer before any written work is submitted.

You are guilty of plagiarism if you copy something from a book, article or website without acknowledging the source and pass it off as your own. In effect you are stealing something that belongs to someone else. This is not only the case when you copy work word-by-word (verbatim), but also when you submit someone else's work in a slightly altered form (paraphrase) or use a line of argument without acknowledging it. You are not allowed to use another student's past written work. You are also not allowed to let anybody copy your work with the intention of passing if of as his/her work.

Students who commit plagiarism will lose all credits obtained in the plagarised work. The matter may also be referred to the Disciplinary Committee (Students) for a ruling. Plagiarism is regarded as a serious contravention of the University's rules and can lead to expulsion from the University. The declaration which follows must be appended to all written work submitted while you are a student of the Department of Mining Engineering. No written work will be accepted unless the declaration has been completed and attached.

I (full names) __Danel Georgina Wessels_____
Student number_____15066097_____
Topic of work A review of the pillar design methodology for manganese mining operations _____

Declaration

1. *I understand what plagiarism is and am aware of the University's policy in this regard.*
2. *I declare that this _____dissertation_____ (e.g. essay, report, project, assignment, dissertation, thesis etc.) is my own original work. Where other people's work has been used (either from a printed source, internet or any other source), this has been properly acknowledged and referenced in accordance with departmental requirements.*
3. *I have not used another student's past written work to hand in as my own.*
4. *I have not allowed, and will not allow, anyone to copy my work with the intention of passing it off as his or her own work.*

Signature _____

ABSTRACT

A REVIEW OF THE PILLAR DESIGN METHODOLOGY FOR MANGANESE MINING OPERATIONS IN SOUTH AFRICA

DANÉL GEORGINA WESSELS

Supervisor: Prof Francois Malan

Department: Mining Engineering

University: University of Pretoria

Degree: M. Eng (Mining Engineering)

This study describes a review of the pillar design at the manganese mining operations in South Africa with specific reference to Nchwaning III Shaft at Black Rock Mine Operations. From a literature study, it is clear that there is uncertainty regarding hard rock pillar strength and the appropriate formulae to use when designing hard rock bord and pillar layouts. The current design at Nchwaning III Shaft is based on the Hedley and Grant power-law formula and a K-value of 133 MPa. This K-value is currently used for all the shafts and all the different geotechnical areas. As a concern, extensive scaling of some of the pillars has been observed by the mine. Thin spray-on liners are currently used to stabilise these pillars and this practice has become a major operational expense.

The literature survey indicated that extensive research has been conducted on the time-dependent failure of coal pillars in South Africa. These studies are exclusively empirical in nature and no attempt was made to conduct numerical modelling of the time-dependent scaling. In contrast, almost no work has been done on the time-dependent scaling of hard rock pillars. Complex numerical modelling to simulate the time-dependent scaling of hard rock pillars is described in the literature, but these models are difficult to calibrate and the results are typically not compared to underground pillar behaviour.

Extensive underground observations and monitoring of pillar behaviour was conducted by the author in six different areas. The observations indicated that significant scaling of the pillars

occur in some areas, while other areas are remarkably stable in spite of the slender pillars (width of 7 m, height exceeding 5.5 m). From the data collected, it is evident that the pillars with a low rock mass rating, which contain many closely spaced joints, are prone to excessive scaling. The pillar design at BRMO therefore needs to be extended to cater for the geotechnical areas with a low rock mass rating. This is an important new finding of this study.

Numerical modelling was conducted to simulate the pillars stress in the areas of interest. The TEXAN displacement discontinuity code was used for this study as it was developed specifically to simulate a large number of small pillars in tabular layouts. The numerical modelling provided valuable data on pillar stress and variations of this stress based on pillar size and position relative to abutments. This is a significant improvement over tributary areas stress calculations. The numerical modelling allowed a back-calculation of the “minimum” K-values for the pillar strength formula in the different areas. Values exceeding 100 MPa were calculated for some of the stable pillars. A limit equilibrium constitutive model in the TEXAN code was used to simulate the pillar scaling observed underground. It was encouraging that the two different types pillar behaviours could be simulated using this approach. More precise calibration of the model will be required in future, however, before it can be used as a design tool.

Monitoring of selected pillars were also conducted by the author over a period of three months to quantify the rate of time-dependent scaling. Contrary to expectations, almost no additional scaling was recorded for the pillars over a three-month monitoring period. The existing scaling distances of the pillars could be measured, however. The amount of scaling for pillars mined three years before the measurement in the areas with a low rock mass rating was on average 0.8 m. This value was 0.5 m for pillars mined approximately five months before the measurements. It therefore seems as if the bulk of the scaling occurred soon after blasting and it may even be attributed to the effects of nearby blasting. A limited amount of additional time-dependent scaling seems to occur after this. Prominent time-dependent scaling is nevertheless present for some pillars as can be seen by the ongoing deterioration of pillars that were reinforced using thin spray-on liners. Numerical simulations of the time-dependent scaling were conducted using TEXAN and a limit equilibrium model. An exponential decay of rock strength at the edges of the pillars resulted in simulated behaviour that is qualitatively similar to underground observations. Similar to the actual pillar behaviour, the rate of pillar scaling becomes small after a long period of time.

Based on the data collected, the numerical modelling results and the observations that the pillar strength is affected by rock mass rating, it is proposed that the following revised pillar design should be adopted at Nchwaning III Shaft:

- Retain the current pillar design for areas where the RMR > 50. This rock mass rating is typically found in the high-grade areas.
- Adopt a revised pillar design for areas with an RMR < 50. This rock mass rating is typically found for the low-grade R5 product areas.

For the revised pillar design in low grade areas (RMR < 50), a new K-value was estimated using principles similar to that proposed for the design rock mass strength (DRMS). A value of K = 90 MPa was derived as a first estimate. This value is confirmed by the numerical modelling and the back-calculation of K-values for pillars subjected to extensive scaling. This revised design for areas with an RMR < 50 must be trialled at the mine. Monitoring of the pillar condition in these areas is required to determine whether this design ameliorates the scaling problem and negates the need for thin spray-on liners.

Additional future work should include an improved calibration of the time-dependent limit equilibrium model and a better quantification of the rate of pillar scaling. This will involve the monitoring of pillars over a longer period of time.

ACKNOWLEDGEMENTS

I want to thank the following organisations and people who made this study possible:

1 Koos Janse Van Vuuren, Senior General Manager at Black Rock Mine Operation.
2 Pelonomi Gae, Rock Engineering Manager at Black Rock Mine Operations.
3 Queen Mahlukani, Rock Engineering Intern at Black Rock Mine Operations.

I would like to extend my sincere thanks to my supervisor, Prof Malan for his continuous support and invaluable advice during my Master's degree. Prof Malan has encouraged me throughout this academic study and in my daily life. I would like to express my sincere gratitude to my father, Dawie and my fiancé, JP for all their unwavering support and belief in me. Without their support and encouragement, it would be impossible for me to complete my research project.

TABLE OF CONTENTS

LIST OF FIGURES

LIST OF TABLES

LIST OF SYMBOLS

APS	Average pillar stress
LEM	Limit Equilibrium Model
BRMO	Black Rock Mine Operations
CPF	Catastrophic Pillar Failure
KMF	Kalahari Manganese Field
mbs	meters below surface
Mt	Megaton
P1, P2, …	Naming terminology for the pillars, e.g. Pillar 1, Pillar 2
SF	Safety factor
TAT	Tributary area theory
UCS	Uniaxial compressive strength
w/h	Width to height ratio

CHAPTER 1

INTRODUCTION

The manganese mining operations in the Kalahari region of South Africa is a major contributor to the economy of the country. In terms of rock engineering designs, there is currently uncertainty regarding the strength of manganese pillars, and it is not clear if the current bord and pillar layouts are optimised for maximum, safe extraction. For manganese pillars, there is almost no empirical data on the strength of the pillars. The Hedley and Grant pillar strength formula is currently used to design these pillars, although there is no scientific justification to use this formula. Mining at greater depths also becomes less attractive owing to the increase in pillar sizes and the decrease in extraction ratio. In the hard rock bord and pillars mines of the other commodity sectors in South Africa, pillar collapses have been recorded. It is therefore important that a better understanding of pillar behaviour in the mines in the Kalahari Manganese Field (KMF) is obtained. This study therefore focuses on the pillar behaviour and the design methodology for manganese mining operations in South Africa. The time-dependent degradation of the pillars was studied and this is a useful first contribution to this field as it has not been attempted for hard rock pillars in South Africa yet. Underground data for this report was collected by the author and additional information was obtained from Black Rock Mine Operations (BRMO).

1.1. Mine Background and General Information

BRMO is situated in the Northern Cape Province in South Africa. It is situated 80 km North-West of Kuruman (Assmang, 2020), and 12 km north-west of the Hotazel village. The Kalahari Manganese Field (KMF) forms part of the Banded Iron Formation (BIF) in the area. The KMF is approximately 2.2 Ga years old and is the world's premier land-based manganese ore reserve. The deposit contains an estimated 150 Mt of manganese ore reserves (Beukes et al., 2016).

Assmang acquired a manganese outcrop in 1940 on a small hillock known as Black Rock. Mining operations started in those early years and it is still continuing in the present. There are currently three operational shafts shafts namely Gloria, Nchwaning II, and Nchwaning III. Gloria was commissioned in 1975 and it is mining medium-grade semi-carbonate ore. Nchwaning II was commissioned in 1981 and Nchwaning III in 2004, with both mining high-grade oxide ore. BRMO commenced with an expansion project in 2014 to increase the output of manganese ore to 4.6 Mt per annum by 2020 (Assmang, 2020). The three mining operations are shown in Figure 1-1.

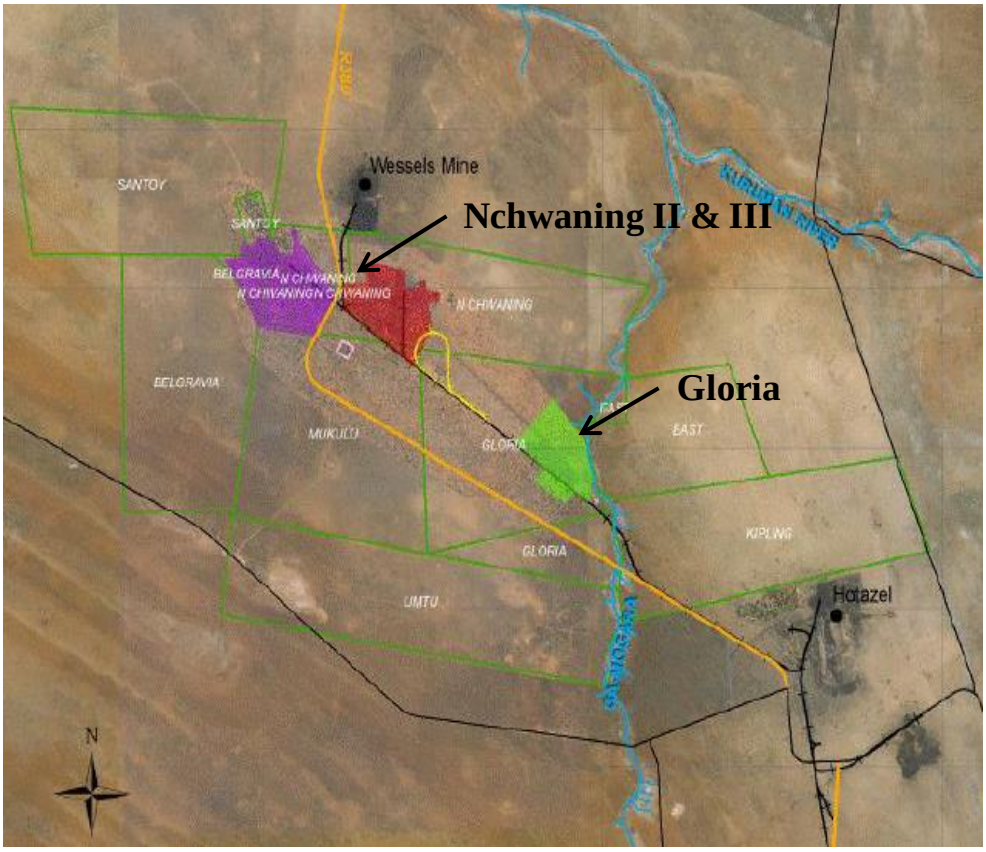

Figure 1-1. The locality of Assmang Black Rock Mine Operations (after EScience Associated, 2018).

1.2. Geological Setting

1.2.1. Regional Geological Setting

The KMF is located within the sediments of the Hotazel Formation of the Griqualand West Sequence, a sub-division of the Proterozoic Transvaal Supergroup. It is estimated that the Hotazel Formation is approximately 40 m in thickness (Assmang, 2020). The Postmasburg, Ghaap, and Olifantshoek Groups of the Griqualand West Sequence are comprised of Basal dolomite and Banded Ironstone. The manganese of the Hotazel Formation, banded ironstone, and basal basaltic andesites are found within the Postmasburg Group (African Rainbow Minerals, 2019). The KMF contains around 80% of the world's high-grade manganese ore reserves. Figure 1-2 illustrates the regional geological map of the area and the location of BRMO located in the Hotazel Formation.

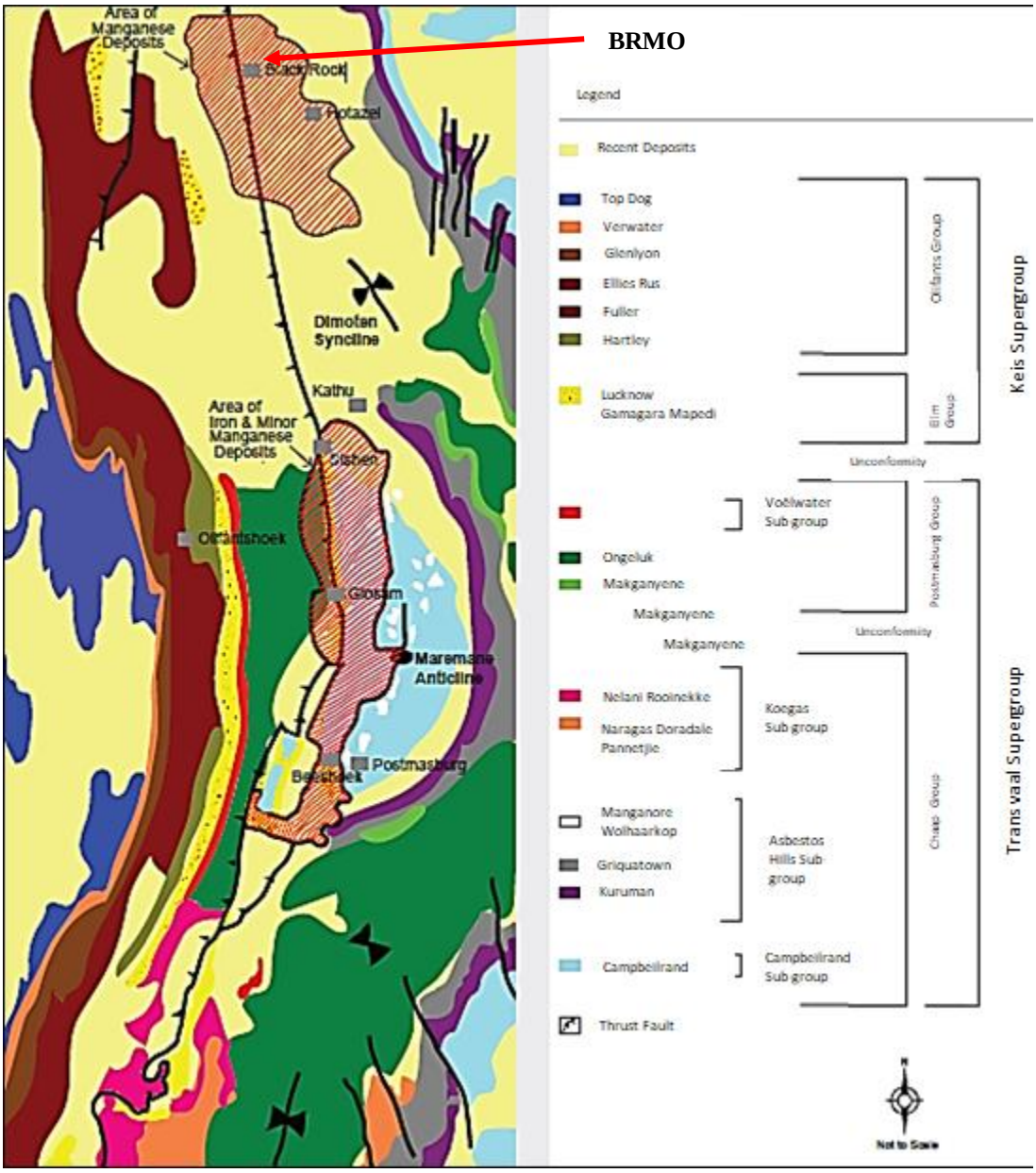

Figure 1-2. Regional geological map (after African Rainbow Minerals, 2019).

Cretaceous-Cenozoic gravel, clay, calcrete, and sand cover the KMF. The KMF is also known for producing a remarkable array of collector's mineral specimens. The Hotazel Formation composed of iron contains three interbeds of sedimentary manganese ore. The three manganese beds are known from top to bottom as the Upper, Middle, and Lower Manganese beds. The Hotazel Formation overlies hyaloclastite and mafic pillow lava of the Ongeluk Formation and is conformably overlain by the Mooidraai Dolomite. Red beds of the Mapedi Formation overlay the unconformity at the top of the Transvaal succession. In the western margin of the Kalahari Deposit, a major low angle thrust fault system exists with a 35 km to 60 km eastward displacement as illustrated in Figure 1-3 (Beukes et al., 2016).

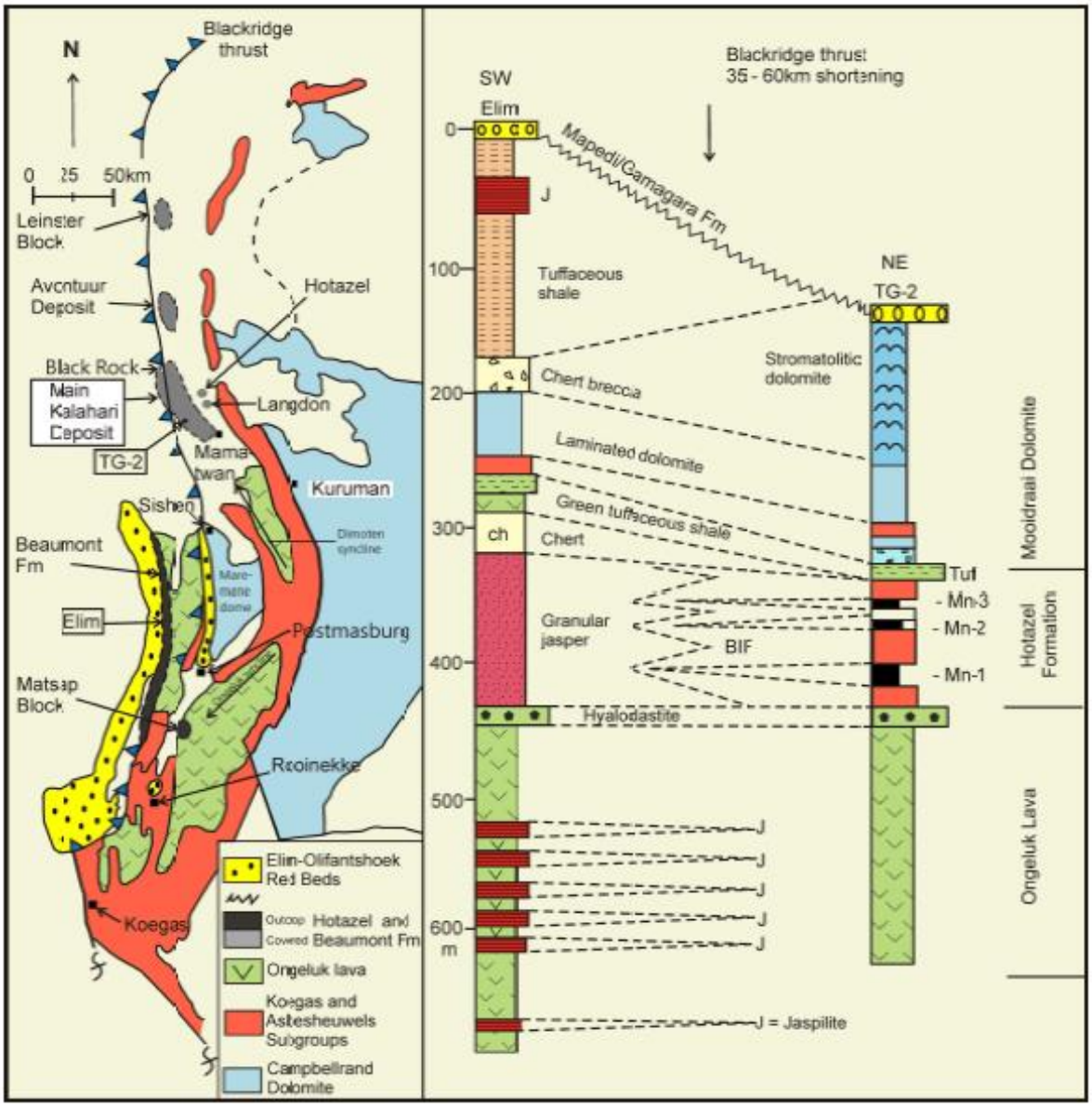

Figure 1-3. Illustration illustrating the lateral interfingering of the Mooidraai and Hotazel formations of the KMF (after Beukes et al., 2016).

1.2.2. Local Geological Setting

The Hotazel Formation, overlain by Mapedi shales and Lucknow quartzite sequences, has been duplicated by thrusting. The thickness of the Hotazel Formation is on average approximately 40 m. The BIF hosted manganese ore bodies occur at three strata bound and stratiform units of variable thickness. Seam 1, the lower part of the ore body, contains a higher grade of manganese compared to seam 2, the top part of the ore body. The seam that is situated in the middle is known as seam 3 and is thin and uneconomic to mine. Figure 1-4 represents the stratigraphic column used at BRMO (African Rainbow Minerals, 2019).

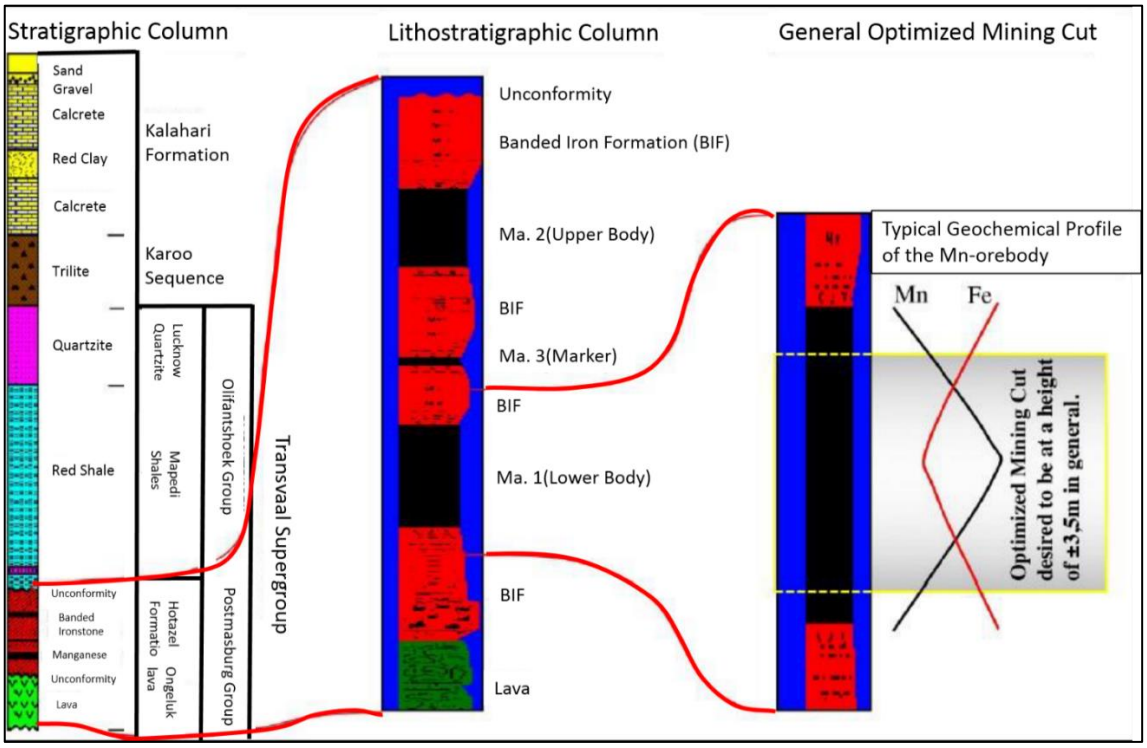

Figure 1-4. A stratigraphic and lithostratigraphic column indicating the optimum cut (after Gae, 2019).

Complex mineralogy is present in these manganese ore bodies. Zoning of the ore body with respect to fault positions is caused by hydrothermal upgrading. Manganese bearing minerals are found in the intermediate areas. Zoning exists in the vertical direction with the top and bottom contact containing high iron content and low manganese content. The central point of the contact contains high manganese content. For mining purposes, the central part of the contact is mined (Assmang, 2020). More than 200 gangue and ore minerals have been found in the manganese ore bodies. Distal areas nearby faults display high-grade hausmannite rich ore and low-grade kutnohorite and braunite. Bixbyite, braunite, and jacobsite among a host of other manganese-bearing minerals are situated in the intermediate areas in the mineralogy. Owing to vertical zoning, mining of the centre portion seam occurs at 4 m to 5 m (African Rainbow Minerals, 2019).

1.3. Pillar Strength Formulae

Malan and Napier (2011) gave an overview of the problems associated with pillar designs in bord and pillar layouts in South Africa. Since this study, very little progress has been made to develop improved pillar design methodologies. A summary is given below to highlight potential problems associated with the Hedley and Grant pillar strength formula used at BRMO. This is an initial introduction and will be discussed in more detail in the literature study.

The use of empirical power-law strength formulae in South Africa is the industry standard to determine pillar strength. The typical form of the power-law formula is given below:

$$\sigma_s = K\frac{w^{\alpha}}{h^{\beta}} \tag{1.1}$$

K is typically modified to reflect the 'strength' of the in-situ rock, *w* is the width of the pillar and *h* is the mining height. This equation is intuitively correct as an increase in the width and a decrease in the height will result in an increase in pillar strength. The more difficult part is the calibration of the constants K, α and β for a particular reef type. The parameters α and β in the famous Salamon and Munro (1967) coal pillar strength formula are equal to 0.46 and 0.66 respectively. This was developed using a South African database of failed coal pillars and this formula worked well in the coal industry for several decades (Malan and Napier, 2011).

For the Hedley and Grant (1972) formula, α = 0.5 and β = 0.75. The calibration of these exponents was done using Canadian data collected in uranium mines and the exponents can be questioned as only a small number of failed pillars were included in the database. The exponents were adopted for South African hard rock mines in the 1970s, and it was never verified or questioned. When using the Hedley and Grant formula, the estimation of the K-value is problematic and it is typically assumed to be between a third and two-thirds of the laboratory uniaxial compressive strength (UCS) strength of the rock. The alternative form of equation (1.1) can be derived by assuming that the pillar volume is given by $V = w^2h$ and the width to height ratio is given by $R = w/h$ (Malan and Napier, 2021):

$$\sigma_s = KV^{(\alpha-\beta)/3}R^{(\alpha+2\beta)/3} \tag{1.2}$$

For equation (1.2), if $\alpha = \beta$, the pillar strength is independent of the pillar volume. For the Hedley and Grant formulation $\beta > \alpha$, and the pillar strength decrease as the pillar volume is increased. Hustrulid (1976) and Bieniawski (1992) disagreed with this prediction. According to Ryder and Jager (2002) the w/h strengthening curve has a zero or positively upwards curvature according to most field and laboratory data. In contrast, the power-law formula predicts a downward curve. Bieniawski (1992) was therefore strongly in favour of a 'linear' equation, with no volumetric size effect:

$$\sigma_s = K\left(A + B\frac{w}{h}\right) \tag{1.3}$$

In this equation, K (MPa) is the "in-situ" strength of a large block (w/h = 1) of pillar material and A and B are dimensionless constants and it is required that A+B = 1 (Malan and Napier, 2011). Ryder

and Jager (2002) state: "*The power law and its derivatives are perhaps too entrenched in coal engineering to warrant withdrawing from them at this time, but in hard rock engineering, the simpler and probably more realistic linear forms are advocated for general use*."

In summary, it is clear from this short description that it is not clear what type of formula to use to predict pillar strength and it is therefore also the case for the manganese pillars in the KMF.

1.4. Project Background and Problem Statement

The Code of Practice (COP) (Assmang, 2020) gives information regarding the design of the pillars at BRMO. The following statement is of importance: "*the methodology followed is one of ensuring mine wide stability by cutting non-yield pillars in a regular pattern and at safety factors exceeding 1.5. The permanent stability of pillars is required to maintain the long-term stability of accesses to new areas, since all development is on-seam.*"

The current pillar design used by the mine is based on a study done by Hanekom (2008). He used the Hedley and Grant pillar formula for this study. To determine the K-value in equation (1.1), Hanekom (2008) describe the back-analysis of 63 pillars. His average minimum K-value was a low value of 43 MPa with a maximum value of 85 MPa. He also described similar studies by other workers at a neighbouring manganese mine which gave a back-calculated value of K = 133 MPa. The data is summarised in Table 1-1. Based on this data, a value of K = 133 MPa was adopted for BRMO, although Hanekom's analysis gave a much lower K-value. Of interest was that the average pillar height at the other manganese mine was 4 m. For the mining heights at 5.5 m and greater encountered at BRMO, this K-value may possibly overestimate the pillar strength.

Table 1-1. Comparison of back-calculated K-values (after Hanekom, 2008).

	Average				
	Pillar Width	Pillar Height	Bord Width	Width:Height ratio	K value (MPa)
Black Rock	6.0	3.3	8.0	1.8	43
Other Mn Mine	3.6	4.0	7.1	0.9	133.0

Based on this assumption for K, Hanekom (2008) produced the pillar width design curves as a function of depth given in Figure 1-5. The pillar stress was calculated using tributary area stress (TAT) calculations for a bord width of 8 m and an overburden density of 2800 kg/m^3. The data in this graph was simplified for the Code of Practice as illustrated in Table 1-2. As an example, at a depth of 450 m to 499 m and a mining height of 5.5 m, the pillar width should be 7 m. If the mining height increases to 6 m, the pillar width should increase to 8 m.

Circumstantial evidence to support this pillar design is that a large number of pillars have been cut at BRMO using this design and no major pillar collapses have been reported over the last decade. The design is nevertheless still subject to the uncertainties caused by the adoption of the Hedley and Grant formulation and there is little experimental evidence supporting the applicability of a value K = 133 MPa. The assumption of TAT may also overestimate the stress acting on the pillars owing to the "regional pillars" left behind (unmined blocks of low-grade ore), but the overburden density used by him may be too low and it needs verification.

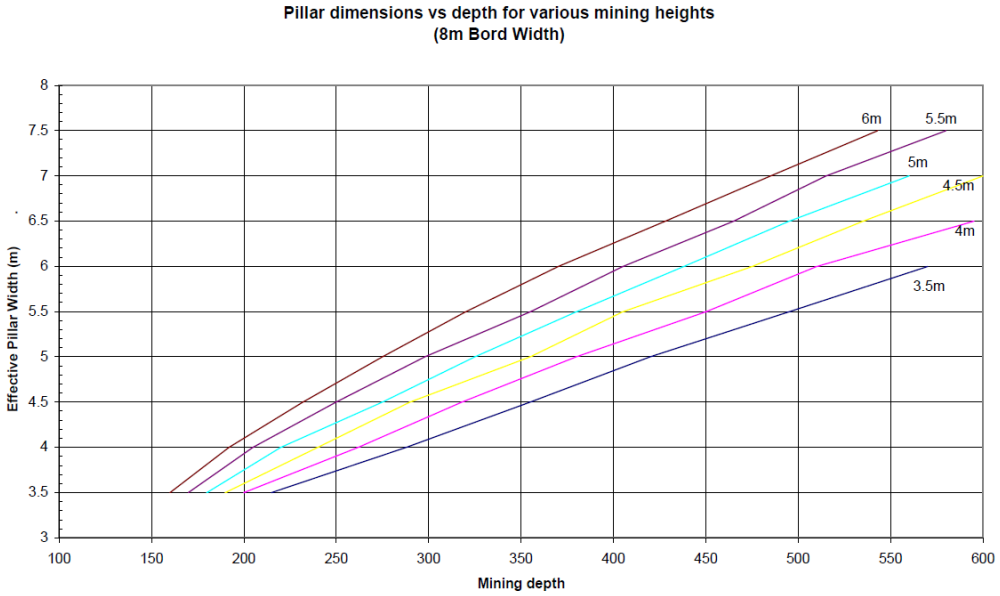

Figure 1-5. Pillar width versus depth for different mining heights (after Hanekom, 2008).

Table 1-2. Pillar widths for different depths and mining heights (after Assmang, 2020)

	Pillar dimensions at specific mining heights					
Mining depth	**3.5 m**	**4 m**	**4.5 m**	**5 m**	**5.5 m**	**6 m**
180 - 299 m	5.0	5.0	5.0	5.0	5.0	6.0
300 - 349 m	5.0	5.0	5.0	6.0	6.0	6.0
350 - 399 m	5.0	6.0	6.0	6.0	6.0	7.0
400 - 449 m	6.0	6.0	6.0	6.0	6.0	7.0
450 - 499 m	6.0	6.0	7.0	7.0	7.0	8.0
500 - 549 m	6.0	7.0	7.0	7.0	8.0	8.0
550 - 599 m	7.0	7.0	7.0	8.0	8.0	8.0
600 - 649 m	7.0	7.0	8.0	8.0	9.0	9.0
650 - 699 m	7.0	8.0	8.0	9.0	9.0	9.0
700 - 749 m	8.0	8.0	9.0	9.0	9.0	10.0

It should be noted that an important part of the design is the pillar stress and this was calculated using the tributary area theory (TAT) stress approach given in equation (1.4). The extraction ratio and the virgin stress are calculated using equations (1.5) and (1.6) respectively.

$$\text{APS} = \frac{q_v}{1-\text{e}} \tag{1.4}$$

$$\text{Extraction ratio (e)} = \frac{(a+c)(b+c)-ab}{(a+b)(b+c)} \times 100\% \tag{1.5}$$

$$\text{q}_\text{v} = pgH \tag{1.6}$$

The Factor of Safety (FoS) can be determined by using equation (1.7) which is the ratio of the strength of a pillar and the stress acting on it.

$$\text{FoS} = \frac{\sigma_s}{\text{APS}} \tag{1.7}$$

Figure 1-6 illustrates the simple pillar layout used at Nchwaning III at the current depths. The tributary area supported by each pillar is 225 m^2. The uniaxial strength of the manganese ore was determined by the mine to be 280 MPa. If the stoping width is assumed to be 5 m, the w/h ratio of these pillars is 1.4 and this is “slender” compared to other hard rock pillars used in the South African bord and pillar mines exploiting other commodities.

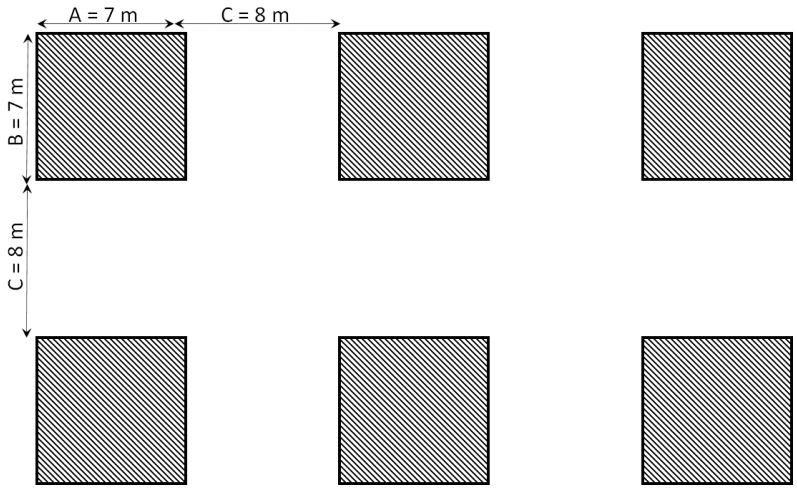

Figure 1-6. Dimensions of the pillar layout at the current depths.

An important implication of the design specified in Table 1-2 is that this is recommended for all the shafts and all the different geotechnical areas at BRMO. Work done by the author for this dissertation

illustrated that the pillars are prone to scaling in some areas, whereas it is more stable in other areas. As a key part of the **problem statement**, different pillar designs for the different geotechnical areas may possibly be required at BRMO. Furthermore, there is uncertainty regarding the strength of manganese pillars, and it is not clear if all the layouts at BRMO are optimised for maximum, safe extraction.

1.5. Objective and Scope of the Study

The scope of the study focussed on the following aspects: All the underground data was collected at Nchwaning III shaft as a number of different geotechnical areas are encountered at this shaft. The study focussed mainly on two geotechnical areas namely the “+45 high-grade product” area and the “R5 low-grade product” area. This was selected as the R5 product area show signs of excessive pillar scaling and the current pillar design may not be applicable in this area. The TEXAN displacement discontinuity code was used for the modelling of these layouts and to accurately determine the stresses acting on the pillars. Modelling using a limit equilibrium constitutive model was done using a time-dependent failure criterion in an attempt to simulate the pillar scaling.

The following formed part of the scope of this study:

- Conduct an underground investigation of the pillar behaviour at BRMO.
- Investigate different geotechnical areas (different grade areas) to identify differences in pillar behaviour.
- Quantify the pillar composition using rock mass rating systems.
- Determine possible causes as to why scaling occurs in certain areas.
- Record the pillar dimensions.
- Attempt to calibrate the input parameters for the TEXAN displacement discontinuity code and the limit equilibrium model (LEM).
- Simulate time-dependent pillar scaling using the LEM.

Five experimental pillar areas were selected. Three of the areas were located in the R5 product area and two areas were located in the +45-product area. Underground visits to the five areas were conducted and the pillars in these areas were studied. The objective of the study was to investigate the time-dependent scaling of the pillars, investigate if the limit equilibrium model can simulate the pillar scaling, determine if the current pillar design is applicable to all areas of the mine and to propose improvements to the pillar design, if possible.

The first step was to conduct a thorough literature review and this is described in the next chapter.

CHAPTER 2

LITERATURE REVIEW

Since the early days of mining, pillar support systems have been used. Owing to the large tensile zone in the hanging wall in shallow mines, possible geological features close to the excavation and the deadweight loading, pillars are typically used as support in these mines. In spite of many studies on pillar behaviour, pillar strength is still not known in many cases as the current empirical equations, as well as numerical modelling approaches, have limitations when designing pillars. A comprehensive literature study was conducted for this study and the different aspects of pillar design are discussed in the following sections.

There is a huge volume of literature available on pillar behaviour and design. This review therefore selectively focussed mainly on two aspects only, namely empirical pillar strength estimations and the associated information relevant to the pillar design at BRMO as well as the time-dependent scaling of the pillars.

2.1. Behaviour of In-Stope Pillar Systems

Various types of in-stope pillars are used in shallow and intermediate-depth mining excavations. These have different functions and include crush pillars, yield pillars and non-yield pillars. In Section 2.1.2 the types of pillars are discussed in more detail. All these pillar types are designed with the same objective in mind namely to provide a stable excavation. As there are many unknowns involved in the design process, the outcome is not always a stable system and when the applied stress exceeds the strength of a pillar, failure will occur. The stress of the failed pillar will then be transferred to the adjacent pillars and this may result in a so-called “pillar run”. Figure 2-1 illustrates a pillar collapse in a base-metal room and pillar mine. According to Dismuke et al. (1994), the pillar failure included approximately 100 pillars. All these pillars collapsed due to the four central pillars that initially failed, leading to catastrophic pillar failure (CPF).

The following characteristics are identified for mines where CPF occurred:

- w/h ratio
  - Coal mines < 3.
  - Metal mines < 1.
  - Non-metal mines ≤ 2.
- The extraction ratio is greater than 60%.
- A minimum of five, and more than ten pillars across the panel widths.

- Absence of barrier pillars with a w/h ratio >10.
- Shallow mines of less than 100 m.

Some of these aspects are applicable to BRMO where the w/h ratio < 1.3, the extraction ratio is planned to be 78% and there are many areas with more than the pillars across panel widths.

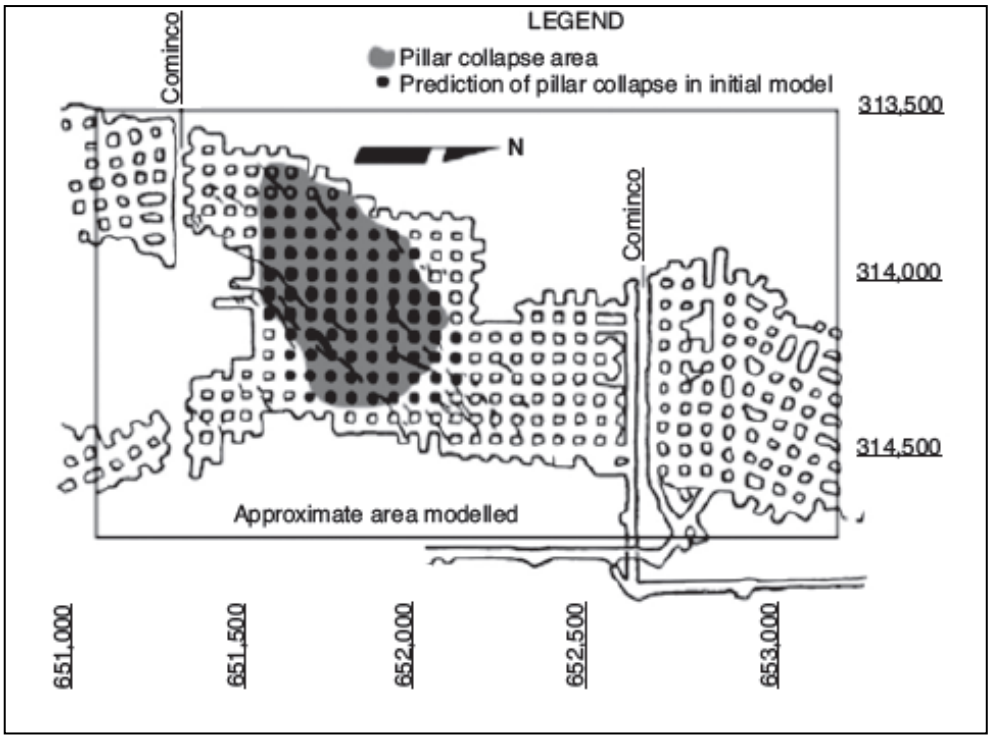

Figure 2-1. A large-scale pillar failure in a bord and pillar layout (after Dismuke et al., 1994).

For the design of in-stope pillars, the stress-strain behaviour of pillars is important, as well as the width to height (w/h) ratio. The strength of pillars plays an important role in pillar stability, and the appropriate empirical strength formulae should be applied for the particular environment. These aspects are discussed in more detail below.

2.1.1. Pillar Stress-Strain Behaviour

When increasing forces are applied to a pillar, the pillar will behave according to the typical stress-strain curve shown in Figure 2-2. The elastic portion of the curve is represented by a straight line up to the yield stress point. The slope of the elastic portion of this graph is the Young's Modulus (E) of the rock type. The yield point (σ_y) represents the beginning of inelastic behaviour or failure of the pillar material. When the yield point is reached, strain hardening will occur until the peak strength (σ_s) is achieved. This is followed by load shedding until the residual strength is reached (Ryder and Jager, 2002).

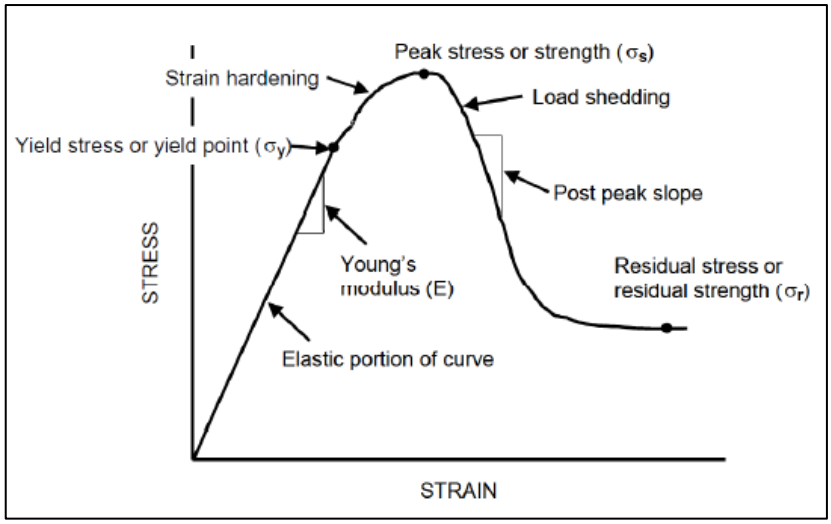

Figure 2-2. The stress-strain behaviour of a typical pillar (after Ryder and Jager, 2002).

The idealised pillar behaviour will be different for pillars with a different w/h ratio as illustrated in Figure 2-3. A well-defined peak stress can be seen in pillars with a w/h ratio of up to four, and the post-peak behaviour of the curve will be a negative slope downwards. The yield stress and the strength of pillars will increase if the w/h ratio increases and the slope of the post-peak portion of the curve will flatten out. When a pillar has a w/h ratio of five, the post-peak slope becomes flat, but near the edges of slender pillars, brittle failure will be experienced. When the w/h ratio tends to be larger than six or seven, these pillars will usually be subjected to strain hardening. Contrarily to popular belief, pillars with a w/h ratio equal to 10 are not indestructible (Ryder and Jager, 2002).

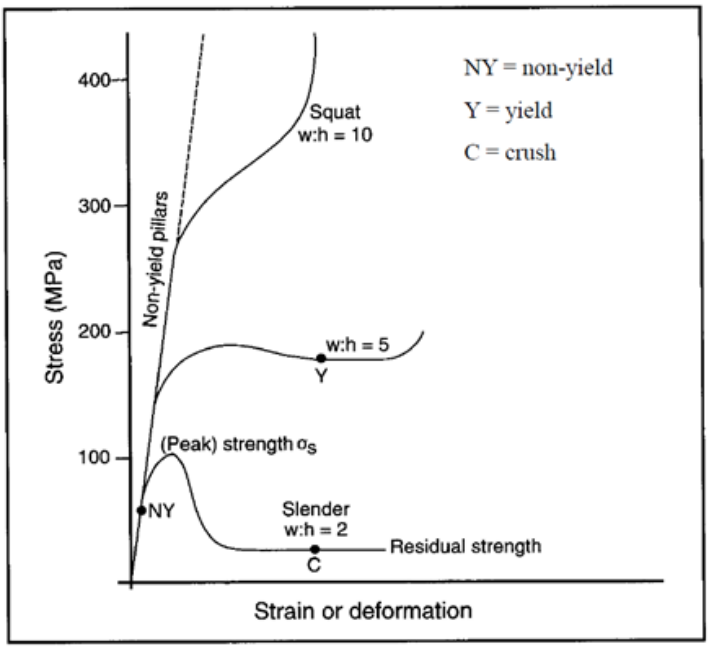

Figure 2-3. The stress-strain behaviour for pillars with different w/h ratios (after Ryder and Jager, 2002).

The curve shown in Figure 2-3 is commonly used in lectures and publications, but it should be noted that the w/h ratios for which the transition from one type of pillar behaviour to the next occurs is still highly uncertain. The “magical” w:h ratio of five may for example not be applicable to all types of pillar material.

For a shallow bord and pillar hard-rock mine, the pillars are commonly designed with a w/h ratio between two and five. It is hypothesised that for these pillars, a well-defined peak stress or strength will be present, and that the stress-strain curve will be characterised by a strain softening post-peak slope. In a shallow mining environment, pillars that are designed with a w/h ratio greater than ten appears to act as squad pillars according to Ryder and Jager (2002).

2.1.2. Different Pillar Types

There are a number of factors that needs to be considered when selecting the type of pillars to use in an underground excavation. Different pillar types will have different functions. Pillars can be used for either regional support or in-panel support. The main difference is that regional support is designed to carry the full overburden weight of the rock to the surface and in-panel support, such as crush pillars, can be designed to only carry the fallout height to a particular weak parting. Mining spans supported by regional pillars range from 100 m to 400 m, and mining span supported by in-panel support range from 10 m to 50 m (Ryder and Jager, 2002).

When considering in-panel pillars, the literature typically refers to three types of pillars namely elastic pillars, crush pillars, and yield pillars. Elastic pillars are used in a shallow mining environment to support the overburden to the surface. It is important to design these pillars correctly to avoid the possibility of catastrophic pillar failure (CPF) as described in Section 2.1 and to prevent damaging surface subsidence. If these pillars are used to support the overburden, it is important to ensure the hanging wall strata remain intact. These pillars should be stiff and should not shed any load. A pillar will be defined as elastic or rigid if the average stress does not exceed the strength of the pillar. Fracturing will occur in the pillar if the load on the pillar exceeds the yield stress (σ_y) (Ryder and Jager, 2002). The w/h ratio of these pillars can go as low as 0.7, but are usually designed to be between two and five (Ozbay et al., 1995). In Figure 2-4 the typical stress-strain behaviour of an elastic pillar is illustrated. The operating point of the pillar should be well below the peak strength of the pillar.

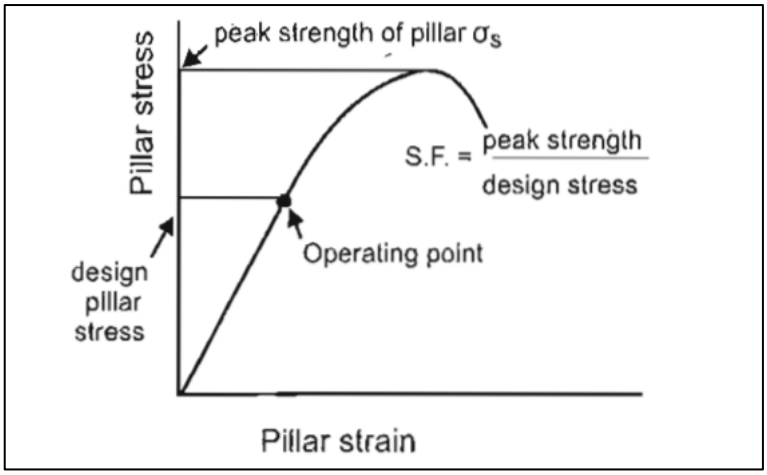

Figure 2-4. Typical stress-strain behaviour for elastic pillars (after Ryder and Jager, 2002).

When designing pillars for a shallow environment, the strength of these pillars must not be exceeded. The maximum panel span (extraction ratio) determines the dimensions of the pillars. The panel span is dependent on the hanging wall geotechnical characteristics. The pillars are also affected by poor blasting practices and should not be designed too small (Ryder and Jager, 2002).

As mining proceeds to an intermediate depth, it will be necessary to increase the pillar sizes and this will lead to a decrease in the extraction ratio. Different types of pillars, such as crush pillars or yield pillars, can be used as an alternative to increase the extraction ratio. Crush pillars are not able to support as much load as stable pillars and should be combined with regional pillars. Crush pillars operate in a post-failure state where the residual strength of the pillar has been reached. To ensure a stable layout, the crushed pillars need to be fully fractured when it is cut at the face. A w/h ratio smaller than three is typically used for crush pillars. The main function of crush pillars is to support the tensile zone between regional support and to support the weight of the rock up to any well-defined parting in the hanging wall (Ryder and Jager, 2002). Figure 2-5, illustrates the typical stress-strain behaviour for crush pillars.

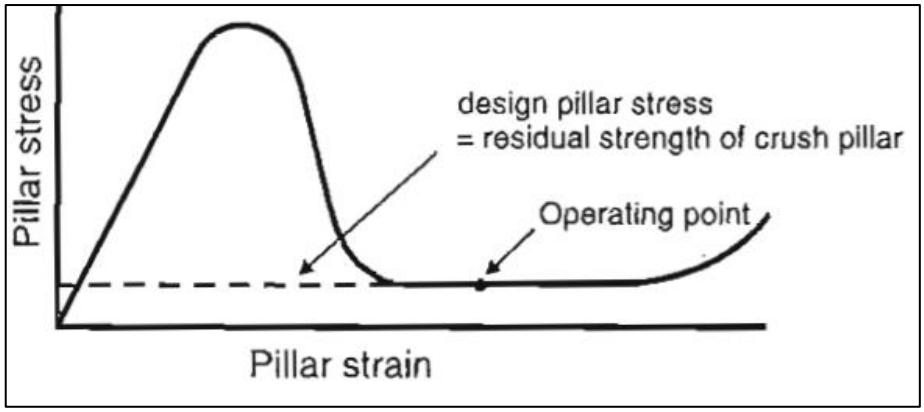

Figure 2-5. Typical stress-strain behaviour for crush pillars (after Ryder and Jager, 2002).

Pillars that are designed to maintain constant stress after the yield point (σ_y) has been reached are known as yield pillars (a special type of crush pillar). Foundation punching and pillar bursting due to high levels of stress have been encountered by these pillars when the pillar was designed with a w/h ratio of five. These pillars are not currently used due to their limitations and the lack of research (Ryder and Jager, 2002). The typical stress-strain behaviour of a hypothetical yield pillar is illustrated in Figure 2-6. Although the concept of these yield pillars has been introduced the South African rock engineering literature, the existence of pillars with a behaviour similar to that in Figure 2-6 is highly doubtful. The concept of a "yield pillar" should probably be scrapped altogether, but this research is beyond the scope of this current study.

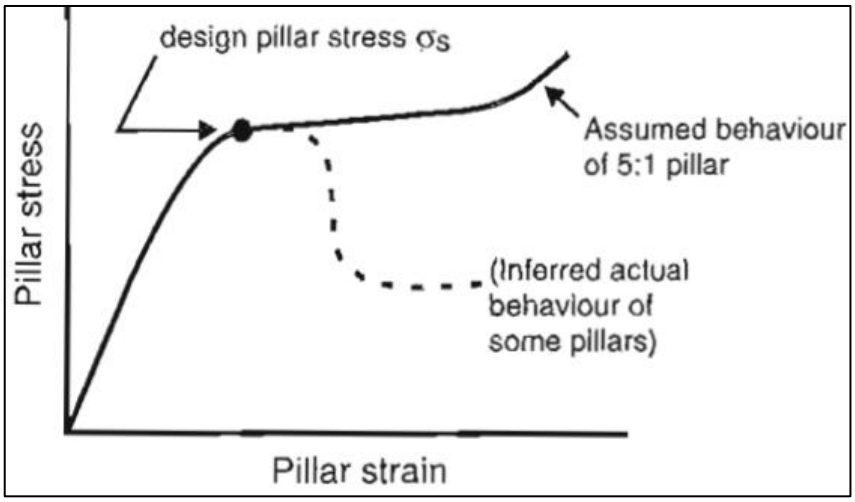

Figure 2-6. Typical stress-strain behaviour of a yield pillar (after Ryder and Jager, 2002).

The main function of regional pillars, apart from supporting the overburden, is to compartmentalise the excavations and prevent the collapse of the entire mine. It also ensures that disasters such as local fires, pillar runs, and floods do not influence neighbouring mines. Regional pillars with spacing

between the pillars ranging from 200 m to 400 m are used to support the overburden when crush pillars or yield pillars are insufficient to support the excavation (Ryder and Jager, 2002).

2.1.3. The Load Acting on the Pillars

Tributary area theory (TAT) can be used to estimate the load acting on a regular layout of pillars. TAT relates the pillar stress to the virgin stress and the extraction ratio. The size of the pillars and the mining span play an important role as it affects the extraction ratio. TAT assumes that each pillar will carry the same amount of overburden load, but it is only justifiable for regular mining layouts as shown in Figure 2-7. When TAT is applied to irregular pillars, it is important to note that large pillars or abutments carry a larger proportionate share of the load of the overburden than pillars that are smaller (Ryder and Jager, 2002).

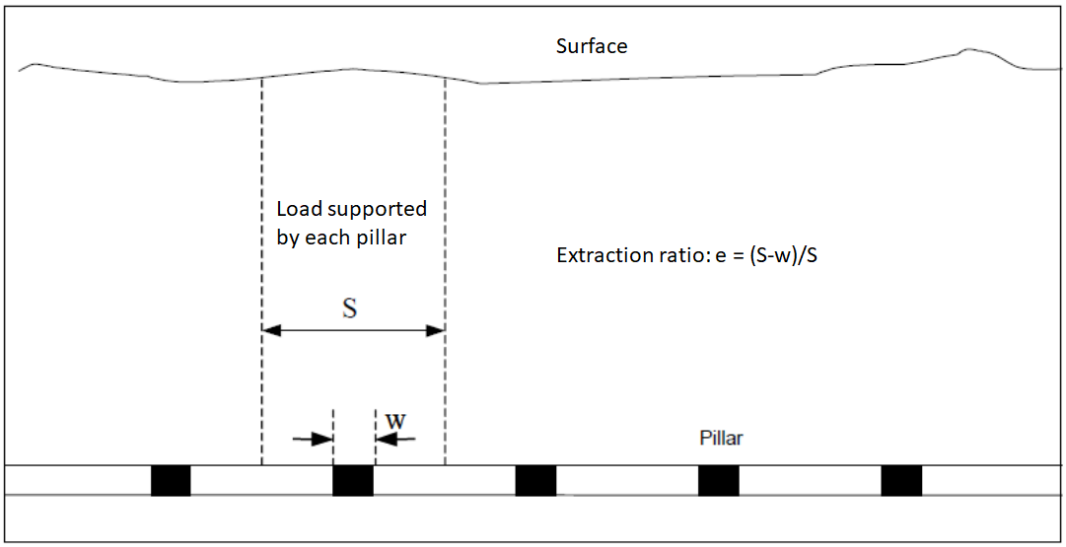

Figure 2-7. Tributary area theory assumes each pillar carries an equal share of the load (after Ryder and Jager, 2002).

Some important considerations regarding TAT are the following (Ozbay et al., 1995):

- The mining depth should be much smaller than the lateral extent of mining.
- The pillar design dimensions are fixed, regardless of depth and seam material.
- Pillars close to permanent abutments or lines of regional pillars, carry lower stress than predicted by TAT.
- Unintentional pillars left due to fault losses or potholes resulting in a lower extraction rate and a lower APS are not catered for by TAT.

TAT is seen as rather conservative in determining the load acting on pillars due to layout irregularities. The irregularities can include large barrier pillars, remnants, and abutments. Numerical modelling should be more routinely applied for irregular layouts (Ryder and Jager, 2002).

A numerical modelling study of a horizontal bord and pillar layout done by Malan and Napier (2011) indicated that as the overall size of the layout area increases, the simulated APS tends towards the tributary area stress (see Figure 2-8). The TEXAN code was used for these simulations. Note that the APS of the pillar adjacent to the abutment is much lower than the values in the centre of the excavation. This also illustrates how TAT overestimates the APS values as it assumes an infinitely large excavation.

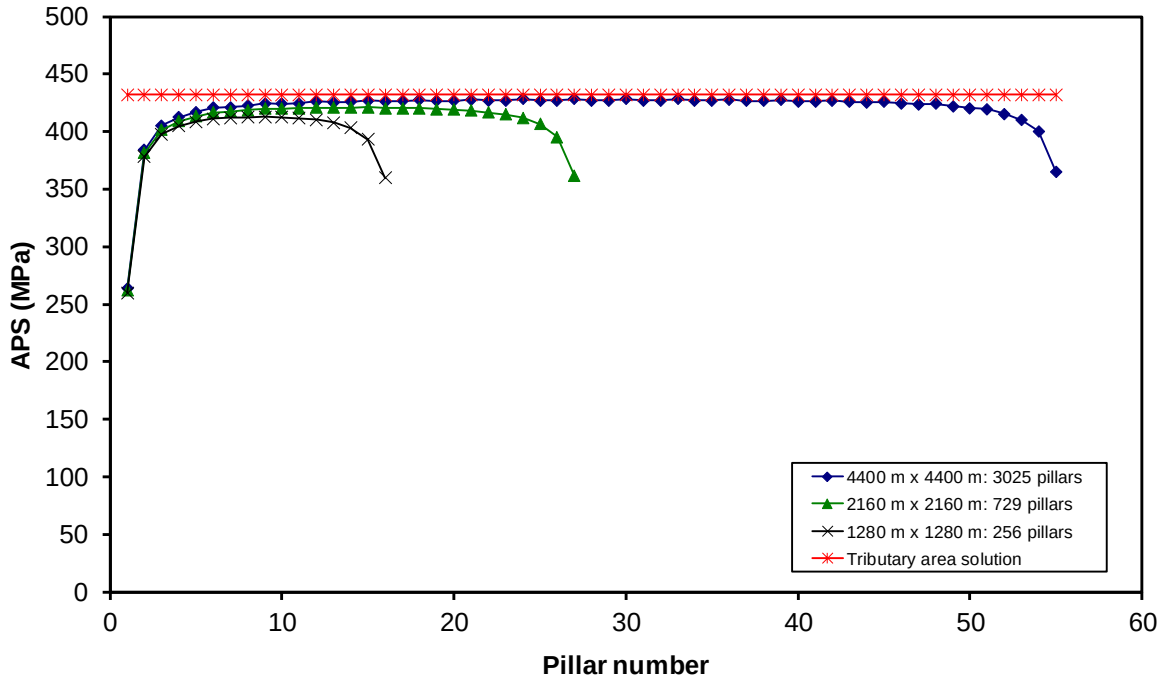

Figure 2-8. Simulated APS values for different sizes of the mined area of the regular pillar layout using TEXAN code (after Napier and Malan, 2011).

In spite of the shortcomings, TAT can provide a good first approximation of the load acting on the pillars. Numerical modelling still needs to be conducted for irregular layouts and excavations with a small span.

The APS of large stabilising pillars, such as those used in the gold mines, is an important design criterion. Numerical modelling can be used to determine if pillar "punching" is likely. The criterion commonly used is that the APS < 2.5 σ_s (Ryder and Jager, 1999). These large stabilising pillars fulfil a different role in the seismically active mines and are not considered further in this study.

2.1.4. The Factor of Safety

The concept of a Factor of Safety (FoS) was adopted for the design of pillars in South African coal mines. Pillars with a high FoS are considered to be more stable, but it can only be seen as a relative measure of pillar stability (Van der Merwe and Mathey, 2013). For pillar design, equation (1.7) is used to determine the FoS. To determine an acceptable FoS, Salamon and Munro (1967) used a statistical back-analysis of a database containing intact and failed coal pillars. Statistical analysis indicated that for a FoS of 1.6, the probability of failure is 0.001. Owing to a lack of research, hard rock mines have also adopted this FoS of 1.6. In areas where damaging subsidence under critical surface structures should be avoided, a higher FoS is used (Ryder and Jager, 2002).

Different types of pillars are designed according to their specific function, for instance, crush pillars are designed with a FoS < 1. These pillars are designed that at an early stage of the pillar life, the strength is exceeded and it will fail, but then remain stable in the crushed state during stoping operations. In comparison, for non-yield pillars, a higher FoS as mentioned above, is used to ensure they remain stable and support the hanging wall to surface (Ryder and Jager, 2002).

FoS is a good indicator of pillar stability and a study done by Lunder and Pakalnis (1997), indicated the following about pillar stability: a SF < 1 indicates failure, a SF > 1.4 indicates an intact pillar, and a SF of 1 < SF < 1.4 indicates that the pillar is unstable.

2.2. Empirical Methods to Estimate Hard Rock Pillar Strength

Based on the success of the Salamon and Munro coal pillar strength formula, a similar power-law strength formula was adopted in the shallow hard rock mines in South Africa. Research was never conducted to calibrate a pillar strength formula for local conditions. The formula adopted was the Hedley and Grant pillar strength formula developed for the uranium mines in Canada. To reflect the local strength of pillars, the K-value was modified. The formula is now the “industry accepted” method for pillar design and this commonly occurs in rock engineering as the original assumptions when deriving an empirical equation are rarely revisited. The original assumptions made for the Hedley and Grant formulation was again published in Malan and Napier (2011) and some of this material is repeated below to highlight the risk of using this empirical equation.

The Hedley and Grant formula is based on data collected in the uranium mines in the Elliot Lake area in Canada. Rib pillars were left in these mines. The pillars that were analysed were typically 2.5 m to 6 m high and 3 m to 6 m wide. The data base of pillars analysed only consisted of three pillars with a w/h ratio of 2.5 and most of the pillars had a w/h ratio close to one. It can therefore be

questioned if the Hedley and Grant formulation applies to square pillars with a w/h ratio greater than 2.5 (Malan and Napier, 2011).

The typical layout of the Elliot Lake mines is illustrated in Figure 2-9. The data set used by Hedley and Grant consisted of 28 pillars in comparison to Salamon and Munro (1967) who used a coal pillar data base of 125 pillars. Of these pillars, 27 were collapsed pillars. The Hedley and Grant failed pillars had a w/h ratio ranging from 1.1 to 1.5. Two of the pillars were partially crushed, and three of these pillars in the database were completely crushed. This information may even be incorrect as it is written in the paper: "*The information on complete pillar crushing was obtained second-hand because it happened in mines which are closed*." TAT was used to determine the APS as this work was conducted before computer-based numerical modelling for irregular layouts was readily available (Malan and Napier, 2011).

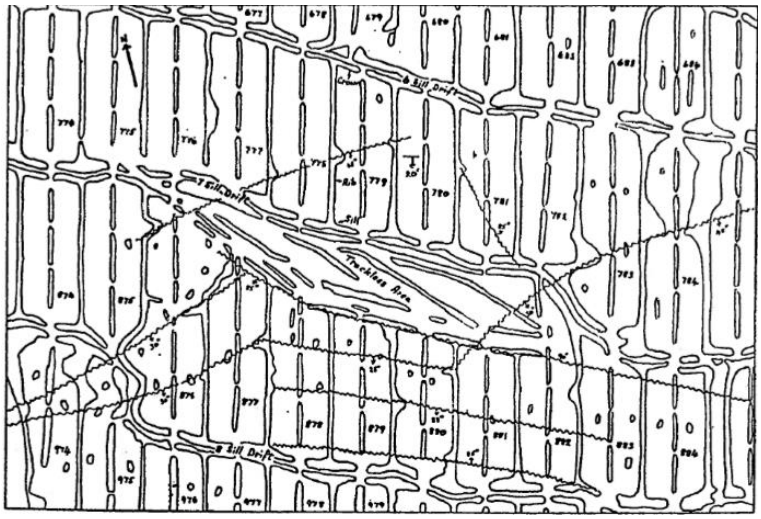

Figure 2-9. Pillar layout in a mine in the Eliot Lake district (after Hedley and Grant, 1972).

To derive the pillar strength formula, a power-law formula similar to Salamon and Munro (1967) was adopted. The assumption was made that the strength of a slender pillar will not be much greater than the strength of a square pillar with a width equal to the minimum width of the slender pillar. The value of K was estimated to be 179 MPa based on laboratory experiments and then extrapolation for a cube of 0.3048 m (one foot). For the parameters 'α' and 'β', values had to be derived. Hedley and Grant decided to adopt a value for 'α' as 0.5 based on what was available in the literature. The value for 'β' was then calculated based on the data obtained from the three failed pillars and a value of 0.75 was obtained. The resulting Hedley and Grant equation is therefore:

$$\sigma_s = K \frac{w^{0.5}}{h^{0.75}} \tag{2.1}$$

It is clear that the Hedley and Grant formulation is based on a number of crude assumptions and its use for the design of hard rock pillars in South Africa is therefore questionable. It was nevertheless used to design a large number of bord and pillar mines, including the BRMO layouts, with the appropriate modification of the K-value. A common practice in South African mines is to assume the value of K to be one-third to two-thirds of the UCS. An important question arises as to why this pillar formulation works and it may even indicate that this formulation is too conservative (Malan and Napier, 2011).

Watson et al. (2008) attempted to develop a new formula that can be applied in South African Merensky Reef platinum mines. He used the maximum likelihood estimation, similar to what Salamon and Munro used, to derive new exponents for the power-law formulation. The database consisted of 197 Merensky Reef pillars, and 109 of the pillars in the database were stable. Most of the pillars had a w/h ratio ranging between 3 and 6. Only one pillar had a w/h ratio of 1. The values derived by Watson et al. (2008) is as follows: K-value = 86 MPa, α = 0.76, and β = 0.36. The *'β'* parameter derived is much lower than the value for the Hedley and Grant formulation. The Watson et al. (2008) formulation predict that pillars have much greater strength compared to a Hedley and Grant formulation, with the K-value assumed as one-third of the UCS. Figure 2-10 illustrates the difference in strength for the two formulae. The applicability of this Merensky formula is also questioned as $\alpha > \beta$ and Malan and Napier (2021) indicated that this predicts an increasing strength if the pillar volume increases (for a constant w/h ratio).

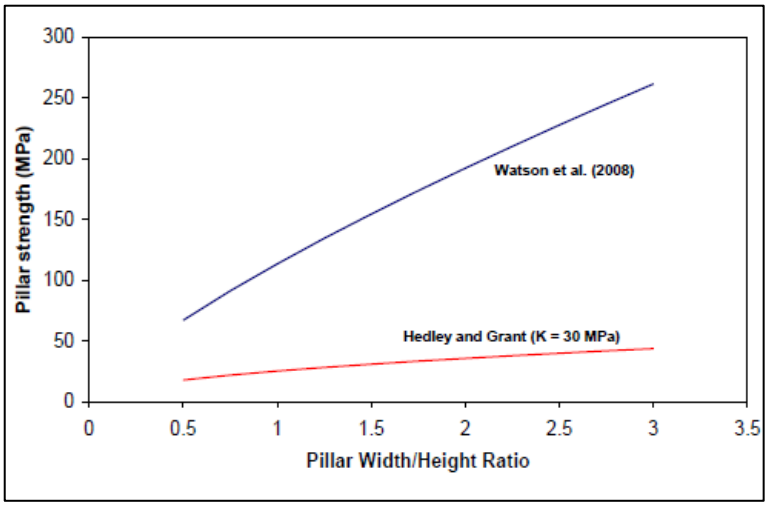

Figure 2-10. A comparison between the Hedley and Grant and Watson strength formulae (after Malan and Napier, 2011).

For the strength formulae above, corrections must be made for rectangular pillars and the "effective width" must be calculated. Wagner (1974) proposed the perimeter rule:

$$w_{eff} = \frac{4 \times A}{C} = \frac{2 \times w \times L}{w + L} \quad (2.2)$$

where:

A = cross-sectional area of the pillar (m^3)

C = perimeter (m)

During large-scale underground tests, observations were made by Wagner. According to Wagner (1974), "*the strength of the circumferential portions of a pillar is virtually independent of the w/h ratio, whereas the strength of the centre increases with increasing w/h ratio*". Ryder and Ozbay (1990) suggested an alternative shape strengthening factor. Ryder and Ozbay (1990) suggested that the factor of f = 1.0/1.1/1.2/1.3 should be used for pillars having w1/w2 ratios of 1/2/4/∞. The perimeter rule according to Wagner is seen as an overestimation of the strengthening effect of very long pillars. There is currently no good experimental data available on how the strength of pillars are affected by the pillar shape. Further research in this area is required.

In other countries, much research on pillar strength has been done since 1972, and these equations are shown in Table 2-1 and Figure 2-11. The strength of the pillars in Table 2-1 is either the maximum stress in the centre of the pillar or the average maximum pillar stress (Martin and Maybee, 2000). These pillar strength equations will not be discussed further in this study as the Hedley and Grant formulation is currently used at BRMO.

Table 2-1. Pillar strength formulae proposed by various workers (after Martin and Maybee, 2000).

Author	Pillar strength formula (MPa)	Rock mass type	UCS (MPa)	Number of Analysed pillars
1972 - Hedley and Grant	$\mathbf{133}\frac{\boldsymbol{w}^{0.5}}{\boldsymbol{h}^{0.75}}$	Quartzites	230	28
1984 - Von Kimmelman	$\mathbf{65}\frac{\boldsymbol{w}^{0.46}}{\boldsymbol{h}^{0.66}}$	Metasediments	94	57
1987 - Krauland	$\mathbf{35.4}(\mathbf{0.778} + \mathbf{0.222}\frac{\boldsymbol{w}}{\boldsymbol{h}})$	Limestone	100	14
1989 - Potvin	$\mathbf{0.42}\boldsymbol{\sigma_c}\frac{\boldsymbol{w}}{\boldsymbol{h}}$	Canadian Shield	-	23
1992 - Sjoberg	$\mathbf{74}(\mathbf{0.778} + \mathbf{0.222}\frac{\boldsymbol{w}}{\boldsymbol{h}})$	Limestone/Skarn	240	9
1997 - Lunder and Pakalnis	$\mathbf{0.44}\boldsymbol{\sigma_c}(\mathbf{0.68} + \mathbf{0.5}\boldsymbol{k})$	Hard rocks	-	178

The effect of the w/h ratio in different strength formulae is illustrated in Figure 2-11. There are differences between these strength formulae, and they should be used with caution.

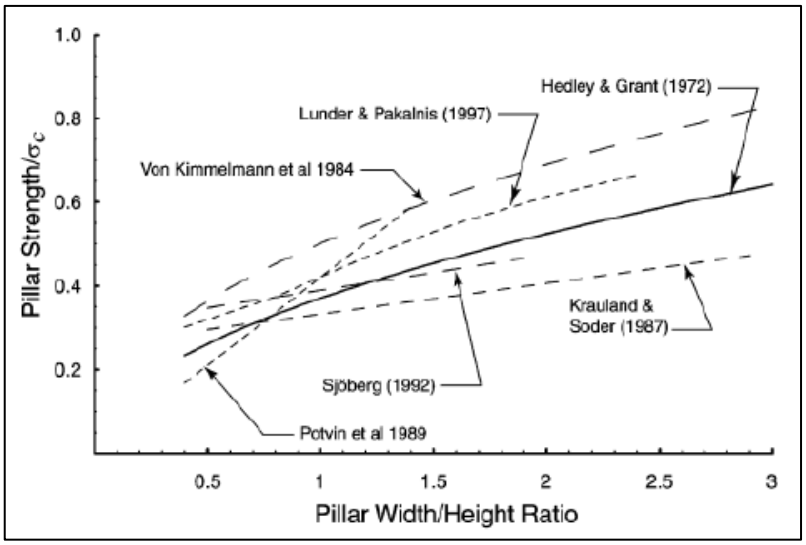

Figure 2-11. The effect of the w/h ratio on the pillar strength (after Malan and Napier, 2011).

The complexity and current uncertainty of appropriate methods to design pillars is probably best summarised by Oke and Kalenchuk (2017). They provided the options given in Table 2-2, Table 2-3, and Table 2-4. The conservative approach should be selected if more than one chart or equation is applicable. The empirical method selected should be calibrated as a second step by formulating a pillar stability chart where site-specific pillar performance and observations are made. This can be done by continuous mapping of the pillars. Multiple data points can be obtained over the operating life of a mine when stress conditions change. As the last step, a site-specific chart can be designed from the data collected. This will also improve the accuracy of the numerical models used on the mine and the calibrated parameters will be more accurate (Oke and Kalenchuk, 2017).

Table 2-2. Square pillar design chart (after Oke and Kalenchuk, 2017).

Rock Quality	Rock Type	UCS (MPa)	Stress	Case Study or Numerical	Authors
Anisotropic Conditions	Schist (Ubiquitous Joint)	60	3D	Numerical	Lorig and Cabrera (2013)
Unknown Rock Quality	Mineralized pegmatoidal pyroxenite	86	3D	South Africa	Watson, Ryder, Kaaka, Kuijpers, and Leteance (2008)
	Metasediments	94	3D	Botswana	Von Kimmelmann, Hyde, & Madgwick (1984)
	Sulphide ore deposits in limestone (marble)	100	Multiple	Greenland	Krauland & Soder (1987)
Rock Mass Quality = Fair	Marble	61 - 104	TA	Spain	Gonzalez-Nicieza, Alvarez-Fernandez, Menendez-Diaz, & Alvarez-Vigil (2006)
Anisotropic Conditions	Simulated Limestone (one major joint set)	122	3D	Numerical (W:H=0.57)	Zhang, Stead, & Elmo (2015)
Rock Quality > Fair	Limestone	135	Multiple	United States	Esterhuizen, Dolinar, & Ellenberger (2008a)
	Stone	152	Multiple	United States	Esterhuizen, Dolinar, & Ellenberger (2008b)

Table 2-3. Long pillar design chart (after Oke and Kalenchuk, 2017).

Rock Quality	Rock Type	UCS (MPa)	Stress	Case Study or Numerical	Authors
Unknown Rock Quality	Fine grained igneous crystalline rock	100	2D	Numerical	Hock and Brown (1980)
	Limestone with Discontinuities	-	2D	Numerical	Esterhuizen (2014)
	Stone (Ubiquitous Joint)	-	2D/3D	Numerical	Iannacchione (1999)
Rock Quality > Fair	Massive Sulphide	172	ER	Canada	Pakalnis, & Vongpaisal (1993)
	Quartzite, Conglomerate	230	2D	Numerical	Martin & Maybee (2000)
	Disseminated ore/Compact ore	240	2.5D	Sweden	Sjoberg (1992)

Table 2-4. Stope pillar design chart (after Oke and Kalenchuk, 2017).

Rock Quality	Rock Type	UCS (MPa)	Stress	Case Study or Numerical	Authors
Rock Quality < Fair	Metasediments + Dyke	70	3D	Canada	Diederichs, Coulson, Falmagne, Rizkalla, &Simser (2002)
Rock Quality > Fair	Canadian Shield	Varies	2D/3D	Canada	Potvin, Hudyma, & Miller (1989)
	Massive Sulphides + Dyke	200	3D	Canada	Diederichs, Coulson, Falmagne, Rizkalla, &Simser (2002)
Unknown	Quartzite	234	ER	Canada	Hedley, & Grant (1972)

2.3. Time-Dependent Pillar Failure in Bord and Pillar Layouts

Occasionally, time-dependent failure of pillars in bord-and-pillar mines leads to surface subsidence in South Africa. Surface subsidence can be caused by these collapses for panel widths ranging from 80 m to over 200 m, mining depths ranging from 40 m to 160 m, and mining heights ranging from 1.5 m to more than 4 m. Pillar failure in South Africa is nevertheless a rare occurrence and it is estimated that of all the coal pillars created, less than 0.3% have failed (Van der Merwe, 2003).

To estimate the life of a pillar is an important factor to consider for overall mine stability. This is especially important when undermining surface structures. Coal pillars lose strength over time,

leading to the eventual failure of the pillars. Predicting the life of pillars or the time of failure will result in more effective monitoring of surface subsidence over a long period of time (Van der Merwe, 2003). It also allows for calculating the risk of pillar collapse in older areas of the mine and whether this may affect the regional stability of the mine.

When mining below surface structures the common method adopted is to use larger pillars with higher factors of safety. Although this effectively makes a stable area even more stable, the additional time the area will be stable is not known (Van der Merwe, 2003). Coal pillars gradually become smaller owing to time-dependent scaling of the pillars. The exact mechanism responsible for pillar scaling is unknown (Van der Merwe, 2016). Time-dependent failure has not been studied in great detail so far.

The type of rock plays an important role in time-dependent degradation. Figure 2-12 illustrates typical skin degradation that takes place in deep hard rock mines. Owing to the failure of the pillar edge, the pillar loses its load-bearing capacity in the immediate sidewall, increasing the load in the centre of the pillar. The factor of safety of the pillars will decrease when strength degradation is sufficiently large. This results in the factor of safety decreasing below a critical value as the stress factor increases (Sainoki and Mitri, 2017).

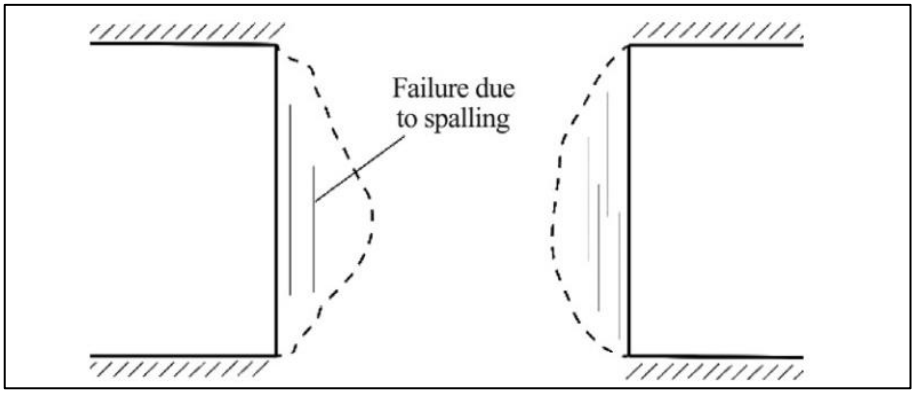

Figure 2-12. Illustration of typical skin degradation of a pillar owing to spalling (after Sainoki and Mitri, 2017).

Constitutive models have been proposed over the years that are able to simulate time-dependent rock behaviour (Lui and Cai, 2020). This allowed for a better understanding of the long-term strength and time-dependent scaling. (Wang and Cai, 2021). Time-dependent scaling has been observed for pillars that have been stable for many years. Figure 2-13 illustrates an example of a limestone mine. It is clear that the sidewalls gradually changed shape over time.

Figure 2-13. A stable limestone mine illustrating concave pillar geometry owing to time-dependent spalling damage (after Wang and Cai, 2021).

Several mechanisms can contribute to the failure of coal pillars. This includes fires, which is a special case, foundation failure, and progressive scaling. In South Africa, foundation failure has been observed in isolated cases. It is considered as a minor mechanism in South Africa, while it is seen as the main failure mechanism in the USA in the Illinois mines. It has been suggested over the years that pillars fail owing to progressive scaling (Van der Merwe, 2003). Figure 2-14 and Figure 2-15 indicate the failure of pillars from two different mining areas in South Africa.

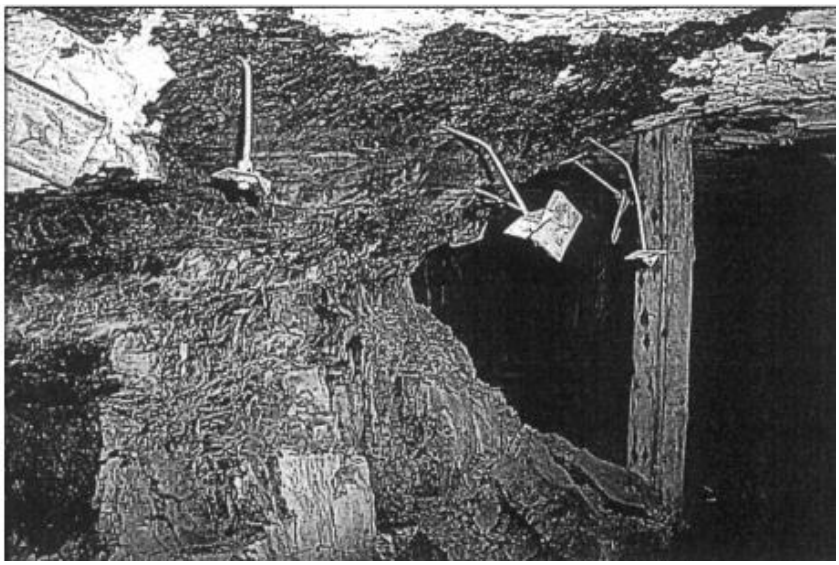

Figure 2-14. Scaling of an old pillar known to consist of weak coal in the Vaal Basin (after Van der Merwe, 2003).

Figure 2-15. Ermelo B seam illustrating pillar scaling in a 90-year-old mining area (after Van der Merwe, 2003).

2.3.1. Mode of Pillar Failure

It is important to understand the mode of pillar failure when considering time-dependent effects. Weakening of the pillars occurs at the edges and works its way into the core of the pillar until it eventually loses its strength and fails. Figure 2-16 is a schematic that illustrates this mechanism. If the pillar has an original width of *w,* and scaling occurs by a distance *d*, then the effective width of the pillar will become *w – d.* This will increase the bord width *B* to *B + d*, but the pillar centre distance will remain unchanged at *B + w* (Van der Merwe, 2003). The scaling distance of a pillar can be defined as the total amount of scaling on opposite sides of a pillar, thus the number of meters the width of the pillar will decrease (Van der Merwe, 2004).

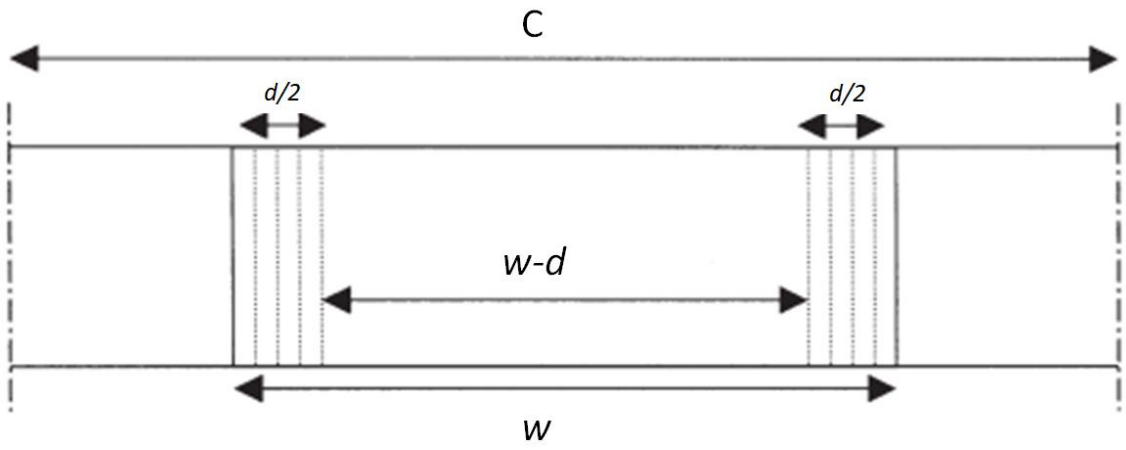

Figure 2-16. A cross-section through a pillar with scaling distances indicated (after Van der Merwe, 2003).

2.3.2. Volume Restriction

Volume restriction is a factor that needs to be considered in terms of pillar stability. According to Salamon et al. (1998), additional scaling can be prevented if the scaling debris is not removed from the excavation. This blocks the open space into which the failed material can move and is referred to as choking. Expressions were developed by Salamon et al. (1998), to determine when choking will occur. It was hypothesised that this would happen when the debris builds up to the roof of the excavation along the edges of the pillars. This build-up of debris would stop further scaling (Van der Merwe, 2003).

As illustrated in Figure 2-17, pillar failure in this case was apparently still observed after debris had indeed built up to the roof. This confirmed the statement made by Salamon et al. (1998), that his expressions should not be applied in practical situations where the failure is stress-driven. Van der Merwe (2003) also noted that it is known that lateral confinement increases the strength of the pillars.

Figure 2-17. An area where scaling debris had built up to the height of the roof and pillar failure still continued (after Van der Merwe, 2003).

According to Kaiser et al. (2011), confinement of the pillar will influence the strength and the failure of pillars. The core of the pillar may experience a different failure mechanism compared to rocks near the pillar surface. Figure 2-18 illustrates different failure criteria and an S-shape criterion was proposed by Kaiser et al. (2011). Brittle spalling was also considered by Esterhuizen (2006). This work indicated that a different pillar strength curve may be applicable for pillars that are confined (Wang and Cai, 2021). Extensive research needs to be conducted to measure the strengthening effect as this is a complex topic (Van der Merwe, 2003).

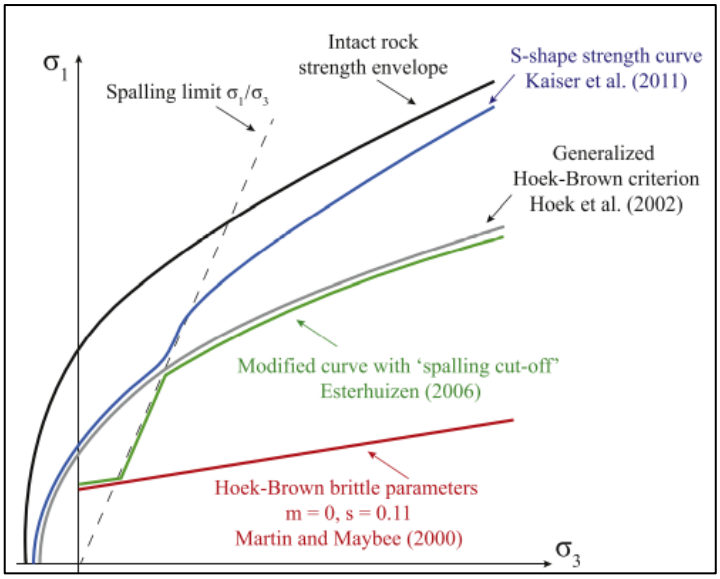

Figure 2-18. Pillar strength simulation using different strength criteria (after Wang and Cai, 2021).

2.3.3. Pillar Rating Systems

To assist with studies on the strength, the condition of pillars and possible time-dependent failure, a pillar rating system can be used. A study conducted on the post-behaviour of two mine pillars confined by using backfill was done using a pillar condition rating system (Tesarik et al., 2003). Table 2-5 illustrates pillar condition ratings that can be assigned to the pillars as observed underground. This makes it easier for future studies conducted to determine if scaling of a pillar is a time-dependent mechanism.

Table 2-5. Pillar rating system based on the condition of the pillar (after Tesarik et al., 2003).

Pillar rating	Pillar condition
1	No indication of stress-induced fracturing. Intact pillar.
2	Spalling on pillar corners, minor spalling of pillar walls. Fractures oriented subparallel to walls and are short relative to pillar height.
3	Increased corner spalling. Fractures on pillar walls more numerous and continuous. Fractures oriented subparallel to pillar walls, and lengths are less than half pillar height.
4	Continuous, subparallel, open fractures along pillar walls. Early development of diagonal fractures (start of hourglassing). Fracture lengths are greater than half pillar height.
5	Continuous, subparallel, open fractures along pillar walls. Well-developed diagonal fractures (classic hourglassing). Fracture lengths are greater than half pillar height.
6	Failed pillar, may have residual load-carrying capacity and be providing local support to stope back. Extreme hourglass shape or major blocks fallen.

According to Wang and Cai (2021), there are five stages of pillar deformation as the vertical stress increases. This is illustrated in Figure 2-19 below. Owing to the gradual spalling on the sidewalls of the pillars, a typical hourglass shape is observed as illustrated below (Wang and Cai, 2021).

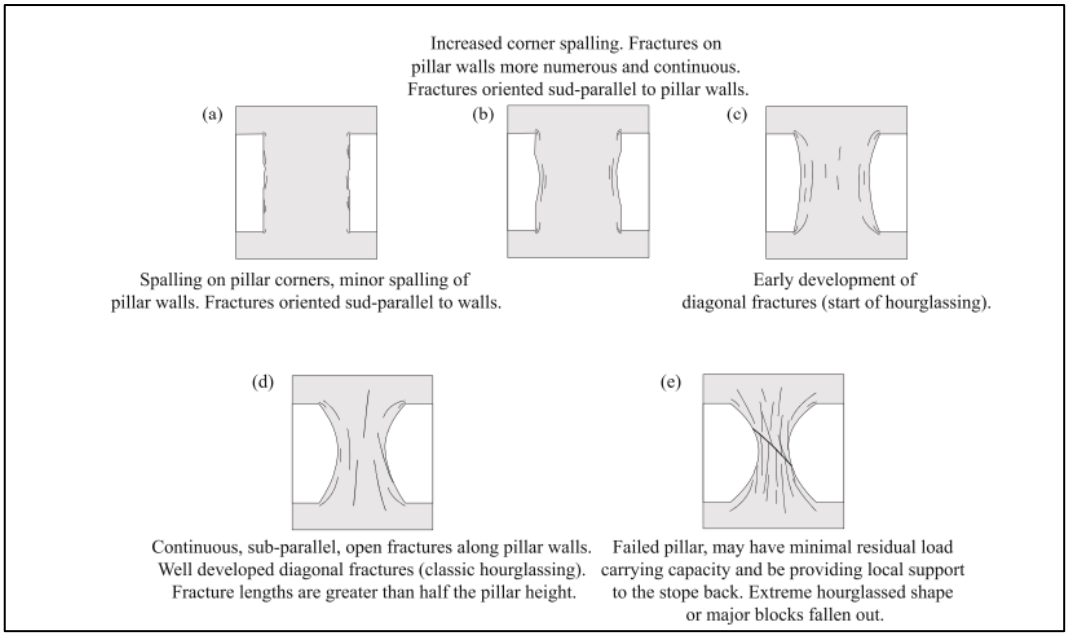

Figure 2-19. Pillar rating system based on the condition of the pillar (after Wang and Cai, 2021).

2.3.4. Attempts to Predict Pillar Life in Bord and Pillar Coal Mines

An extended pillar design philosophy is to also focus on the life of the pillars. Previous attempts have been made to predict the life of pillars in coal and hard rock bord and pillar mines. Some of the attempts made are only briefly mentioned below as they are not considered applicable to South African mines.

A time delay formula was published by Van Besien and Rockaway (1988), based on stresses acting on pillars. This formula represents the time delay between the start of pillar failure and mining. It was assumed that if failure had not occurred by the time predicted, it would never happen. This method is purely empirical without any reference to the mode of failure and it was based on case studies in the United States of America.

Hao and Chug (1992) conducted an analysis on 24 pillars in a bord and pillar mine in Illinois. It was concluded from their study that the collapse mechanism was failure of the floor. A formula was developed to predict the life of the pillars, but as this formula only considers failure of the floor, it is not considered in this current study.

The failure of pillars in the Vaal Basin was observed and analysed by Van der Merwe (1993). He concluded that the mode of pillar failure was progressive pillar scaling. A correlation was found between the rate of scaling and the mining height. Van der Merwe (1993) developed a method to

predict the pillar life. This method was, however, only applicable to the Vaal Basin area (Van der Merwe, 2003).

This method proposed by Van der Merwe's (1993) was also investigated by Salamon et al. (1998). They used a statistical method to predict the probability of failure at a certain point in time. For the analysis, the original pillar dimensions were used. This is not considered a valid approach owing to the dimensions of the pillars at that stage being different compared to when they were originally cut (Van der Merwe, 2003).

More detailed descriptions of the studies of coal pillar life is presented below by Van der Merwe (2003, 2004, 2016, 2019). There is almost no information available on pillar life and time-dependent failure in hard rock bord and pillar mines and therefore the author included these coal studies as valuable background.

2.3.4.1 Study 1 - Predicting Coal Pillar Life in South Africa

Van der Merwe (2003) describes observations made on the progressive weakening of pillars from the edges towards the core of the pillar. It was hypothesised that at some stage the remaining core will be too small to handle the imposed load and it will fail completely. The time of failure can be predicted by investigating the rate of scaling for different areas and seams in South Africa. The rate of scaling was studied by comparing the actual life spans to the predicted time of failure for the pillars in the database of failed pillars.

Van der Merwe (2003) conducted his analysis by using the following equations to determine a relationship between pillar life, scaling rate, and scaling distance. To determine the strength of the coal pillars before scaling occurs, equation (2.3) was used:

$$\text{Strength} = 3.5\ \frac{w}{h}\ \text{[MPa]} \tag{2.3}$$

where w is the width of the pillar and h is the height. The load acting on the pillars are determined by using the tributary area theory and was written as follows:

$$\text{Load} = 0.025H\left[\frac{C^2}{w^2}\right]\ \text{[MPa]} \tag{2.4}$$

Where C is the pillar centre distance and H is the mining depth. When scaling occurs, it will influence the factor of safety of the pillars. The factor of safety of a pillar can then be written as:

$$\text{Safety factor } (S_n) = 3.5\frac{(w-d)}{h}\left[\frac{(w-d)^2}{0.025HC^2}\right] \quad (2.5)$$

where d is the scaling distance of the pillar. In order to determine the critical scaling distance d_c , the minimum safety factor S_m at which failure would occur can be written as illustrated in equation (2.6). This was derived from equation (2.5) by assuming a value of S_m= 0.4. To determine the average rate of scaling for each pillar at the time of failure R, when the actual life of the pillar L is known, equation (2.7) was defined.

$$d_c = w - [0.00714S_m HhC^2]^{0.333} \quad (2.6)$$

$$R = \frac{d_c}{L} \quad (2.7)$$

This makes an important assumption and that is that the rate of scaling can be adequately defined by an “average” rate. The rate may possibly be more similar to an exponential decay and this is discussed later in this dissertation. The database used for his study was an extended database which included collapsed pillars from the weak coal areas. It did not include pillars that failed due to roof or floor failure, pillars that failed less than one year after mining occurred, and where the life of the pillars could not be determined owing to data not being available. The database included 51 cases of pillar failures and is shown in Figure 2-20.

Appendix A: Data base of failed pillars used for the time of failure study

In this appendix, the prefix 's' in the case numbers refers to cases collected by Salamon and Munro (1967), 'm' refers to cases collected by Madden and 'n' refers to cases collected after 1995.

Case no.	Colliery	Seam	Coal Field	Depth	Pillar width	Bord width	Mining height
s12	Coronation	W1	Witbank	25.9	3.7	8.5	3.1
s16	M Steam	W2	Witbank	21.3	4.0	8.2	4.6
s17	Wolvekrans	W2	Witbank	29.6	5.2	7.0	5.5
s40	Wolvekrans	W2	Witbank	33.5	6.1	6.7	5.5
s41	Crown Douglas	W2	Witbank	30.5	4.6	7.6	3.7
s57	Koornfontein	W2	Witbank	88.4	7.2	6.6	4.9
s116	Waterpan	W2	Witbank	61.0	6.1	6.1	4.6
s118	Waterpan	W2	Witbank	57.9	6.1	7.6	4.0
m149	Koornfontein	W2	Witbank	90.0	7.5	6.0	4.8
m151	Tweefontein	W2	Witbank	62.0	7.5	6.4	4.0
m162	Tweefontein	W2	Witbank	62.0	7.3	6.2	4.0
m166	Tweefontein	W2	Witbank	62.0	6.1	6.1	4.0
m167	Tweefontein	W2	Witbank	62.0	6.1	6.1	4.0
n171	Wolvekrans	W2	Witbank	41.0	6.4	6.4	6.2
n172	Wolvekrans	W2	Witbank	41.0	6.4	6.4	6.2
n173	Wolvekrans	W2	Witbank	41.0	6.4	6.4	6.2
n200	New Largo	W4	Witbank	43.0	4.8	6.2	2.8
s9	New Largo	W4	Witbank	30.5	3.4	6.4	2.6
s64	South Witbank	W4	Witbank	61.0	4.7	6.9	3.5
s119	W. Consolidated	W4	Witbank	41.1	4.3	6.4	3.1
m148	New Largo	W4	Witbank	28.5	3.8	5.8	2.7
m148a	New Largo	W4	Witbank	34.0	3.5	6.7	2.7
m148b	New Largo	W4	Witbank	34.0	3.5	6.7	2.7
m163	South Witbank	W4	Witbank	56.0	5.1	6.5	3.3
n198	New Largo	W4	Witbank	32.0	3.3	6.4	2.3
n199	New Largo	W4	Witbank	32.5	3.2	6.5	2.1
s42	South Witbank	W5	Witbank	53.3	5.2	6.4	3.7
s55	Blesbok	W5	Witbank	68.6	3.4	5.8	1.5
s58	South Witbank	W5	Witbank	57.9	5.2	6.4	5.5
m165	Springbok	W5	Witbank	22.0	3.5	6.5	1.6
n174	Matla	W5	Witbank	35.5	5.5	5.5	2.2
n185	Umgala	Alfred	Utrecht	101.0	9.0	6.0	3.8
n186	Umgala	Alfred	Utrecht	100.0	8.5	6.5	3.3
n187	Umgala	Alfred	Utrecht	97.0	9.0	6.6	3.7
n188	Umgala	Alfred	Utrecht	51.5	6.0	6.0	3.9
s66	Springfield	Main	South Rand	193.2	15.9	5.5	5.5
s67	Springfield	Main	South Rand	184.7	15.9	5.5	5.5
s122	Springfield	Main	South Rand	167.6	15.9	5.5	5.5
m168	Springfield	Main	South Rand	165.7	15.0	5.0	5.9
m169	Springfield	Main	South Rand	195.0	17.0	6.0	4.9
m170	Springfield	Main	South Rand	205.0	17.0	6.0	5.9
s126	Vierfontein	Main	Free State	87.8	6.1	6.1	2.0
n175	Springlake	Bottom	Klip River	70.0	7.5	5.0	1.8
n176	Springlake	Bottom	Klip River	63.5	7.5	5.0	2.1
s120	Cornelia	OFS1	Vaal Basin	128.0	9.8	5.5	3.7
m157	Sigma	OFS2	Vaal Basin	112.0	10.6	6.5	2.8
m159	Sigma	OFS2	Vaal Basin	108.0	10.6	6.5	3.2
n180	Sigma	OFS3	Vaal Basin	82.0	10.0	5.0	2.8
n181	Sigma	OFS3	Vaal Basin	96.0	12.0	6.0	2.9
n184	Sigma	OFS2a	Vaal Basin	112.0	11.5	5.5	2.9
n196	Sigma	OFS2a	Vaal Basin	104.0	12.0	6.0	3.0

Figure 2-20. Failed coal pillar database of 51 pillars (after Van der Merwe, 2003).

According to Van der Merwe's (2003) study, by comparing the factors of safety and the actual pillar life of the pillars in the database, there seemed to be no correlation between these two parameters. The majority of the failures occurred within 10 years after the pillars were cut. To determine the average rate of scaling, equations (2.6) and (2.7) were used for the failed pillars. It was concluded that there was no correlation between the scaling rate and the pillar widths, width-to-height ratio, safety factor, and pillar stress. He plotted the relationship between time and the scaling rate as illustrated in Figure 2-21. This graph is confusing as the time to failure is used to calculate the average scaling rate. It is therefore not two independent parameters plotted in the graph and this requires further examination.

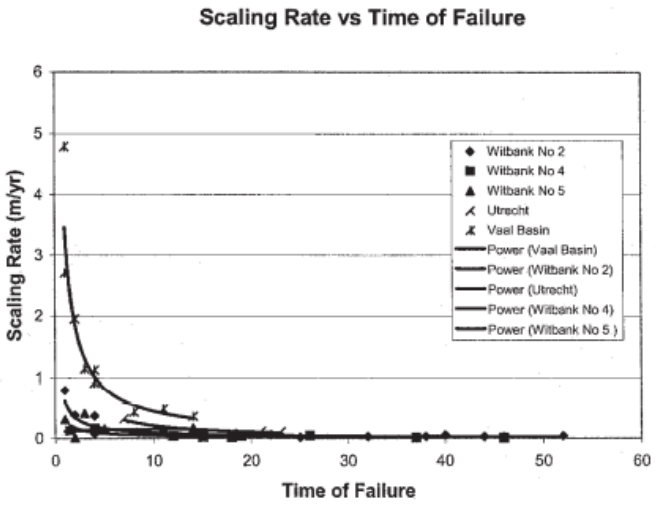

Figure 2-21. The relationship between the scaling rate and the time of failure (after Van der Merwe, 2003).

Van der Merwe (2003) indicated that the scaling rate has an inverse relationship to time and a direct relationship to the mining height. Figure 2-22 indicates the relationship between the scaling rate and the mining height over time (h/T) for different mining areas.

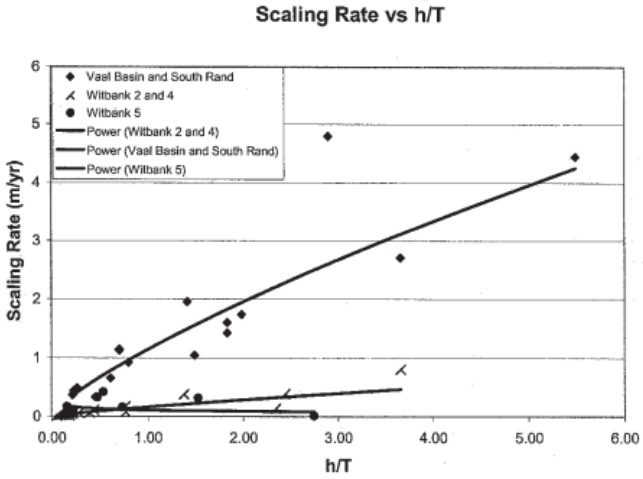

Figure 2-22. The relationship between the scaling rate and the parameter h/T (after Van der Merwe, 2003).

Van der Merwe (2003) proposed the following relations based on the information in Figure 2-22:

$$R = m\left[\frac{h}{T}\right]^{x} \tag{2.8}$$

where x and m are dimensionless constants. This is an awkward equation as the rate will not have units of (length/time) unless $x = 1$. For the different areas, equation (2.8) was fitted to the data and the values are and the correlation coefficients are illustrated in Table 2-6.

Table 2-6. The correlation coefficients, m and x values for the different mining areas (after Van der Merwe, 2003).

	m-Value	*x*-Value	R^2
Vaal Basin	1.3888	0.804	0.94
Witbank No. 2 and 4 Seams	0.1624	0.8135	0.81
Witbank No. 5 Seam	0.105	-0.3061	0.09

In order to predict the time of failure T, equations (2.7) and (2.8) were combined. The life of the pillars is given by:

$$T = \left[\frac{d_c}{mh^{x}}\right]^{\frac{1}{1-x}} \tag{2.9}$$

It is, however, not clear that the right hand side of equation (2.9) has units of time as m and x are dimensionless and the pillar height and scaling distance will be measured in metres. Van der Merwe (2003), determined the life spans of the pillars that are known to have failed in different areas, and the Witbank No. 5 seam results are illustrated in Figure 2-23. Van der Merwe (2003) concluded that, as the time of failure depends on the maximum amount of scaling, it allows the safety factor to indirectly come into play as it relates to factors such as the load acting on the pillar and the width-to-height ratio.

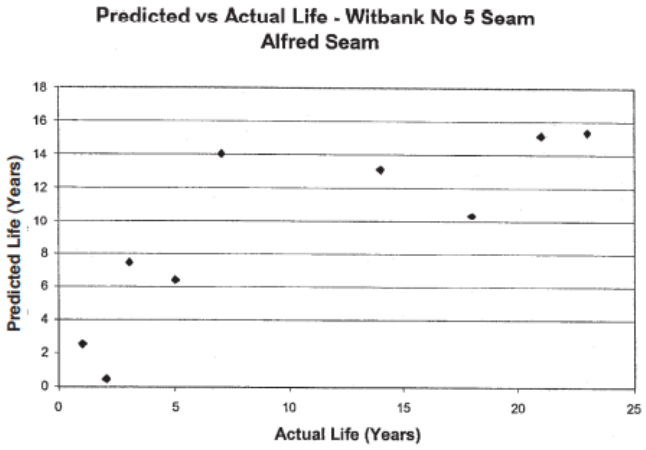

Figure 2-23. A comparison between the predicted and the actual life of the failed pillars in the Witbank No 5 seam (after Van der Merwe, 2003).

This study concluded that all pillars scale and that only some pillars will fail immediately. It was assumed by Van der Merwe (2003), that there was a specific minimum size of a pillar that relates to a minimum safety factor whereby a pillar will fail. He assumed this minimum safety factor was 0.4 and mentioned there was no good data was available. With the known minimum safety factor, the scaling distance could be determined as well as the average scaling rate based on the lifespans of the pillars. This formed the basis of the pillar life prediction method. However, it is important to consider the assumptions made and some of the equations appear not to be dimensionally correct.

2.3.4.2 Study 2 - Verification of Pillar Life Prediction Method

Further verification of the pillar life prediction described above was conducted by Van der Merwe (2004). Pillar measurements were done as part of this verification. The position of measurement had to be selected as the pillars had different shapes as illustrated in Figure 2-24. The shapes of pillars will differ depending on the location and the direction of scaling. It was found that shape (a), was recorded, but it was not common. Shapes (b), and (c), were found in areas where planes of weakness were present in the coal. Shape (d) was found where the pillar failure mode was dominated by prominent slips. The most common shape observed underground was shape (e), where maximum scaling was at the mid-height of the pillar. A decision was therefore made to measure at mid-height, except where the pillars were distorted into a completely different shape.

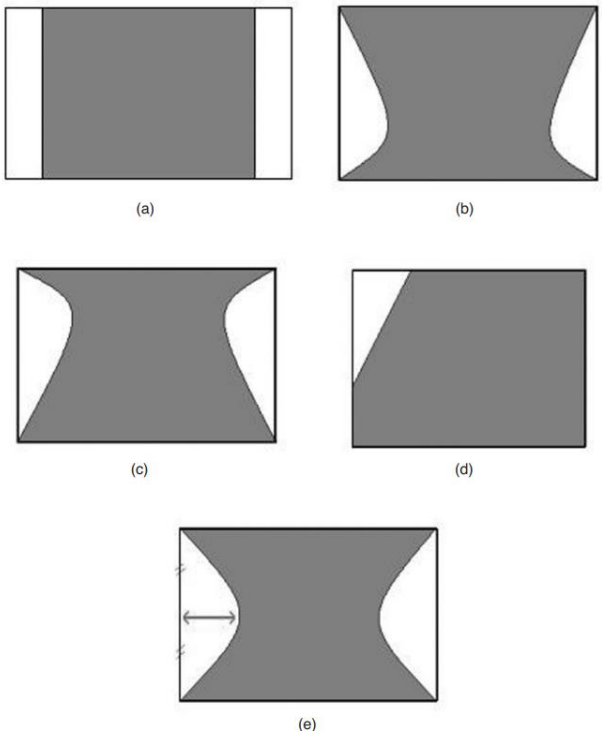

Figure 2-24. Different shapes of pillars after scaling occurred (after Van der Merwe, 2004).

From the measurements recorded, it was found that there is no significant difference in the scaling distance on the different sides of the pillars and that pillar corners do not scale more than the mid-pillar areas. It was therefore assumed that the scaling measurements taken on one side of the pillar could be used for the others as well.

For each pillar in the database, the average scaling rates were determined based on when the pillars were first cut. This was then compared to the predicted rate as described in the paper written by Van der Merwe (2003). It was confirmed that there is a trend in the inferred data and this is shown in Figure 2-25 for the No 2 and 4 seams.

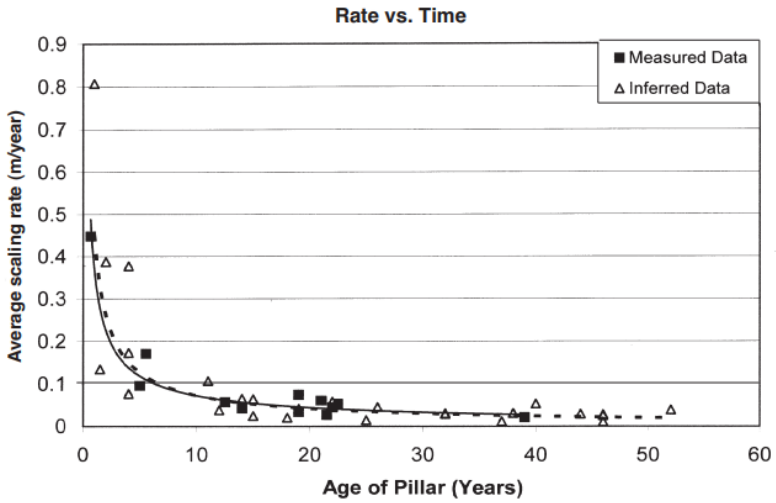

Figure 2-25. A comparison of the average scaling rate and time between the measured data and the inferred data (after Van der Merwe, 2004). The correlation coefficient was determined to be 0.98.

The expression for the rate of scaling for the No 2 and 4 seams is given in equation (2.10) where h is the mining height and T is the time in years.

$$R = 0.1624 \left[\frac{h}{T}\right]^{0.8135} \quad (2.10)$$

The predicted and the measured scaling rates are given in Figure 2-26.

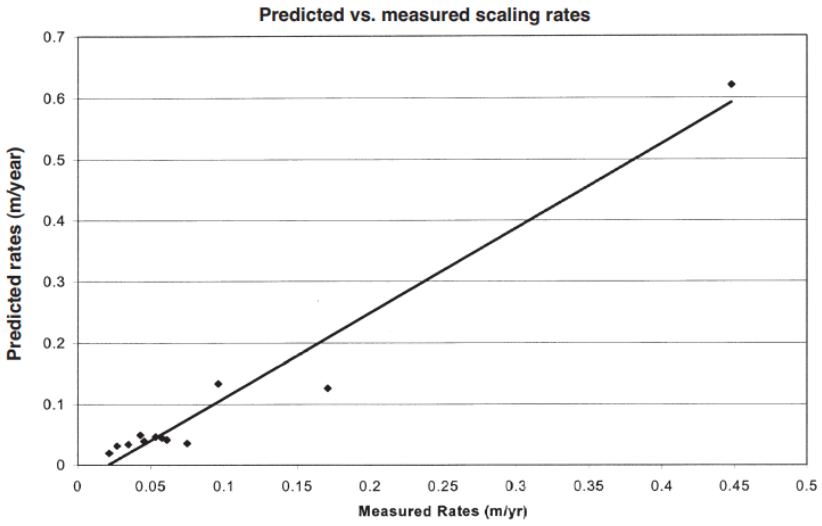

Figure 2-26. A comparison between the predicted and measured scaling rates (after Van der Merwe, 2004).

This study only focused on the rate of scaling and not the mechanism of pillar failure. Further research should be conducted to determine these mechanisms.

2.3.4.3 Study 3 - Review of Coal Pillar Life for the Witbank and Highveld Coal Seams

Van der Merwe (2016) conducted an additional study based on a new database of pillars and pillar strength equations. For this study, direct measurements were taken of pillars that showed signs of scaling. The data is shown in Figure 2-27. The two constants m and x are 0.1799 and 0.7549 respectively.

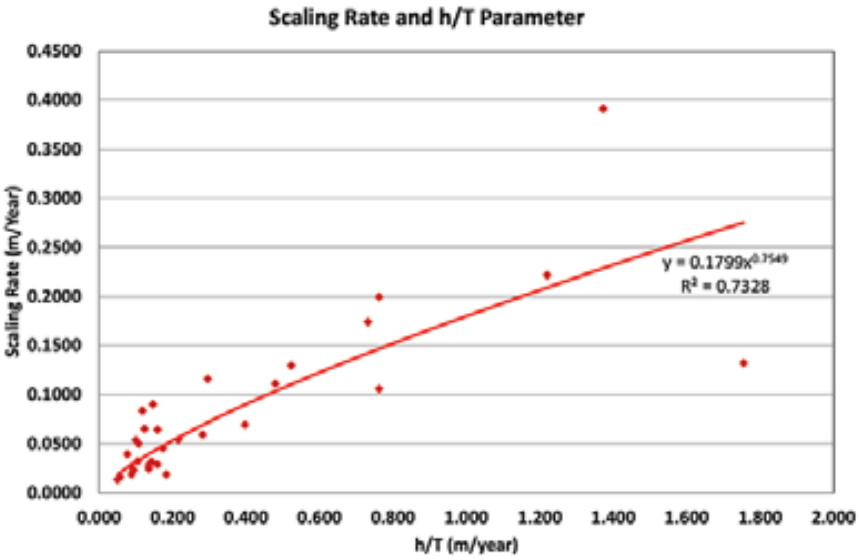

Figure 2-27. The scaling rate as a function of the h/T parameter (after Van der Merwe, 2016).

The revised expression for the rate of scaling is given in equation (2.11) where h is the mining height and T is the time in years.

$$R = 0.1799\left[\frac{h}{T}\right]^{0.7549} \tag{2.11}$$

2.3.4.4 Study 4 - Coal Pillar Strength Analysis Based on the Size at the Time of Failure

A shortcoming of the statistical back-analysis of coal pillar strength is that it uses the pillar dimensions when the pillars are cut and does not take the time-dependent pillar scaling, resulting in smaller sizes, into account. Van der Merwe (2019) developed a new pillar strength formula that included the time-dependent width of the pillars w_T. He did this by applying the rate of pillar scaling in the databases of failed and intact coal pillars. This new formula is given by:

$$\sigma_{S,T} = k_T \frac{{w_T}^{\alpha}}{h^{\beta}} \text{ [MPa]} \tag{2.12}$$

This was expanded by him to give the equation

$$\sigma_{S,T} = k_T \frac{(w_0 - mh^x T^{1-x})^\alpha}{h^\beta} \text{ [MPa]} \quad (2.13)$$

where:

w_0 = the as-mined pillar width

m = constant, 0.1799

h = mining height

T = age of pillars (years)

The new formula predicts greater pillar strength that found from previous statistical analyses. The load acting on the pillar can be expressed as:

$$\sigma_{L,T} = \frac{0.025HC^2}{{w_T}^2} \text{ [MPa]} \quad (2.13)$$

where:

H = depth to the floor of mining (m)

C = pillar centre distance (m)

w_T = reduced pillar width (m)

The factor of safety SF_T at any given point of time is

$$SF_T = \frac{\sigma_{S,T}}{\sigma_{L,T}} \quad (2.14)$$

Van der Merwe (2019) considered the probability of failure as an accurate indicator of the stability of the pillars than the factor of safety. The probability of failure is determined by comparing the number of failed cases to the number of total cases in each interval of the factor of safety. As the pillar reduces in size, the probability of failure increases. He derived a new probability of failure equation and this is given in equation (2.14).

$$PoF = \exp(-0.93 SF_T^{4.28}) \quad (2.14)$$

The increase in the probability of failure is shown in Figure 2-28

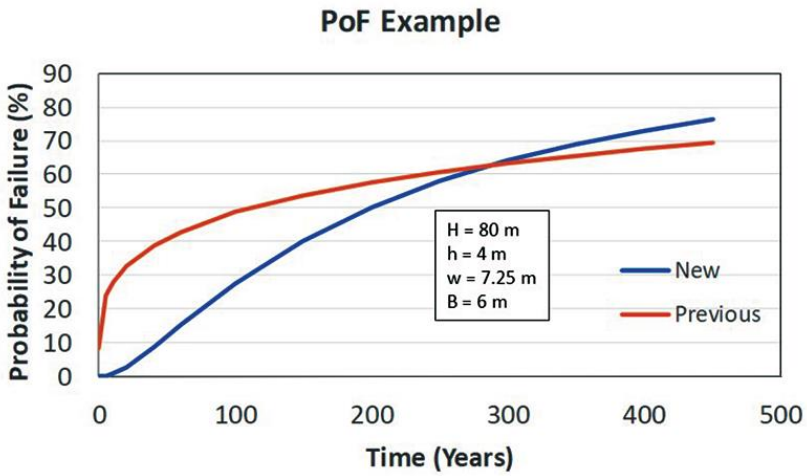

Figure 2-28. Example of comparison of the increase in probability of failure over time (after Van der Merwe, 2016).

2.3.5. Numerical Investigations of Time-Dependent Pillar Failure

Numerical modelling to simulate time-dependent pillar failure is an alternative method to study this kind of behaviour. Napier and Malan (2012) simulated the time-dependent crush pillar behaviour in South African platinum mines. Although this was done for crush pillars and not stable elastic pillars, the numerical technique is of value and is also used in this dissertation. The time-dependent limit equilibrium model in a boundary element code can simulated the progressive scaling of the pillar edges. This approach was used in this dissertation and detailed information is given in later chapters.

A further example of complex modelling of the time-dependent scaling of pillars is given in the paper by Sainoki and Mitri (2017). A non-linear rheological model was used in the model. The numerical study considered pillar failure occurring over a long period of time. These types of studies are especially important when there is a risk of surface subsidence caused by the collapse of pillars. The numerical code used for their study was FLAC3D and the model is illustrated in Figure 2-29. Symmetry was used for this model.

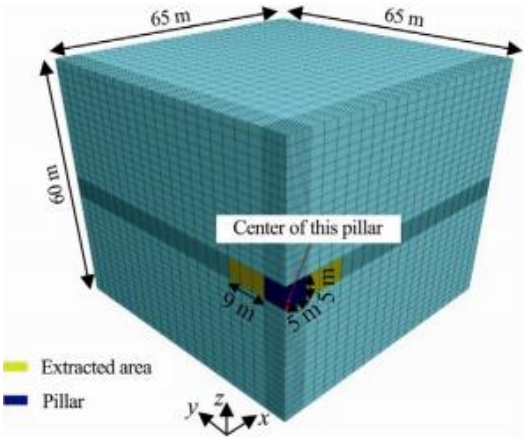

Figure 2-29. Numerical model of the pillar simulated using FLAC3D (after Sainoki and Mitri, 2017).

The simulated damage in the pillar is shown Figure 2-30. Note how the depth of scaling of the pillar increases with time. This clearly illustrates the value of these kinds of models, but a major drawback is that the complex constitutive models required for this type of modelling is extremely difficult to calibrate.

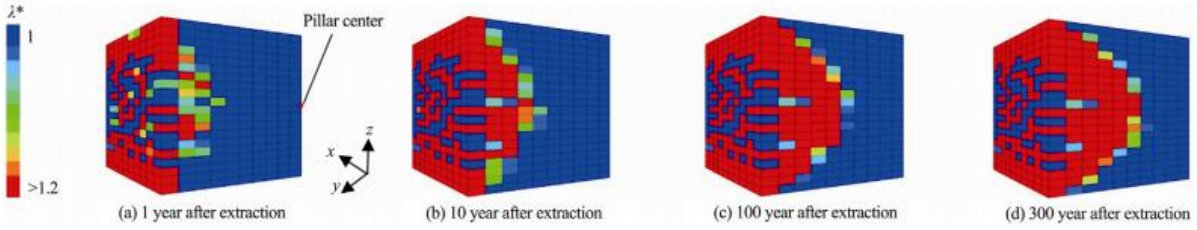

Figure 2-30. Simulation of the time-dependent scaling of a pillar (after Sainoki and Mitri, 2017).

A numerical modelling study was also conducted by Wang and Cai (2021) to investigate the time-dependent deformation of pillars. A grain-based time to failure model (GBM-TtoF) was used to study the time-dependent deformation of a pillar. The model geometry simulated is illustrated in Figure 2-31. To govern the creep deformation of the grains in the model, the Burgers creep model was adopted (Aydan et al., 2013). Figure 2-32 illustrates the GBM-TtoF model and the strength degradation (Wang and Cai, 2021).

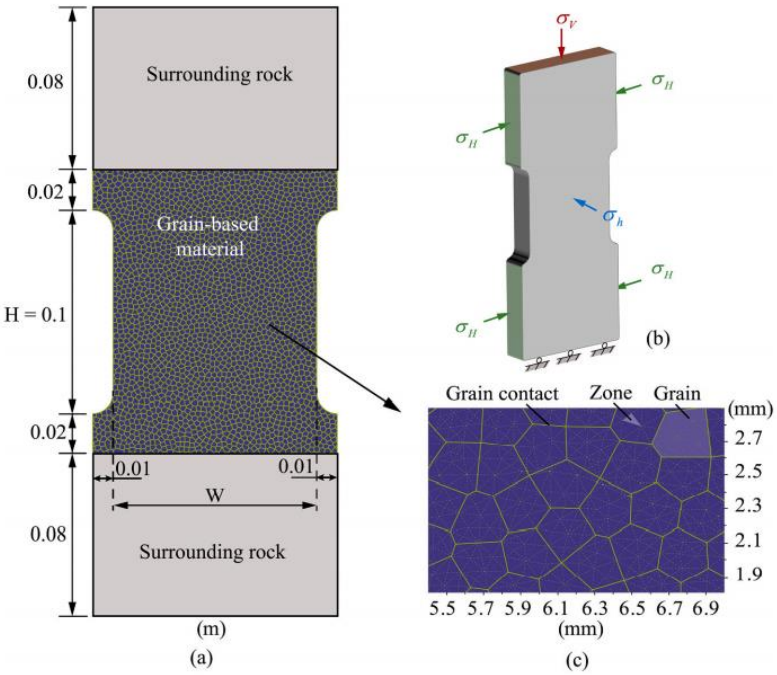

Figure 2-31. Grain-based pillar model, illustrating the dimensions, loading conditions, and an enlarged view (after Wang and Cai, 2021).

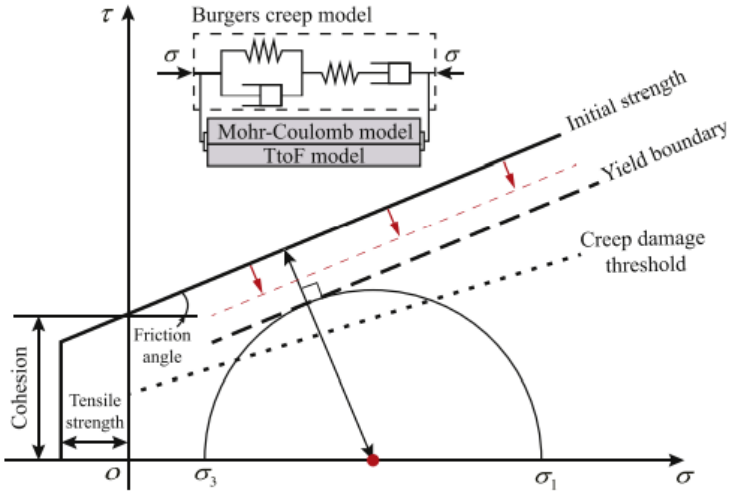

Figure 2-32. The GBM-TtoF model illustrates the strength degradation (after Wang and Cai, 2021).

Figure 2-33 below illustrates the time-dependent crack initiation and the pattern of propagation for the two different models. Again, it was illustrated that the time-dependent pillar spalling can be simulated, but that calibration of the model will be difficult for full-sized pillars. These models are typically also not compared with underground observations and actual pillar behaviour.

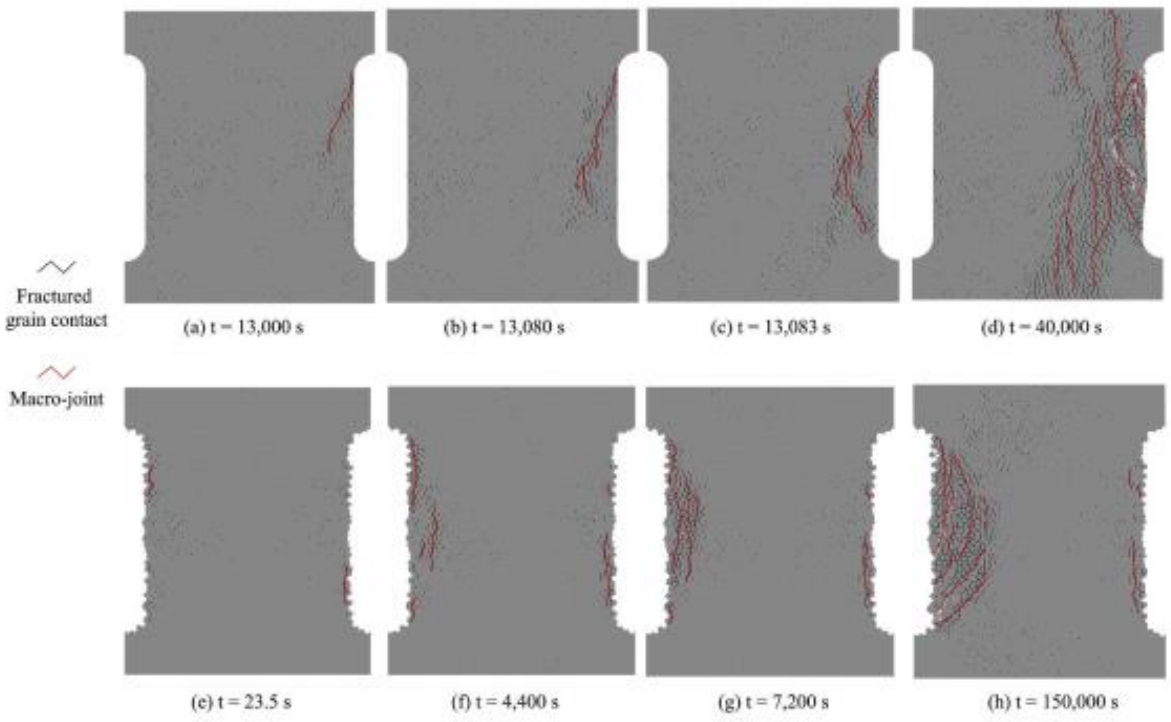

Figure 2-33. Numerical modelling of two different boundary profiles illustrating the time-dependent crack initiation and propagation, (a-d) smooth boundary profile, and (e-h) rough boundary profile (after Wang and Cai, 2021).

2.4. Summary

From the literature study, it is clear that extensive research has been conducted on the time-dependent failure of coal pillars in South Africa. These studies are exclusively empirical in nature and there was no attempt to conduct numerical modelling of the time-dependent scaling. In contrast, almost no work has been conducted on hard rock pillars. Even though workers such as Martin and Maybee (2000) mention that: "*Observations of pillar failures in Canadian hard-rock mines indicate that the dominant mode of failure is progressive slabbing and spalling*", the time-dependent nature of this progressive slabbing was not quantified. Complex numerical modelling to simulate the time-dependent scaling of hard rock pillars have been done in the past, but these models are difficult to calibrate and, in these publications, the results are typically not compared to actual pillar behaviour underground. One of the key objectives of the author was therefore an attempt to simulate time-dependent scaling of pillars in a hard rock bord and pillar mine and to compare the numerical results with field observations.

The next chapter discusses the pillar observations made by the author at BRMO.

CHAPTER 3

PILLAR OBSERVATIONS

The observations made for a number of pillars is presented in this chapter. Six different areas at Nchwaning III Shaft were identified for monitoring and numerical modelling. Note that a large amount of data was collected, but only the most relevant information for some pillars is given below. Appendix A contains additional information and the photographs for each pillar are given in Appendix B. This additional information is included in the dissertation as the literature survey indicated that the older pillar databases for other commodity types are often rather obscure. Unfortunately photographs of the conditions of the pillars recorded many years ago are not readily available and therefore the additional information is provided in the Appendices as a reference to future researchers.

“Modified” rock mass ratings were done on the selected pillars based on the RMR and Q-rating methodologies. The general methods to do these rock mass ratings could not be followed as for example, drill cores for each pillar was not available to do RQD ratings, and it was simply estimated based on the spacings of the joints. It was nevertheless very valuable to compare the rock mass quality of pillars in different areas. This data is given in Appendix A. The classification given by Esterhuizen et al. (2006), shown in Figure 3-1, was also useful to classify the amount of damage observed. Although this work was done for limestone pillars in the US, it was found particularly useful at BRMO. Esterhuizen et al. (2006) noted that pillars with condition ratings of 1 to 3 can typically be made safe by using mesh and bolting and by doing regular barring (scaling). Pillars with a condition rating of 4 and 5 typically get barricaded off by mine operators. Alternatively, extensive support systems are installed in these areas to maintain the integrity of the pillars.

For this study, areas with different managanese grades and products were studied as it seems that these grades are typically associated with different joint spacings, which was a key parameter that defined the ground control districts. Interestingly, it therefore seems as if the managanese grades are a good proxy of the ground conditions at BRMO.

Table 1. Pillar Stress Rating

Rating	Sketch	Description
1 None	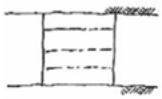	No stress related fracturing or spalling observed. Joint or blast related damage may exist.
2 Minor	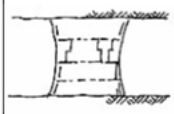	Minor slabs or spalling, fractures through intact rock at corners, pillar corners and walls may be concave, does not typically deteriorate after initial mining and scaling.
3 Moderate	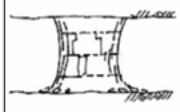	Slabbing, onion-skin, fractures more than 1m long, joints opened, corner damage, pillars may need re-scaling after initial development. Original square pillar shape maintained.
4 Severe		Spalling to hourglass shape. Open cracks in pillar more than 1m long, debris around pillar, original square shape of pillar no longer visible, saw tooth slabs on ribs
5 Very Severe		Formation of large open cracks, extreme hourglass. Pillar likely lost most of its residual strength.

Table 2. Geological Structure Rating

Rating	Sketch	Description
1 None		Less than 0.3 m (1 ft) of joint related fallout during blasting. Blast damage may exist.
2 Minor		Pillar shape affected by 0.3- 1 m (1-3 ft). Some joint or bedding fallout during blasting, may form step at bedding planes. No or little further fallout after initial scaling.
3 Moderate		Pillar shape affected by 1-3 m (3-10 ft). Joint or bedding controlled fallout. Fallout can continue after initial mining and scaling.
4 Severe		Large block fallout >3 m (>10 ft). Pillar shape compromised by large block extrusion or block sliding on steep plane. Falls continue after initial mining and scaling.
5 Very Severe		Pillar bisected by through-going structure dipping at more than 35 degrees. Potential or actual loss of top half of pillar. Pillar strength depends on discontinuity strength.

Figure 3-1. Pillar rating system proposed for limestone (after Esterhuizen et al., 2006).

3.1. Nchwaning III Pillar Investigation and Observations

The six areas selected for monitoring and modelling at Nchwaning III Shaft are illustrated in Figure 3-2. Area 1 was of particular interest owing to extensive pillar scaling recorded by the mine in this area. This was also noted for some pillars in Area 6. Selected pillars in Areas 2 to 5 were marked with paint to monitor for time-dependent pillar scaling (see Chapter 6). These areas were visited during May and August 2021. The pillars in Area 6 were already covered with shotcrete in 2020 and additional monitoring of time-dependent scaling was not possible in this area. This area was nevertheless valuable as it was used to do a preliminary “calibration” of the limit equilibrium model.

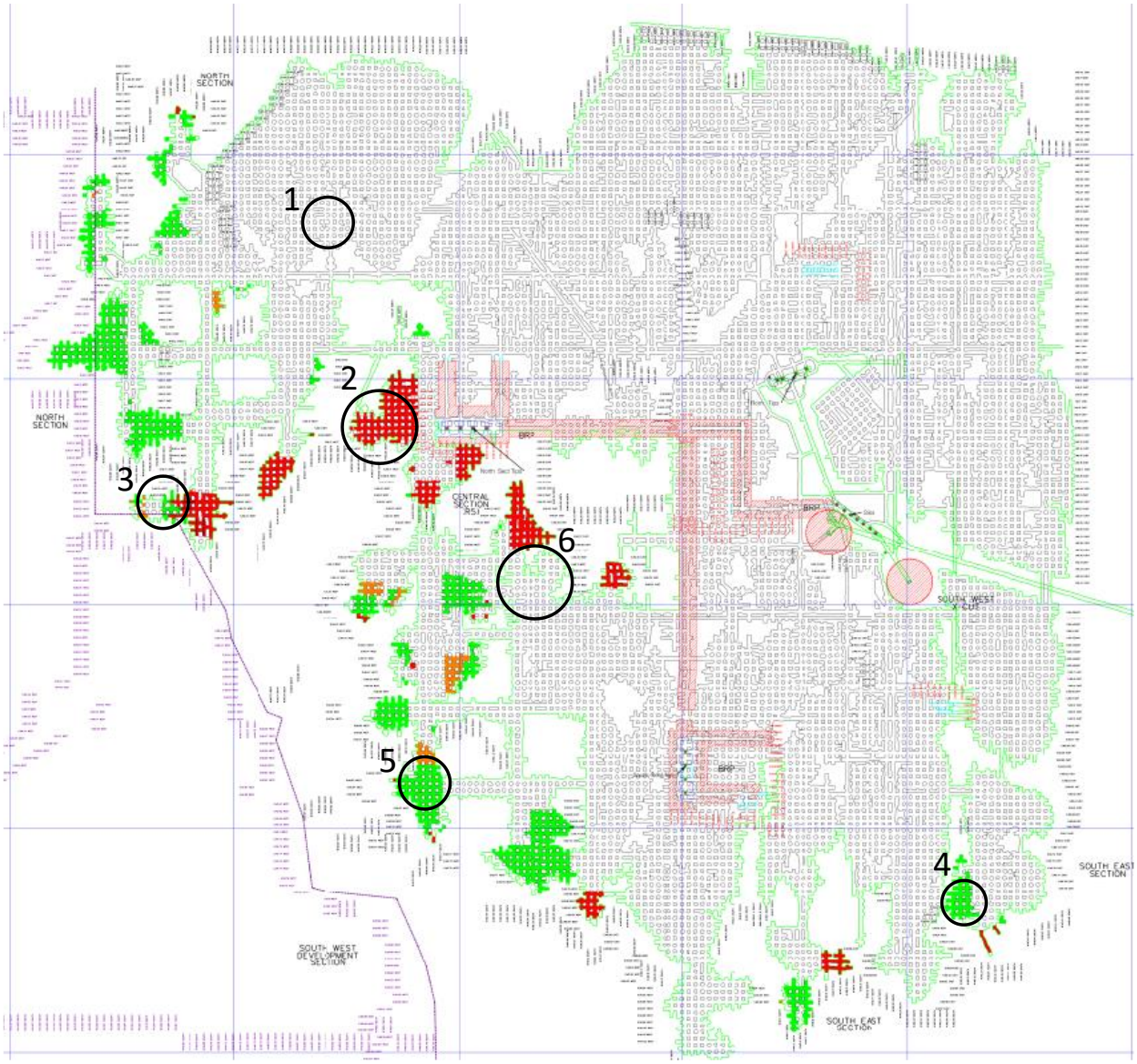

Figure 3-2. Areas selected for monitoring and modelling at Nchwaning III Shaft.

According to mine personnel, the areas where the pillars show signs of scaling, predominately occur in the so-called low-grade “R5 product” areas. This is a naming convention for one of the manganese products mined with a guaranteed minimum manganese percentage of 38%. It is a lumpy product with 40% of the product size between size 63 mm and 32 mm and 37% between 32 mm and 12 mm. The areas were selected to ensure that Areas 1, 2 and 3 are in the R5 area and Areas 4 and 5 are in high-grade areas. No pillar scaling was observed in the high-grade areas. The product mix at Nchwaning III is illustrated in Figure 3-3 and the six areas shown in Figure 3-2 are also indicated in Figure 3-3. The orange areas are the R5 product areas. Large portions of the remaining resources are the R5 product type and poor pillar conditions may be expected in many of the future mining areas. Figure 3-4 illustrates the manganese grade. The R5 product is part of the orebody where the grades are less than 42% manganese (blue area).

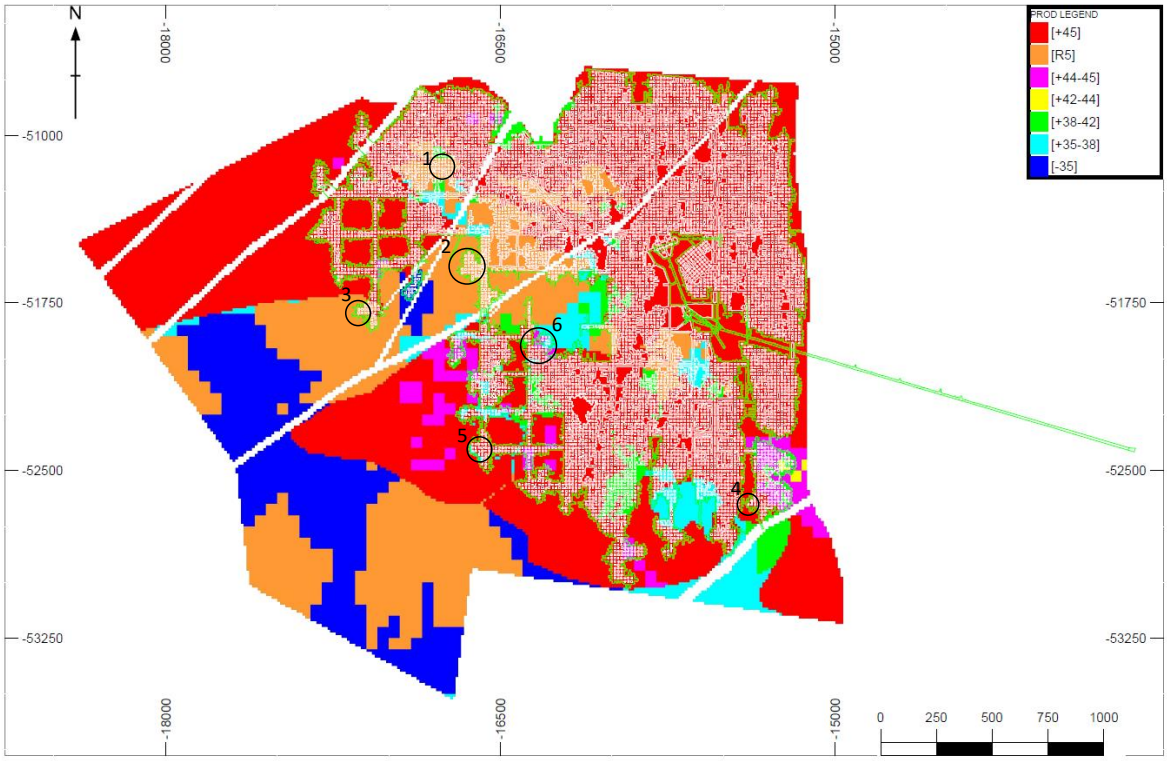

Figure 3-3. Areas selected for monitoring and modelling at Nchwaning III Shaft. The colours indicate the different types of products.

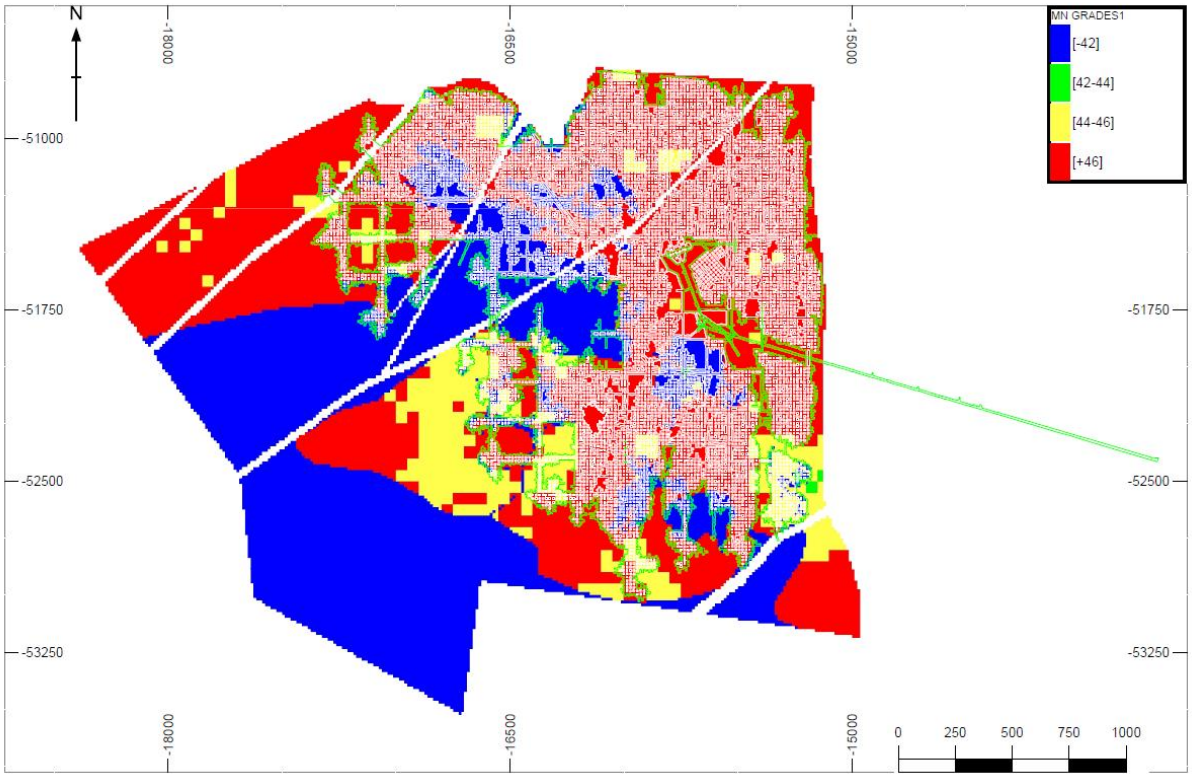

Figure 3-4. Manganese grade distribution at Nchwaning III Shaft.

3.1.1. Measurements conducted

To study the time-dependent pillar scaling at BRMO, the author established a number of monitoring stations. A problem with any type of “quantitative” monitoring of time-dependent pillar scaling is that stable reference points are required. Distance measurements from these stable reference points to particular points on the pillar sidewalls are required over a period of time. As the pillar sidewalls are subjected to scaling, however, it is difficult to ensure that the measurements are conducted between the same positions on the pillar and the reference points. As a crude attempt to overcome this measurement problem, large crosses were painted on the sidewalls of the pillars, as well as the pillars adjacent to the pillar being monitored (Figure 3-5). The distance between the painted crosses of opposing pillars was then measured using a distomat (Figure 3-6). If parts of a cross are lost owing to scaling, the centre position can still be estimated from the remaining portions of the lines. Although both pillars scale, the scaling distance will then be simply estimated to be half the increase in measured distance. Although rather crude, this method proved useful to indicate that almost no scaling occurred during a three-month monitoring period.

Figure 3-5. Measurement point painted on pillar N3_1 at Nchwaning III shaft. The photograph on the left was taken on 6 May 2021 and the photograph on the right on 18 August 2021. The lines were still pristine on the second date and no scaling occurred during this three-month period.

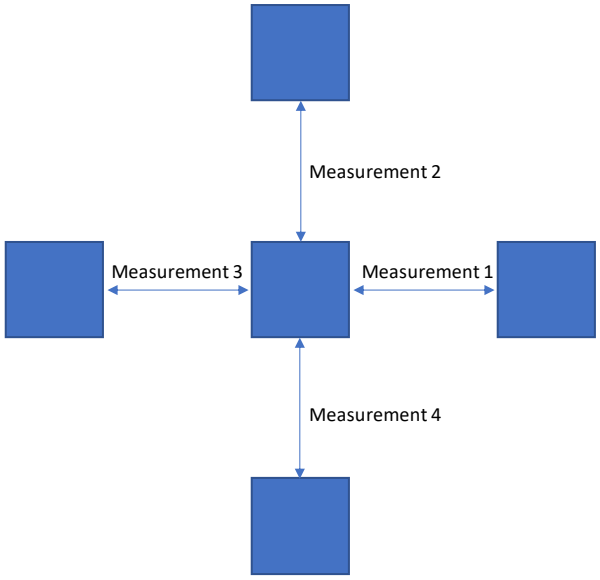

Figure 3-6. Measurements between the reference crosses painted on the pillars.

Figure 3-7 and Figure 3-8 illustrates additional photographs of particular pillars taken approximately three months apart. Some localised scaling could be seen in some areas of the pillars, but in most cases, no major scaling could be seen during this period. This was even true for pillar N3_1, which has a low rock mass rating. For pillar N3_25 (Figure 3-8) many portions of the white lines have already scaled away before this pillar was selected for monitoring. It therefore appears that there is a rapid rate of scaling soon after the pillar is formed, which gradually decreases with time.

Figure 3-7. Almost no scaling was recorded for most of the pillars over a three-month monitoring period. As an example, this is pillar N3_1 at Nchwaning III Shaft. The photograph on the left was taken on 6 May 2021 and the photograph on the right on 18 August 2021.

Figure 3-8. Pillar N3_25 at Nchwaning III Shaft. The photograph on the left was taken on 6 May 2021 and the photograph on the right on 18 August 2021. The broken white lines give an indication of a time-dependent scaling process, but this occurred prior to the monitoring done for this study.

A rock mass rating was conducted in all the areas visited to link this rating with the observed pillar behaviour. These results are discussed in Section 3.2. As described above, it is important to note that no drill core for the pillars were available and therefore the RQD was approximated along a horizontal line on the pillar edges, so it is essentially the vertical joint spacing. The dimensions of the experimental pillars were also measured to determine if the dimensions of the pillars change over time. The scaling distance was measured similar to the method proposed by Van der Merwe (2004) illustrated in Figure 2.24(e).

The four sides of a pillar were marked as A, B, C and D. Notation such as N3_1D therefore refers to Nchwaning III (3) Shaft, pillar 1, side D.

3.1.2. Experimental Area 1

Figure 3-9 illustrates the layout of this area and the three pillars that were selected for monitoring to determine the rate of time-dependent scaling. Significant pillar scaling was observed in this area. These pillars were cut approximately 3 years before the monitoring was done. The joint spacing was small as indicated in the figures below. The high density of joints facilitated the extensive scaling of the pillars.

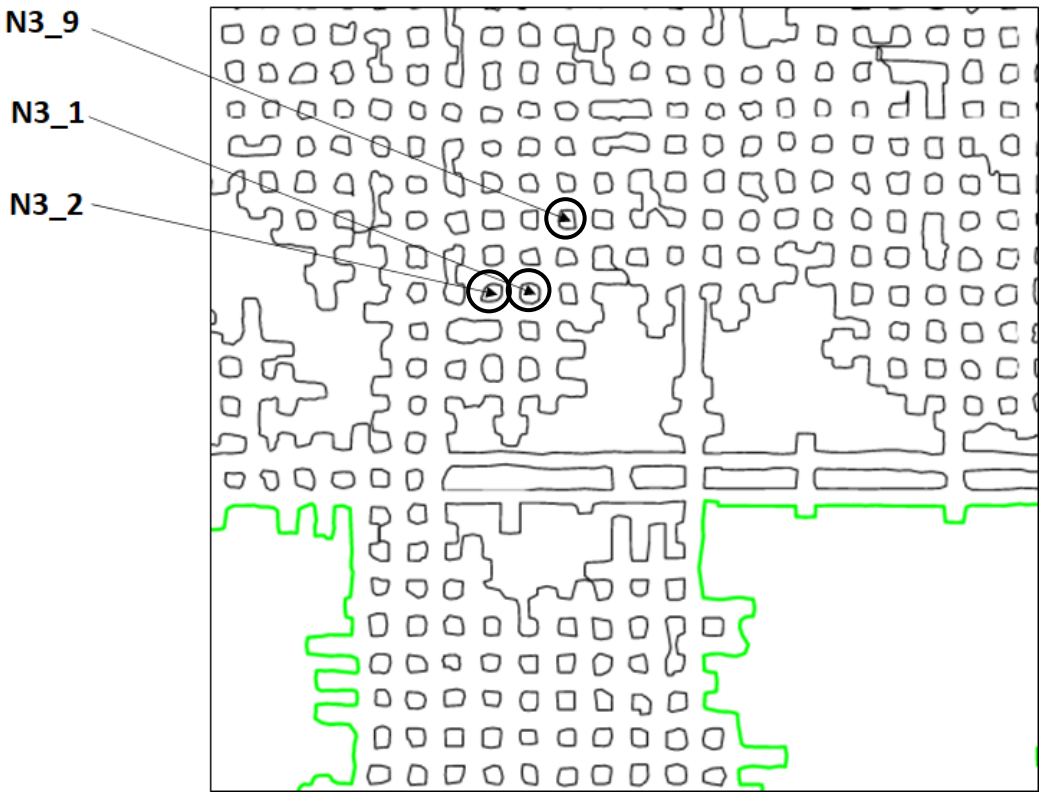

Figure 3-9. Enlarged view of monitoring Area 1.

Only pillar N3_9 is discussed below and the two additional pillars (N3_1 and N3_2) illustrated in Appendix A. The observed behaviour of the three pillars were essentially similar.

Pillar N3_9

The extensive scaling of this pillar is shown in Figure 3-10. Note the blocky nature of the scaling owing to the closely spaced, intersecting joint sets. The vertical joints are closely spaced and this spacing ranged from 1 cm to 5 cm in some areas (on N3_9B and N3_9D) to 15 cm to 30 cm on the other two sides. The spacing of the horizontal joints was approximately 30 cm, but also varies across the perimeter of the pillar. The pillar had an hourglass shape and the failed slabs seemed to bulge outwards in some areas. The joints were almost vertical and no shallow dipping joints were observed.

A rock mass rating was very difficult to do as there are significant changes in joint spacing over short distances and the pillars are heavily crushed in many areas. The small vertical joint spacings led to significant scaling and damage. Figure 3-11, Figure 3-12, and Figure 3-13 illustrate the variation of joint spacings. It was therefore difficult to estimate RQD along a horizontal line as it varies from less than 25% to approximately 50%.

Figure 3-10. Extensive scaling of pillar N3_9.

Figure 3-11. Side B of the pillar illustrates the closely spaced joint sets. This creates extensive scaling on the sides of the pillar.

Figure 3-12. Extensive scaling of pillar N3_9. The scaling is facilitated by the intersecting horizontal and vertical joint sets.

Figure 3-13. Spacing of the joints in pillar N3_9.

Figure 3-14 indicates that no scaling occurred between the time of the first and the second visit. Table 3-1 summarises the measurements recorded for pillar N3_9. This pillar was established between March and June 2018. Some variation of bord spans was recorded, but this was attributed to measurement error as the photographs indicated that the measurement points were still intact.

From the measurements taken and the photographic evidence, it is clear that no measurable scaling of the pillar occurred during the two measurement dates.

Figure 3-14. Side A of pillar N3_9 at Nchwaning III shaft observed on the 4th of May (left) and on the 18th of August 2021 (right).

Table 3-1. Measurements for pillar N3_9 in the R5 area. Measurements were taken on the 4th of May 2021 and on the 18th of August 2021. The variation in bord span is attributed to measurement error.

Pillar N3_9			
Bord span		Bord span measured on 2021/05/04	Bord span measured on 2021/08/18
	N3_9A to N3_10A	8.92 m	8.91 m
	N3_9B to N3_11A	6.71 m	6.98 m
	N3_C to N3_12A	9.50 m	9.49 m
	N3_D to N3_13A	8.10 m	8.05 m
Dimensions of pillar	Side of pillar	Width	Height
	N3_9A	7.21 m	4.50 m
	N3_9B	5.42 m	4.34 m
	N3_9C	5.67 m	4.40 m
	N3_9D	6.39 m	4.56 m
Approximate scaling distance and age	Side of pillar	Approximate scaling distance	Age of pillar (months)
	N3_9A	1.4 m	36
	N3_9B	0.7 m	36
	N3_9C	1.2 m	36
	N3_9D	0.9 m	36

3.1.3. Experimental Areas 2 and 3

These two areas are also located in the geotechnical area that produces the low-grade R5 product. The pillars that were selected for monitoring are illustrated in Figure 3-15. Pillars N3_15 and N3_20 are in Area 2 and pillar N3_25 is in Area 3. The pillars in Area 2 are in a better condition compared to the pillars of Area 1. This agrees with a slightly higher value for the rock mass ratings as illustrated in Section 3.2.

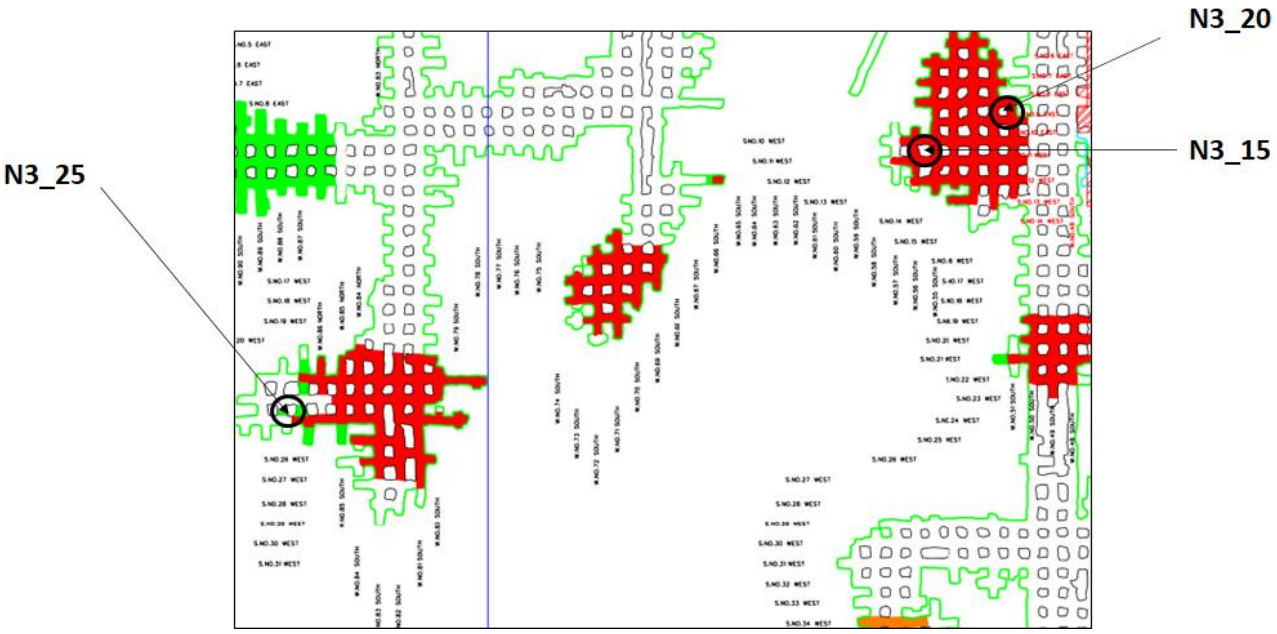

Figure 3-15. Enlarged view of monitoring Areas 2 and 3.

The observations for pillar N3_20 and pillar N3_25 are given below. Information regarding pillar N3_15 is given in Appendix A.

Pillar N3_20

For this pillar, closely spaced joints were observed and the spacing of the joints varies across the perimeter of the pillar from 1 cm to 5 cm. The horizontal joints were spaced between 15 cm to 80 cm. The pillar had an hourglass shape and was “blocky” owing to the intersection of the vertical and horizontal joints. A total number of three joint sets was observed. Figure 3-16 and Figure 3-17 illustrate the joint spacing on Sides A and C, respectively. Two sides of the pillar (Side B and C) illustrate a vertical joint spacing ranging from 1 cm to 5 cm.

Figure 3-16. The pillar corner at side A illustrates the vertical joints with a spacing of 1 cm to approximately 6 cm.

Figure 3-17. The horizontal joint spacing of side C ranges from 15 cm to 25 cm.

Table 3-2 illustrates the measurements recorded for pillar N3_20. This pillar was established in January 2021. The scaling of the pillar did not continue during the three-month monitoring period and this is illustrated in Figure 3-18.

Figure 3-18. Side A of pillar N3_20 at Nchwaning III shaft as photographed on the 6 May 2021 (left) and on 18 August 2021 (right).

Table 3-2. Measurements recorded for pillar N3_20. The variation in bord span is attributed to measurement error.

N3_20			
Bord span		Bord span measured on 2021/05/06	Bord span measured on 2021/08/18
	N3_20A to N3_21	7.60 m	7.59 m
	N3_20B to N3_22	7.37 m	7.36 m
	N3_20C to N3_23	7.33 m	7.45 m
	N3_20D to N3_24	6.97m	6.96 m
Dimensions of pillar	Side of pillar	Width	Height
	N3_20A	6.63 m	4.05 m
	N3_20B	6.37 m	4.70 m
	N3_20C	5.92 m	4.57 m
	N3_20D	6.40 m	4.58 m
Approximate scaling distance and age	Side of pillar	Approximate scaling distance	Age of pillar (months)
	N3_20A	0.33 m	4
	N3_20B	0.82 m	4
	N3_20C	0.63 m	4
	N3_20D	0.40 m	4

Pillar N3_25

For this pillar, the vertical joint spacing varies from 3 cm in some places to 10 cm. The horizontal joint spacing was observed to be between 10 cm to 15 cm. The spacing of the joint sets is difficult to determine as they vary across the perimeter of the pillar. On side B, a horizontal joint spacing of up to 50 cm was observed while it was up to 80 cm on side C. The intersecting horizontal and vertical joints create scaling in the form of small blocks (fist-size).

Pillar N3_25 had a lower rock mass rating than pillar N3_20 in Area 2. Views of N3_25 are illustrated in Figure 3-19, Figure 3-20, and Figure 3-21. The closely spaced joints result in the pillar edge breaking into small blocks (Figure 3-22). The rock mass rating of this pillar is comparable to that in Area 1. Overall, the pillar is still in a reasonable condition and the reason is probably that it is not as old as the pillars in Area 1. Area 1 was mined in June 2018, while pillar N3_25, was mined in February 2021. The stress acting on N3_25 and the pillars in Area 1 is approximately similar (refer to the numerical modelling in Chapter 4). It seems as if time-dependent scaling leads to the ongoing deterioration of the pillars.

Figure 3-19. Side A of pillar N3_25 illustrates the joint spacing in the vertical direction.

Figure 3-20. Complex jointing observed for pillar N3_25. Note the high density and curvature of the joints.

Figure 3-21. The vertical and horizontal joint spacing observed on side C of pillar N3_25. Note the varying joint spacing.

Figure 3-22. Small block sizes were found adjacent to pillar N3_25. These block sizes are controlled by the closely spaced joint sets.

Table 3-3 summarises the measurements recorded for pillar N3_25. This pillar was established in February 2021. Figure 3-23 confirms that no scaling occurred in the time period between the first and the second visit.

Figure 3-23. Side B of pillar N3_25 at Nchwaning III shaft as photographed on 6 May 2021 (left) and on 18 August 2021 (right).

Table 3-3. Measurements recorded for pillar N3_25. The variation in bord span is attributed to measurement error.

N3_25			
Bord span		Bord span measured on 2021/05/06	Bord span measured on 2021/08/18
	N3_25A to N3_26A	6.61 m	6.62 m
	N3_25B to N3_29A	7.12 m	7.16 m
	N3_25C to N3_28A	6.72 m	6.72 m
	N3_25D to N3_27A	9.30 m	9.20 m
Dimensions of pillar	Side of pillar	Width	Height
	N3_25A	7.75 m	4.54 m
	N3_25B	9.50 m	3.92 m
	N3_25C	6.03 m	3.80 m
	N3_25D	8.05 m	3.83 m
Approximate scaling distance and age	Side of pillar	Approximate scaling distance	Age of pillar (months)
	N3_25A	0.1 m	3
	N3_25B	0.5 m	3
	N3_25C	0.3 m	3
	N3_25D	0.5 m	3

3.1.4. Experimental Area 4

Area 4 was selected as a control area as it is located in a high-grade area and no pillar scaling was reported by the mine in this area. Two pillars were selected for monitoring are shown in Figure 3-24. The joint spacing is much larger than that observed in the R5 areas. The pillars are in a good condition and this is illustrated below.

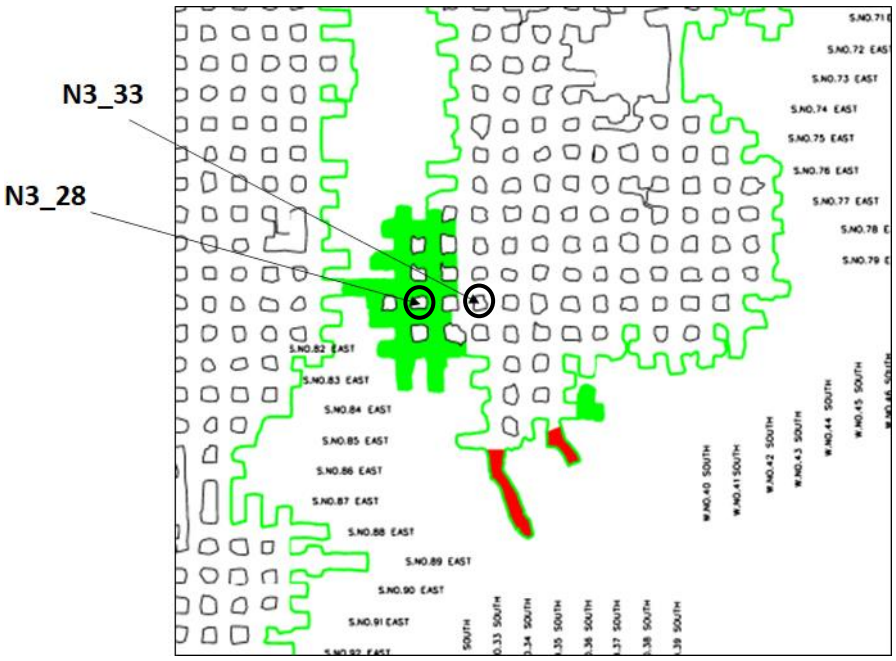

Figure 3-24. An enlarged view of Area 4 and the pillars selected for monitoring.

The data for pillar N3_28 is presented below and information regarding pillar N3_33 can be found in Appendix A. The characteristics of these two pillars were similar.

Pillar N3_28

The pillars in this "+45 grade product" area are in much better condition as compared to the R5 area. The vertical joints in this area are not prominent and almost no signs of scaling were observed. The spacing of the vertical joint sets was difficult to determine as they were only clearly visible on the corners. The vertical joint set on side C was approximately 20 cm and no random joints were present. The horizontal joints seem to be the prominent joint set with the joint spacing varying from 20 cm to greater than 50 cm. The corners of the pillar had an "hourglass" shape. Figure 3-25 and Figure 3-26 illustrate the variation of joint spacing in the pillar.

Figure 3-25. Side A of the pillar illustrates the horizontal joints with an approximate spacing of 50 cm.

Figure 3-26. The vertical joint spacing is observed on side C of the pillar with a spacing of approximately 20 cm.

Table 3-4 summarises the measurements recorded for pillar N3_28. This pillar was established between March and December 2020. Figure 3-27 indicates that no scaling occurred in the time period between the first and the second visit.

Figure 3-27. Side B of pillar N3_28 at Nchwaning III shaft as observed on 17 May 2021 (left) and on 18 August 2021 (right)

Table 3-4. Measurements for pillar N3_28. The variation in bord span is attributed to measurement error.

N3_28			
Bord span		Bord span measured on 2021/05/17	Bord span measured on 2021/08/18
	N3_28A to N3_31A	7.80 m	8.06 m
	N3_28B to N3_32A	8.40 m	8.43 m
	N3_28C to N3_29A	8.35 m	8.33 m
	N3_28D to N3_30A	7.50 m	7.55 m
Dimensions of pillar	Side of pillar	Width	Height
	N3_28A	7.70 m	4.97 m
	N3_28B	6.00 m	4.63 m
	N3_28C	6.92 m	4.80 m
	N3_28D	6.38 m	4.55 m
Approximate scaling distance and age	Side of pillar	Approximate scaling distance	Age of pillar (months)
	N3_28A	0.30 m	10
	N3_28B	0.30 m	10
	N3_28C	0.47 m	10
	N3_28D	0.37 m	10

3.1.5. Experimental Area 5

A second area in the high-grade zone was selected as an additional control area and this is illustrated in Figure 3-28. The pillar behaviour was similar to Area 4 and it is distinctly different compared to those in the R5 area.

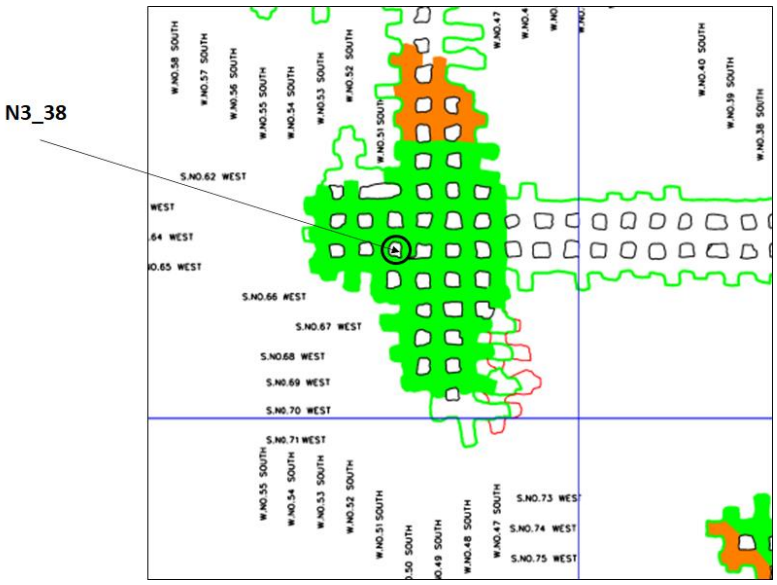

Figure 3-28. An enlarged view of Area 5 and the pillar selected for monitoring.

Pillar N3_38

The vertical joints in this area are not prominent and only minor scaling was observed. The horizontal joints seem to be the prominent joint set with the spacing varying from 15 cm to greater than 50 cm. The corners of the pillar had an hourglass shape (Figure 3-29). The pillar shape was irregular, making it difficult to measure its dimensions. The overall condition of the pillar is stable. The spacing of the vertical joint sets varied from approximately 8 cm to 50 cm across the perimeter. Figure 3-30 illustrates one of the prominent vertical joints.

Figure 3-29. The corner of the pillar as viewed from side A. An hourglass shape was observed.

Figure 3-30. An illustration of the prominent vertical joint on sides A.

Table 3-5 summarises the measurements recorded for pillar N3_38. This pillar was established between March and June 2020. Figure 3-31 indicates that no scaling occurred in the time period between the first and the second visit.

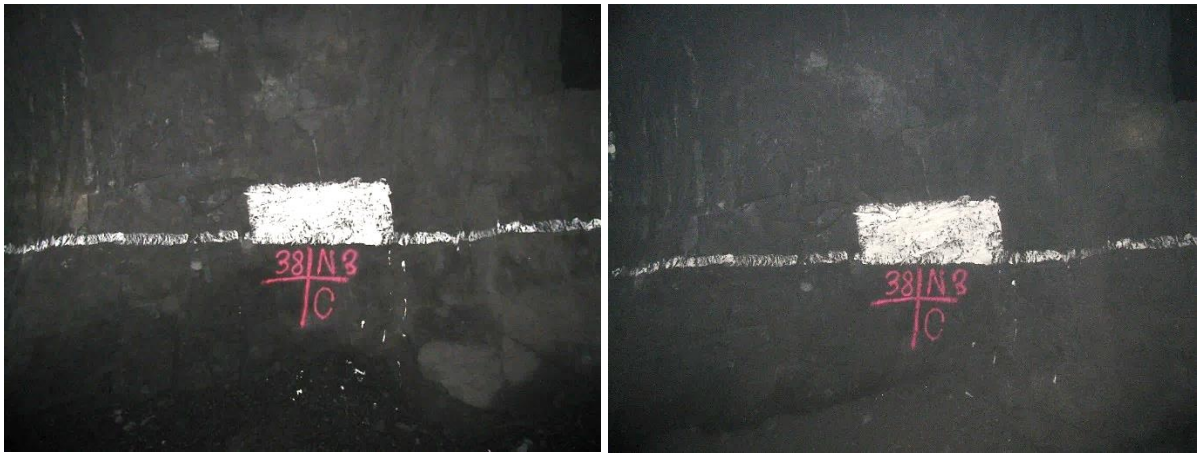

Figure 3-31. Side C of pillar N3_38 at Nchwaning III shaft as photographed on 18 May 2021 (left) and on 18 August 2021 (right).

Table 3-5. Measurements for pillar N3_38. The variation in bord span is attributed to measurement error.

N3_38			
Bord span		Bord span measured on 2021/05/18	Bord span measured on 2021/08/18
	N3_38A to N3_39A	7.80 m	7.74 m
	N3_38B to N3_40A	7.80 m	7.76 m
	N3_38C to N3_41A	8.30 m	8.35 m
	N3_38D to N3_42A	8.00 m	8.07 m
Dimensions of pillar	Side of pillar	Width	Height
	N3_38A	5.99 m	4.70 m
	N3_38B	7.40 m	5.00 m
	N3_38C	6.00 m	5.95 m
	N3_38D	6.40 m	5.18 m
Approximate scaling distance and age	Side of pillar	Approximate scaling distance	Age of pillar (months)
	N3_38A	0.26 m	12
	N3_38B	0.43 m	12
	N3_38C	0.50 m	12
	N3_38D	0.44 m	12

3.1.6. Experimental Area 6

This area was studied in 2020 by the author and these earlier observations are included as extensive pillar scaling was recorded by the mine in this area in 2019. Figure 3-32 illustrates a portion of the mine plan of this area where the pillars were scaling. The pillar numbers were assigned by the mine and these are numbered 1 to 10. These pillars have since been rehabilitated by applying a 100 mm thick shotcrete layer and also confining the pillar using cable straps.

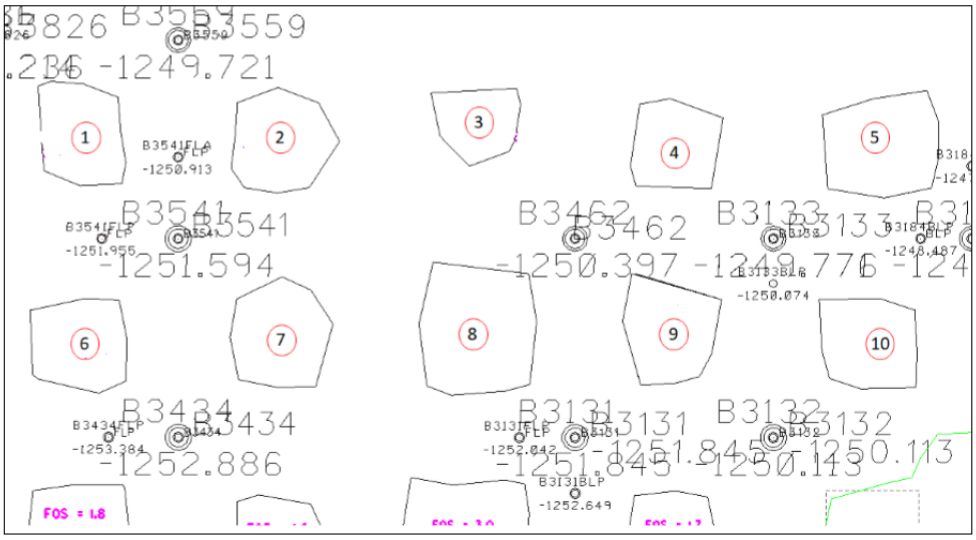

Figure 3-32. Pillar shapes in the area where excessive scaling was observed by the mine in 2019.

Figure 3-33 illustrates photographs of pillar scaling as supplied by the mine. It illustrates that significant scaling of some of the pillars occurred. It was reported by the mine that the pillars labelled 1, 3, 4 and 6 have “failed”, with the pillar widths at that stage estimated to be less than half the initial planned width (Shiri, 2019). In this area, the mining height exceeded 6 m.

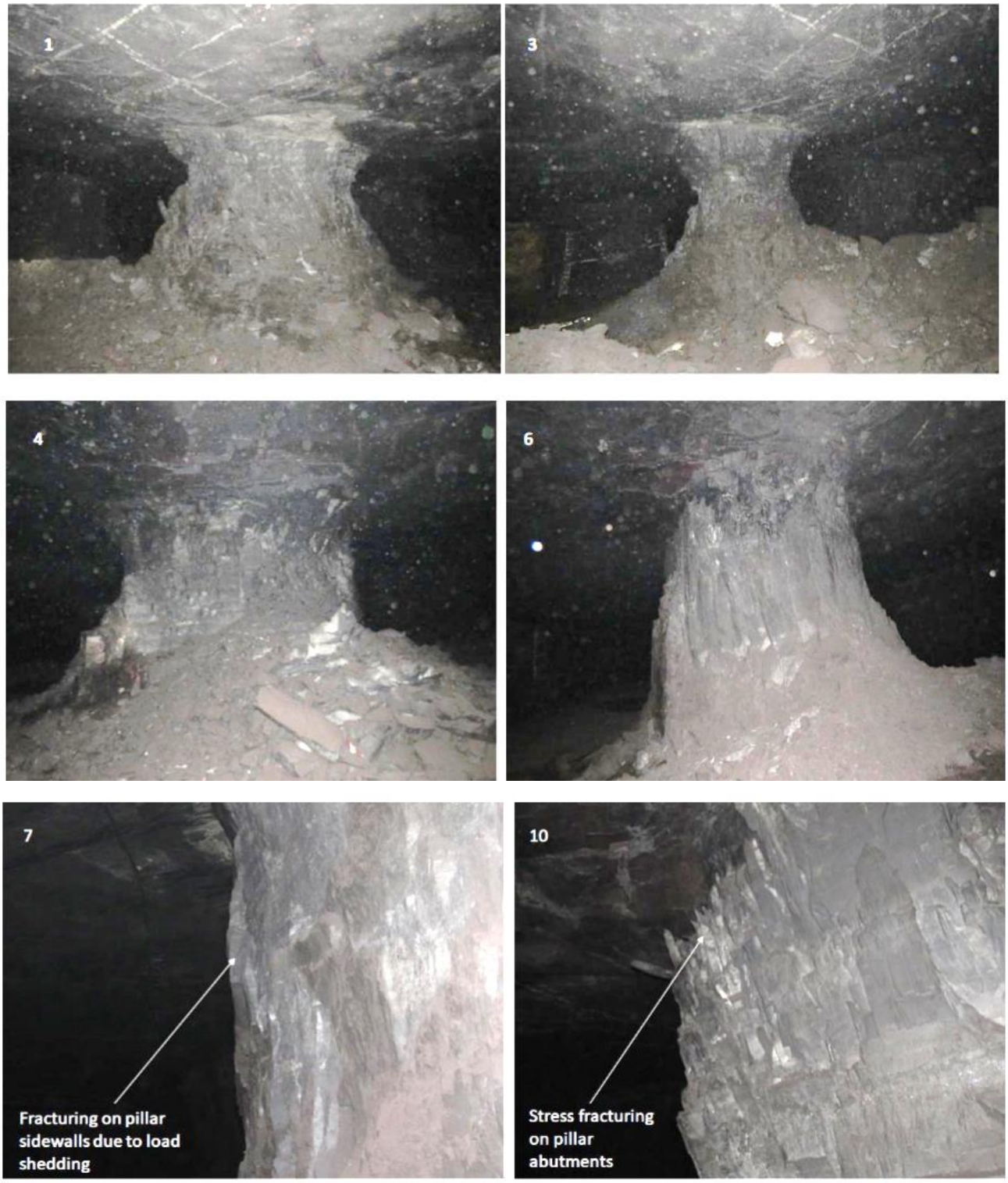

Figure 3-33. Condition of the pillars as photographed by the mine in 2019 (after Shiri, 2019). The numbers on the photographs refer to the pillar numbering in Figure 3-32.

During the author's visit, the pillars were already reinforced using shotcrete and strapping. Pillar 3 is illustrated in Figure 3-34 and Figure 3-35.

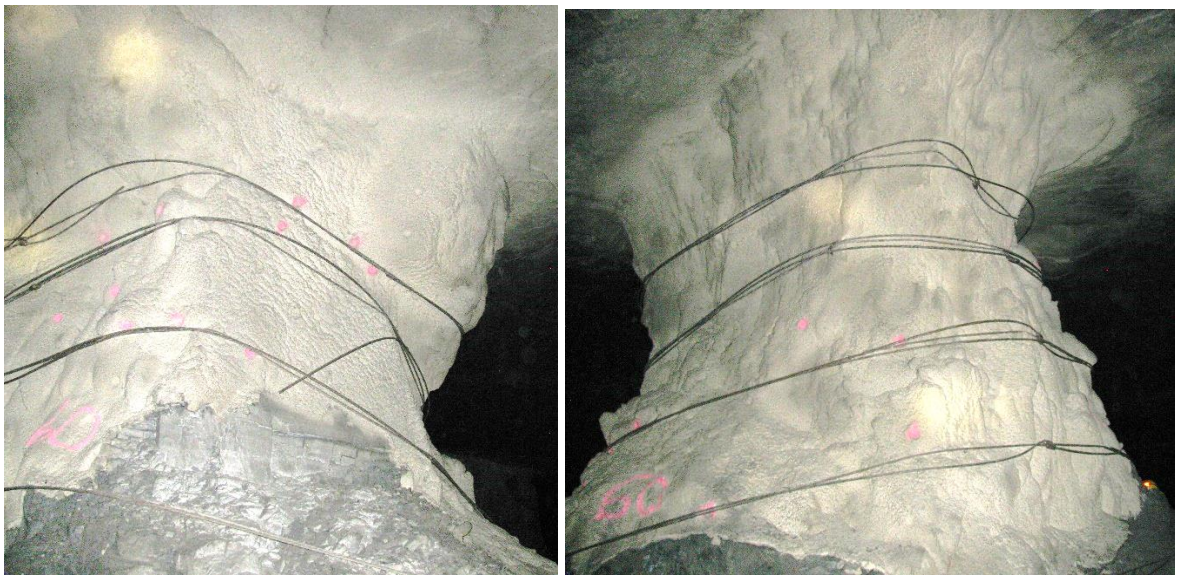

Figure 3-34. Pillar 3 was photographed by the author during October 2020.

Figure 3-35. An area of pillar 3 where the shotcrete failed (left). Note the high density of jointing and the rock mass characteristics is reminiscent of that observed in Area 1. The small joint spacing is also visible in the photograph of an adjacent pillar (right).

3.2. Rock mass ratings and pillar behaviour

As mentioned above, rock mass ratings were done on the sidewalls of the pillars selected for monitoring. These ratings are summarised in Table 3-6 and additional detail is given in Appendix A. The overall condition of the pillar was also assessed and a pillar rating was given according to the classification by Esterhuizen et al. (2006) (see Figure 3-1). The rock mass ratings for the pillars in Area 6 could not be done as these pillars were already covered with shotcrete. The pillar rating of these pillars seems to be a 4 and by examining the photographs supplied by the mine (Figure 3-33), the RMR and Q-ratings were also low. These observations support the correlation between the pillar rating and rock mass rating as shown in Table 3-6.

It is evident from Table 3-6 that the pillars with a low RMR and Q-ratings are the pillars prone to excessive scaling. This is important evidence that the pillar design at BRMO needs to be adapted for the different geotechnical areas and it is one of the important findings from this study. The current design methodology as discussed in Section 1.4, which assumes a uniform pillar strength across the property, does not cater for these differences in strength. Rock mass ratings should be done on the pillar sidewalls and the design adapted in areas where excessive pillar scaling is experienced. Figure 3-36 illustrates the relationship between RMR and Q-ratings for the pillars monitored at BRMO. Although only limited data points were collected, it is encouraging that it loosely follows the empirical trend often quoted in literature (e.g. Bieniawski, 1984) namely:

$$\mathrm{RMR} = 9\ln(\mathrm{Q}) + 44 \tag{3.1}$$

Table 3-6. A comparison of rock mass ratings and pillar condition.

Pillar	RMR	Q-rating	Pillar rating*
N3_1	46	3	4
N3_2	46	2	4
N3_9	49	2	4
N3_15	59	6	2
N3_20	59	6	2
N3_25	44	2	3
N3_28	83	23	1
N3_33	83	10	1
N3_38	63	8	2

*based on classification by Esteruizen et al. (2006)

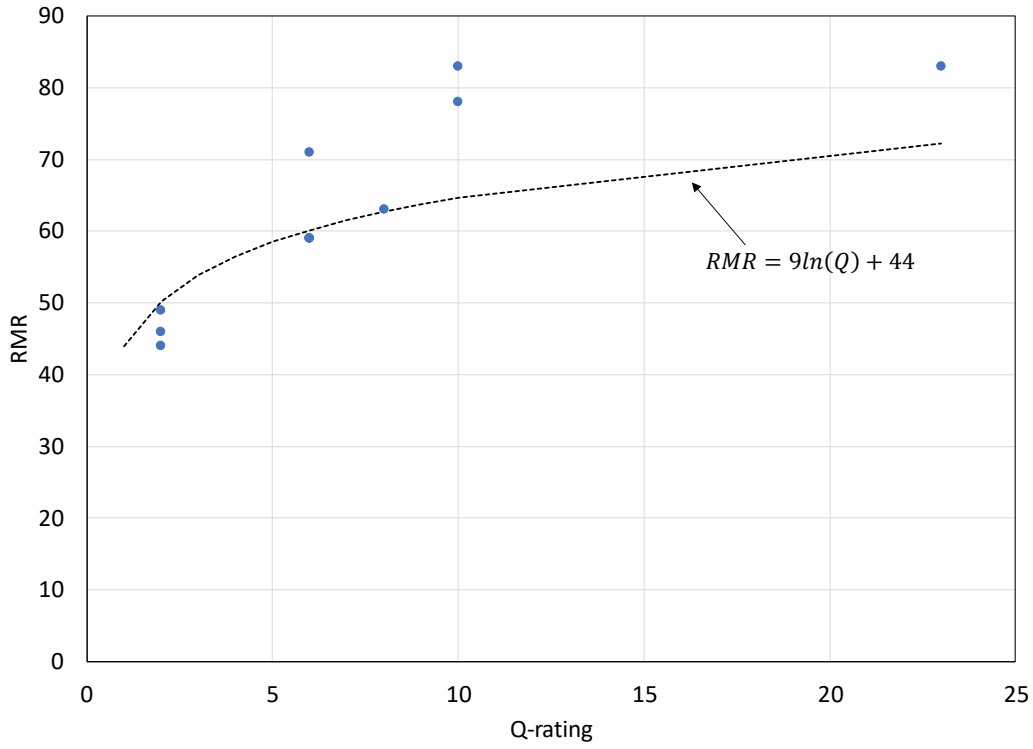

Figure 3-36. Relationship between rock mass rating (RMR) and Q-ratings for the pillars at BRMO. The typical relationship between RMR and Q- rating found in literature is also plotted in the figure.

In summary, the underground observations indicated that the behaviour of the pillars at Nchwaning III shaft is controlled by the characteristics of the joint sets. In areas with closely spaced joints and multiple intersecting joint sets, extensive scaling of the pillars occurs. The time-dependent nature of the scaling behaviour will also be affected by the nature of the joints. The current pillar design methodology does not cater for this difference in behavior as it assumes a uniform pillar strength in all geotechnical areas. The designs should therefore be adapted in areas where excessive pillar scaling is experienced. The stresses acting on the pillars are required to conduct a back-analysis of pillar strength. These stresses are determined in the next chapter which describes the numerical modelling conducted for this study.

Chapter 4

NUMERICAL MODELLING APPROACH

The previous study done on pillar strength at BRMO estimated the pillar stress using TAT (Hanekom, 2008). TAT is a conservative approach as it assumes a regular layout that continues to infinity in the lateral directions. The effect of large pillars and abutments are not considered and this typically results in an overestimation of the pillar stress (Napier and Malan, 2011). For this study, the average pillar stress (APS) was simulated using a numerical modelling technique to obtain more accurate estimates of the pillar stresses.

The simulation of pillar failure in bord and pillar layouts present a difficult modelling problem. A large area needs to be simulated to accurately model the stress acting on the pillars. In these large-scale models, it is often not practical to include the failure of pillars as there are constraints in the codes, such as the requirements of small element sizes to accurately represent the depth of failure. Furthermore, in hard rock bord and pillar mines, the pillar cutting is usually poor and the pillar shapes are therefore irregular. Building an accurate geometry of the layout and the actual irregular pillar shapes is a daunting task. As a result, three-dimensional finite element or finite difference models are seldom used to simulate bord and pillar layouts on a large scale. These codes are nevertheless useful to simulate the failure of a single pillar and the detailed failure mechanisms can be studied. On the other hand, displacement discontinuities boundary element (DD) models overcome the problem of building the large-scale models, but it is typically impossible for most of these codes to simulate the failure of the pillars. As an example, for a platinum mine, Leach (2007) used a DD code to simulate two scenarios namely a “worst-case” scenario where the in-panel pillars were not included and a second approach where it was attempted to simulate the effect of the small pillars using a “backfill-soup”. The calibration of this backfill material is problematic and it is questionable if it is a realistic representation of the effect of failed pillars.

The TEXAN code used in this study is a DD code and it was developed specifically to simulate a large number of small pillars in tabular layouts (Napier and Malan, 2007; Esterhuyse and Malan, 2018). The user can select triangular boundary elements and these elements circumvent the problem of “partially mined” elements when using square elements (Malan and Napier, 2006). The use of TEXAN to simulate small crush pillars is described in Du Plessis and Malan (2018). As the code can explicitly simulate small pillars and the scaling of the pillars using a limit equilibrium model, there is no need to attempt to use a “backfill-soup” as described by Leach (2007). It is therefore also probably a good approach to simulate the Nchwaning III layouts. Owing to the restrictions on the

number of elements that can be practically solved in TEXAN, smaller areas were simulated in detail as shown for the different areas below. To simplify the digitising of the outlines and the meshing procedure, the pillar outlines were approximated with straight line segments.

The mined areas were covered using a triangular mesh. In terms of element sizes, the centroids of adjacent triangular elements are spaced approximately 1.5 m apart. The pillars of interest also had to be covered with a triangular mesh to enable the calculation of the APS in these pillars. Not all the pillars had to be meshed as the nature of the displacement discontinuity codes is such that any area not covered by elements is considered as solid rock material. Regarding element size, it is known that when using displacement discontinuity boundary element modelling, the average pillar stress (APS) is affected by the element size. This was explored by Napier and Malan (2011). For known analytical solutions of APS, it was found that the simulated APS approximates the analytical values closely if the element size tends to zero. Small element sizes are therefore needed for these simulations. For the purposes of this study, the 1.5 m sizes were considered adequate, and it should be noted that this is significantly smaller than the typical 5 m - 10 m element sizes used in industry for MINSIM-type simulations in the gold mines. The small element sizes were also required for the limit equilibrium constitutive model discussed in Chapter 5.

4.1. Numerical Modelling Parameters

Simplified layouts were generated for the five experimental areas discussed in Chapter 3. Mine plans were supplied by the mine for each area. The sizes of the areas simulated typically had dimensions of 500 m $\times$ 500 m.

The parameters used for the simulations are given in Table 4-1. The only parameter that is different for the five areas is the depth below surface. This is given in each section below and was determined by using pegs on the plans and the collar elevation. The dip of the reef is small at Nchwaning III ($\approx$7°) and it was therefore simulated with no dip in the models for simplicity. Some uncertainty exists regarding the appropriate density of the overburden that needs to be used as it will have a significant effect on the simulated APS values. Stress measurements were conducted in 2013 at Nchwaning II shaft, but these were done inside pillars (with the stress magnitude therefore dependent on the layout and pillar size) and the author of that study made no mention of the estimated overburden density (Van der Heever, 2013). The average density of the overburden was assumed to be 3000 kg/m^3 and the k-ratio was assumed to be 1 in both horizontal directions. As this is boundary element modelling, it also implicitly assumes that the rock is homogenous, elastic, and isotropic.

Information obtained from the mine indicated that Young's modulus of the seam material is 91 GPa and the surrounding rock mass is 119 GPa. Boundary element codes typically only allow a single modulus to be specified and therefore a value of 90 GPa was adopted for the elastic modelling. This value is not considered critical as it does not affect the simulated APS values on the pillars as no total closure occurs in these bord and pillar layouts. Note that the amount of elastic deformation in the bords will be affected by Young's modulus, but this was not considered in this study.

Table 4-1. Parameters used for the elastic models solved with the TEXAN code.

Parameter	Value
Young's Modulus	90 GPa
k-ratio	1
Average overburden density	3000 kg/m^3
Poisson's ratio	0.25

A first step to understanding the pillar behaviour is to assume a simple elastic rock mass model. The pillars were not allowed to fail and were simply modelled as "rigid" pillars that are not allowed to deform. This is an efficient method to calculate the APS on the pillars (Napier and Malan, 2011).

4.2. Simulation of Area 1

Figure 4-1 illustrates the area that was approximated using straight line segments. Figure 4-2 illustrates the mesh that was generated for this area. The individual triangles are too small to be visible in this diagram. Only a few of the pillars were meshed to investigate the APS values and these are illustrated in Figure 4-3.

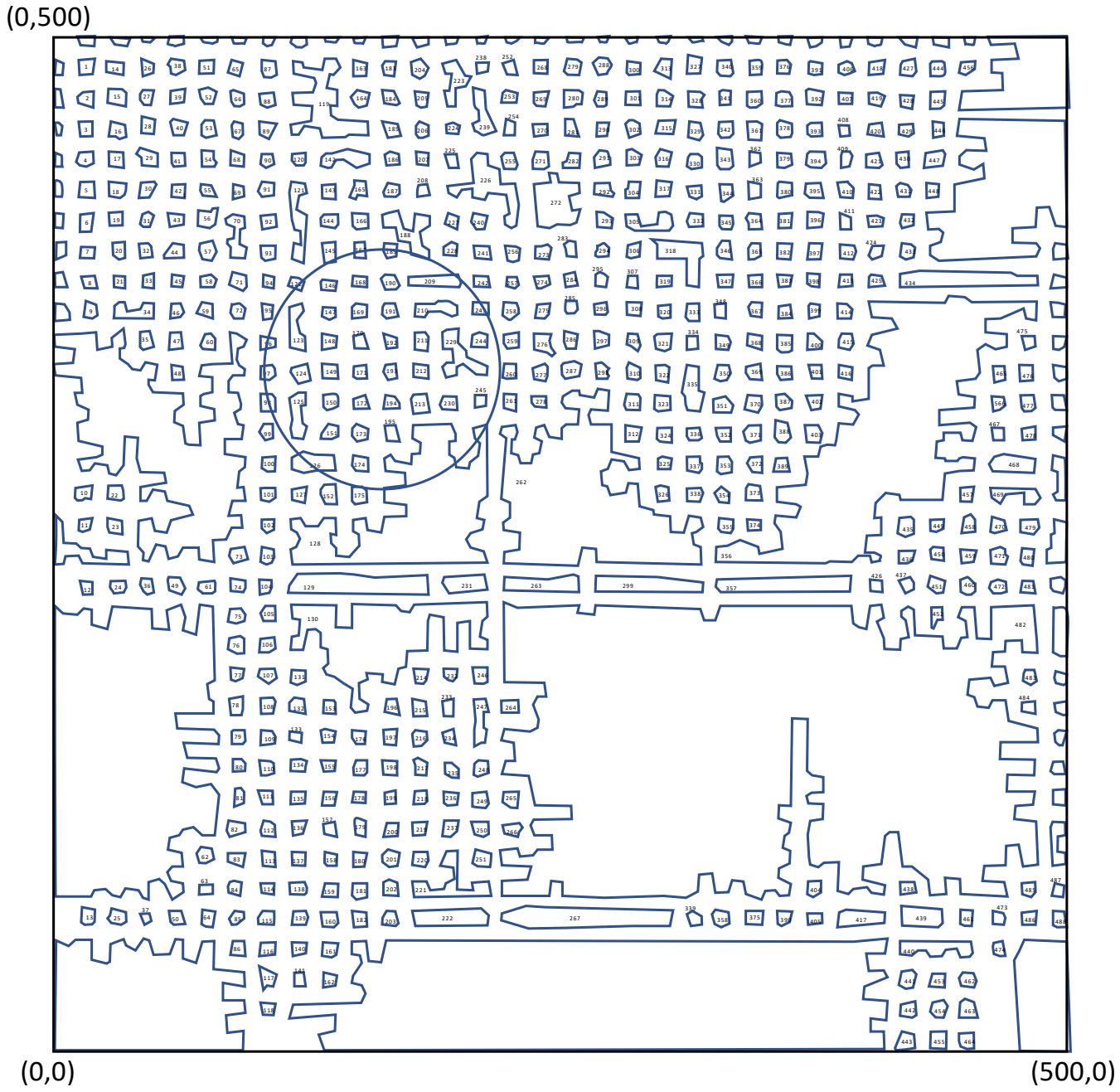

Figure 4-1. Size of the model to calculate the stresses acting on the pillars of monitoring Area 1 (the area of interest is indicated by the circle).

Pegs on the plan of Area 1 indicate typical values ranging between -1259.4 m to -1268.86 m below datum and the collar elevation is -779.197 m below datum. This gives an average depth below surface of 485 m.

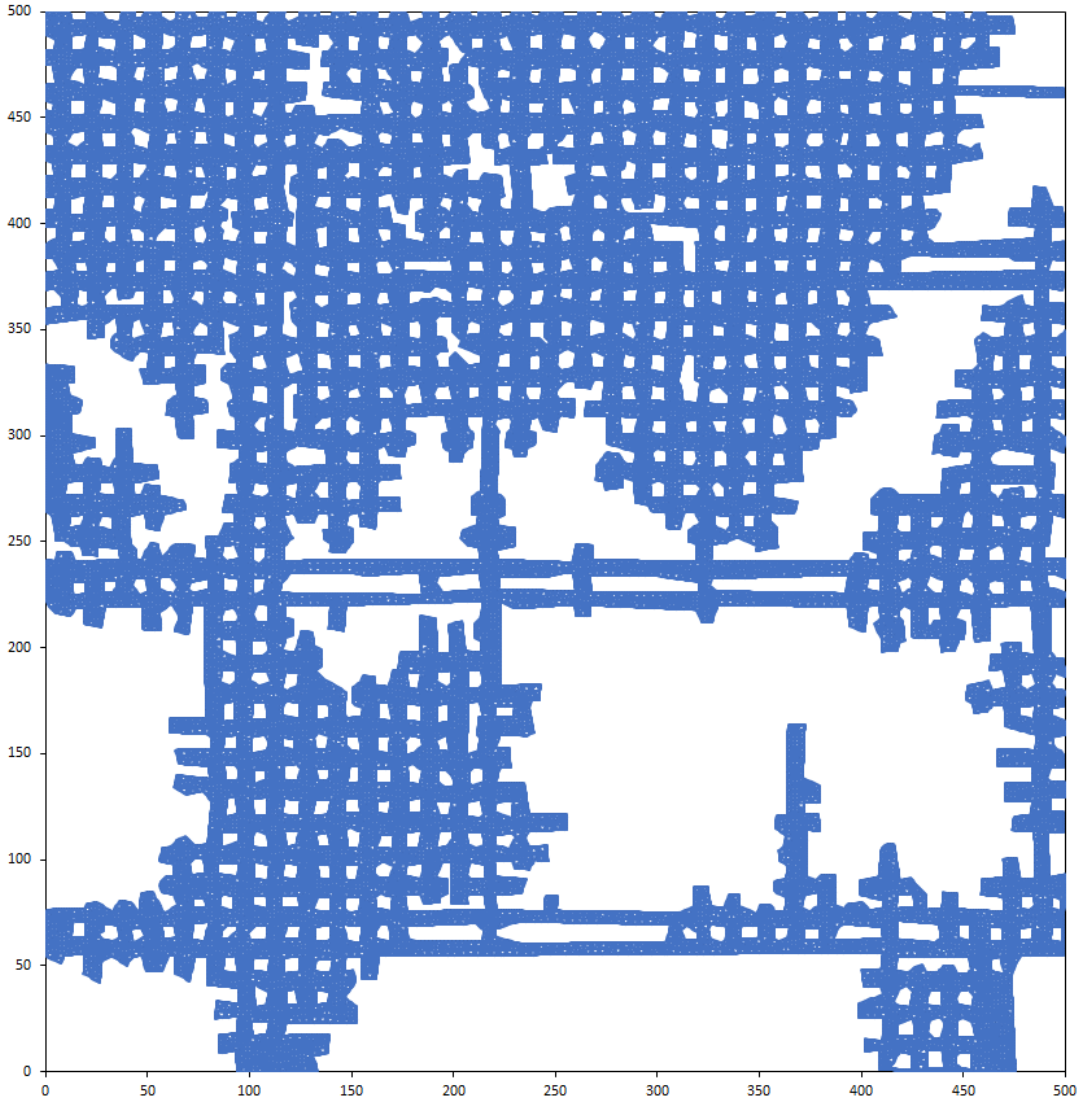

Figure 4-2. Triangular mesh generated to simulate Area 1. The triangular elements are too small to be seen in the diagram. This model consisted of 62 925 elements.

As discussed in Chapter 3, the pillars with extensive scaling that were studied in detail were N3_1, N3_2, and N3_9. Figure 4-3 illustrates the mesh that was generated for the pillars in this area and the three pillars of interest is labelled using red text.

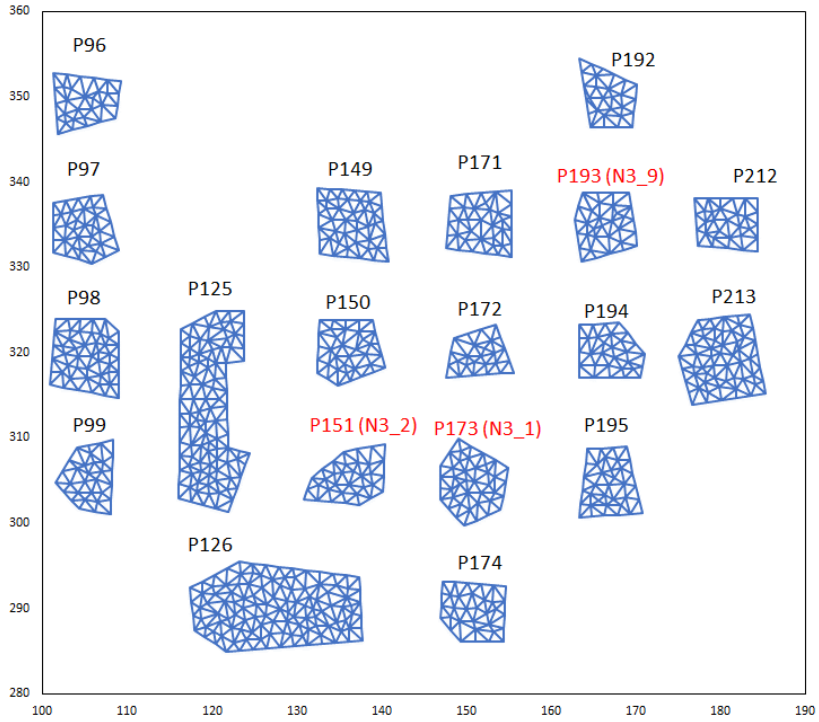

Figure 4-3. The pillars that were studied in the area of interest (Area 1). The pillar numbers in red are the pillars discussed in Section 3.1.1.

The virgin vertical stress at a depth of 485 m for the assumed rock density (3000 kg/m^3) is 14.55 MPa. This gives a TAT value of 66 MPa for an extraction ratio of 78%. As shown below in Figure 4-4, the simulated APS on some small pillars, therefore, exceeds the virgin stress by a factor of more than five and is significantly higher than the TAT value. This indicates the benefits of using numerical modelling to simulate the APS as this stress is greatly dependent on the size and position of a particular pillar. The table with the simulated APS values is given in Appendix C.

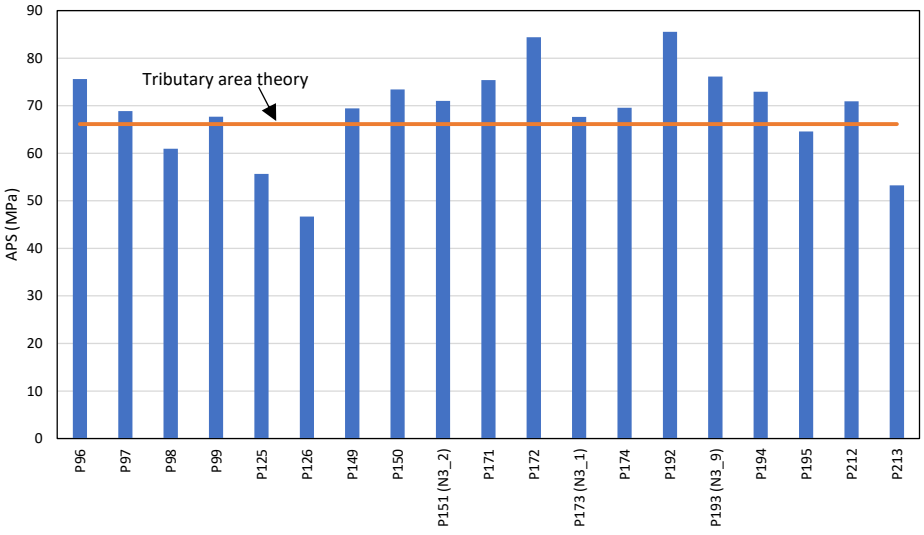

Figure 4-4. Simulated APS values of the pillars in experimental Area 1.

From this data, the K-value for the Hedley and Grant pillar strength formula was back-calculated as illustrated in Table 4-2. The three pillars of interest are highlighted in the table. These pillars are currently subjected to significant scaling and this is not deemed to be stable pillar behaviour. The back-calculated K-values vary from 78 MPa to 92 MPa for these pillars. This is an indication that the current pillar strength design formula (K = 133 MPa) may overestimate the pillar strength in areas where the joint spacing is small. For pillars in the R5 product area (Figure 3-4), a reduced K-value possibly needs to be adopted.

Table 4-2. Simulated APS and back-calculated K-values for the Hedley and Grant pillar strength formula for the pillars in Area 1.

Pillar number	Simulated APS (MPa)	TAT (MPa)	Area (m^2)	Circum-ference (m)	Effective width (m)	Height (m)	K-value (MPa)
P96	75.6	66.1	42.5	26.7	6.4	4.8	97.1
P97	68.9	66.1	48.2	26.8	7.2	4.8	83.3
P98	60.9	66.1	64.9	31.8	8.2	4.8	69.2
P99	67.7	66.1	41.2	25.8	6.4	4.8	86.9
P125	55.7	66.1	144.4	61.6	9.4	4.8	59.0
P126	46.7	66.1	173.2	54.0	12.8	4.8	42.3
P149	69.4	66.1	60.6	31.4	7.7	4.8	81.0
P150	73.4	66.1	49.1	27.1	7.2	4.8	88.4
P151 (N3_2)	71.0	66.1	46.4	27.8	6.7	5.0	91.9
P171	75.4	66.1	51.8	28.9	7.2	4.8	91.3
P172	84.4	66.1	33.9	24.0	5.6	4.8	115.2
P173 (N3_1)	67.7	66.1	56.5	28.5	7.9	4.8	77.9
P174	69.6	66.1	47.7	27.0	7.1	4.8	84.9
P192	85.5	66.1	37.8	25.6	5.9	4.8	114.2
P193 (N3_9)	76.1	66.1	47.2	26.9	7.0	4.5	88.8
P194	72.9	66.1	43.0	25.7	6.7	4.8	91.5
P195	64.6	66.1	47.9	28.2	6.8	4.8	80.4
P212	70.9	66.1	42.7	26.4	6.5	4.8	90.4
P213	53.2	66.1	81.3	35.1	9.3	4.8	56.7

4.3. Simulation of Areas 2 and 3

Areas 2 and 3 are also part of the R5 product area (Figure 3-3). The rock mass ratings are also low in this area. It differs from Area 1 in terms of the age of the pillars. The pillars in these two areas were cut in 2021 while the pillars in Area 1 are more than three years old. Figure 4-5 illustrates the size of the area simulated for Area 2 and Figure 4-6 illustrates the mesh that was generated. Note that there are large areas of unmined reef surrounding the area of interest.

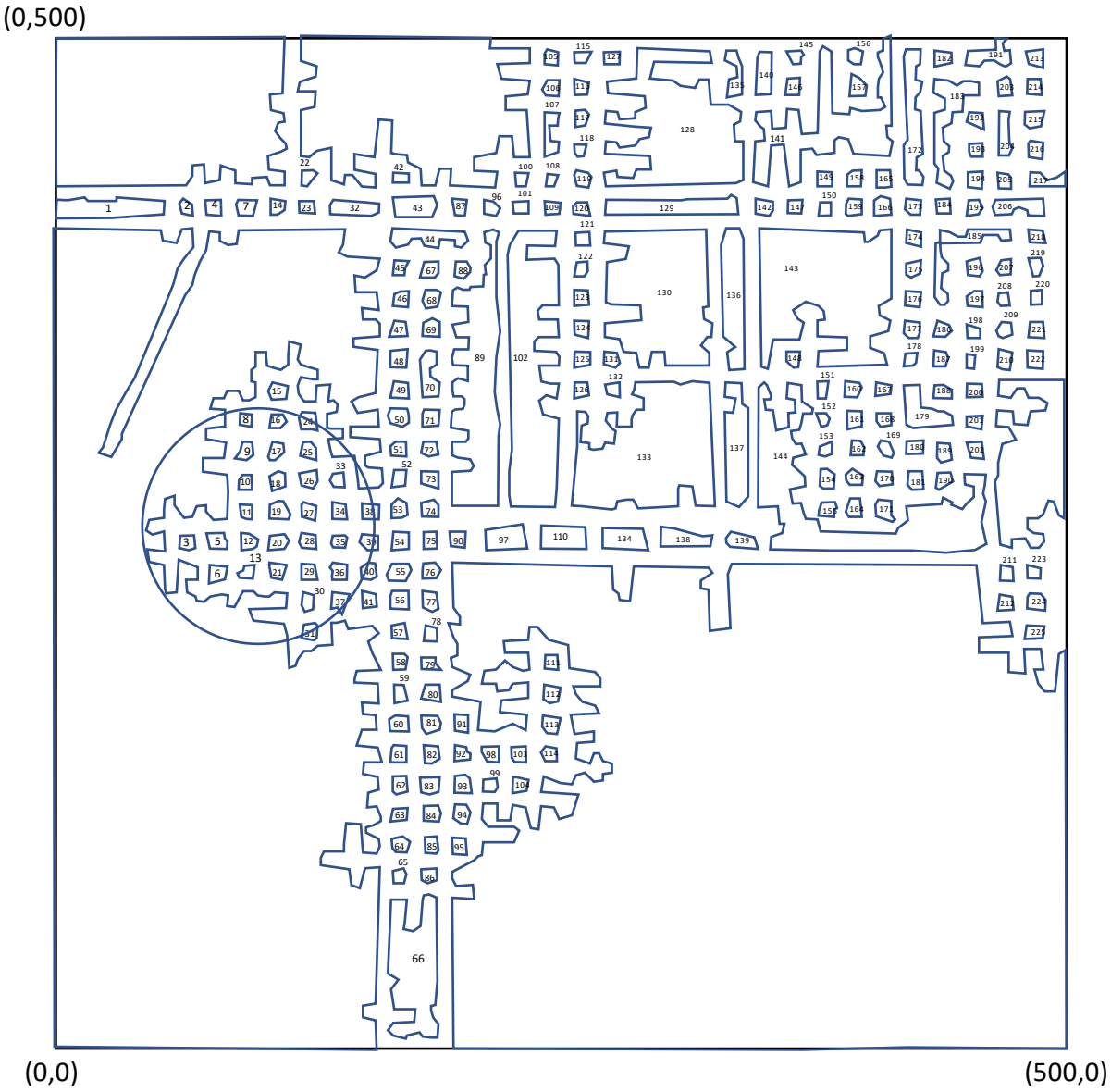

Figure 4-5. Size of the model to calculate the stresses acting on the pillars of monitoring Area 2 (the area of interest is indicated by the circle).

Pegs on the plan of Area 2 indicate typical values ranging between -1254.9 m to -1259.1 m below datum and the collar elevation is -779.197 m below datum. This gives an average depth below surface of 478 m.

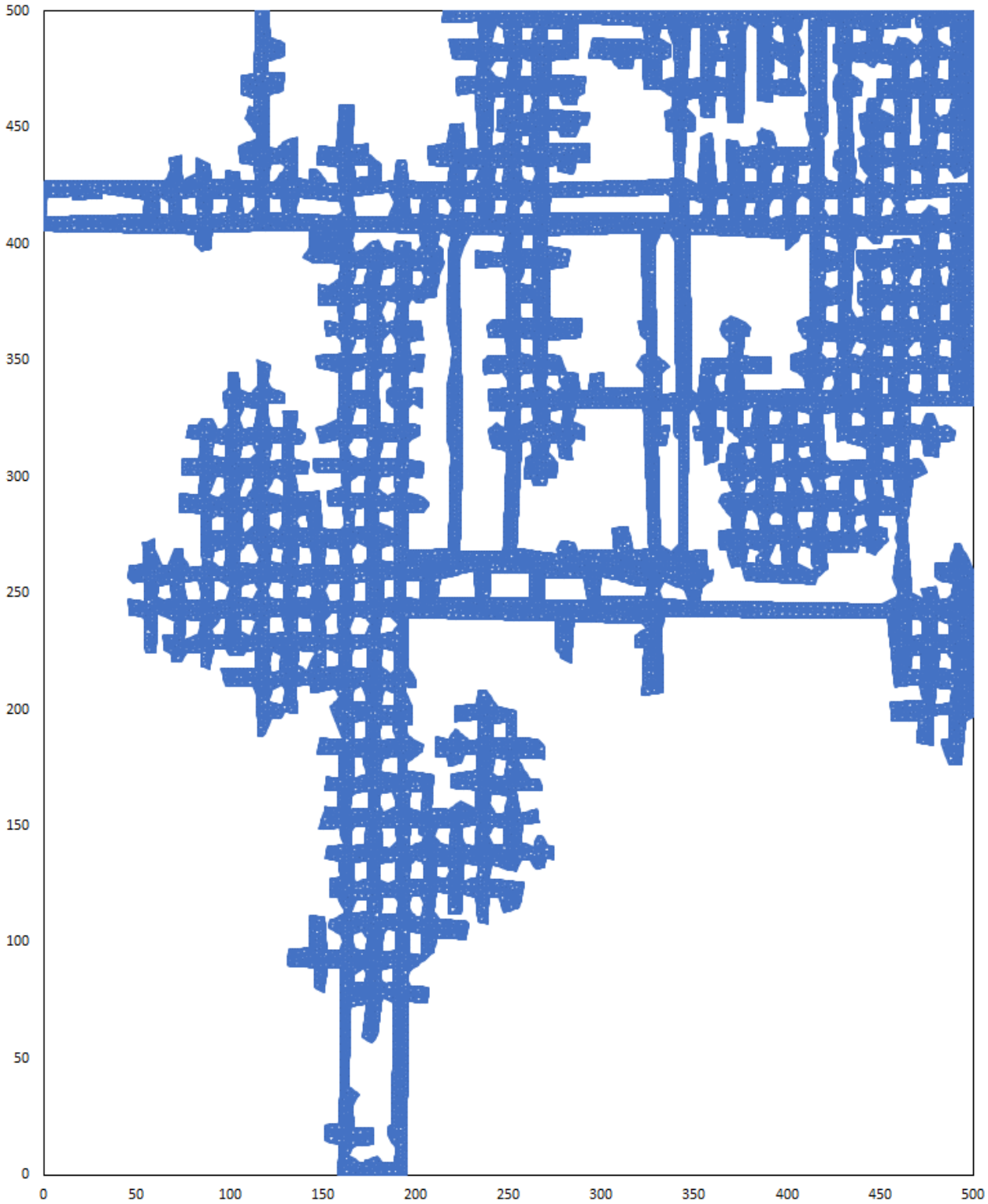

Figure 4-6. The mesh generated for Area 2. The triangular elements are too small to be seen in the diagram.

Two pillars in this area are described in detail in Chapter 3 and these are N3_15 and N3_20. The one pillar was close to the active faces (Figure 4-7, left) and the second was further into the back area (Figure 4-7, right).

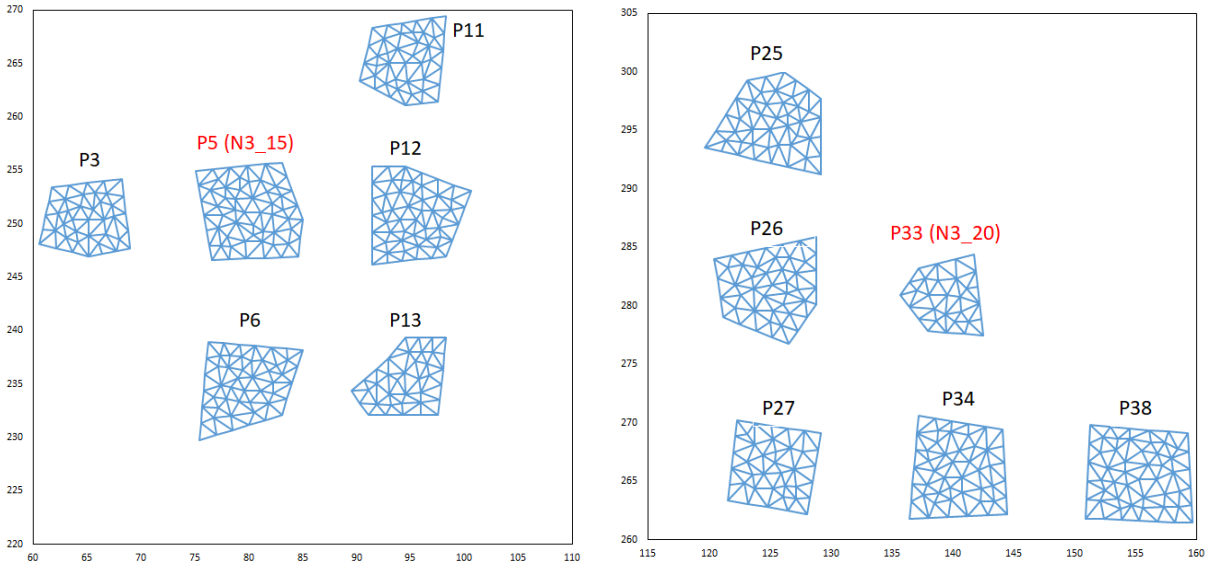

Figure 4-7. The pillars that were studied in the area of interest (Area 2). The pillar numbers in red are the pillars discussed in Section 3.1.2.

The layout used to simulate Area 3 is given in Figure 4-8. Figure 4-9 illustrates the mesh that was generated. Some of the pillars also had to be covered with a triangular mesh to enable the calculation of the average pillar stress.

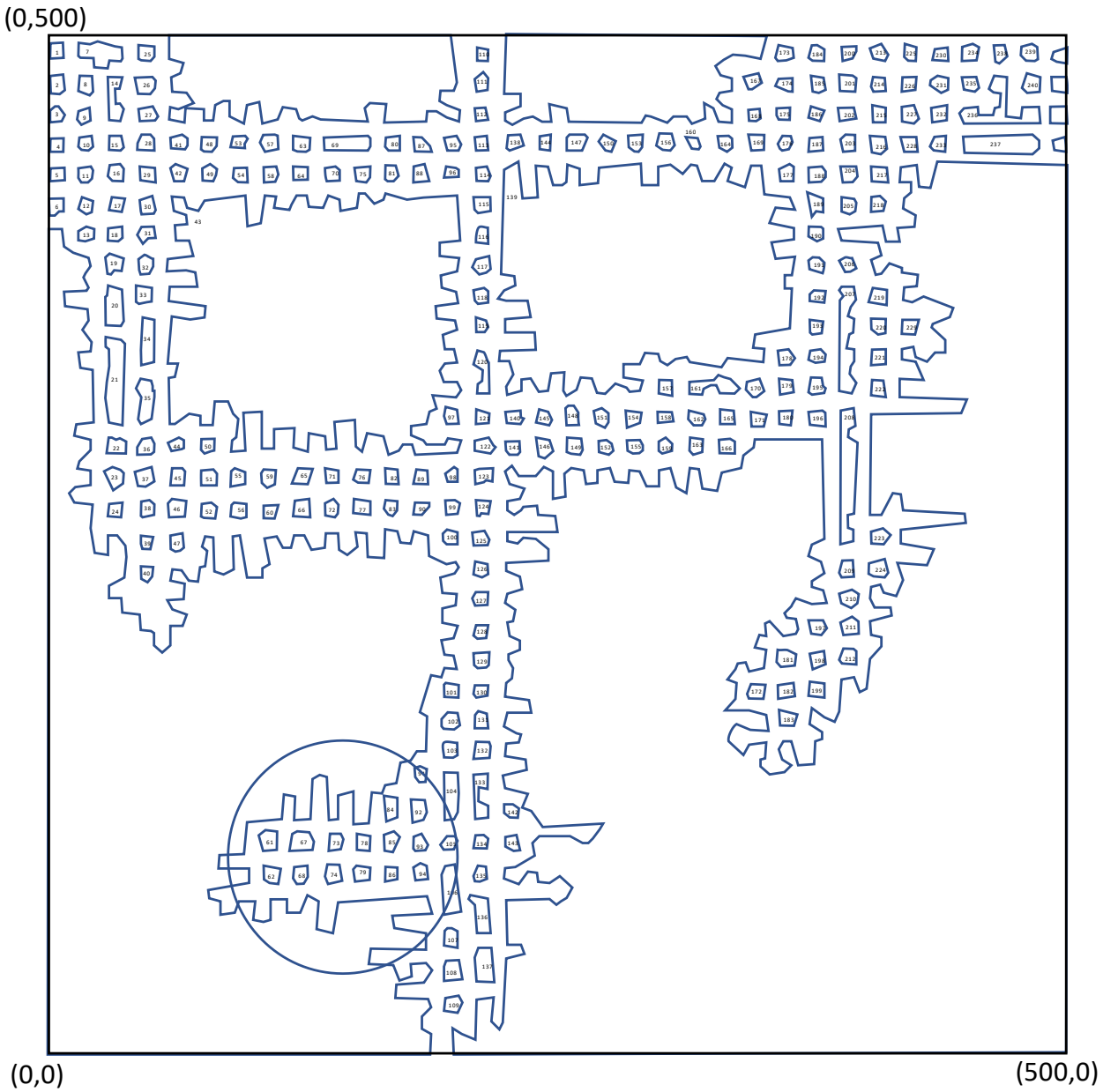

Figure 4-8. Size of the model to calculate the stresses acting on the pillars of monitoring Area 3 (the area of interest is indicated by the circle).

Pegs on the plan of Area 3 indicate typical values of -1324.9 m below datum and the collar elevation is -779.197 m below datum. This gives a depth below surface of 546 m.

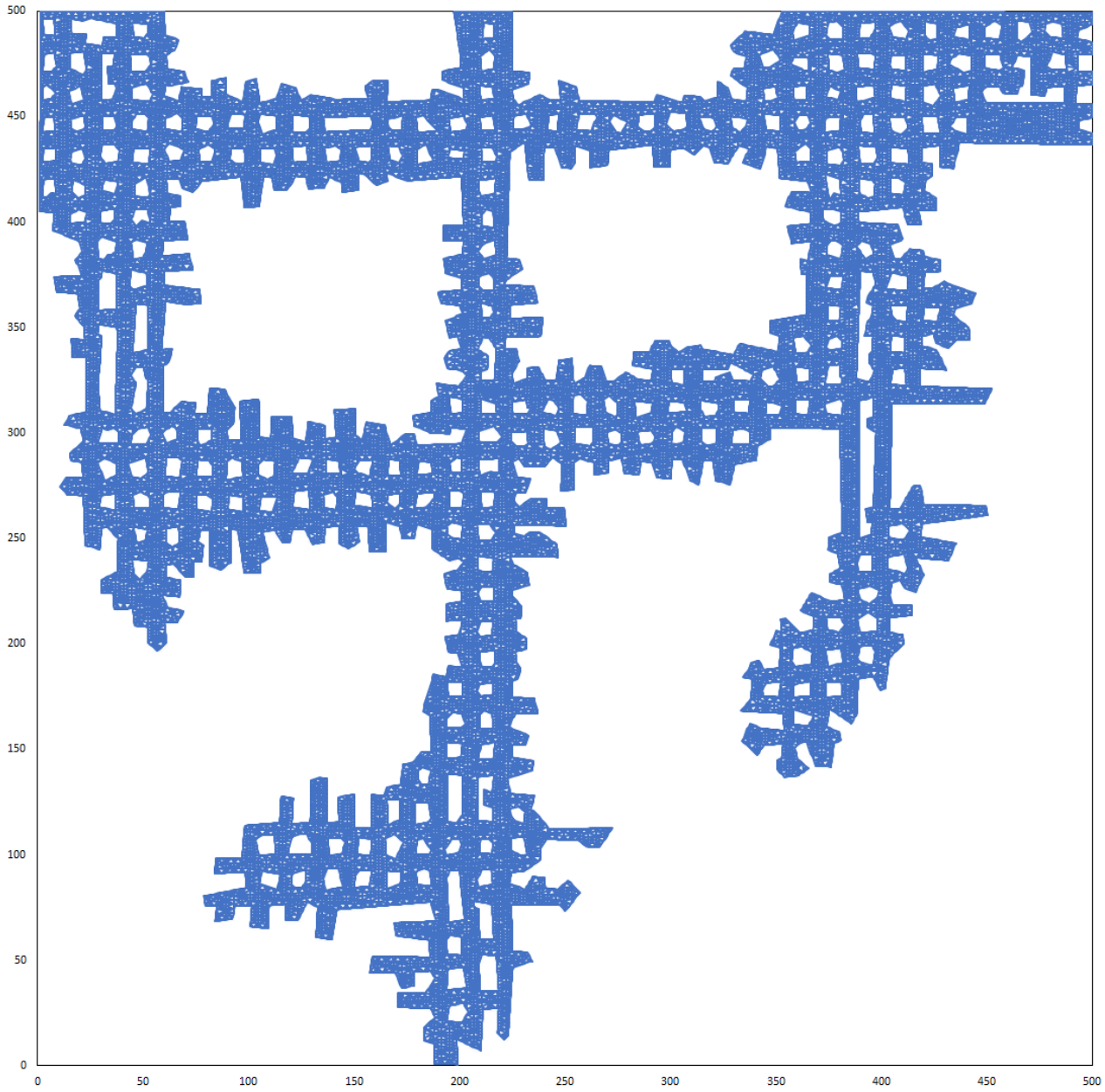

Figure 4-9. The mesh generated for Area 3. The triangular elements are too small to be seen in the diagram.

The pillar selected for monitoring was also close to the face (Figure 4-10) and this was pillar P68 (N3_25). This area was isolated with small spans and large areas of solid reef surrounding it. Some scaling was nevertheless already visible for this pillar (see Section 3.1.2).

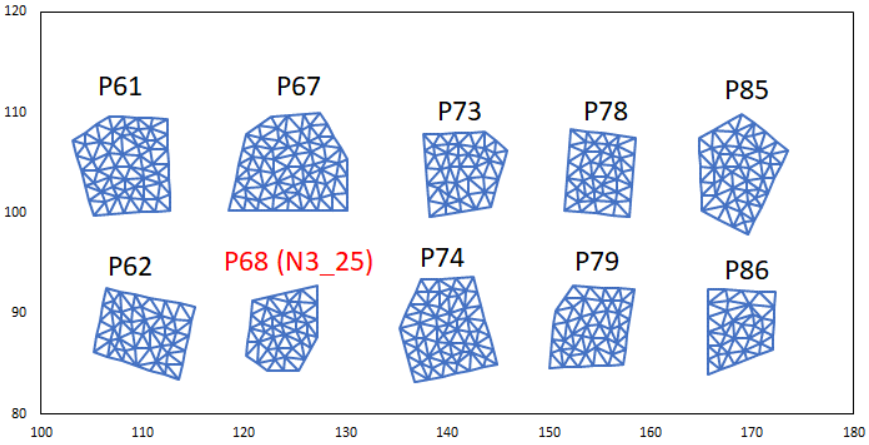

Figure 4-10. The pillars that were studied in the area of interest (Area 3). The pillar number in red is the pillar discussed in Section 3.1.2.

The simulated APS for Areas 2 and 3 are given in Figure 4-11 and Table 4-3 illustrates the back-calculated K-values. The TAT value differs slightly for the two areas owing to the difference in depth. Area 2 was simulated at a constant depth of 478 m below surface and Area 3 at a depth of 546 m below surface.

From this data, the K-value for the Hedley and Grant pillar strength formula was back-calculated. The three pillars of interest are highlighted in the table. These pillars are currently characterised by moderate scaling. The back-calculated K-values vary from 47 MPa to 88 MPa and this is an indication that the current pillar strength design formula (K = 133 MPa) may overestimate the pillar strength.

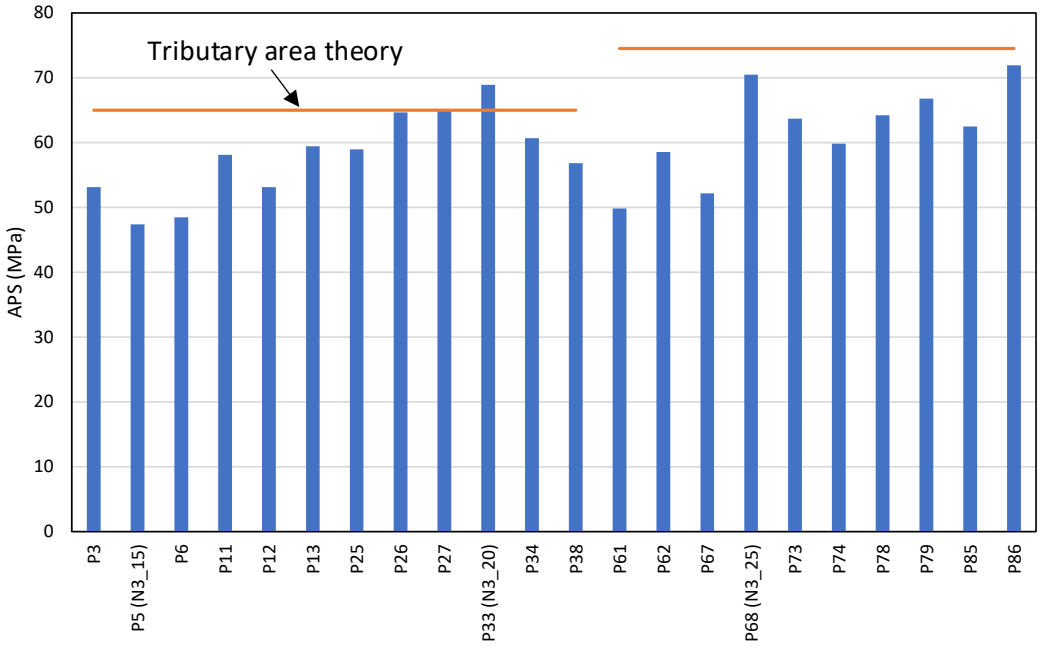

Figure 4-11. Simulated APS values for Area 2 (left) and Area 3 (right). The two areas are at slightly different depths and therefore the APS predicted by tributary area stress is slightly different for the two areas.

Table 4-3. Simulated APS and back-calculated K-values for the Hedley and Grant pillar strength formula for the pillars in Areas 2 and 3.

Pillar number	Simulated APS (MPa)	TAT (MPa)	Area (m^2)	Circum-ference (m)	Effective width (m)	Height (m)	K-value (MPa)
P3	53.1	65.0	47.9	27.1	7.1	4.2	58.7
P5 (N3_15)	47.4	65.0	73.9	33.7	8.8	4.2	46.9
P6	48.5	65.0	61.5	32.3	7.6	4.2	51.5
P11	58.1	65.0	50.4	27.9	7.2	4.2	63.4
P12	53.1	65.0	65.5	31.1	8.4	4.2	53.8
P13	59.4	65.0	45.8	30.1	6.1	4.2	70.6
P25	59.0	65.0	55.1	29.9	7.4	4.2	63.7
P26	64.7	65.0	55.6	29.3	7.6	4.2	68.8
P27	65.0	65.0	47.9	27.4	7.0	4.2	72.1
P33 (N3_20)	68.9	65.0	33.2	22.8	5.8	4.5	88.2
P34	60.7	65.0	59.6	31.0	7.7	4.2	64.2
P38	56.8	65.0	65.6	32.5	8.1	4.2	58.7
P61	49.8	74.5	78.7	34.4	9.1	4.2	48.3
P62	58.5	74.5	61.1	31.6	7.7	4.2	61.7
P67	52.2	74.5	92.6	37.7	9.8	4.2	48.8
P68 (N3_25)	70.5	74.5	46.4	26.4	7.0	4.0	75.2
P73	63.7	74.5	54.8	28.9	7.6	4.2	67.9
P74	59.8	74.5	73.0	33.4	8.8	4.2	59.4
P78	64.2	74.5	50.8	28.7	7.1	4.2	70.8
P79	66.8	74.5	56.2	29.6	7.6	4.2	71.1
P85	62.5	74.5	68.1	32.3	8.4	4.2	63.1
P86	71.9	74.5	45.6	27.5	6.6	4.2	82.0

4.4. Simulation of Area 4

Area 4 was one of the high-grade areas with a low joint density studied. The size of the area simulated is shown in Figure 4-12. The depth below surface was 366 m. Figure 4-13 illustrates the mesh that was generated.

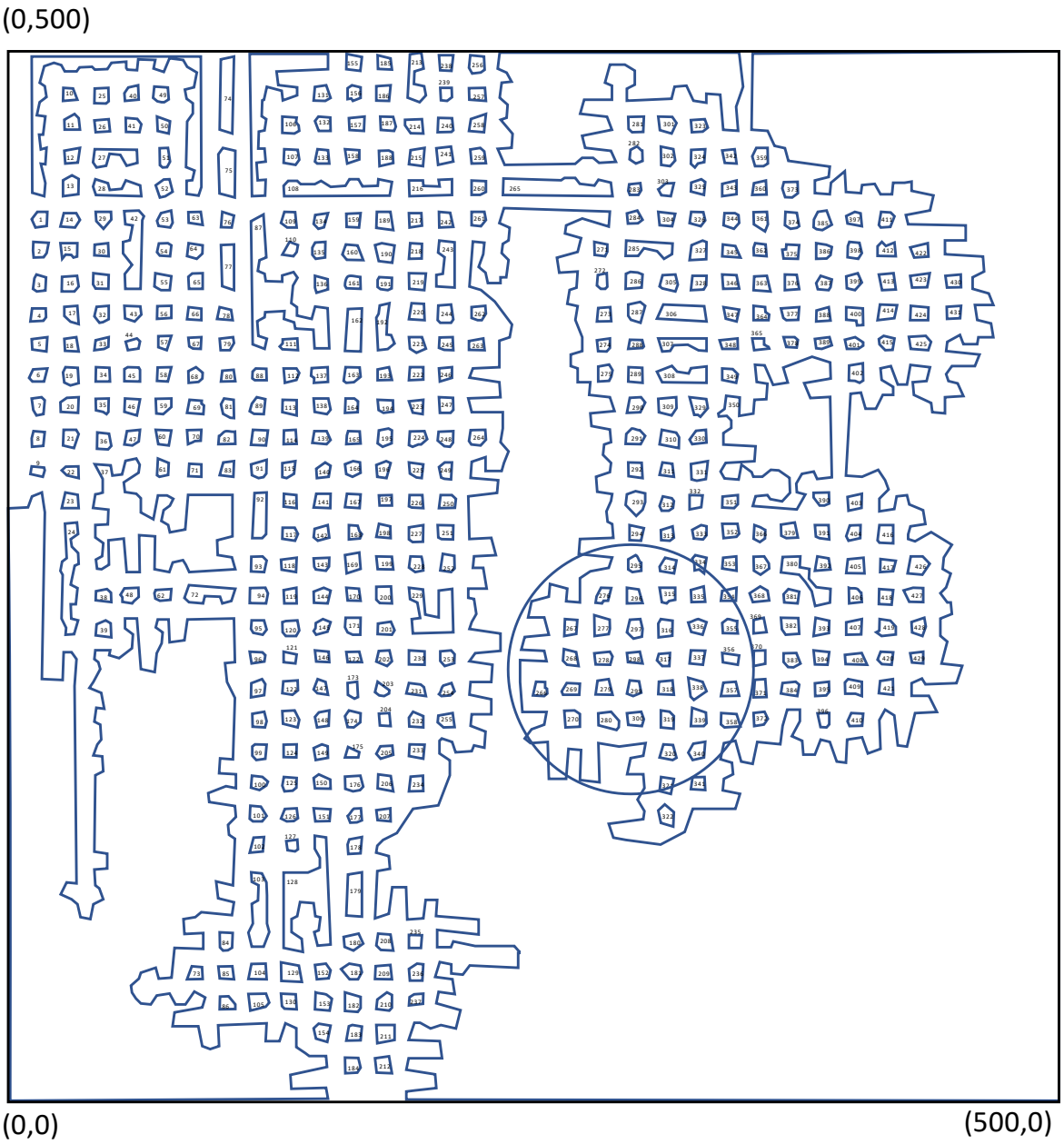

Figure 4-12. Size of the model to calculate the stresses acting on the pillars of monitoring Area 4 (the area of interest is indicated by the circle).

Pegs on the plan of Area 4 indicate typical values ranging between -1143.9 m and -1147.3 m below datum and the collar elevation is -779.197 m below datum. This gives a depth below surface of 366 m.

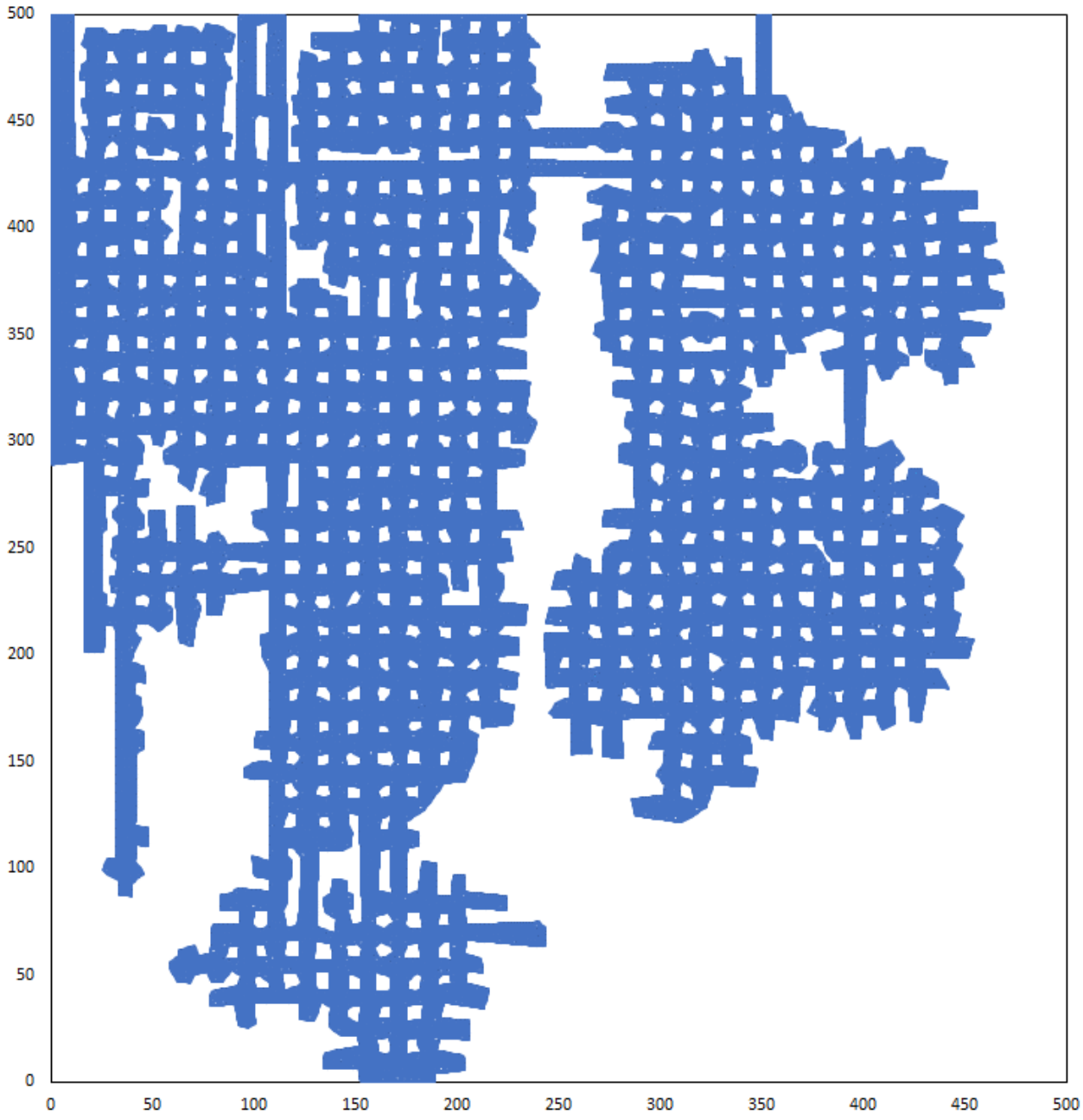

Figure 4-13. The mesh generated for Area 4. The triangular elements are too small to be seen in the diagram.

The pillars studied are shown in Figure 4-14 below. The pillars studied in this area were P296 (N3_28) and P299 (N3_33). The mesh generated for these pillars is illustrated in the figure.

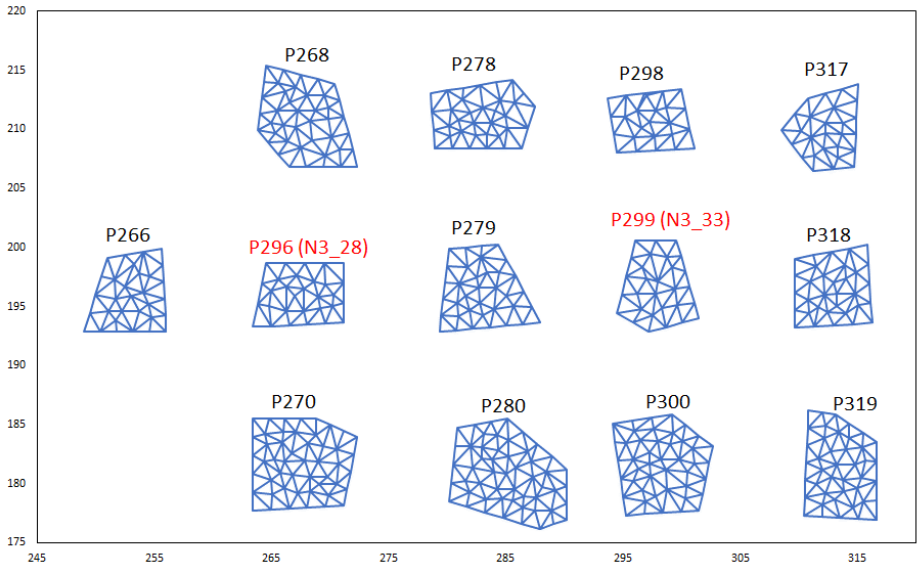

Figure 4-14. The pillars that were studied in the area of interest (Area 4). The pillar numbers in red are the pillars discussed in Section 3.1.3.

The simulated APS values for the pillars in Area 4 are given in Figure 4-15 and Table 4-4 illustrates the back-calculated K-values. These pillars are in excellent condition and in contrast to Area 1, the back-calculated K-value of 76 MPa seems to be a low estimate of the actual K-value that can be used for these high-grade pillars. The virgin vertical stress at a depth of 366 m for the assumed rock density (3000 kg/m^3) is 10.98 MPa. As shown below, the APS on some pillars, therefore, exceeds the virgin stress by a factor of three to four. From the figures generated above, both pillars of interest had higher APS values than the TAT value of 50 MPa. This is caused by the small sizes of these pillars of 37.66 m^2 and 38.49 m^2 respectively. This is lower than the designed pillar size of 49 m^2.

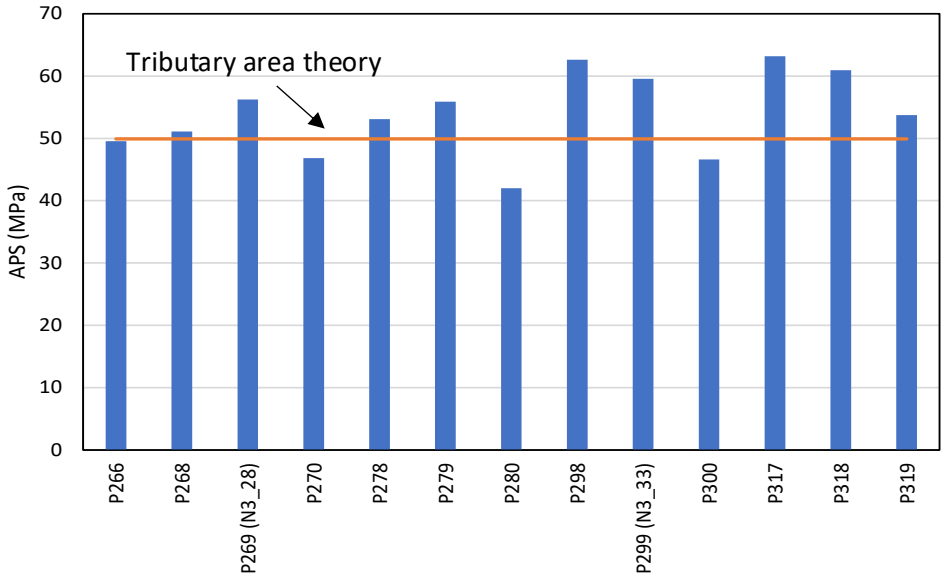

Figure 4-15. Simulated APS values for the pillars in experimental Area 4.

Table 4-4. Simulated APS and back-calculated K-values for the Hedley and Grant pillar strength formula for the pillars in Area 4.

Pillar number	Simulated APS (MPa)	TAT (MPa)	Area (m^2)	Circum-ference (m)	Effective width (m)	Height (m)	K-value (MPa)
P266	49.5	49.9	38.2	25.2	6.1	4.4	61.2
P268	51.1	49.9	52.4	28.7	7.3	4.4	57.5
P269 (N3_28)	56.3	49.9	37.7	27.0	5.6	4.7	76.0
P270	46.8	49.9	61.3	30.8	8.0	4.4	50.4
P278	53.1	49.9	42.8	25.9	6.6	4.4	62.7
P279	55.9	49.9	44.4	27.4	6.5	4.4	66.7
P280	42.0	49.9	68.8	32.1	8.6	4.4	43.6
P298	62.6	49.9	31.7	22.8	5.6	4.4	80.7
P299 (N3_33)	59.5	49.9	38.5	24.4	6.3	4.0	67.0
P300	46.6	49.9	57.0	30.0	7.6	4.4	51.4
P317	63.2	49.9	33.4	23.0	5.8	4.4	79.5
P318	60.9	49.9	40.0	25.4	6.3	4.4	73.7
P319	53.7	49.9	49.1	28.3	6.9	4.4	62.0

4.5. Simulation of Area 5

Area 5 was selected as a second control area in the high-grade zone where little to no scaling of the pillars was observed. The size of the area simulated is shown in Figure 4-16. The depth below surface used to simulate this area was 500 m. Figure 4-17 illustrates the mesh that was generated.

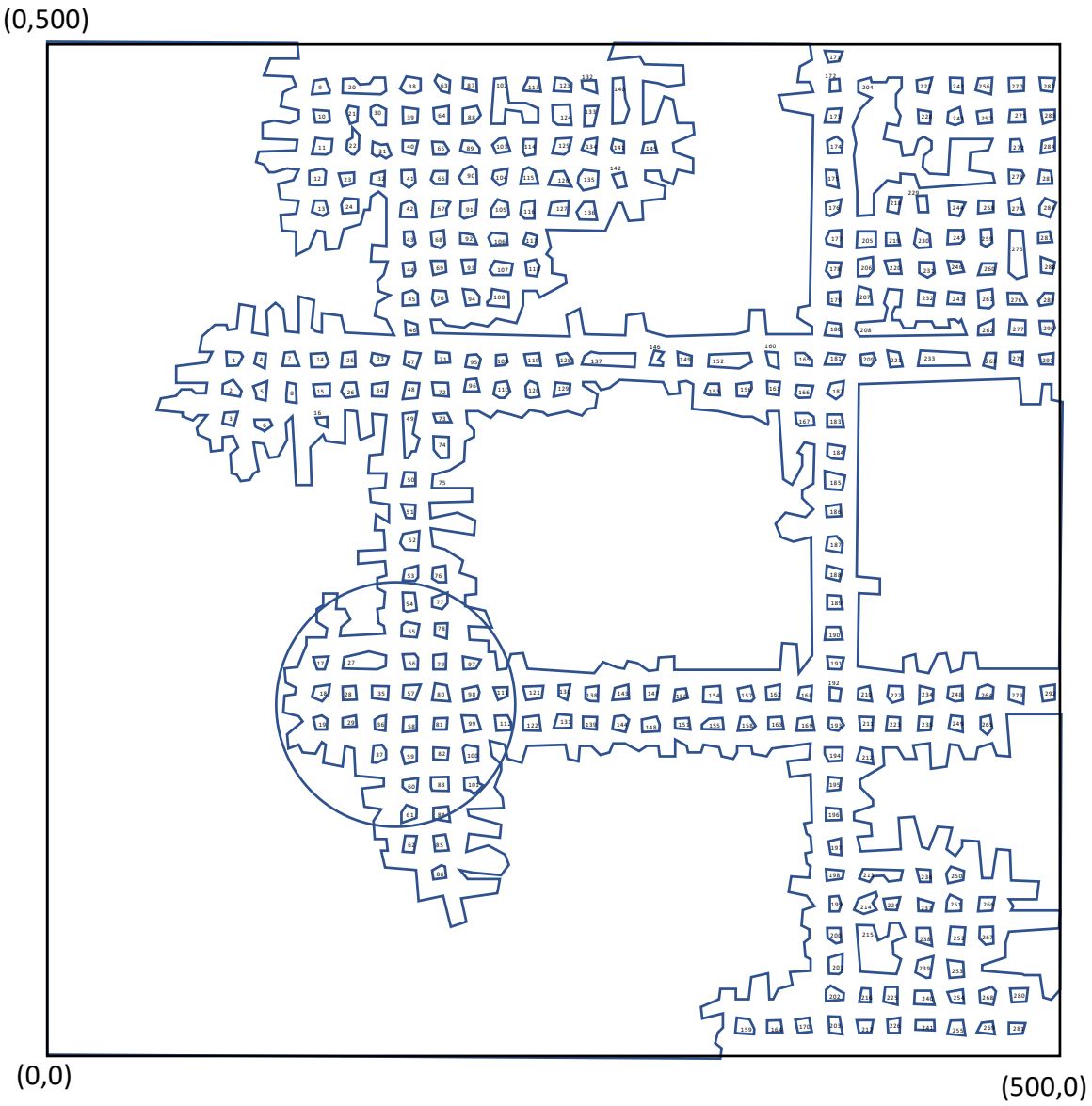

Figure 4-16. Size of the model to calculate the stresses acting on the pillars of monitoring Area 5 (the area of interest is indicated by the circle).

Pegs on the plan of Area 5 indicate typical value of -1278.5 m below datum and the collar elevation is -779.197 m below datum. This gives a depth below surface of 500 m.

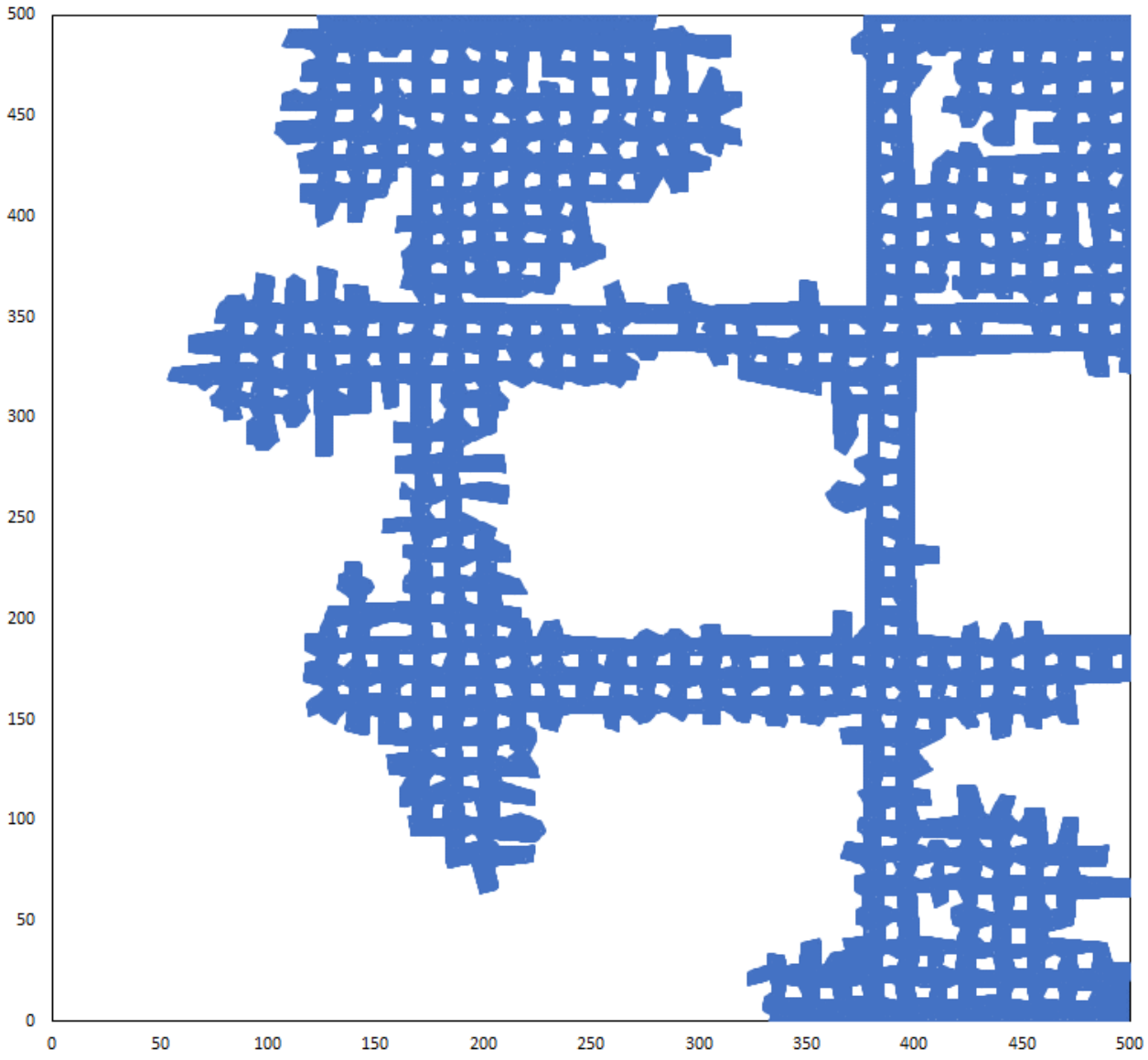

Figure 4-17. The mesh generated for Area 4. The triangular elements are too small to be seen in the diagram.

The pillars studied in this area are shown in Figure 4-18. The pillar of interest in this area is P36 (N3_38). The mesh generated for this pillar is illustrated in Figure 4-18.

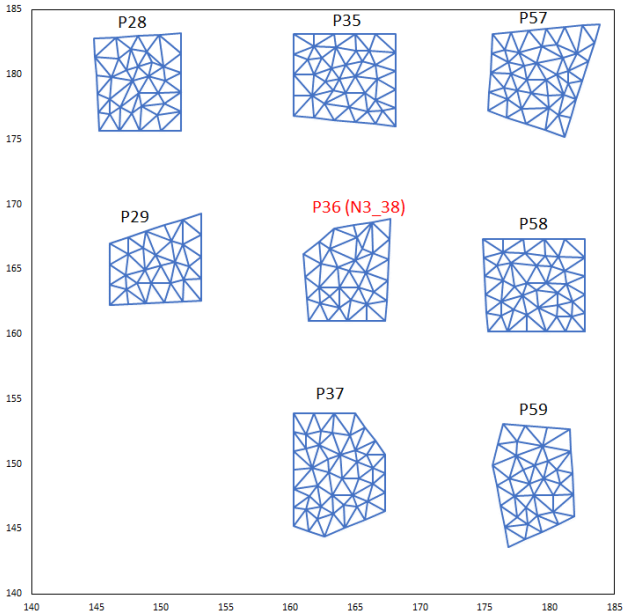

Figure 4-18. The pillars that were studied in the area of interest (Area 5). The pillar number in red is the pillar described in Section 3.1.4.

The simulated APS for the pillars in Area 5 is given in Figure 4-19 and Table 4-5 illustrates the back-calculated K-values. Similar to Area 4, these pillars are in excellent condition and in contrast to Area 1, the back-calculated K-values are very low estimates of the actual K-value that can be used for the high-grade pillars. Noteworthy is that pillar N3_38 has a value of K = 97 MPa. Another slightly smaller pillar has a value of 102 MPa. The virgin vertical stress at a depth of 500 m for the assumed rock density (3000 kg/m^3) is 15 MPa. As shown below, the APS on some pillars, therefore, exceeds the virgin stress by a factor of three to four.

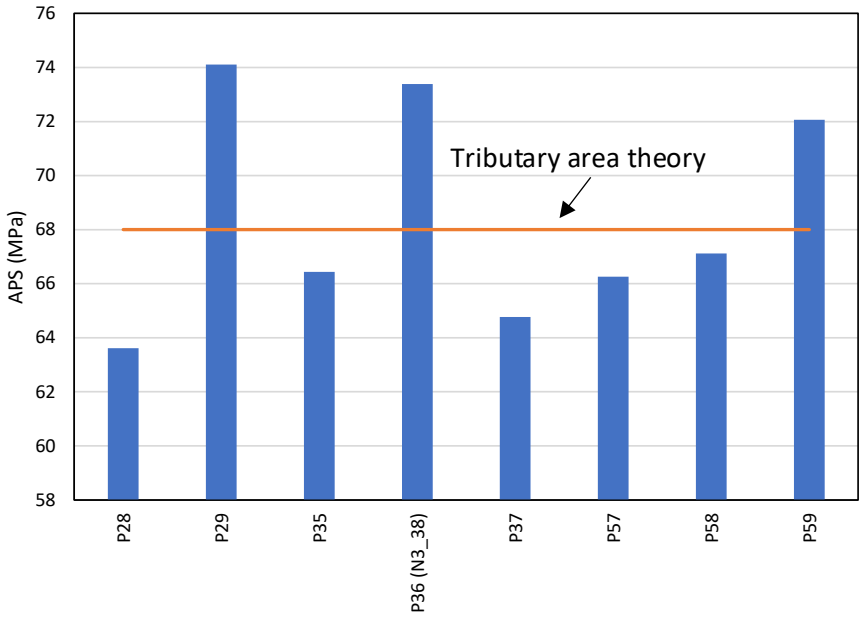

Figure 4-19. Simulated APS values for the pillars simulated in experimental Area 5.

Table 4-5. Simulated APS and back-calculated K-values for the Hedley and Grant pillar strength formula for the pillars in Area 5.

Pillar number	Simulated APS (MPa)	TAT (MPa)	Area (m^2)	Circum-ference (m)	Effective width (m)	Height (m)	K-value (MPa)
P28	63.6	68.0	47.7	27.7	6.9	5.2	83.5
P29	74.1	68.0	40.7	26.1	6.2	5.2	102.1
P35	66.4	68.0	53.0	29.3	7.2	5.2	85.0
P36 (N3_38)	73.4	68.0	44.5	26.5	6.7	5.2	97.4
P37	64.8	68.0	58.0	29.4	7.9	5.2	79.3
P57	66.3	68.0	52.9	29.6	7.1	5.2	85.4
P58	67.1	68.0	54.7	29.6	7.4	5.2	85.0
P59	72.1	68.0	46.3	27.2	6.8	5.2	95.1

4.6. Simulation of Area 6

In 2020, this area was simulated by the author. A summary of the results is discussed below and it provides an additional data point for pillars where the behaviour is controlled by joint sets with a small spacing. The size of the area simulated is shown in Figure 4-20 and the average depth in this area was 450 m. The pillars studied in detail are shown in Figure 4-21.

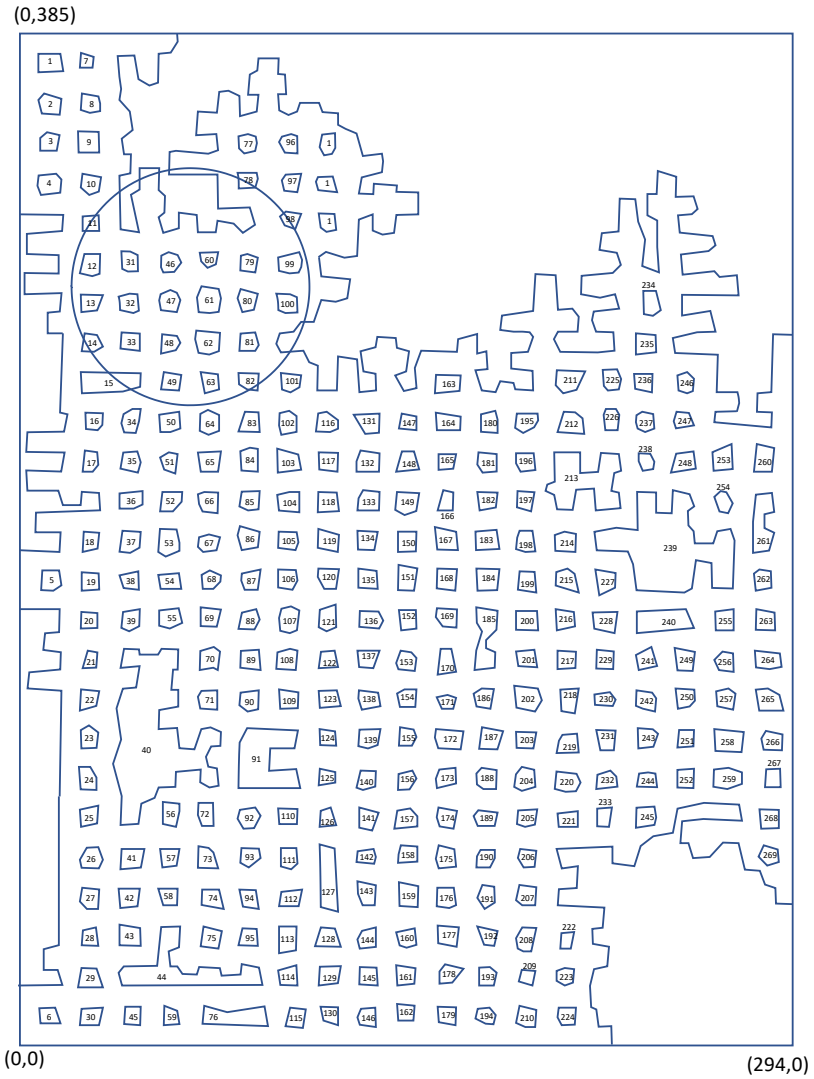

Figure 4-20. Size of the model to calculate the stresses acting on the pillars of monitoring Area 6 (indicated by the circle).

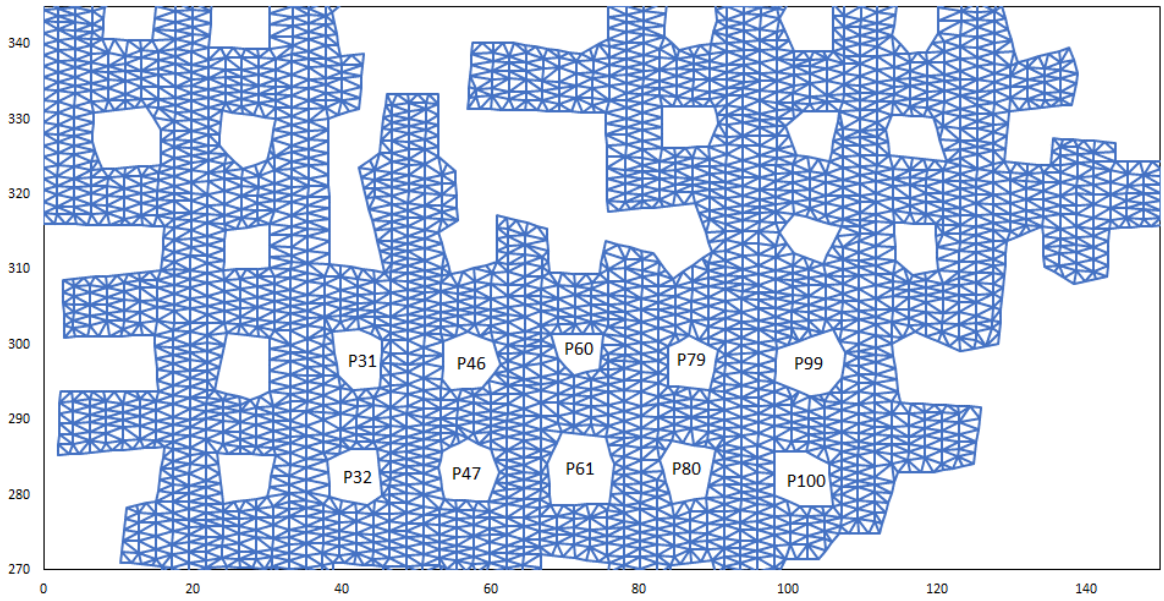

Figure 4-21. The pillars that were studied in the area of interest (Area 6).

The simulated APS for the pillars in Area 6 is given in Figure 4-22 and Table 4-6 illustrates the back-calculated K-values. Excessive scaling was observed in this area. Pillar P60 is of interest as it is also discussed in Chapter 3 (see Section 3.1.5). The back-calculated K-value is 106 MPa. This is too large an estimate to design a stable pillar for this type of seam material as there is excessive scaling of the pillar and the mine considers it as a failed pillar. It should be noted that this back-calculated K-value is not even as large as the K = 133 MPa currently used for pillar design at the mine.

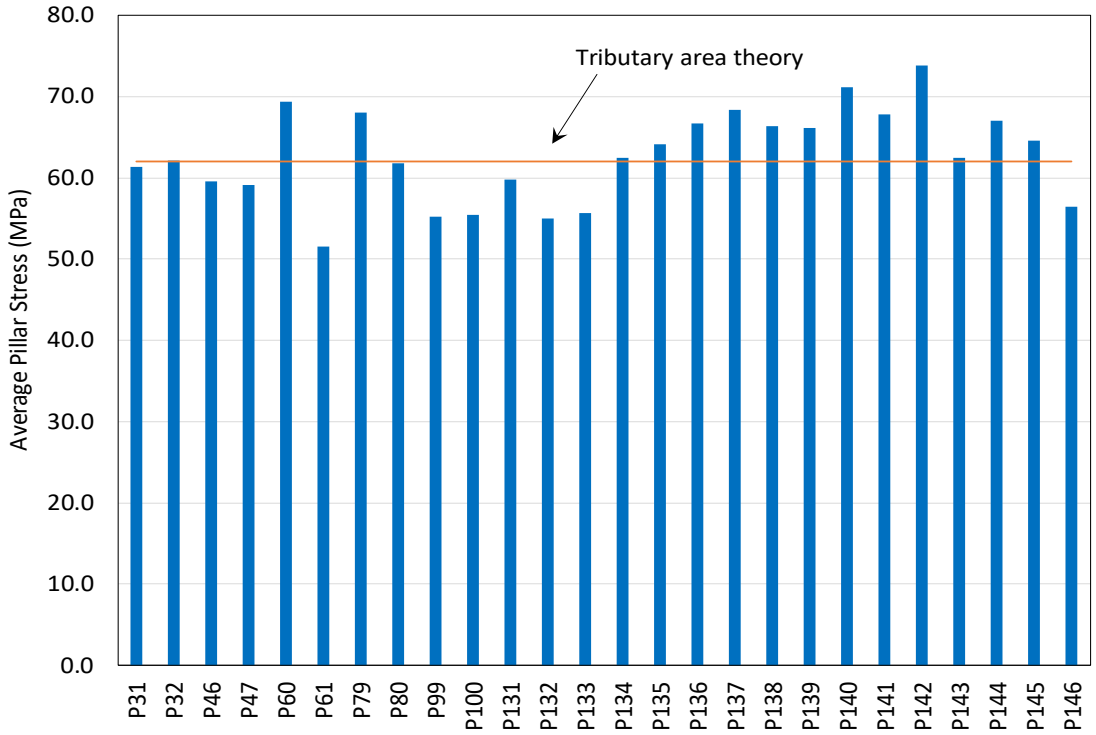

Figure 4-22. Simulated APS values for the pillars in experimental Area 6.

Table 4-6. Simulated APS and back-calculated K-values for the Hedley and Grant pillar strength formula for the pillars in Area 6.

Pillar number	Simulated APS (MPa)	TAT (MPa)	Area (m^2)	Circum-ference (m)	Effective width (m)	Height (m)	K-value (MPa)
P31	61.3	62.0	44.5	25.9	6.9	5.5	84.0
P32	62.1	62.0	46.0	25.9	7.1	5.5	83.6
P46	59.6	62.0	47.6	24.2	7.9	5.5	76.3
P47	59.1	62.0	52.9	27.1	7.8	5.5	75.9
P60	69.4	62.0	30.2	21.9	5.5	5.5	106.1
P61	51.5	62.0	75.2	33.2	9.1	5.5	61.4
P79	68.0	62.0	38.6	23.9	6.5	5.5	96.1
P80	61.8	62.0	45.7	26.3	6.9	5.5	84.2
P99	55.2	62.0	61.7	29.7	8.3	5.5	68.8
P100	55.5	62.0	49.7	27.4	7.3	5.5	73.9
P131	59.8	62.0	53.3	30.2	7.1	5.5	80.7
P132	55.0	62.0	64.1	31.6	8.1	5.5	69.3
P133	55.7	62.0	58.0	30.3	7.7	5.5	72.3
P134	62.5	62.0	47.4	27.6	6.9	5.5	85.7
P135	64.1	62.0	46.1	27.3	6.8	5.5	88.5
P136	66.7	62.0	46.8	26.9	7.0	5.5	90.7
P137	68.4	62.0	46.2	27.6	6.7	5.5	95.0
P138	66.4	62.0	47.9	27.1	7.1	5.5	89.8
P139	66.1	62.0	50.9	28.0	7.3	5.5	88.1
P140	71.1	62.0	43.0	25.4	6.8	5.5	98.1
P141	67.8	62.0	44.6	27.1	6.6	5.5	94.9
P142	73.8	62.0	30.5	22.1	5.5	5.5	112.9
P143	62.5	62.0	53.7	29.4	7.3	5.5	83.0
P144	67.0	62.0	39.8	24.8	6.4	5.5	95.0
P145	64.6	62.0	42.2	26.2	6.5	5.5	91.3
P146	56.4	62.0	43.7	25.7	6.8	5.5	77.7

Numerical modelling of the six experimental areas indicated that the TAT is conservative and that for irregular pillar layouts, numerical modelling should be used. The back-calculated values for these areas illustrated that for the R5 product area, the value of K = 133 MPa is probably too high and a reduced value should be used for this geotechnical area.

Of particular interest is the simulation of the scaling of the pillars and this is discussed in the next chapter.

CHAPTER 5

NUMERICAL MODELLING OF PILLAR SCALING

5.1. Description of the Model

The limit equilibrium model, as implemented in the TEXAN code, was used in this study as it provides a convenient method to simulate pillar scaling and pillar failure in bord and pillar layouts. To highlight the characteristics of the model, Figure 5-1 illustrates the force equilibrium of a slice of rock inside a pillar. The detailed derivation of the constitutive model is given in a number of publications, such as Napier and Malan (2007, 2014), and it will not be repeated here. A more detailed derivation of the extended time-dependent version of the limit equilibrium model is given in Chapter 6.

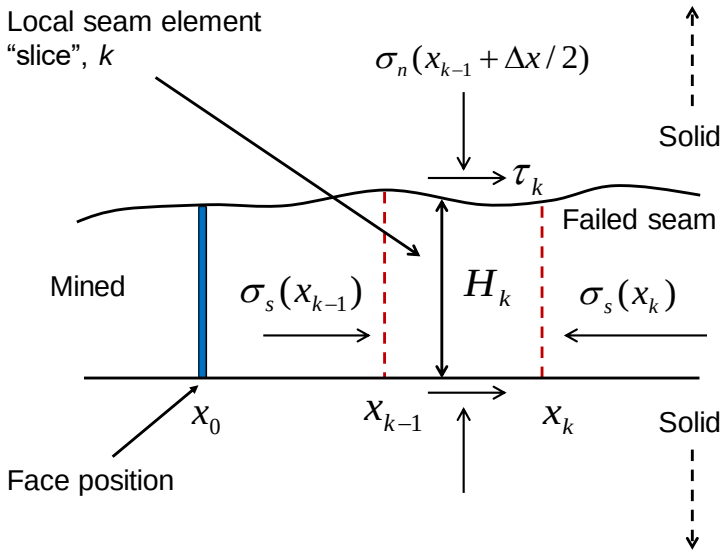

Figure 5-1. Force equilibrium of a slice of rock at the edge of a stope or a pillar (after Napier and Malan, 2014).

The notation adopted by Napier and Malan (2014) is used below. For the basic limit equilibrium model, as illustrated in Figure 5-1, it is assumed that within segment k, the average seam height is H_k. The seam normal stress σ_n is a function of the seam parallel stress σ_s and this is given by the following assumption:

$$\sigma_n(x) = S_k + m_k \sigma_s(x) \tag{5.1}$$

where m_k and S_k are strength parameters. Furthermore

$$\mu_k = \tan(\phi_k) \tag{5.2}$$

where ϕ_k is the friction angle on the interfaces between the pillar and hangingwall and footwall. A state of equilibrium then exists in the slice of rock if the following equation is satisfied (Napier and Malan, 2014):

$$H_k \frac{d\sigma_s}{dx} = 2\tau_k = 2\mu_k(S_k + m_k\sigma_s) \tag{5.3}$$

Integrating equation (5.3) illustrates that the seam normal and seam parallel stress increases exponentially from the edge of the pillar to the boundary between the failed edge and the intact portion of the pillar. Based on equation (5.1), initial failure is assumed to occur at a point in the pillar if the seam normal stress reaches the intact strength given by

$$\sigma_n = S^0 + m^0\sigma_s \tag{5.4}$$

where S^0 and m^0 are the intact strength parameters. Once failure accurs, the strength parameters can decrease to specified residual values where S^c and m^c and the residual strength is then given by:

$$\sigma_n = S^c + m^c\sigma_s \tag{5.5}$$

In summary, the model assumes that if the pillar material fails, a relationship exists between the reef normal and parallel stress inside the failed portion of the pillar. The reef-parallel stress $\sigma_s(x)$ at a particular position is balanced by a frictional shear traction $\mu_k\sigma_n$ at the interfaces between the fractured material and the intact reef. The implication of this model and its assumptions is that the normal stress increases exponentially from the edge of the pillar towards the intact portion of the pillar. A further drawback of the model is that the failure is restricted to the plane of the reef, but this is considered an acceptable assumption for the typical pillar problems studied in bord and pillar layouts. In these cases, the pillar failure is often restricted to the plane of the reef only. In spite of the shortcomings, it is an elegant model to simulate pillar failure on the reef horizon in a large-scale model containing many pillars with irregular shapes (Napier and Napier, 2021).

5.2. Simulating Pillar Scaling at BRMO using the Limit Equilibrium Model

For this part of the study, the scaling of the pillars at BRMO in the different geotechnical areas was simulated using the basic limit equilibrium model described above. No time-dependent scaling was included in this chapter. A key objective of the modelling was to understand if a preliminary calibration of the limit equilibrium model can simulate the distinctly different pillar behaviours in the different geotechnical areas. It should be noted that this model is only an approximation of the pillar failure mechanism at BRMO as the persistent joint sets, illustrated in previous chapters, cause a discontinuous unravelling of the pillar edges. The limit equilibrium model does not explicitly simulate these joints and subsequent formation of the loose blocks. It is therefore only an approximation of the failure mechanism. The modelling results in this chapter nevertheless illustrate that it is a valuable model to simulate the pillar failure over a large area of the mine.

Similar to other inelastic models, the limit equilibrium model in TEXAN requires a large number of parameters to be calibrated and these are listed in Table 5-1. The number of parameters increases further if time-dependent behaviour is considered and this is discussed in the next chapter.

Table 5-1. Parameters used for the limit equilibrium model.

Parameter	Value
Intact strength intercept, S^0	60 MPa and 85 MPa
Intact strength slope, m^0	7
Initial residual strength intercept, S^c	4 MPa
Initial residual strength slope, m^c	7
Effective seam height, H	5.5 m
Intact rock Young's modulus, E	90 GPa
Intact rock Poisson's ratio, v	0.2
Intact seam stiffness modulus, k_s	16363 MPa/m
Fracture zone interface friction angle	30°

A preliminary calibration of the parameters was done as follows: Napier and Malan (2021) studied an experimental pillar mining section with a number of intact and failed pillars in a platinum mine. They conducted a number of simulations with different parameters until a good fit with the underground observations were obtained. These parameters were used as a starting point in this current study, except for specifying the much larger seam height of 5.5 m used at BRMO. These preliminary parameters gave surprisingly good results for the areas with significant scaling (e.g. Area

1 and 6) and then as a next step, for Areas 4 and 5, the intact strength intercept, S_0, was increased until the absence of scaling observed underground was also reflected in the model. The only difference in the calibrated values was that $S_0 = 60\ MPa$ was used for the areas with signficiant scaling and $S_0 = 85\ MPa$ was used for the areas with no scaling. This seems intuitively correct as the spacing of the joint sets will affect the intact rock mass strength and a closer joint spacing will result in a lower strength.

In summary, the work in this chapter illustrates qualitatively the value of the limit equilibrium model, but it also highlights its Achilles heel, and that is the calibration of the parameters. If, for example, the slope and residual strength parameters are modified, a different intact strength intercept value will be required to match the observations. Additional work to calibrate the parameters will have to be done in future. This will require an extensive study and is beyond the scope of this current investigation.

For the modelling discussed below, the parameters given in Table 5-1 was used for all the areas. For the areas in the R5 product area (Areas 1,2, 3 and 6), an intact strength intercept of 60 MPa was used and for the +45 high grade area (Areas 4 and 5) an intact strength intercept of 85 MPa was used. **Note that the full model geometries, as shown in Chapter 4 were simulated, but only the pillars of interest are shown in the figures below to clearly indicate the extent of failure in these pillars. The other parts of the modelling geometries are not shown below and the reader is referred to Chapter 4.** The difference between the modelling in Chapter 4 and Chapter 5 is that in Chapter 4 the pillars were simulated as rigid pillars and no failure was allowed, while in Chapter 5, the limit equilibrium model was used for the pillars to simulate the scaling.

5.2.1. Simulation of Area 1

Figure 5-2 illustrates the simulated scaling of the pillars in this area. The red dots are the failed limit equilibrium elements and the grey dots are the intact elements. The dots are not regularly spaced as it is the centroids of the triangular elements and this reflects the varying sizes and shapes of the triangles. Similar to the underground observations, pillars P151 (N3_2), P172, P173 (N3_1), P192, and P193 (N3_9) are subjected to excessive scaling. The depth of scaling is comparable to that measured underground (≈ 1 m). Figure 5-3 illustrates the simulated APS on the pillars. This is compared to the numerical model where no pillar failure was allowed (see Chapter 4). Note the significant decrease in APS compared to the scenario where the pillars were not allowed to fail. A table with the simulated APS values is given in Appendix C.

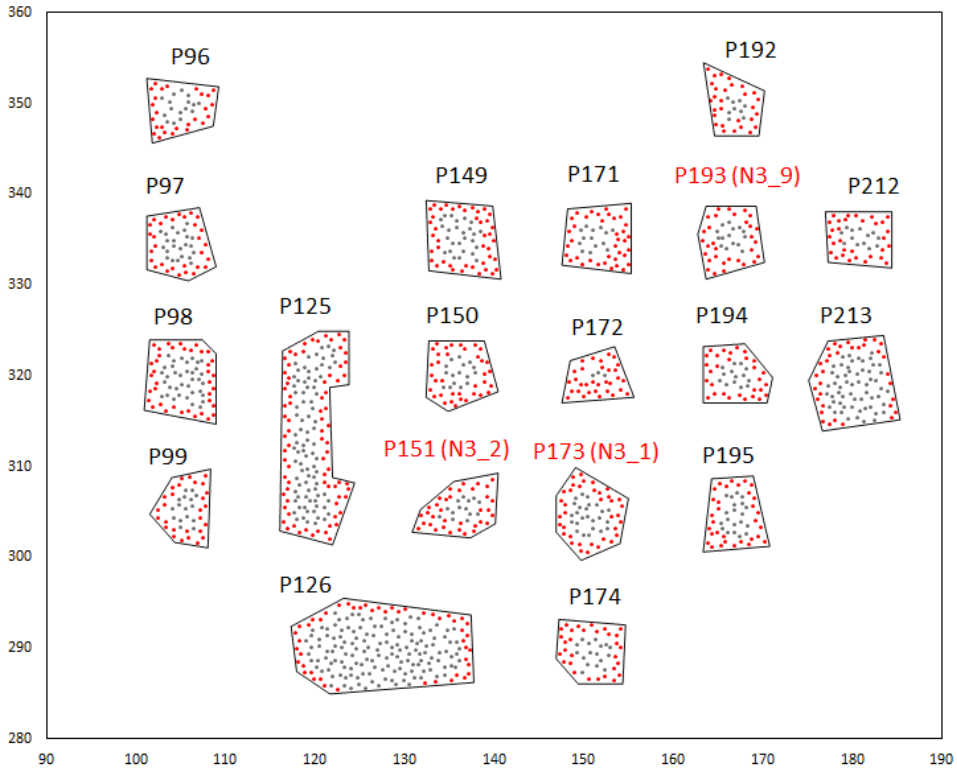

Figure 5-2. Scaling of the edges of the pillars as simulated by the limit equilibrium model in TEXAN for Area 1. The red dots are the collocation points of the failed elements. The grey dots represent the intact elements.

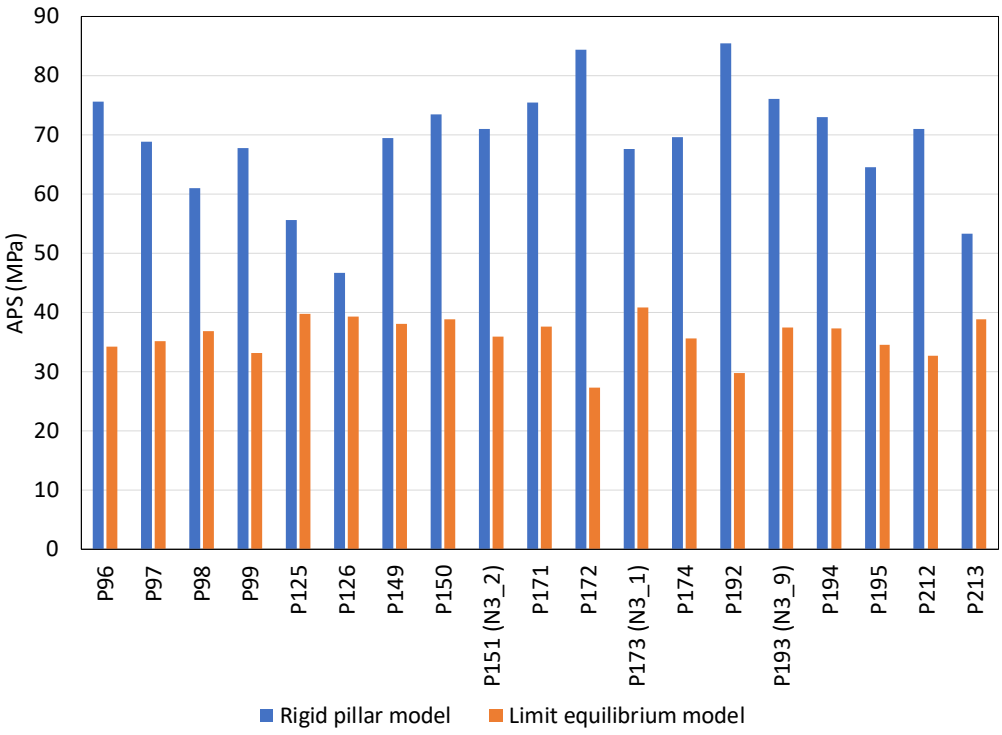

Figure 5-3. A comparison between the APS values for the model with rigid pillars and the limit equilibrium model for Area 1.

Figure 3-10 in Chapter 3 already illustrated the extensive scaling in this area and it is comparable to the modelling illustrated above. A further example of the scaling is given in Figure 5-4 and this illustrates the condition of pillar N3_1. There seems to be a good agreement between the modelling using the parameters given in Table 5-1 and the underground observations for this area.

Figure 5-4. The condition of pillar N3_1 in Area 1 illustrating excessive scaling of the pillar.

5.2.2. Simulation of Areas 2 and 3

Figure 5-5 illustrates the simulated scaling of the pillars for Area 2. Similar parameters were used as those for Area 1 above. Of interest is that almost no scaling is simulated for pillar N3_15, while more scaling is seen for pillar N3_20. Their relative positions in the geometry were shown in Figure 3-15 in Chapter 3 and this explains the difference in simulated behaviour. N3_15 is larger in size and closer to the face and therefore the stress acting on this pillar is less. The difference in simulated stresses are illustrated in Figure 5-6.

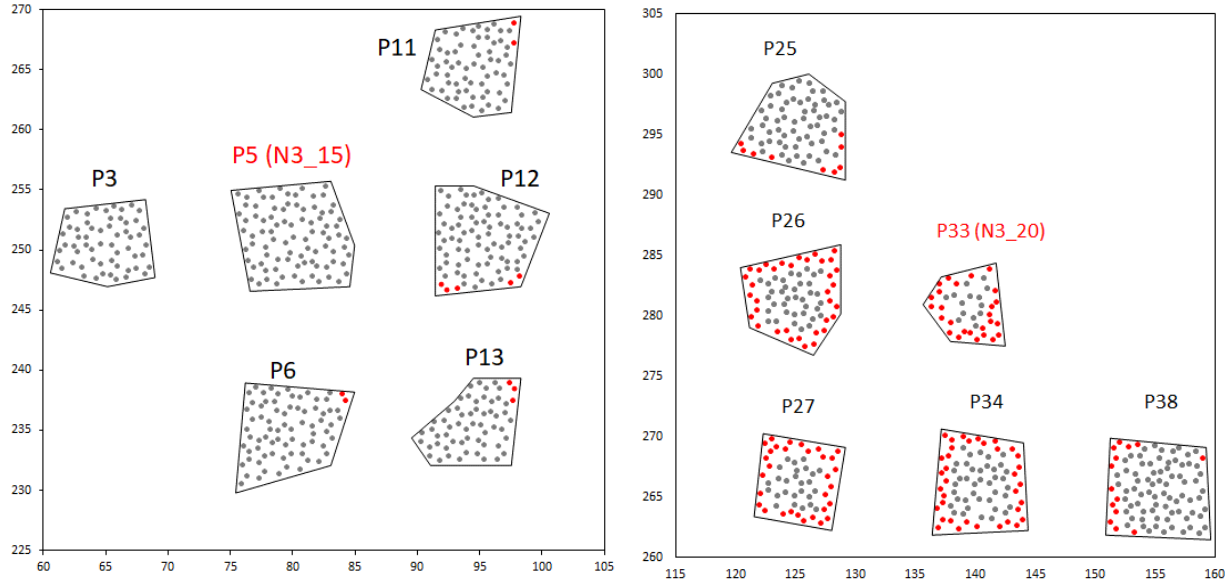

Figure 5-5. Scaling of the edges of the pillars as simulated by the limit equilibrium model in TEXAN for Area 2. The red dots are the collocation points of the failed elements.

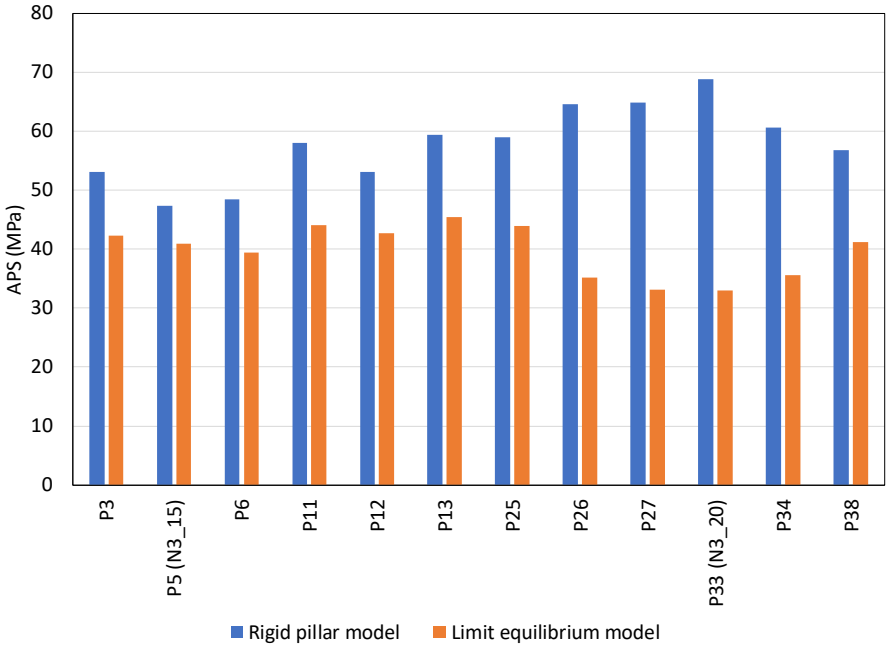

Figure 5-6 A comparison between the APS values for the model with rigid pillars and the limit equilibrium model for Area 2.

An illustration of the condition of the pillars are given in Figure 5-8. There seems to be a qualitative agreement with the modelling, as more scaling is seen for pillar N3_20 compared to N3_15.

N3_15

N3_20

Figure 5-7 An illustration of the scaling of N3_15 and N3_20. Note the extensive "hour glassing" for N3_20 at the bottom right.

Figure 5-8 illustrates the simulated scaling of the pillars for Area 3. Extensive scaling is predicted for pillar N3_25. Figure 5-9 illustrates the simulated APS values on the pillars using the limit equilibrium model and for rigid pillars. The simulated stress on pillar N3_25 is relatively high owing to its smaller size and this resulted in extensive scaling similar to that observed underground. This is illustrated in Figure 3-21 and Figure 3-22 in Chapter 3 and a further example is given in Figure 5-10. There also seems to be a good qualitative agreement with the scaling predicted by the modelling and the underground observations for this particular pillar.

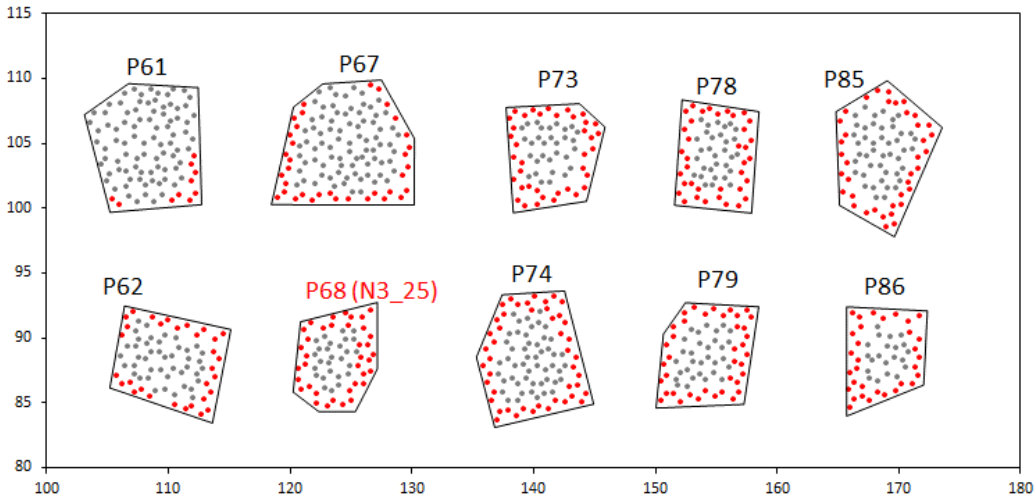

Figure 5-8. Scaling of the edges of the pillars as simulated by the limit equilibrium model in TEXAN for Area 3. The red dots are the collocation points of the failed elements.

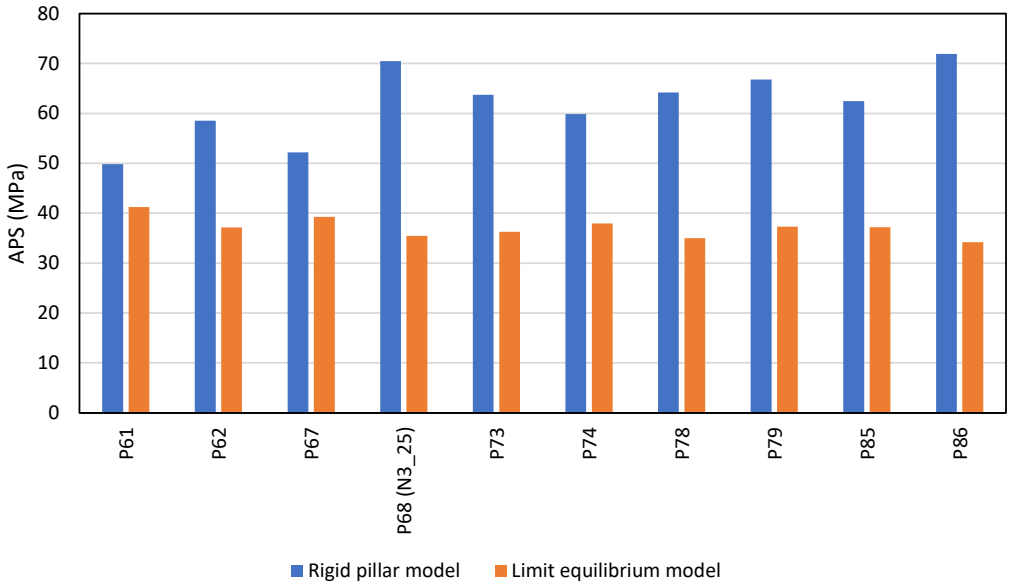

Figure 5-9. A comparison between the APS values for the rigid pillar model and the limit equilibrium model for Area 3.

Figure 5-10. Extensive scaling of pillar N3_25.

5.2.3. Simulation of Area 4

This area is one of the high-grade areas monitored and almost no pillar scaling is observed in this area. This increase in pillar strength was simulated by increasing the intact strength intercept, S_0, in a trial and error manner until no scaling was simulated for this area. A value of $S_0 = 85$ MPa resulted in the absence of any scaling as shown in Figure 5-11. This is the minimum value that gave no scaling in the modelling and it may in fact be even higher for these pillars. This again emphasises the need for additional work to calibrate the limit equilibrium model. The modelling is nevertheless in agreement with the observations made during the underground visit. The pillar condition is illustrated in Chapter 3 and a further example is given in Figure 5-12.

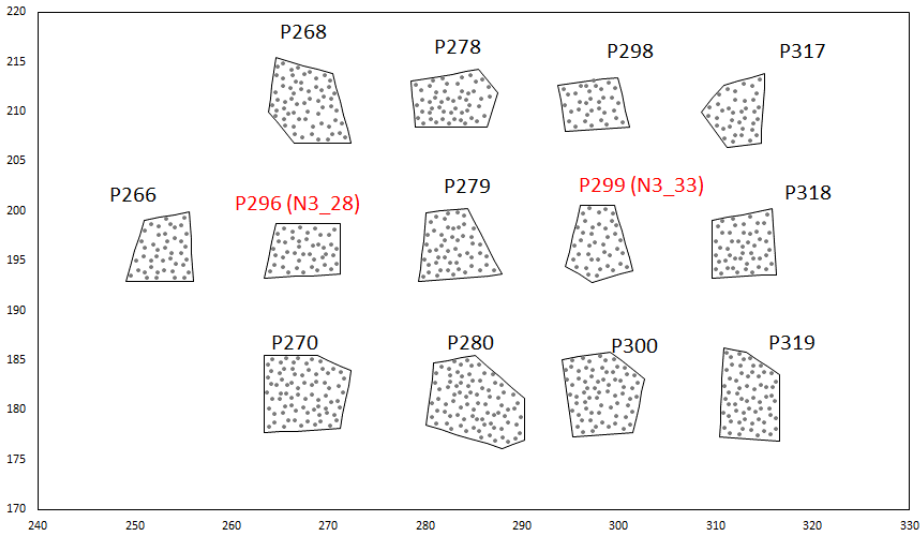

Figure 5-11. Simulating the pillars using the limit equilibrium model in TEXAN for Area 4.

Figure 5-12. Typical condition of the pillars in Area 4. No scaling was observed.

5.2.4. Simulation of Area 5

This area is the second of the high-grade areas monitored and similarly, no pillar scaling was observed in this area. Figure 5-13 illustrates the results from the limit equilibrium model with a value of $S_0 = 85\ MPa$ and no failure is simulated.

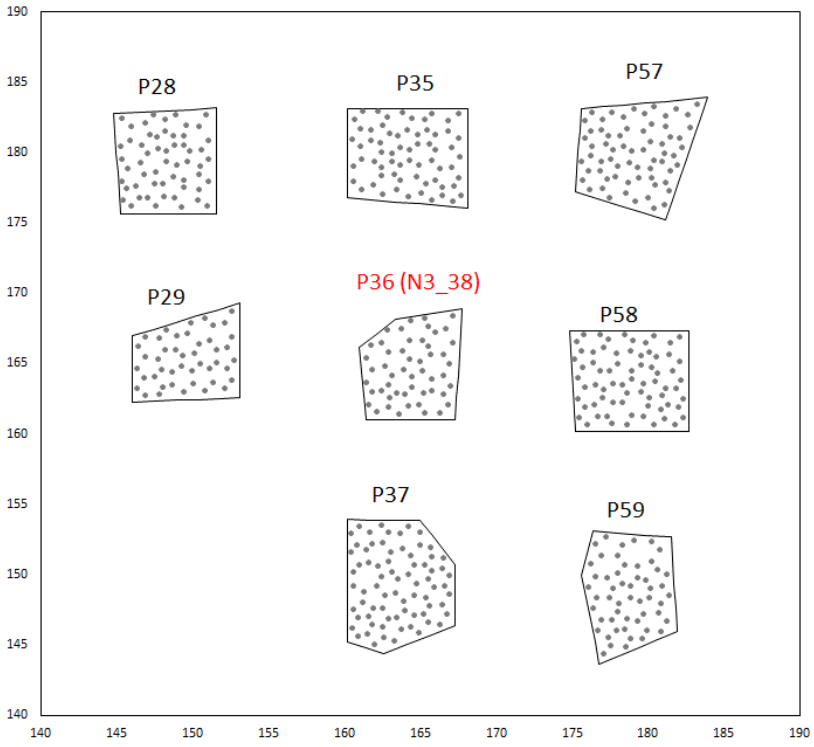

Figure 5-13. Simulating the pillars using the limit equilibrium model in TEXAN for Area 4.

The conditions of the pillars in this area has already been illustrated in Chapter 3. Figure 5-14 illustrates a further example of the condition of pillar N3_38. The pillar is an excellent condition and no scaling is observed. This agrees with the numerical modelling.

Figure 5-14. Two views of pillar N3_38 at Nchwaning III shaft illustrating the excellent condition of the pillar.

5.2.5. Simulation of Area 6

Area 6 was another interesting area as extensive pillar scaling was observed in this area and the pillars had to be reinforced by the mine. These observations were already described in Chapter 3. This area was also simulated using similar limit equilibrium parameters compared to the other areas that experienced extensive scaling. The results are shown in Figure 5-15 and this illustrates the extensive scaling of the pillars. Figure 5-16 illustrates the simulated APS and this is compared to the model where no pillar failure was allowed. Note the significant decrease in APS compared to the scenario where the pillars were not allowed to fail.

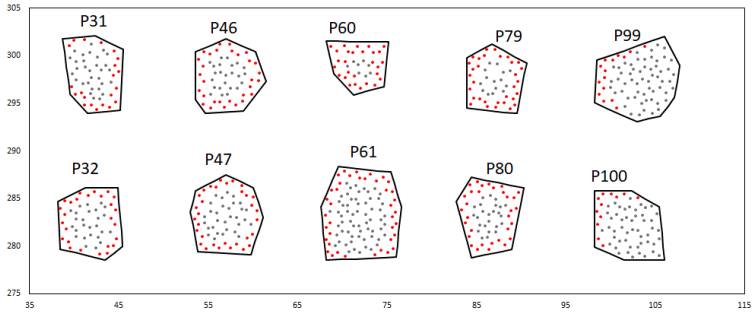

Figure 5-15. Scaling of the edges of the pillars as simulated by the limit equilibrium model in TEXAN. The red dots are the collocation points of the failed elements.

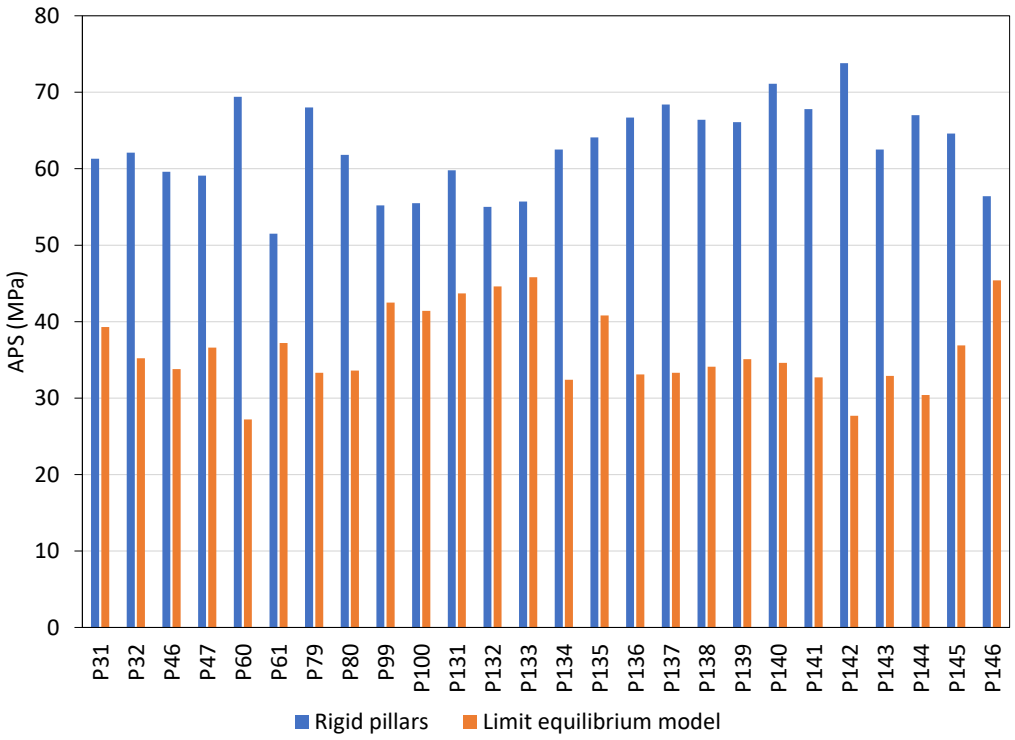

Figure 5-16. Simulated APS for the pillars that were allowed to fail according to the limit equilibrium model.

To compare with the modelling, Figure 5-17 and Figure 5-18 illustrate the condition of pillars P60 and P79 respectively. This highlights the significant scaling that these pillars experienced. These observations also qualitatively similar to the modelling results.

Figure 5-17. Condition of pillar P60.

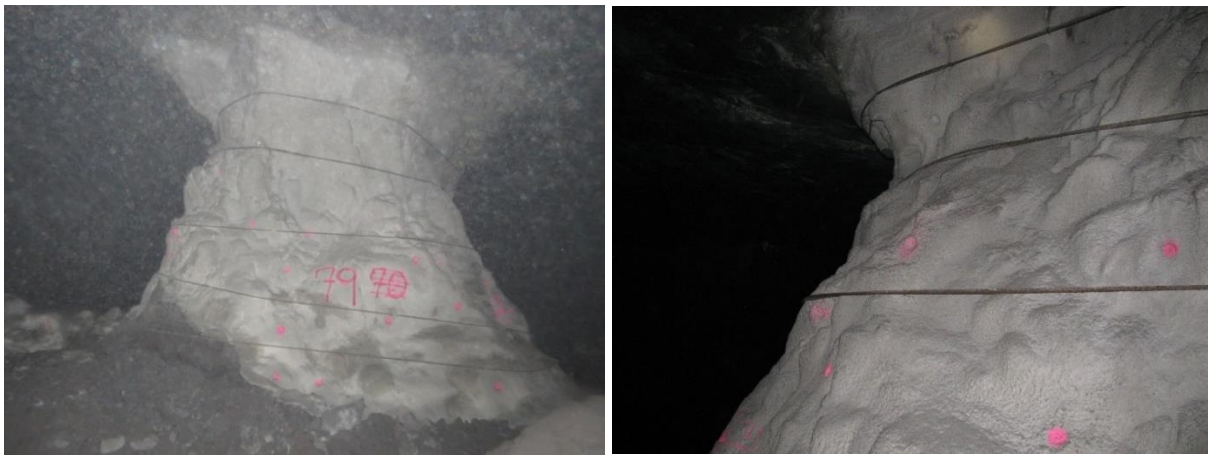

Figure 5-18. Condition of pillar P79.

5.3. Summary

In summary, a good qualitative agreement was obtained between the observed pillar behaviour and the simulations using a limit equilibrium constitutive model. A preliminary calibration of the model is given in this chapter and the difference in pillar behaviour between the two major geotechnical areas could be simulated by modifying the value of the intact strength intercept S_0. This chapter nevertheless illustrated the difficulty of calibrating the parameters. Additional work in this regard will have to be done in future. This will require an extensive study and is beyond the scope of this current investigation.

An aspect not considered above is the time-dependent deterioration of the pillars. This may be a key factor affecting the long-term pillar strength and this is explored in the next chapter.

CHAPTER 6

TIME-DEPENDENT PILLAR SCALING

The observations made by the author in 2020 and 2021 indicated that in some areas of the mine, time-dependent pillar scaling may occur. An example is illustrated in Figure 6-1 of a pillar that has undergone significant scaling. This typically results in the mine supporting these pillars using thin spray-on liners (see Figure 3-34 in Section 3.1.6). In some cases, the thin spray-on liners fail and the deterioration continues as shown in Figure 6-1 (right). This is used as evidence that some time-dependent scaling of the pillars occurs and this ongoing deterioration may affect the pillar strength over a period of time. The rate of scaling at BRMO was therefore investigated and the results are described in this chapter. This was an important study as no work has been done on time-dependent pillar scaling in South African hard rock mines and no methodology exists to account for this phenomenon in pillar design.

Figure 6-1. Example of pillar scaling at Nchwaning III shaft (left). This failure seems to occur in a time-dependent fashion. For the pillar on the right, a thin spray-on liner was applied to the pillar, but the scaling persisted and the liner failed.

In Chapter 3, the type of measurements conducted in an attempt to quantify the rate of time-dependent scaling is described. The measurements were conducted over a three-month period, but these illustrated no time-dependent scaling. The measurement period was probably too short and it also seems as if the bulk of the scaling occur very soon after the pillar has formed and then the rate of scaling decreases with time when the pillar assumes an “hourglass” shape. The duration of a

short post-graduate study may in fact be too short to accurately record the rate of scaling of these hard rock pillars.

As an alternative, in Area 1, another type of measurement was conducted. This was the estimated distance that the pillars have already scaled. The original position of the pillar edge against the hanging wall could be easily identified and the distance from this position to the maximum scaling depth was measured as illustrated in Figure 6-2. In many cases, the scaling resulted in the pillar assuming an “hourglass” shape. Incidentally, Van der Merwe (2004) also found this to be the most common shape formed by the time-dependent scaling of coal pillars. The measured scaling distance for the various areas studied at BRMO is given in Table 6-1. Area 1, with the low rock mass rating, has the largest scaling distance. Values as large as 2 m were measured with an average value of 0.8 m. The areas of the pillars have been substantially reduced as a result and this increases the stress on the pillars and reduces the factor of safety.

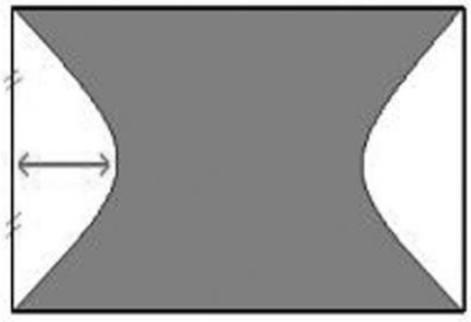

Figure 6-2. Measurement of the maximum scaling distance (after Van der Merwe, 2004). The pillars in Area 1 also tend to form this shape as a result of the excessive scaling.

The pillars in Area 1 were cut during the period from March to June 2018, whereas the pillars in Areas 2 and 3 were only cut during January and February 2021 respectively. As a first crude estimate of the scaling rate of the pillars with a low rock mass rating, it appears that 0.5 m of scaling occurs during the first 3 months after the pillar is formed and then another 0.3 m occurs during the next three years. As the time-dependent scaling is such a slow process, it explains why no prominent scaling was recorded by the author during the short three-month monitoring period.

Table 6-1. Measured scaling distance for the various pillars studied in the areas with a low rock mass rating. The letters A, B, C and D after the pillar number refer to the different sides of the particular pillar.

Pillar (Area 1)	Scaling distance (m)	Pillar (Areas 2 and 3)	Scaling distance (m)
N3_1A	2.0	N3_15A	0.6
N3_1B	1.0	N3_20A	0.3
N3_1C	1.7	N3_20B	0.8
N3_1D	0.9	N3_20C	0.6
N3_2A	0.8	N3_20D	0.4
N3_2B	1.3	N3_25A	0.1
N3_2C	0.8	N3_25B	0.5
N3_2D	0.5	N3_25C	0.3
N3_9A	1.4	N3_25D	0.5
N3_9B	0.7	**Average**	**0.5**
N3_9C	1.2		
N3_9D	0.9		
N3_3	0.5		
N3_4	0.8		
N3_5	0.7		
N3_6	0.7		
N3_10	0.6		
N3_11	0.5		
N3_12	0.5		
N3_13	0.6		
N3_43	0.7		
N3_44	1.1		
N3_45	0.5		
N3_46	0.5		
N3_47	0.6		
N3_48	0.4		
N3_49	0.6		
N3_50	0.6		
Average	**0.8**		

To simulate this time-dependent pillar scaling, a time-dependent limit equilibrium model proposed by Napier and Malan (2014) was investigated.

6.1. Time-Dependent Limit Equilibrium Model

The limit equilibrium model presented in Chapter 5 does not consider the time-dependent aspect. Napier and Malan (2014, 2018) gives the details of the time-dependent limit equilibrium model. The derivation of this model is given below in more detail as it was useful to the author to better understand the implications of the various assumptions in the model. The steps below are also a useful introduction to the concept for students not familiar with this concept.

Consider a pillar with two bords mined adjacent to it as illustrated in Figure 6-3. The pillar is fractured on its two edges and it has a solid intact core. The force equilibrium of a thin section of rock in the fractured portion of the pillar is also indicated in the figure and it is assumed that this section is in equilibrium. As described in Chapter 5, the seam normal stress is depicted by σ_n and the seam parallel stress by σ_s.

At the contact with the hanging wall and footwall, there is a parting present. The friction angle on these interfaces are given by ϕ and the coefficient of friction $\mu_I = tan\phi$. This is one of the drawbacks of this simplified limit equilibrium model as it assumes a symmetrical model with the same friction on both contacts. The edges of the pillar will fail if the stress exceeds the rock strength. For high stress levels, the pillar may be completely fractured or alternatively, the core of the pillar may still be intact.

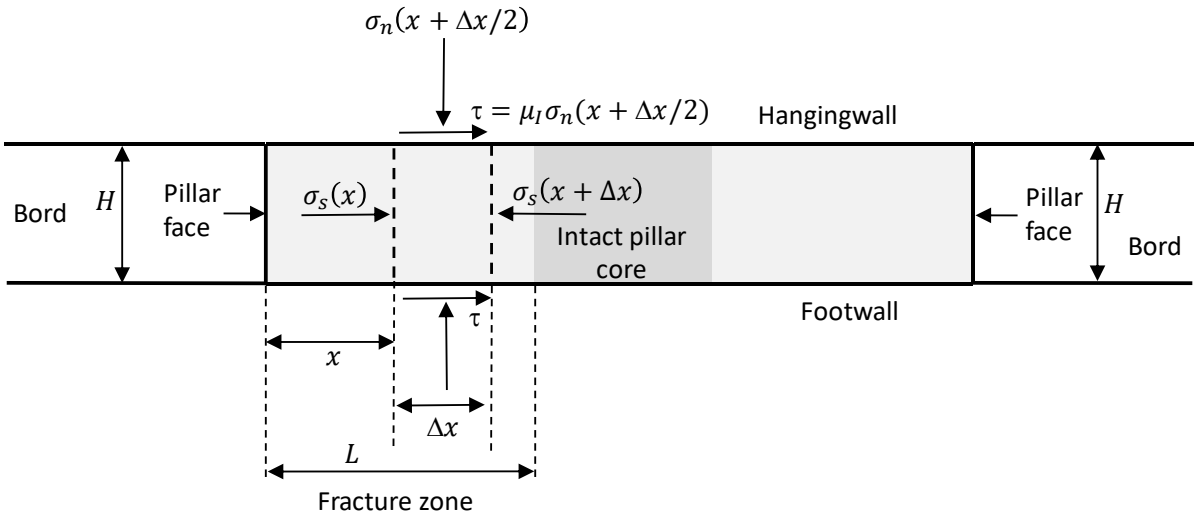

Figure 6-3. Force equilibrium of a slice of rock in a pillar. The lighter shade of grey is the failed zone on the edges of the pillar and the darker grey is the intact core of the pillar.

For this basic model, it is assumed that the material is unconfined at the edge of the pillar. For the thin section of rock to be in equilibrium, it is required that:

$$H\sigma_s(x+\Delta x) = H\sigma_s(x) + 2\tau\Delta x \tag{6.1}$$

This equation can be rearranged to give:

$$\frac{\boldsymbol{\sigma_s(x+\Delta x)-\sigma_s(x)}}{\boldsymbol{\Delta x}} = \frac{\boldsymbol{2\tau}}{\boldsymbol{H}} \tag{6.2}$$

This can be written in the form of a differential equation if the width of the slice tends to zero:

$$\lim_{\Delta x\to 0} \frac{\sigma_s(x+\Delta x)-\sigma_s(x)}{\Delta x} = \frac{2\tau}{H} \tag{6.3}$$

or

$$\frac{d\sigma_s}{dx} = \frac{2\tau}{H} \tag{6.4}$$

The following assumptions are made to solve this equation. As indicated in the diagram, τ is related to the normal stress σ_n by the following frictional condition:

$$\tau = \mu_l\sigma_n = \tan\phi(\sigma_n) \tag{6.5}$$

where ϕ is the friction angle on the interface.

Furthermore a failure relationship is assumed to relate the seam normal stress, σ_n, to the seam parallel stress, σ_s, as follows:

$$\sigma_n = m\sigma_s + S \tag{6.6}$$

where S and m are specified strength constants. Once failure occur, S, can be considered as the strength of the failed pillar material and m is a slope parameter.

Inserting equations (6.5) and (6.6) into equation (6.4) gives:

$$\frac{d\sigma_s}{dx} = \frac{2\tan\varphi}{H}(m\sigma_s + S) \tag{6.7}$$

Integration of Equation (6.7) gives:

$$\frac{\ln(m\sigma_s+S)}{m} = \frac{2x\tan\phi}{H} + A \tag{6.8}$$

The constant A can be found by considering that at $x = 0$, it is known that $\sigma_s = 0$. This gives the value of A as

$$A = \frac{\ln(S)}{m} \tag{6.9}$$

Equation (6.8) therefore becomes

$$\frac{\ln(m\sigma_s+S)}{m} = \frac{2x\tan\phi}{H} + \frac{\ln(S)}{m} \tag{6.10}$$

This can be simplified as

$$\frac{1}{m}\ln\left(\frac{m\sigma_s+S}{S}\right) = \frac{2x\tan\phi}{H} \tag{6.11}$$

This can be written as

$$\frac{m\sigma_s+S}{S} = e^{2mx\tan\varphi/H} \tag{6.12}$$

and from this the solution of the seam-parallel stress follows as

$$\sigma_s = \frac{S}{m}\left(e^{2mx\tan\phi/H} - 1\right) \tag{6.13}$$

Substituting equation (6.13) into equation (6.6) gives:

$$\sigma_n = Se^{2mx\tan\phi/H} \tag{6.14}$$

Equation (6.14) predicts that for this simple limit equilibrium model, the normal stress increases exponentially away from the pillar edge. It should be noted that when assigning parameter values, it is a requirement that $S > 0$ otherwise $\sigma_n = 0$ for all values of x.

For practical implication of this model in TEXAN, different values of the parameters S and m are adopted for intact and failed material. The current implementation in TEXAN provides the option to use three strength envelopes having the form of equation (6.6) (Napier and Malan, 2018).

1. The strength of the intact rock can be defined as an unconfined strength value S^0 and by a slope parameter m^0.
2. Once the material fails, a strength drop is assumed to occur immediately to an initial limit strength envelope defined by intercept and slope parameters S^c and m^c respectively.
3. Once the material has failed, the strength can decay in a time-dependent manner to a residual strength envelope specified by parameters S^f and m^f.

These strength envelopes are illustrated in Figure 6-4. The initial strength drop does not occur if $S^0 = S^c$ and $m^0 = m^c$. Similarly, no time-dependent strength decay occurs if $S^c = S^f$ and $m^c = m^f$.

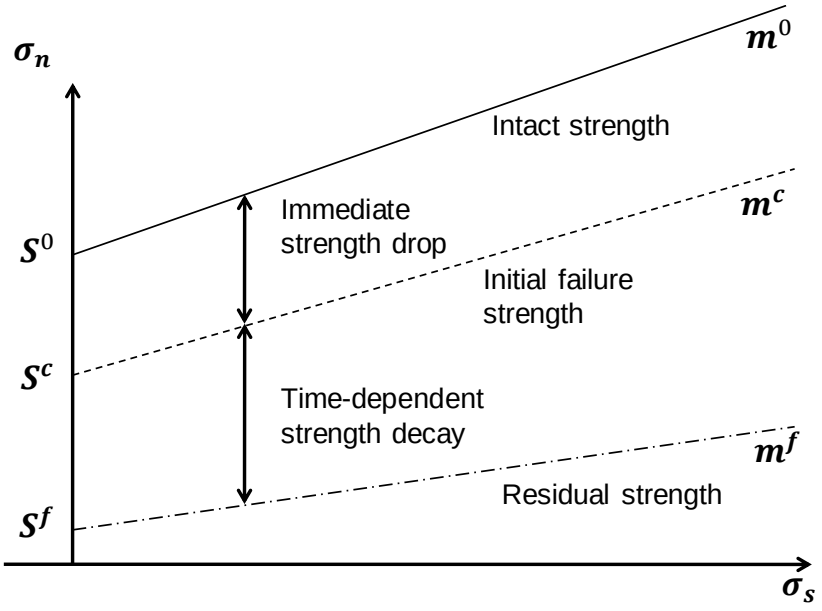

Figure 6-4. Different seam strength envelopes adopted for the time-dependent limit equilibrium model.

The transition between the initial limit strength and the residual limit strength envelopes is assumed to be governed by a strength decay function $F(\tau)$ that depends on the elapsed time $\tau = t - T(x)$ between the current time t and the initial time of failure, $T(x)$, at point x. The model assumes the following (Napier and Malan, 2018):

$$S(t) = S^f + F\left(t - T(x)\right)\left(S^c - S^f\right) \tag{6.15}$$

$$m(t) = m^f + F\left(t - T(x)\right)\left(m^c - m^f\right) \tag{6.16}$$

where $F(\tau)$ is the decay function. It is assumed that $F(\tau) = 1$ if $\tau < 0$ and that $F(\tau)$ is a simple exponential function of the form:

$$F(\tau) = \left(\frac{1}{2}\right)^{\frac{\tau}{\lambda}} = e^{-\alpha\tau} \tag{6.17}$$

when $\tau \geq 0$. λ is a half-life parameter. For equation (6.17):

$$\ln\left(\frac{1}{2}\right)^{\frac{\tau}{\lambda}} = \ln(e^{-\alpha\tau}) \tag{6.18}$$

which is:

$$\frac{\tau}{\lambda}\ln\left(\frac{1}{2}\right) = -\alpha\tau \tag{6.19}$$

This can be simplified to give the exponential decay exponent as:

$$\lambda = \frac{\ln(2)}{\alpha} \tag{6.20}$$

This choice of exponential decay model for the rock is supported by the work presented in Malan and Napier (2018). They recorded and simulated time-dependent closure profiles in gold mine stopes. Exponential decay is also very common in nature of which the well-known example is radioactivity.

To obtain some insight into the model, equation (6.15) was plotted using the numerical modelling parameters, where t is in months, $S^f = 5\ \text{MPa}$ and $S^0 = 50\ \text{MPa}$. It was assumed that $T(x) = 0$. Figure 6-5 illustrates $S(t)$ against *t* (months). The effect of the half-life parameter (strength decay) is illustrated. This indicates that as the half-life parameter increases, the parameter $S(t)$ will be larger over the short term than for a smaller half-life value. A large half-life value therefore leads to a slower reduction in strength and a slower rate of scaling when considering Figure 6-4.

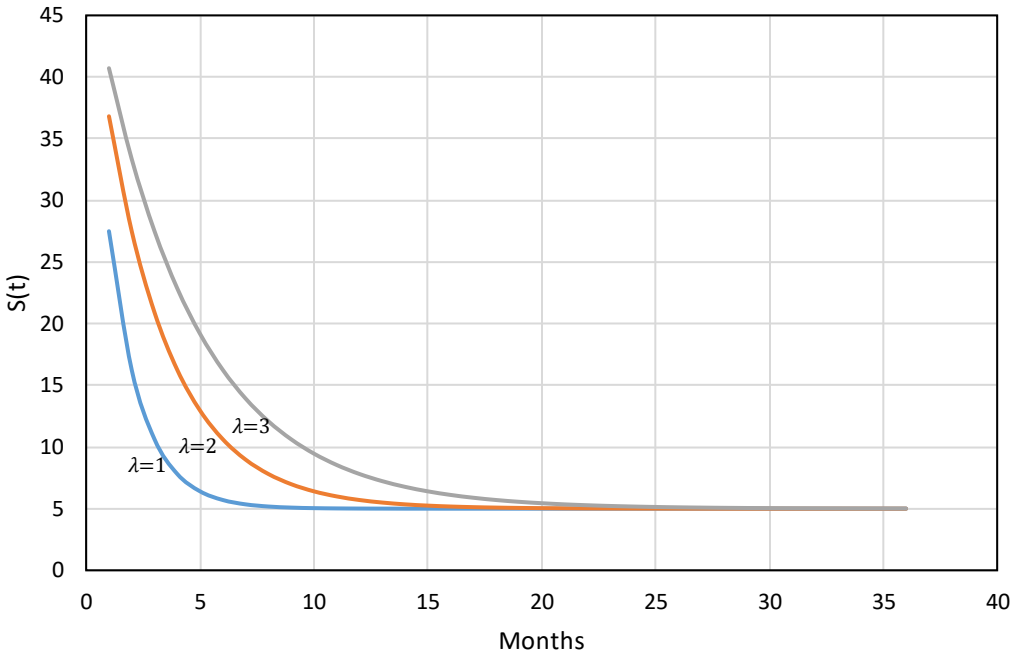

Figure 6-5. The time-dependent reduction in the value of the "intercept" parameter for different values of half-life.

6.2. Numerical Results for an Idealised Layout

As an initial geometry to test the time-dependent constitutive model, a small idealised layout consisting of 25 pillars was simulated. The standard pillar and bord dimensions at BRMO were used. This is illustrated in Figure 6-6. Different simulations using this geometry were conducted and the results are given in the sections below.

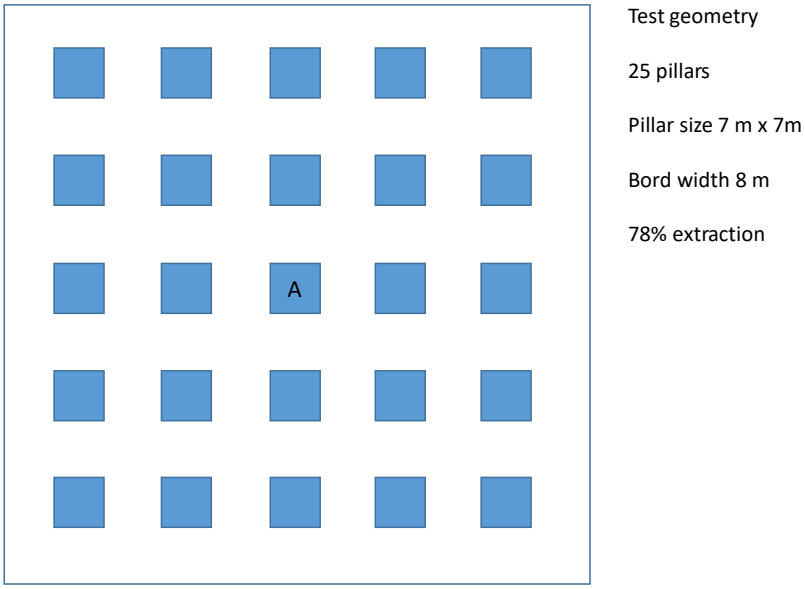

Figure 6-6. A simple idealised pillar geometry was used to test the time-dependent limit equilibrium model.

Three different types of simulations using the idealised layout are illustrated in the next sections. For the first set of simulations, no immediate strength drop was assumed and therefore $S^0 = S^c$ and $m^0 = m^c$ (see Figure 6-4). This was used to illustrate the effect of the half-life parameter on the time-dependent fracturing of the pillars. For the second set of simulations an immediate strength drop of 40 MPa was assumed in an attempt to better simulate the higher rate of scaling early in the life of the pillars. For the third set of simulations, the limit equilibrium parameters were modified in an attempt to fit the rate of scaling observed underground.

Small triangular elements were used for these models and each 7 m $\times$ 7 m pillar contained 574 elements. This is an average element size of 0.085 m^2. The total number of elements used for the geometry in Figure 6-6 was 57 302. The large number of elements and the required time steps for the time-dependent model resulted in very long run times.

6.2.1. Numerical Results without an Immediate Strength Drop

This section describes the simulations without an immediate strength drop. Table 6-2 illustrates the limit equilibrium parameters used for these simulations. Although there was no immediate strength drop, a small final residual strength ($S^f = 5\ MPa$) was assumed.

Table 6-2. Parameters used for the time-dependent limit equilibrium model. The model assumes no immediate strength drop ($S^0 = S^c$) and ($m^0 = m^c$).

Parameter	Value
Intact strength intercept, S^0	50 MPa
Intact strength slope, m^0	7
Initial residual strength intercept, S^c	50 MPa
Initial residual strength slope, m^c	7
Final residual strength intercept, S^f	5 MPa
Final residual strength slope, m^f	7
Effective seam height, H	5.5 m
Intact rock Young's modulus, E	90 GPa
Intact rock Poisson's ratio, v	0.2
Intact seam stiffness modulus, k_s	16363 MPa/m
Fracture zone interface friction angle	30°
Half-life, λ	1, 2 and 3 months

The time-dependent limit equilibrium model resulted in the gradual failure of the pillars. This is illustrated in Figure 6-7 for pillar A (see Figure 6-6). The larger half-life values resulted in a slower rate of "scaling" of the pillar. This is illustrated in Figure 6-7. Of significance is that after a period of time, the rate of scaling becomes very slow and this qualitatively agrees with the limited data collected underground. The time-dependent failure of the pillars after certain intervals are illustrated in Figure 6-8 to Figure 6-10. Note how the number of failed collocation points increase with time.

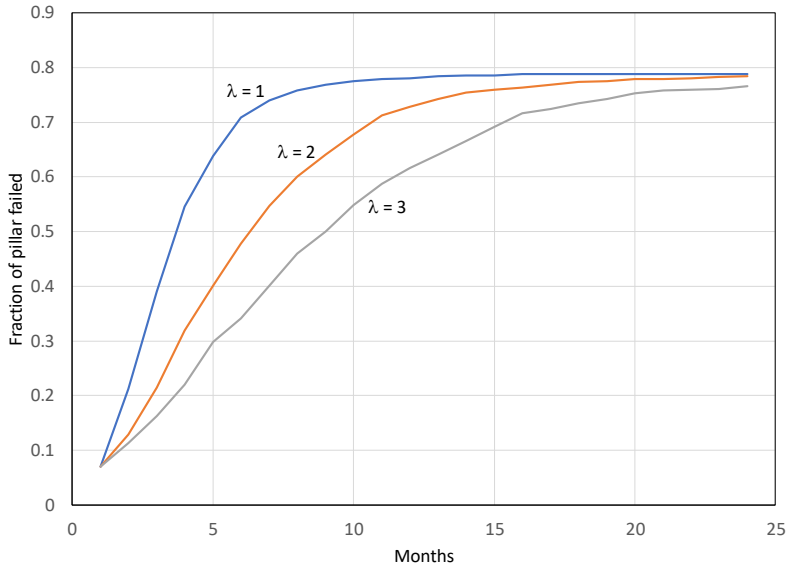

Figure 6-7. Progressive failure of the pillar A (Figure 6-6) for different values of λ. The fraction of the pillar that failed was simply the number of failed elements divided by the total number of elements in the pillar.

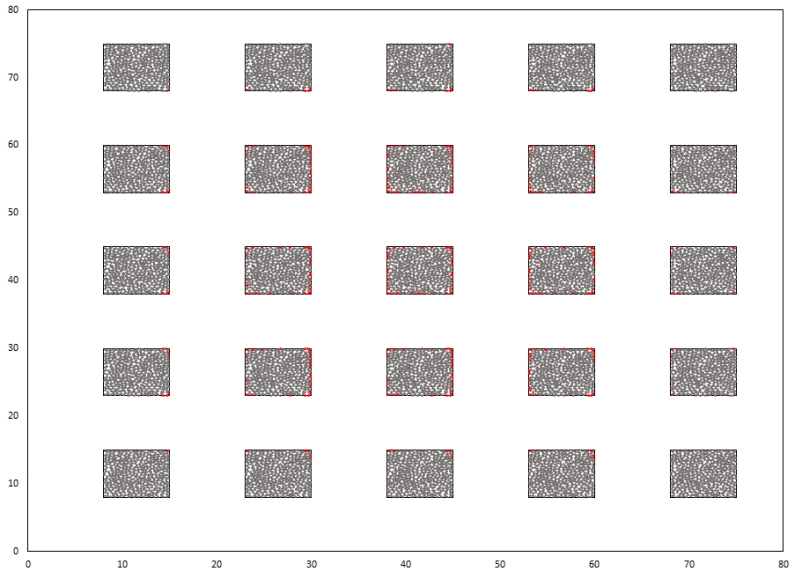

Figure 6-8. Failure of the pillar elements (red dots) for λ = 3 after 1 month.

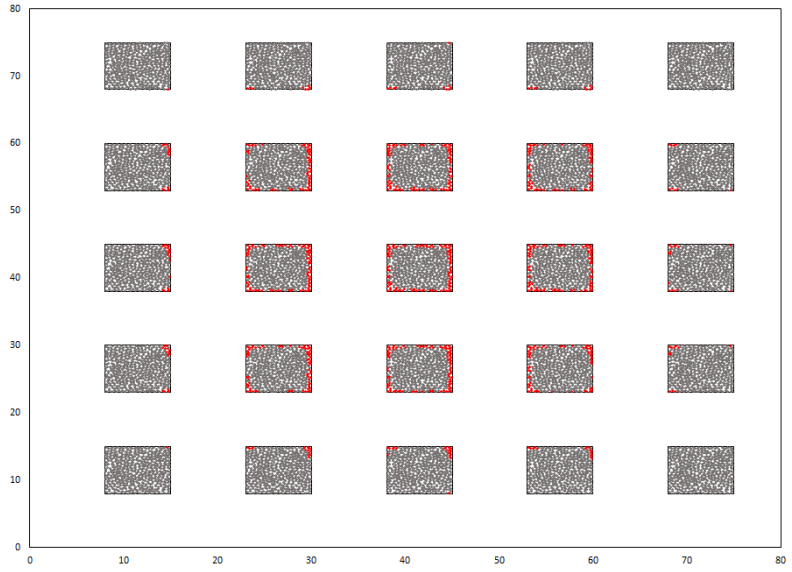

Figure 6-9. Failure of the pillars (red dots) λ = 3 after 4 months.

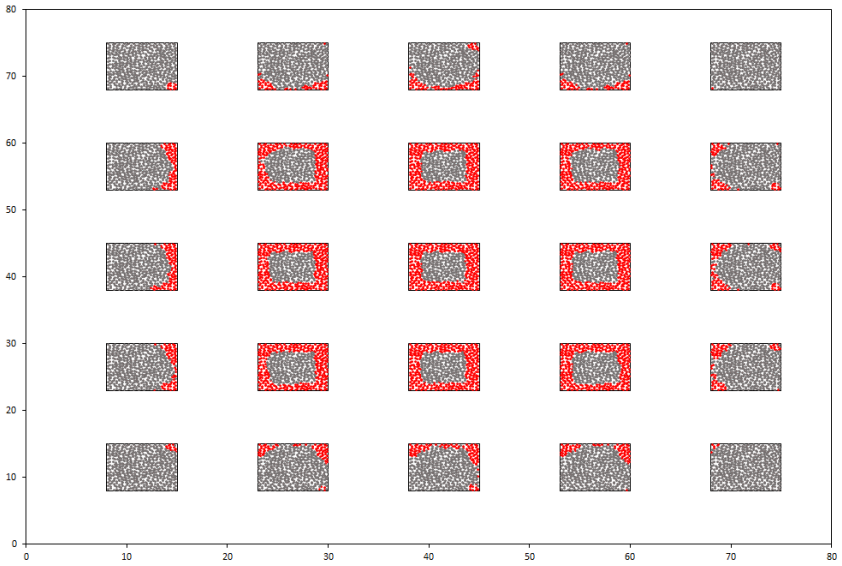

Figure 6-10. Failure of the pillars (red dots) λ = 3 after 12 months.

The results above are encouraging as it indicates that the model seems capable to simulate the time-dependent scaling of the pillars. The results in Figure 6-7 does, however, not mimic the more rapid scaling in the first few months as observed underground. The limit equilibrium model does allow for an initial stress drop after failure and this may be a useful feature to simulate the initial scaling caused by factors such as poor blasting. This was simulated and described in the next section.

6.2.2. Numerical Results with an Immediate Strength Drop

For the second set of simulations, an immediate strength drop was used to simulate the more rapid scaling of the pillars immediately after it is formed. As mentioned above, this may be blasting damage and nearby blasting, as the faces move away, may cause the blocky scaling to dislodge from the pillars. Table 6-3 lists the parameters used for this model. An arbitrary strength drop of 40 MPa was used.

Table 6-3. Parameters used for the time-dependent limit equilibrium model. This assumes an immediate strength drop ($S^0 > S^c$).

Parameter	Value
Intact strength intercept, S^0	50 MPa
Intact strength slope, m^0	7
Initial residual strength intercept, S^c	10 MPa
Initial residual strength slope, m^c	7
Final residual strength intercept, S^f	5 MPa
Final residual strength slope, m^f	7
Effective seam height, H	5.5 m
Intact rock Young's modulus, E	90 GPa
Intact rock Poisson's ratio, v	0.2
Intact seam stiffness modulus, k_s	16363 MPa/m
Fracture zone interface friction angle	30°
Half-life, λ	1, 2 and 3 months

The parameters listed above resulted in a more rapid failure of the pillars at the beginning of the time period. The time-step used in the model was one month and therefore the initial part of the failure curve is not vertical, but is plotted with a steep slope. Thereafter, the time-dependent failure of the pillars continued, but owing to the choice of parameters, less of the subsequent failure occurred in a time-dependent fashion when compared to the results in Figure 6-7. The time-dependent failure of the pillars for this set of parameters is illustrated in Figure 6-12 to Figure 6-14.

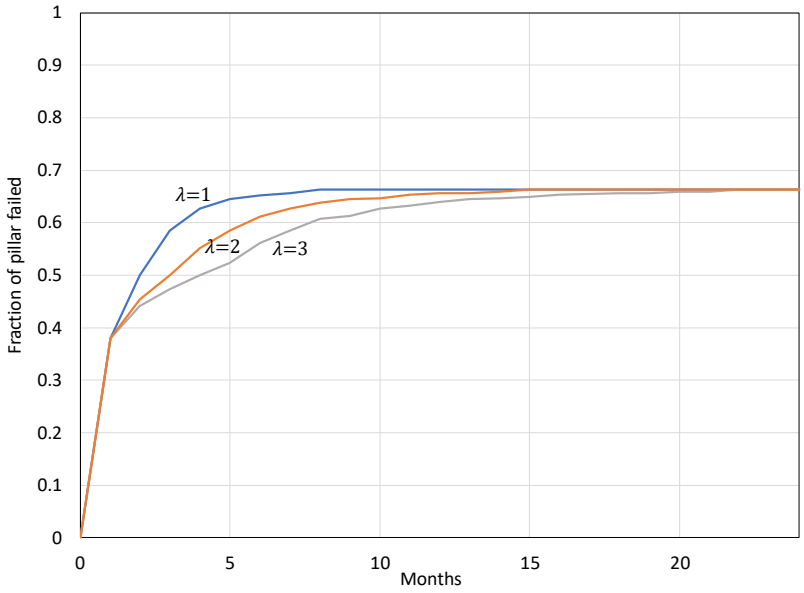

Figure 6-11. Progressive failure of the pillar A for different values of λ. For this simulation, there was an immediate strength drop of 40 MPa. The fraction of the pillar that failed was simply the number of failed elements divided by the total number of elements in the pillar.

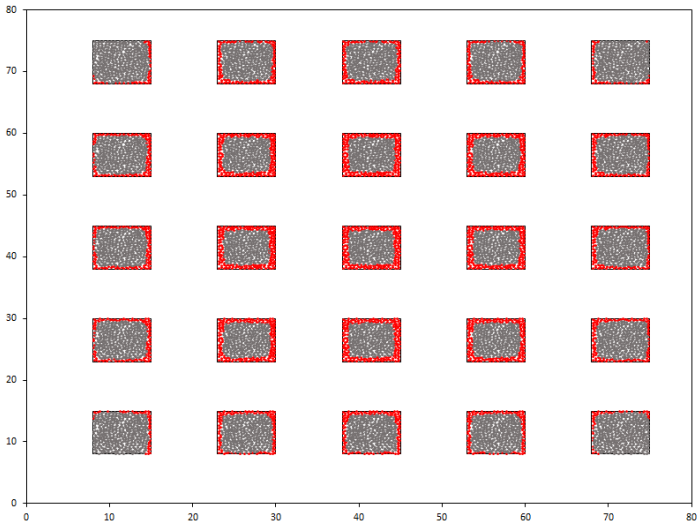

Figure 6-12. Failure of the pillars (red dots) for λ = 3 after 1 month. For this model, there was an immediate strength drop of 40 MPa and therefore the pillars are more extensively failed compared to Figure 6-8.

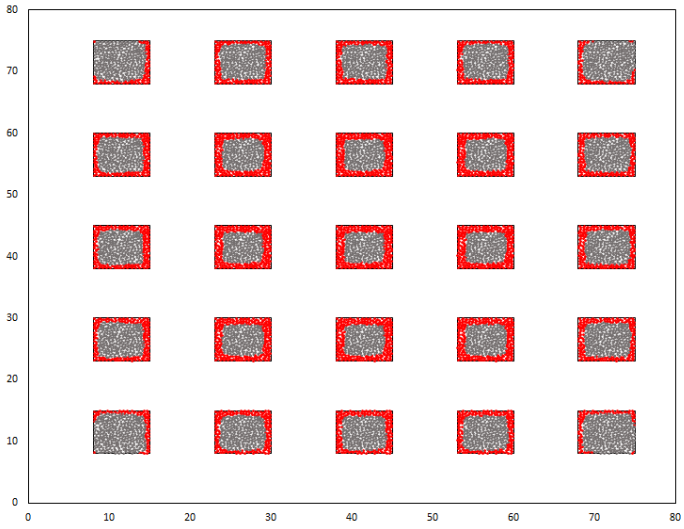

Figure 6-13. Failure of the pillars for λ = 3 after 4 months. For this model, there was an immediate strength drop of 40 MPa.

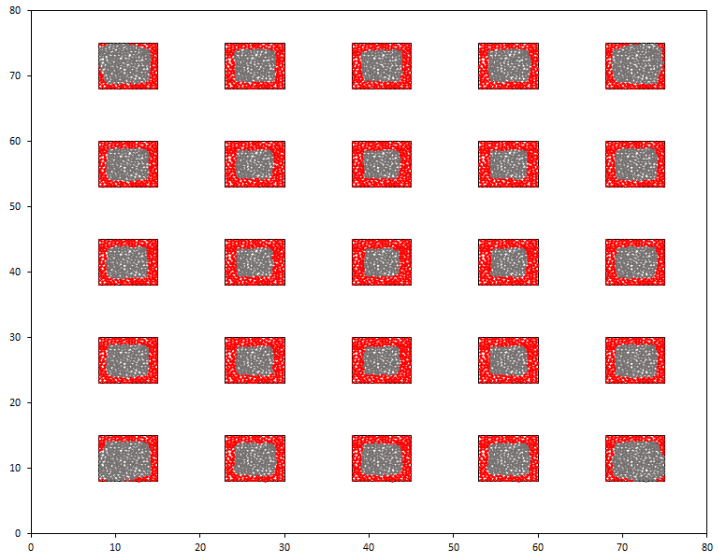

Figure 6-14. Failure of the pillars (red dots) for λ = 3 after 12 months. For this model, there was an immediate strength drop of 40 MPa.

6.2.3. Simulation of the LEM Parameters to Approximate the Data Collected

From the data of scaling distance presented in Table 6-1, the fraction of the pillar failed was calculated. The standard planned pillar size of 7 m x 7 m was used for this calculation, so it is only an approximate value. The data is illustrated in Figure 6-15 (blue dots) and plotted as a function of the age of the pillar. Only the approximate age of the pillars was known and therefore the data seem to be stacked in columns.

There is no clear trend in the data, except that it seems that the scaling does increase with time. It was also attempted to fit a numerical solution of the progressive failure of a pillar to this data using trial and error. A number of parameters were tested. The best fit parameters are given in Table 6-4. Note that the model with the initial stress drop seems to be at least a reasonable approximation of the data. As future work, additional data needs to be collected from underground to establish a clearer trend in terms of rate of scaling. This can then be modelled and a better understanding of the validity of the model obtained.

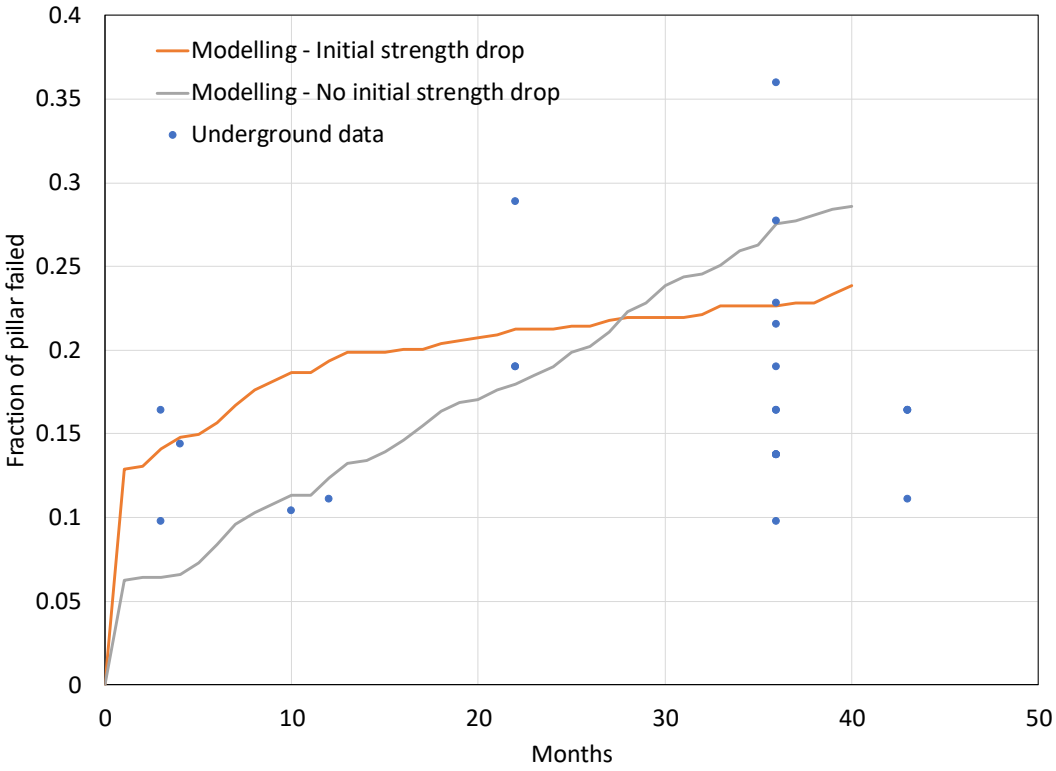

Figure 6-15. The fraction of the pillars failed as a function of the age of the pillar.

Table 6-4. Parameters used to simulate the time-dependent scaling of the underground pillars.

Parameter	Value
Intact strength intercept, S^0	50 MPa
Intact strength slope, m^0	7
Initial residual strength intercept, S^c	30 MPa and 50 MPa
Initial residual strength slope, m^c	7
Final residual strength intercept, S^f	20 MPa
Final residual strength slope, m^f	7
Effective seam height, H	5.5 m
Intact rock Young's modulus, E	90 GPa
Intact rock Poisson's ratio, v	0.2
Intact seam stiffness modulus, k_s	16363 MPa/m
Fracture zone interface friction angle	30°
Half-life, λ	12 months

CHAPTER 7

PROPOSED REVISED PILLAR DESIGN

This study investigated the pillar behaviour and pillar design at Nchwaning III shaft. The current design at the shaft is based on the Hedley and Grant power-law formula and a K-value of 133 MPa. This design is currently used for all the shafts and for all the different geotechnical areas. Of concern is that extensive scaling of some the pillars have been observed and it appears from a preliminary study that this scaling is time-dependent in nature. Spray-on liners are currently used by the mine to stabilise these pillars and this practice has become a significant operational expense.

The observations made by the author indicated that significant scaling of the pillars occur in some areas, while other areas are stable. Rock mass ratings were done on the pillars and both the RMR and Q ratings were computed. From the data collected, it is evident that the pillars with a low rock mass rating (high density of joints) are prone to excessive scaling. The pillar design at BRMO therefore needs to be extended to cater for geotechnical areas with a low rock mass rating. This is an important finding from this study. Extending the pillar design is nevertheless not an easy task as completely failed pillars are rare at the mine and a statistical analysis using a failed/intact pillar database similar to Salamon and Munro (1967) is therefore not possible. The approach below is a first approximation of an extended pillar design using all data available to the author.

When revising the pillar design methodology at BRMO, a number of important aspects need to be considered:

- In 2008, a design methodology using the Hedley and Grant power strength formula with a value, K = 133 MPa, was adopted for BRMO (Hanekom, 2008). A large number of pillars have been cut using this methodology during the last fourteen years and no major pillar collapses have been reported. Especially in the high-grade areas, the pillars appear stable and in a very good condition. Although the Hedley and Grant formula can at best be considered as an approximation of pillar strength, there is no evidence that this approximation is not a good estimate for the high-grade areas.
- The pillar behaviour seems to be strongly controlled by the spacing of the joint sets and the rock mass rating. In the R5 areas, with the small spacings between the joints and a low rock mass rating, extensive scaling of the pillars is observed. The pillars are not stable anymore and the numerical modelling study gave back-calculated K-values as low as 75 MPa to 106 MPa. The assumption of K = 133 MPa is therefore not appropriate for these areas. The K-value in the R5 area should probably be less than 100 MPa to ensure a stable pillar design.

Figure 7-1 illustrates the general observed trend of decreasing pillar stability for a decrease in rock mass rating. The pillar condition corresponds to the ratings given in Chapter 3 in Figure 3-1 and Table 3-6. The current design methodology does not cater for this behaviour and a uniform design approach is used for all geotechnical areas. Furthermore, the pillar scaling seems to be a time-dependent process and the pillars prone to this behaviour (in the R5 area) gradually deteriorate over time.

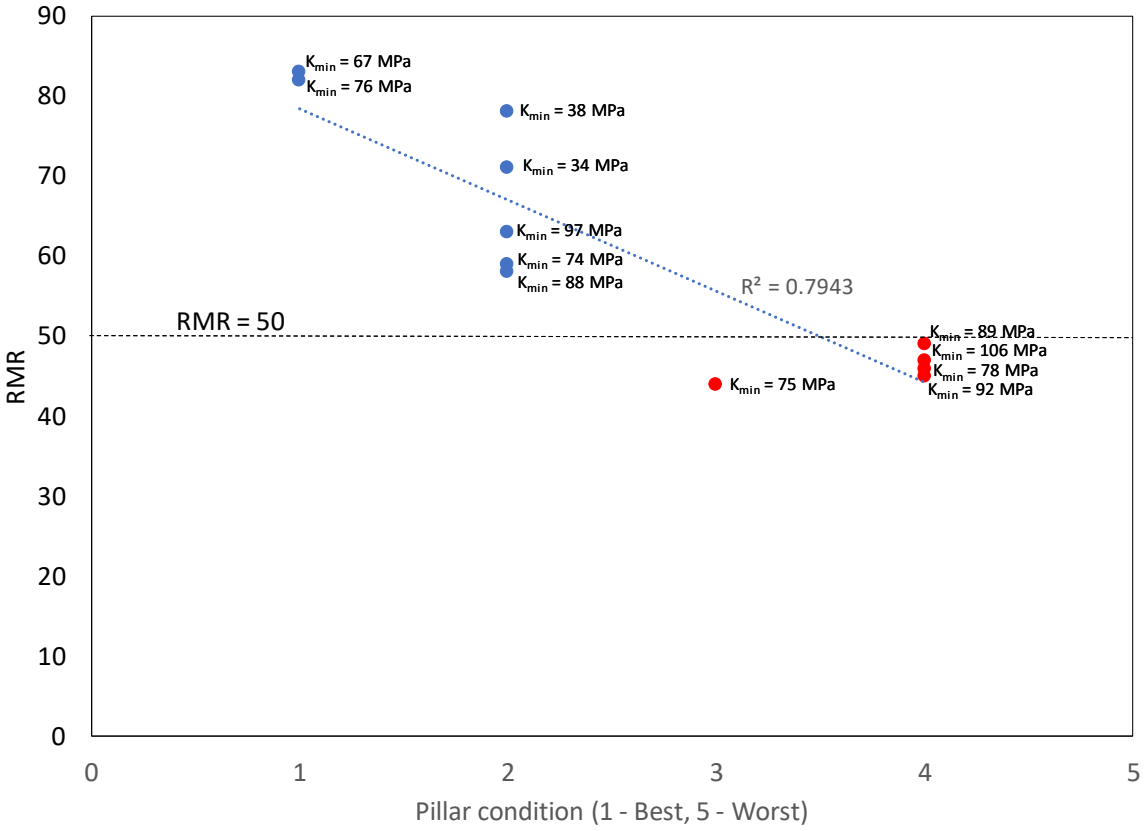

Figure 7-1. Empirical relationship between pillar condition and rock mass rating at BRMO. The red dots indicate the unstable pillars or the pillars with severe scaling. The pillar conditions correspond to the rating given in Table 3-6. The K_{min} values are the back-calculated values using the numerical modelling and a Hedley and Grant pillar formula.

Based on these considerations, it is proposed to extend the pillar design methodology into two components. The motivation for this is that it needs to be a practical design and too many pillar sizes to cater for the entire range of RMR values will not be feasible. From Figure 7-1, it appears that RMR = 50 separates the stable and unstable cases. The two designs proposed will therefore be:

- A pillar design for areas with an RMR > 50. This methodology is similar to the current methodology. As discussed above, a large number of stable pillars were designed using this methodology over a period of 14 years.

- A pillar design for areas with an RMR < 50. A reduced value of K needs to be adopted for these areas.

To determine the reduced K-value for the areas with an RMR < 50, the principle adopted by Laubscher (1990) and Stacey and Swart (2001) of a design rock mass strength (DRMS) for the K-value was mimicked. They proposed that the pillar strength should be determined by the following equation:

$$\sigma_s = \text{DRMS}\ \frac{w^{0.5}}{h^{0.75}} \tag{7.1}$$

Laubscher (1990) proposed that the DRMS can be determined from an empirical rock mass strength (RMR) which is adjusted to consider weathering, mining induced stresses, joint orientation and blasting effects. His full proposed equation for DRMS is:

$$\text{DRMS} = \text{IRS}\ \times 0.8 \times \frac{\text{RMR}-\text{IRS}_{\text{rating}}}{80} \times \text{Weathering}_{\text{adj}} \times \text{Orientation}_{\text{adj}} \times \text{Stress}_{\text{adj}} \times \text{Blasting}_{\text{adj}} \tag{7.2}$$

where:

IRS - intact rock strength

$\text{Weathering}_{\text{adj}}$ - a possible adjustment for weathering of the rock

$\text{Orientation}_{\text{adj}}$ - a possible adjustment for the joint orientation

$\text{Stress}_{\text{adj}}$ - a possible adjustment for the difference between the maximum and minimum stress

$\text{Blasting}_{\text{adj}}$ - an adjustment based on the quality of blasting

Equation (7.2) is a complex mixture of empirical factors and a large number of parameters need to be estimated. Probably for this reason, it is rarely used in practical designs in the South African hard rock bord and pillar mines. The assumption by Laubscher (1990) to adjust the IRS to 80% of the laboratory value ($\times\ 0.8$) is based on studies done in two mines in Zimbabwe and may therefore not be applicable to BRMO. Owing to the complexity of equation (7.2), it is simplified by combining most of the parameters and the stripping the IRS from the RMR rating into a single constant, A, and this gives:

$$\mathbf{DRMS = IRS \times A \times RMR} \tag{7.3}$$

The essence of DRMS, that the rock mass strength is affected by the RMR, is adequately captured. To estimate parameter A, it is known that the DRMS value that gives a stable design for RMR > 50 is 133 MPa. The intact rock strength (IRS) is estimated to be 280 MPa (Hanekom, 2008). The average RMR for the stable pillars in Figure 7-1 is 76. These values are inserted into equation (7.3):

$$133\ \text{MPa} = 280\ \text{MPa} \times \text{A} \times 71 \tag{7.4}$$

This gives a value $\text{A} = 0.0067$

For the pillars in condition 3 and 4 (poor) in Figure 7-1 (also see Table 3-6), the average RMR is 46. This value and the "calibrated" value of A can also be inserted into equation (7.3) to calculate the reduced K-value (DRMS):

$$\text{DRMS} = 280\ \text{MPa} \times 0.0067 \times 46 = 86\ \text{MPa} \tag{7.5}$$

A number of assumptions were made to derive this value, but it seems meaningful as it is in the same order as the back-calculated K-value for the pillars in a poor condition. The average K-value for these pillars is 88 MPa. Some of these pillars are considered as "failed" by the mine and excessive scaling was observed by the author for these pillars. The factor of safety on the pillars must therefore be close to 1. Owing to the number of assumptions made, a practical K-value of 90 MPa is adopted for the pillars in the R5 areas.

For pillars with an RMR < 50, the pillar strength should therefore be approximated by:

$$\sigma_s = 90\ \text{MPa}\ \frac{w^{0.5}}{h^{0.75}} \tag{7.6}$$

7.1. Design Methodology

Similar to the work of Hanekom (2008), a factor of safety (FOS) of 1.5 will be adopted. The following equations are repeated to illustrate the design methodology followed. The factor of safety is given by:

$$\text{FOS} = \frac{\sigma_s}{\text{APS}} \tag{7.7}$$

For design, the TAT value for APS is typically assumed and this is given by:

$$\mathrm{APS} = \frac{\rho g H}{1-e} \tag{7.8}$$

where:

ρ = overburden density

g = gravitational acceleration

H = depth below surface

For square pillars and a layout where the bord and holing widths are similar, the extraction ratio is given by:

$$e = \frac{(w+b)^2 - w^2}{(w+b)^2} \tag{7.9}$$

where:

w = pillar width (m)

b = bord and holing width (m)

Designing a bord and pillar layout can be a difficult task. For a fixed bord width and a selected factor of safety, changing the pillar width will change the pillar strength in equation (7.6), but also the extraction ratio in equation (7.9) and FOS in equation (7.7). An iterative process, therefore, needs to be followed. By inserting equation (7.9) in (7.8):

$$\mathrm{APS} = \frac{\rho g H}{1-\frac{(w+b)^2 - w^2}{(w+b)^2}} \tag{7.10}$$

By rearranging equation (7.10) and inserting equation (7.7):

$$\sigma_s = \frac{\mathrm{FOS}\rho g H}{1-\frac{(w+b)^2 - w^2}{(w+b)^2}} \tag{7.11}$$

This can be set equal to equation (7.6) (K was substituted for the parameter 90 MPa) and after rearranging:

$$w^{0.5}\left(1 - \frac{(w+b)^2 - w^2}{(w+b)^2}\right) = \frac{\mathrm{FOS}\rho g H h^{0.75}}{K} \tag{7.12}$$

This can be simplified to:

$$\frac{w^{2.5}}{(w+b)^2} = \frac{FOS\rho gHh^{0.75}}{K} \quad (7.13)$$

Equation (7.13) was used to solve w for increasing depths and the following parameters were used:

- b = 8 m
- FOS = 1.5
- ρ = 2800 kg/m^3
- g = 10 m/s^2
- h = various values (3.5 m, 4 m, 4.5 m, 5 m, 5.5 m, 6 m)

A density of 2800 kg/m^3 was adopted to give complementary results to the graph and table published in Hanekom (2008). As an iterative process is required to solve for w in equation (7.13), the function "Goal Seek" was used in Excel. This function automatically modifies the value of w, until the left-hand side of equation (7.13) is equal to the right-hand side. The pillar widths for these areas with RMR < 50 are given in Figure 7-2 and Table 7-1.

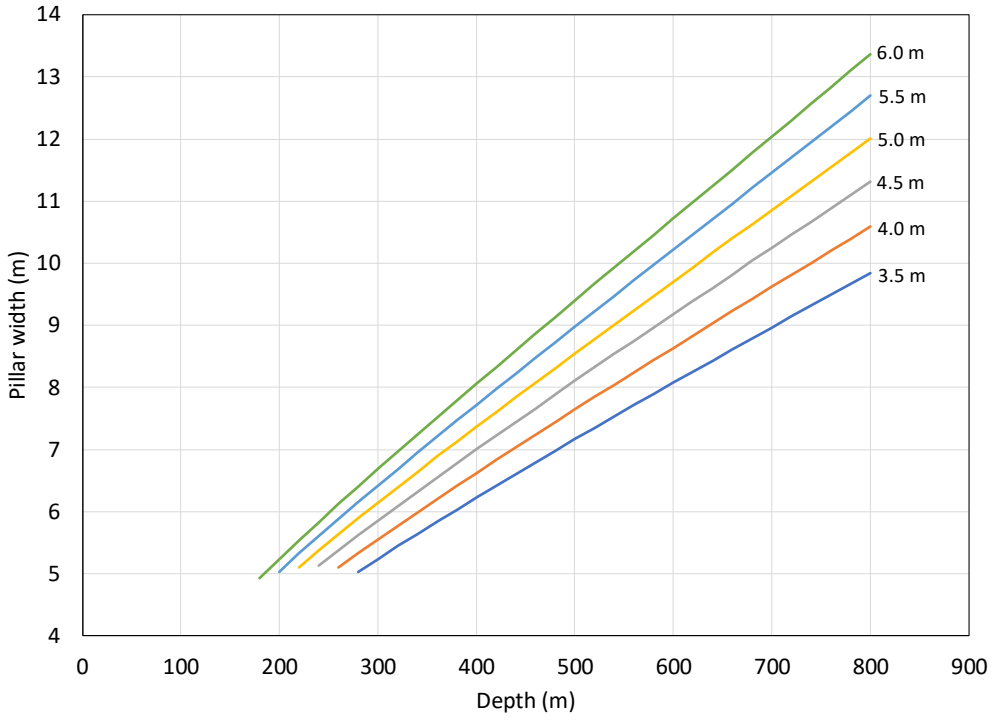

Figure 7-2. Calculated pillar widths versus depth for different mining heights for the areas with an RMR < 50 (e.g. R5 product area).

Table 7-1. Simplified pillar widths for different depths and mining heights. This was calculated for a bord width of 8 m and the other parameters given above.

	RMR < 50: Pillar dimensions at specific mining heights					
Mining depth	3.5 m	4 m	4.5 m	5 m	5.5 m	6 m
180 - 299 m	5.0	6.0	6.0	6.0	6.0	7.0
300 - 349 m	6.0	6.0	6.0	7.0	7.0	7.0
350 - 399 m	6.0	7.0	7.0	7.0	8.0	8.0
400 - 449 m	7.0	7.0	8.0	8.0	8.0	9.0
450 - 499 m	7.0	8.0	8.0	9.0	9.0	9.0
500 - 549 m	8.0	8.0	9.0	9.0	10.0	10.0
550 - 599 m	8.0	9.0	9.0	10.0	10.0	11.0
600 - 649 m	8.0	9.0	10.0	10.0	11.0	11.0
650 - 699 m	9.0	10.0	10.0	11.0	12.0	12.0
700 - 749 m	9.0	10.0	11.0	12.0	12.0	13.0

These pillar dimensions can be compared to those given in the COP (Table 1-2). The drawback of the revised formula for the RMR < 50 areas is that the pillar sizes will be larger. For example, at a depth of 450 m to 499 m and a mining height of 5.5 m, the pillar size will be 7 m for the high-grade areas (RMR > 50), but 9 m for the R5 areas (RMR < 50). The extraction ratio based on the pillar dimensions given in Table 7-1 for a bord span of 8 m is given in Table 7-2.

Table 7-2. Extraction ratio for the areas with an RMR < 50.

	Extraction ratio (8 m bords)					
Mining depth	3.5 m	4 m	4.5 m	5 m	5.5 m	6 m
180 - 299 m	0.85	0.82	0.82	0.82	0.82	0.78
300 - 349 m	0.82	0.82	0.82	0.78	0.78	0.78
350 - 399 m	0.82	0.78	0.78	0.78	0.75	0.75
400 - 449 m	0.78	0.78	0.75	0.75	0.75	0.72
450 - 499 m	0.78	0.75	0.75	0.72	0.72	0.72
500 - 549 m	0.75	0.75	0.72	0.72	0.69	0.69
550 - 599 m	0.75	0.72	0.72	0.69	0.69	0.66
600 - 649 m	0.75	0.72	0.69	0.69	0.66	0.66
650 - 699 m	0.72	0.69	0.69	0.66	0.64	0.64
700 - 749 m	0.72	0.69	0.66	0.64	0.64	0.62

7.2. Summary of the Revised Design

Based on the data collected, numerical modelling results and recognising that the pillar strength is affected by rock mass rating, it is proposed that the following pillar design be adopted at BRMO.

- Retain the current pillar design for areas where the RMR > 50. This is typically the high-grade areas.
- Adopt the revised pillar design for the areas with an RMR < 50. This is typically for the R5 low-grade areas.

A summary of the combined pillar design based on RMR is given in Table 7-3.

Table 7-3. Revised combined pillar design for BRMO based on RMR.

	RMR > 50: Pillar dimensions at specific mining heights					
Mining depth	**3.5 m**	**4 m**	**4.5 m**	**5 m**	**5.5 m**	**6 m**
180 - 299 m	5.0	5.0	5.0	5.0	5.0	6.0
300 - 349 m	5.0	5.0	5.0	6.0	6.0	6.0
350 - 399 m	5.0	6.0	6.0	6.0	6.0	7.0
400 - 449 m	6.0	6.0	6.0	6.0	6.0	7.0
450 - 499 m	6.0	6.0	7.0	7.0	7.0	8.0
500 - 549 m	6.0	7.0	7.0	7.0	8.0	8.0
550 - 599 m	7.0	7.0	7.0	8.0	8.0	8.0
600 - 649 m	7.0	7.0	8.0	8.0	9.0	9.0
650 - 699 m	7.0	8.0	8.0	9.0	9.0	9.0
700 - 749 m	8.0	8.0	9.0	9.0	9.0	10.0

	RMR < 50: Pillar dimensions at specific mining heights					
Mining depth	**3.5 m**	**4 m**	**4.5 m**	**5 m**	**5.5 m**	**6 m**
180 - 299 m	5.0	6.0	6.0	6.0	6.0	7.0
300 - 349 m	6.0	6.0	6.0	7.0	7.0	7.0
350 - 399 m	6.0	7.0	7.0	7.0	8.0	8.0
400 - 449 m	7.0	7.0	8.0	8.0	8.0	9.0
450 - 499 m	7.0	8.0	8.0	9.0	9.0	9.0
500 - 549 m	8.0	8.0	9.0	9.0	10.0	10.0
550 - 599 m	8.0	9.0	9.0	10.0	10.0	11.0
600 - 649 m	8.0	9.0	10.0	10.0	11.0	11.0
650 - 699 m	9.0	10.0	10.0	11.0	12.0	12.0
700 - 749 m	9.0	10.0	11.0	12.0	12.0	13.0

CHAPTER 8

CONCLUSION

This study describes a review of the pillar design at manganese mining operations in South Africa with specific reference to Nchwaning III shaft. From the literature study, it is clear that there is uncertainty regarding hard rock pillar strength and the appropriate formulae to use when designing hard rock bord and pillar layouts. The Hedley and Grant formulation is based on a number of crude assumptions and its use for the design of hard rock pillars in South Africa is therefore questionable. It was nevertheless used to design a large number of bord and pillar mines, including the BRMO layouts, with a mine-specific modification of the K-value. The current design at BRMO is based on the Hedley and Grant power-law formula and a K-value of 133 MPa. This value is substantially higher compared to that used in other hard rock bord and pillar mines in South Africa. This K-value is currently used for all the shafts and all the different geotechnical areas. Although this pillar design approach at BRMO appears to be successful, the time-dependent pillar scaling at the mine has never been studied. The extensive scaling of some the pillars observed by the mine was the motivation for this study. Spray-on liners are currently used to stabilise these pillars and this practice has become a major operational expense.

The literature survey indicated that extensive research has been conducted on the time-dependent failure of coal pillars in South Africa. These studies are exclusively empirical in nature and there was no attempt to conduct numerical modelling of the time-dependent scaling. In contrast, almost no work has been conducted on the time-dependent behaviour of hard rock pillars. Complex numerical modelling to simulate the time-dependent scaling of hard rock pillars have been done in the past, but these models are difficult to calibrate and, in these publications, the results are typically not compared to actual pillar behaviour underground.

Extensive underground observations of pillar behaviour were made by the author in six different underground areas. The observations indicated that significant scaling of the pillars occur in some areas, while other areas are stable. Rock mass ratings were done on the pillars and both the RMR and Q ratings were computed. From the data collected, it is evident that the pillars with a low rock mass rating are prone to excessive scaling. The pillar design at BRMO therefore needs to be extended to cater for geotechnical areas with a low RMR. This is an important new finding from this study.

Numerical modelling was conducted to simulate the pillar stress in the areas of interest. The TEXAN displacement discontinuity code was used in this study as it was developed specifically to simulate a large number of small pillars in tabular layouts. It can solve problems using triangular displacement discontinuity boundary elements and these elements circumvent the problem of "partially mined" elements in the traditional boundary element codes. It can therefore easily simulate the irregular pillar shapes. The code can also explicitly simulate the scaling and complete failure of the pillars using a time-dependent limit equilibrium model. The numerical modelling provided valuable data on actual pillar stress and stress variations depending on pillar size and position relative to abutments. This is a significant improvement over tributary areas stress calculations which were used for the 2008 study to develop the current pillar design methodology. The numerical modelling allowed a back-calculation of the K-values for the pillar strength formula in the different areas. Values exceeding 100 MPa were calculated for some of the stable pillars.

Monitoring of selected pillars were also conducted by the author over a period of three months to quantify the rate of time-dependent scaling. Contrary to expectations, almost no additional scaling occurred for the pillars monitored from early May 2021 to middle August 2021. The scaling distances of pillars, that were mined three years ago in the areas with a low RMR, was on average 0.8 m per side. This value was 0.5 m for pillars mined early in 2021. It therefore seems as if the bulk of the scaling occurred soon after blasting and it may even be mainly attributed to the blasting. A limited amount of additional time-dependent scaling seems to occur after this. Prominent time-dependent scaling is nevertheless present for some pillars as can be seen by the ongoing deterioration of pillars that were supported by spray-on liners. Numerical simulations of the time-dependent scaling were conducted using TEXAN and a limit equilibrium model. An exponential decay of rock strength at the edges of the pillars resulted in behaviour that is qualitatively similar to that observed underground. Similar to the observations, the rate of pillar scaling become small after a long period of time.

Based on the data collected, the numerical modelling results and the observations that the pillar strength is affected by rock mass rating (RMR), it is proposed that the following revised pillar design should be adopted at BRMO:

- Retain the current pillar design for areas where the RMR > 50. This rock mass rating is typically found in the high-grade areas.
- Adopt a revised pillar design for areas with an RMR < 50. This rock mass rating is typically found for the low-grade R5 product areas.

For the revised pillar design in low grade areas (RMR < 50), a new K-value was estimated using principles similar to that proposed for the design rock mass strength (DRMS). A value of K = 90 MPa was derived. This value is confirmed by the numerical modelling and the back-calculation of K-

values for pillars subjected to extensive scaling. A summary of the combined pillar design based on RMR is given below. The table on the left is similar to that current specified in the COP and the table on the right is the extension developed as part of this study.

	RMR > 50: Pillar dimensions at specific mining heights					
Mining depth	**3.5 m**	**4 m**	**4.5 m**	**5 m**	**5.5 m**	**6 m**
180 - 299 m	5.0	5.0	5.0	5.0	5.0	6.0
300 - 349 m	5.0	5.0	5.0	6.0	6.0	6.0
350 - 399 m	5.0	6.0	6.0	6.0	6.0	7.0
400 - 449 m	6.0	6.0	6.0	6.0	6.0	7.0
450 - 499 m	6.0	6.0	7.0	7.0	7.0	8.0
500 - 549 m	6.0	7.0	7.0	7.0	8.0	8.0
550 - 599 m	7.0	7.0	7.0	8.0	8.0	8.0
600 - 649 m	7.0	7.0	8.0	8.0	9.0	9.0
650 - 699 m	7.0	8.0	8.0	9.0	9.0	9.0
700 - 749 m	8.0	8.0	9.0	9.0	9.0	10.0

	RMR < 50: Pillar dimensions at specific mining heights					
Mining depth	**3.5 m**	**4 m**	**4.5 m**	**5 m**	**5.5 m**	**6 m**
180 - 299 m	5.0	6.0	6.0	6.0	6.0	7.0
300 - 349 m	6.0	6.0	6.0	7.0	7.0	7.0
350 - 399 m	6.0	7.0	7.0	7.0	8.0	8.0
400 - 449 m	7.0	7.0	8.0	8.0	8.0	9.0
450 - 499 m	7.0	8.0	8.0	9.0	9.0	9.0
500 - 549 m	8.0	8.0	9.0	9.0	10.0	10.0
550 - 599 m	8.0	9.0	9.0	10.0	10.0	11.0
600 - 649 m	8.0	9.0	10.0	10.0	11.0	11.0
650 - 699 m	9.0	10.0	10.0	11.0	12.0	12.0
700 - 749 m	9.0	10.0	11.0	12.0	12.0	13.0

The revised design for areas with an RMR < 50 must be trialled at the mine. Monitoring of the pillar condition in these areas is required to determine whether this design ameliorates the scaling problem and negates the need for spray-on liners.

CHAPTER 8

RECOMMENDATIONS AND FUTURE WORK

Good progress was made in this study and an improved understanding of the behaviour of the manganese pillars was obtained. Further work is required, however, and this is listed below:

- A more precise calibration of the limit equilibrium model is required. This should possibly involve laboratory work to determine rock strengths and friction angles of the manganese ore. A physical model in the laboratory may be valuable to test the applicability of this constitutive model and to gain an improved understanding of the various parameters. Such a laboratory experiment needs to be very carefully designed to ensure that useful results can be obtained.

- It is not clear if the limit equilibrium model is a good approximation of the pillar failure mechanism at the manganese mines. The failure is controlled by the various intersecting joint sets and these form small blocks that facilitate the scaling. This mechanism should be simulated using a distinct element code, such as UDEC, and the results should be compared to the limit equilibrium model in TEXAN.

- Underground monitoring of the time-dependent scaling of the pillars should be conducted over a longer period of time. Regular monitoring should be conducted, especially when the new pillars are still close to the face to determine if the concussion from the blasting causes the blocks to scale out. From this, a rate of scaling should be determined and this can be used to determine the long-term stability of these pillars.

- The revised pillar design proposed in this document should be trialled at the mine. A number of assumptions had to be made based on the data available and this should be verified. The larger pillars sizes will not be an attractive solution to the mine as it will reduce the extraction ratio and possibly production rates. A trade-off study needs to be done to determine if continued use of the thin spray-on liners is not the better solution. If this is the case, the best methods to reinforce the pillars should be investigated.

- There is still some uncertainty regarding the exact pillar strength and the appropriate formula to use. Some experimental pillar mining work should be considered where failure is artificially

induced in an instrumented pillar. This will serve as further verification of pillar strength. Such experiments have been done in the platinum mines, therefore it is feasible.

- Large areas of extensive pillar scaling should be identified and recorded by the mine. Numerical modelling should be conducted on high-risk areas to ensure that collapses in these areas will not affect adjacent areas or damage key access routes to the various areas of the mine.

- The average density of the overburden is a critical parameter for the modelling and this needs to be verified for future studies. Stress measurements should possibly be conducted to verify the simulated stress values.

References

REFERENCES

African Rainbow Minerals, 2019. Mineral Resource and Mineral Reserves 2019. pp 1-62.

Assmang.co.za., 2020. Manganese Ore | Assmang Proprietary Limited. [online] Available at: https://assmang.co.za/manganese-ore.

Aydan, Ö., Ito, T., Özbay, U., Kwasniewski, M., Shariar, K., Okuno, T., Özgenoğlu, A., Malan, D.F. and Okada, T., 2013. ISRM suggested methods for determining the creep characteristics of rock. In *The ISRM Suggested Methods for Rock Characterization, Testing and Monitoring: 2007-2014*. pp. 115-130. Springer, Cham.

Beukes, N.J., Swindell, E.P. and Wabo, H., 2016. Manganese deposits of Africa. *Episodes Journal of International Geoscience*. Volume 39(2), pp.285-317.

Bieniawski Z.T. 1984. Rock Mechanics Design in Mining and Tunnelling, p. 272. Balkema, Rotterdam.

Bieniawski, Z.T., 1992. A method revisited: coal pillar strength formula based on field investigations. *In Proceedings of the workshop on coal pillar mechanics and design. Pittsburgh, PA: US Department of the Interior, Bureau of Mines*, IC. Volume 93(15), pp. 158-165.

Cai, M. and Kaiser, P.K., 2014. In-situ rock spalling strength near excavation boundaries. *Rock mechanics and rock engineering*. Volume 47(2), pp.659-675.

Cording, E.J., Hashash, Y.M.A. and Oh, J., 2015. Analysis of pillar stability of mined gas storage caverns in shale formations. *Engineering Geology*. Volume 184, pp.71-80.

Dismuke, S.R., Forsyth, W.W. and Stewart, S.B.V., 1994. The evolution of mining strategy following the collapse of the Window Area at the Magmont Mine, Missouri. In *Proceedings, CIM Annual General Meeting, District 6, Metal Mining*. pp. 3-8.

Du Plessis, M. and Malan, D.F., 2018. Mining with crush pillars, *The Journal of The Southern African Institute of Mining and Metallurgy*. Volume 118(3), pp. 211-216.

EScience Associated, 2018. Assmang (PTY) LTD Black Rock Mine Operations, Hotazel, Northern Cape. pp. 1-290.

Esterhuizen, G.S., 2006. An evaluation of the strength of slender pillars. Trans Soc Min Metall Explor. Volume 320, pp. 69–76.

Esterhuizen, G.S., Iannacchione, A.T., Ellenberger, J.L. and Dolinar, D.R., 2006. Pillar stability issues based on a survey of pillar performance in underground limestone mines. *International Conference on Ground Control in Mining*. pp. 354-361.

Esterhuyse, J.C., Malan, D.F., 2018. Some rock engineering aspects of multi-reef pillar extraction on the Ventersdorp Contact Reef. *The Journal of The Southern African Institute of Mining and Metallurgy,* Volume 118(12), pp. 1285-1296.

Gae, P.Y., 2019. Bord support design evaluation for Black Rock Mine Operations. *University of Pretoria*. pp. 1-107

Hanekom, J., 2008. Investigation into pillar optimisation on the Black Rock Operations, *Assmang, MIDDindi Consulting (Pty) Ltd*, Report No. Brock3.2008.

Hao, Q.W. and Chugh, Y.P., 1992. An engineering approach to predict subsidence likelihood over abandoned coal mines in Illinois. In *Proceedings of the third workshop on surface subsidence due to underground mining*.

Hedley, D.G.F. and Grant, F., 1972. Stope-and-pillar design for Elliot Lake Uranium Mines. *Bull. Can. Inst. Min. Metal.*, Volume 65, pp. 37-44.

Hustrulid, W.A., 1976. A review of coal pillar strength formulas. *Rock Mechanics*, Volume 8, pp. 115-145.

Jager, A.J. and Ryder, J.A., 1999. A handbook on rock engineering practice for tabular hard rock mines. *Safety in Mines Research Advisory Committee, Johannesburg*, Volume 46.

Kaiser, P.K., Kim, B., Bewick, R.P. and Valley, B., 2011. Rock mass strength at depth and implications for pillar design. *Mining Technology*, Volume 120(3), pp.170-179.

Laubscher, D,H, 1990. A geomechanics classification system for the rating of rock mass in mine design. *Journal of the Southern African Institute of Mining and Metallurgy*, Volume 90(10): 257-273.

Leach, A.R., 2007. Review of shaft pillar stability as part of the revised mining plan for Impala 16 Shaft. *Itasca Africa Consultancy Report.*

Liu, G. and Cai, M., 2020. Modeling time-dependent deformation behavior of brittle rock using grain-based stress corrosion method. *Computers and Geotechnics*, Volume 118, pp.103-323.

Lunder, P.J. and Pakalnis, R.C., 1997. Determination of the strength of hard rock mine pillars. *Bulletin of the Canadian Institute of Mining and Metallurgy.* Volume 68, pp. 55-67

Malan, D.F., 2012. Pillar Design in the Hard Rock Mines of South Africa. *International Journal of Mining and Geo-Engineering*, Volume 46(2), pp.163-191.

Malan D.F. and Napier J.A.L. 2006. Practical Application of the Texan Code to Solve Pillar Design Problems in Tabular Excavations", SANIRE Symposium "Facing the challenges", Rustenburg, pp. 55-74, 2006.

Malan, D.F. and Napier, J.A.L., 2011. The design of stable pillars in the Bushveld Complex mines: a problem solved?. *The Journal of The Southern African Institute of Mining and Metallurgy,* Volume 11, pp. 821-836.

Malan, D.F. and Napier, J.A.L., 2018. Reassessing continuous stope closure data using a limit equilibrium displacement discontinuity model. *Journal of the Southern African Institute of Mining and Metallurgy*, Volume 118(3), pp.227-234.

Malan, D.F. and Napier, J.A.L., 2021. A review of the role of underground measurements in the historic development of rock engineering in South Africa, J. S. Afr. Inst. Min. Metall, vol. 121, no. 5, pp. 201–216.

Martin, C.D. and Maybee, W.G., 2000. The strength of hard-rock pillars. *International Journal of Rock Mechanics and Mining Sciences*, Volume *37*(8), pp.1239-1246.

Napier, J.A.L. and Malan, D.F., 2007. The computational analysis of shallow depth tabular mining problems. *The Journal of The Southern African Institute of Mining and Metallurgy,* Volume 107, pp. 725-742.

Napier, J.A.L. and Malan, D.F. 2011. Numerical computation of average pillar stress and implications for pillar design. J. S. Afr. Inst. Min. Metall., vol. 837-846.

Napier, J.A.L. and Malan, D.F., 2012. Simulation of time-dependent crush pillar behaviour in tabular platinum mines, J. S. Afr. Inst. Min. Metall., vol. 112, pp. 711-719.

Napier, J.A.L., and Malan, D.F., 2014. A simplified model of local fracture processes to investigate the structural stability and design of large-scale tabular mine layouts. In 48th US Rock Mechanics / Geomechanics Symposium, Minneapolis, USA.

Napier, J.A.L. and Malan, D.F., 2018. Simulation of tabular mine face advance rates using a *simplified* fracture zone model. *International Journal of Rock Mechanics and Mining Sciences*, Volume 109, pp.105-114.

Napier, J.A.L. and Malan, D.F., 2021. A limit equilibrium model of tabular mine pillar failure. *Rock Mechanics and Rock Engineering*, Volume 54:71-89.

Oke, J. and Kalenchuk, K., 2017. Selecting the most applicable hard rock pillar design method. In *51st US Rock Mechanics/Geomechanics Symposium*. OnePetro.

Ozbay, M.U., Ryder, J.A., and Jager, A.J., 1995. The design of pillar systems as practised in shallow hard-rock tabular mines in South Africa. *Journal of the Southern African Institute of Mining and Metallurgy*, Volume *95*(1), pp.7-18.

Ryder, J.A. and Jager, A.J., 2002. A textbook on rock mechanics for tabular hard rock mines. *Safety in Mines Research Advisory Committee, Johannesburg*. pp.207.

Ryder, J.A. and Ozbay, M.U., 1990, September. A methodology for designing pillar layouts for shallow mining. In *ISRM International symposium*. OnePetro.

Sainoki, A. and Mitri, H.S., 2017. Numerical investigation into pillar failure induced by time-dependent skin degradation. *International Journal of Mining Science and Technology*, Volume *27*(4), pp.591-597.

Salamon, M.D.G. and Munro, A., 1967. A study of the strength of coal pillars. *Journal of the Southern African Institute of Mining and Metallurgy*, Volume 68(2), pp.55-67.

Salamon, M.D.G., Ozbay, M.U., and Madden, B., 1998. Life and design of bord-and-pillar workings affected by pillar scaling. *Journal of the Southern African Institute of Mining and Metallurgy*, Volume 98(3), pp.135-145.

Shiri, R., 2019. Rock engineering report and recommendations on pillar failures, South West development Nchwaning III Shaft, *BRMO_Rock Engineering Report on Pillar Failures, South West Development*, Nchwaning 3 Shaft.

Stacey, T.R. and Swart, A.H. 2001. Booklet – Practical rock engineering practice for shallow and opencast mines. SIMRAC, October 2001.

Tesarik, D.R., Seymour, J.B., and Yanske, T.R., 2003. Post-failure behavior of two mine pillars confined with backfill. *International Journal of Rock Mechanics and Mining Sciences*, Volume 40(2), pp.221-232.

Van Besien, A.C. and Rockaway, J.D., 1988. Influence of overburden on subsidence development over room and pillar coal mines. *Geological Society, London, Engineering Geology Special Publications*, Volume 5(1), pp.215-219.

Van der Heever, P.K., 2013. Determination of in-situ stresses within reef pillars at Black Rock Mine, *Groundwork Consulting report,* Report number CR428_MS076.

Van der Merwe, J.N., 1993. Revised strength factor for coal in the Vaal Basin. *Journal of the Southern African Institute of Mining and Metallurgy*, Volume 93(3), pp.71-77.

Van der Merwe, J.N., 2003. Predicting coal pillar life in South Africa. *Journal of the Southern African Institute of Mining and Metallurgy*, Volume 103(5), pp.293-301.

Van der Merwe, J.N., 2004. Verification of pillar life prediction method. *Journal of the Southern African Institute of Mining and Metallurgy*, Volume 104(11), pp.667-675.

Van der Merwe, J.N., 2016. Review of coal pillar lifespan prediction for the Witbank and Highveld coal seams. *Journal of the Southern African Institute of Mining and Metallurgy*, Volume 116(11), pp.1083-1090.

Van der Merwe, J.N., 2019. Coal pillar strength analysis based on size at the time of failure. *Journal of the Southern African Institute of Mining and Metallurgy*, Volume 119(7), pp.681-692.

Van der Merwe, J.N. and Mathey, M., 2013. Probability of failure of South African coal pillars. *Journal of the Southern African Institute of Mining and Metallurgy*, Volume 113(11), pp.849-857.

Wagner, H., 1974. Determination of the complete load-deformation characteristics of coal pillars. In *proceedings of the third international congress on rock mechanics. National Academy of Sciences*, Volume 2, pp. 1076-1081.

Wang, M. and Cai, M., 2021. Numerical modeling of time-dependent spalling of rock pillars. *International Journal of Rock Mechanics and Mining Sciences*, Volume 141, p.104725.

Watson, B.P., Ryder, J.A., Kataka, M.O., Kuijpers, J.S. and Leteane, F.P., 2008. Merensky pillar strength formulae based on back-analysis of pillar failures at Impala Platinum. *Journal of the Southern African Institute of Mining and Metallurgy*, Volume 108(8), pp.449-461.

APPENDIX A

ROCK MASS RATING AND Q-RATINGS

Additional pillar observations are presented below as a record for future researchers. This information could not be included in the main body of the document owing to the large volume of material.

Area 1 - Pillar N3_1

In summary, the vertical joints are closely spaced with the joint spacing varying over the perimeter of the pillar. Scaling at the corners is prominent. Buckling of the failed slabs on the left side of Side D was observed with an hourglass shape on the righthand side of Side D. The vertical joint spacing varies between 2 cm and 4.5 cm in some places and in other places the joint spacing is 10 cm to 20 cm. The spacing of the joints on Sides A and C was found to be 40 cm and Sides B and D were 10 cm. No random joints were observed and in total, three joint sets were observed. The joint sets are mostly vertical, and no infilling was observed. The joints are smooth and planar with extensive failure on Sides A and C. Figure 11-2 illustrates the typical hourglass shape of the pillar.

A rock mass rating was very difficult as there are significant changes in joint spacing over short distances and the pillars are heavily crushed in many areas. It is noticeable that the vertical joint spacings of 10 cm led to significant scaling and damage. Figure 11-1 and Figure 11-3 illustrate the variation of joint spacing on the same pillar side (N3_1D). The one side illustrates a joint spacing of 1 cm and the other side approximately 10 cm. Sides A and C had larger joint spacings of 40 cm in some areas. As the edges of the pillar on these sides fail on the closely spaced joints parallel to the plane, it had a smooth appearance in some places.

Figure 11-1. Joint spacing on Side D (left corner).

Figure 11-2. Depth of pillar scaling for pillar N3_1. Note the hourglass shape of the pillar.

Figure 11-3. Joint spacing on Side D (right corner) of the pillar indicates a vertical joint spacing of approximately 10 cm.

Table 11-1 illustrates the measurements recorded for pillar N3_1. This pillar was established between March and June 2018.

Table 11-1. Measurements for pillar N3_1 in the R5 area. Measurements were taken on the 4th of May 2021 and on the 18th of August 2021.

Pillar N3_1			
Bord span		Bord span measured on 2021/05/04	Bord span measured on 2021/08/18
	N3_1A to N3_2A	9.279m	9.263m
	N3_1B to N3_3A	8.2m	8.185m
	N3_1C to N3_4A	10.41m	10.425m
	N3_1D to N3_5A	7.73m	7.73m
Dimensions of pillar	Side of pillar	Width	Height
	N3_1A	7.17 m	5.05 m
	N3_1B	6.29 m	4.36 m
	N3_1C	8.68 m	5.233 m
	N3_1D	5.223 m	4.359 m
Approximate scaling distance	Side of pillar	Approximate scaling distance	Age of pillar (months)
	N3_1A	1.97 m	36
	N3_1B	0.97 m	36
	N3_1C	1.74 m	36
	N3_1D	0.9 m	36

Area 1 - Pillar N3_2

The vertical joints of this pillar were spaced approximately 10 cm to 30 cm. These spacings vary across the perimeter of the pillar. Random joints were observed. The vertical joints seem to terminate at the horizontal joints, causing small blocky scaling. On Side A, the left corner had a horizontal joint spacing ranging from 4 cm to 10 cm. The pillar had an hourglass shape and the scaling buckled at the edges of the pillar. Overall, the joint spacing was difficult to determine as it varies across the perimeter of the pillar. A total of three joint sets were observed, plus a random joint.

It is noticeable that the vertical joint spacings led to significant scaling and damage. Figure 11-4 and Figure 11-5 illustrate the variation of joint spacing on the same pillar side (N3_2A). The one side illustrates a joint spacing ranging from 1 cm to 5 cm. The vertical joint spacing ranges from 10 cm to 30 cm in different areas making it difficult to determine the RQD as it ranges from less than 25% to approximately 75%.

Figure 11-4. Joint spacing on the left-hand corner of Side A. The spacing ranged from 5 cm to 20 cm.

Figure 11-5. The vertical joint spacing on the right-hand side of the pillar. It was difficult to determine as the spacing of the joints as it varies across the perimeter of the pillar.

Table 11-2 illustrates the measurements recorded for pillar N3_2. This pillar was cut between March and June 2018.

Figure 11-6. Side B of pillar N3_2 at Nchwaning III shaft observed on the 4th of May and on the 18th of August 2021.

Table 11-2. Measurements for pillar N3_2 in the R5 area. Measurements were taken on the 4th of May 2021 and on the 18th of August 2021.

Pillar N3_2			
Bord span		Bord span measured on 2021/05/04	Bord span measured on 2021/08/18
	N3_2A to N3_1A	9.271 m	9.263 m
	N3_2B to N3_6A	8.142 m	8.103 m
	N3_2C to N3_7A	8.3 m	8.221 m
	N3_2D to N3_8A	7.75 m	7.835 m
Dimensions of pillar	Side of pillar	Width	Height
	N3_2A	7.02 m	5.19 m
	N3_2B	6.34 m	5.09 m
	N3_2C	6.75 m	4.86 m
	N3_2D	7.71 m	4.57 m
Approximate scaling distance	Side of pillar	Approximate scaling distance	Age of pillars (months)
	N3_2A	0.83 m	36
	N3_2B	1.3 m	36
	N3_2C	0.8 m	36
	N3_2D	0.5 m	36

Area 2 - Pillar N3_15

There are three joint sets present and one random joint. The horizontal joint spacing was observed to be greater than 1 m in some places. It varies across the perimeter of the pillar ranging between 30 cm to 50 cm. Some of the horizontal joints are clamped tightly and the spacing varies. Horizontal joints also had a spacing that varied. The vertical joint spacing was observed to be between 3 cm and 10 cm in some places. Sides A and C have a random joint dipping at 45°. The pillar has an hourglass shape. The vertical joints seem to terminate on the horizontal joints, facilitating the scaling. Figure 11-7 illustrates the dip of the random joint set and Figure 11-8 illustrates the joint spacing on Side C. Figure 11-9 illustrates a random joint striking in the direction of Sides B and D.

Figure 11-7. Side A illustrates an hourglass shape.

Figure 11-8. Side C illustrates the joint spacing, ranging from 5 cm to 20 cm.

Figure 11-9. Random joint striking in the direction of Sides B and D. Angle of random joint, 45°.

Table 11-3 illustrates the measurements taken at pillar N3_15. This pillar was established in February 2021. The author was unable to take measurements of this pillar after the first visit as this area was sprayed with TSL.

Table 11-3. Measurements for pillar N3_15 in the R5 area. Measurements were taken on the 6th of May 2021 and for the second visit, the area was already covered with thin shotcrete lining.

N3_15			
Bord span		Bord span measured on 2021/05/06	Bord span measured on 2021/08/18
	N3_15A to N3_17	7.04 m	TSL applied
	N3_15B to N3_16	8.06 m	TSL applied
	N3_15C to N3_19	7.36 m	TSL applied
	N3_15D to N3_18	7.24 m	TSL applied
Dimensions of pillar	Side of pillar	Width	Height
2021/05/06	N3_15A	7.4 m	4.42 m
	N3_15B	7.24 m	4.0 m
	N3_15C	7.69 m	3.75 m
	N3_15D	7.57 m	4.64 m
Approximate scaling rate	Side of pillar	Approximate scaling distance	Age of pillars (months)
2021/05/06	N3_15A	0.6 m	3

Area 4 - Pillar N3_33

The vertical joints in this area are not prominent and almost no signs of scaling were observed. In this particular area, the horizontal joints seem to be the prominent joint set. This joint spacing varies along the perimeter of the pillar, ranging from 30 cm to greater than 50 cm. On the sides of the pillar, the vertical joint spacing was determined to be approximately 20 cm. The corners of the pillars had the shape of an hourglass. The overall condition of the pillar is stable and intact. Only two joint sets were observed, one horizontal and one vertical. Figure 11-10 illustrates the joint spacing across Side B. The vertical joint sets were spaced approximately 40 cm apart. It was difficult to determine the spacing as these joints are not prominent. Figure 11-11 illustrates the hourglass shape of the pillar as observed underground.

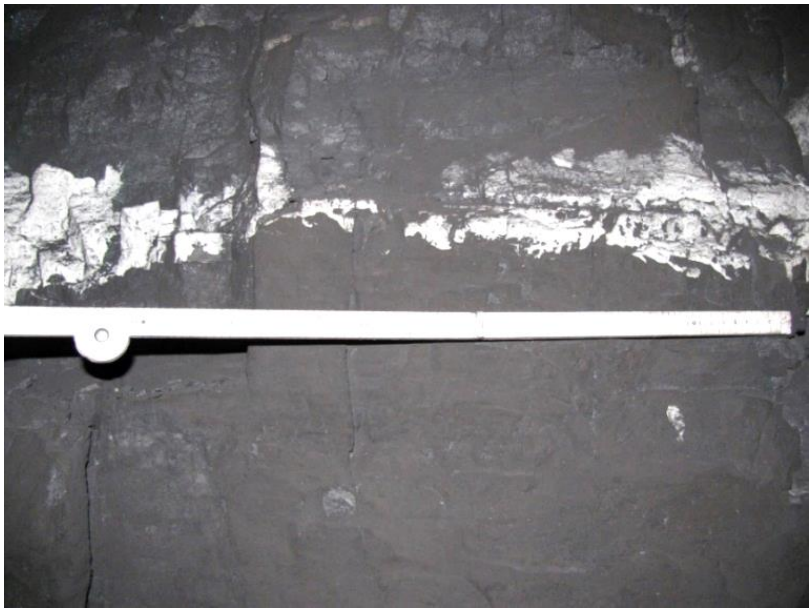

Figure 11-10. Side B illustrates the vertical joint spacing of approximately 40 cm.

Figure 11-11. Side C illustrates an hourglass shape of the corners of the pillars. The pillar corners are still intact.

Table 11-4 illustrates the measurements recorded for pillar N3_33. This pillar was established between March and June 2018.

Figure 11-12. Side D of pillar N3_33 at Nchwaning III shaft, illustrating the right-hand corner of the pillar observed on the 17th of May and on the 18th of August 2021.

Table 11-4. Measurements for pillar N3_33 in the +45-grade area. Measurements were taken on the 17th of May 2021 and on the 18th of August 2021.

N3_33			
Bord span		Bord span measured on 2021/05/17	Bord span measured on 2021/08/18
	N3_33A to N3_34A	6.9 m	6.963 m
	N3_33B to N3_35A	7.8 m	full of waste
	N3_33C to N3_36A	8.8 m	8.854 m
	N3_33D to N3_37A	8.0 m	8.097 m
Dimensions of pillar	Side of pillar	Width	Height
2021/05/17	N3_33A	6.92 m	4.0 m
	N3_33B	6.78 m	4.39 m
	N3_33C	6.17 m	4.07 m
	N3_33D	6.42 m	3.58 m
Approximate scaling rate	Side of pillar	Approximate scaling distance	Age of pillars (months)
2021/05/17	N3_33A	0.4 m	36
	N3_33B	0.3 m	36
	N3_33C	0.38 m	36
	N3_33D	0.291 m	36

The tables below illustrate the RMR and the Q-ratings for the pillars of interest.

Table 11-5. Rock mass rating and Q-rating for pillar N3_1.

Pillar N3_1		
Rock mass rating		**Rating**
Strength of intact rock material	>250MPa	15
Drill core quality (RQD)	<25%	3
Spacing of discontinuities	<60mm	5
Condition of discontinuities	Separation 1-5mm	10
Groundwater	Completely dry	15
Adjustment for discontinuity orientation	Favourable	-2
Total		46

Q-rating		
RQD	<25%	25
Jn (joint number)	3 joints	9
Jr (joint roughness)	smooth planar	1
Ja (joint alteration number)	Unaltered joint walls	1
RSF (Joint water reduction factor)	Dry conditions	1
SRF (Stress reduction factor)		1
Total		3

Table 11-6. Rock mass rating and Q-rating for pillar N3_2.

Pillar N3_2		
Rock mass rating		**Rating**
Strength of intact rock material	>250MPa	15
Drill core quality (RQD)	<25%	3
Spacing of discontinuities	<60mm	5
Condition of discontinuities	Separation 1-5mm	10
Groundwater	Completely dry	15
Adjustment for discontinuity orientation	Favourable	-2
Total		46

Q-rating		
RQD	<25%	25
Jn (joint number)	3 joints, random	12
Jr (joint roughness)	smooth planar	1
Ja (joint alteration number)	Unaltered joint walls	1
RSF (Joint water reduction factor)	Dry conditions	1
SRF (Stress reduction factor)		1
Total		2

Table 11-7. Rock mass rating and Q-rating for pillar N3_9.

Pillar N3_9		
Rock mass rating		**Rating**
Strength of intact rock material	>250MPa	15
Drill core quality (RQD)	<25%	3
Spacing of discontinuities	60mm to 200mm	8
Condition of discontinuities	Separation 1-5mm	10
Groundwater	Completely dry	15
Adjustment for discontinuity orientation	Favourable	-2
Total		49

Q-rating		
RQD	<25%	25
Jn (joint number)	3 joints, random joints	12
Jr (joint roughness)	smooth planar	1
Ja (joint alteration number)	Unaltered joint walls	1
RSF (Joint water reduction factor)	Dry conditions	1
SRF (Stress reduction factor)		1
Total		2

Table 11-8. Rock mass rating and Q-rating for pillar N3_15.

Pillar N3_15		
Rock mass rating		**Rating**
Strength of intact rock material	>250MPa	15
Drill core quality (RQD)	50% to 75%	13
Spacing of discontinuities	60mm to 200mm	8
Condition of discontinuities	Separation 1-5mm	10
Groundwater	Completely dry	15
Adjustment for discontinuity orientation	Favourable	-2
Total		59

Q-rating		
RQD	50% to 75%	50
Jn (joint number)	3 joints	9
Jr (joint roughness)	smooth planar	1
Ja (joint alteration number)	Unaltered joint walls	1
RSF (Joint water reduction factor)	Dry conditions	1
SRF (Stress reduction factor)		1
Total		6

Table 11-9. Rock mass rating and Q-rating for pillar N3_20.

Pillar N3_20		
Rock mass rating		**Rating**
Strength of intact rock material	>250MPa	15
Drill core quality (RQD)	50% to 75%	13
Spacing of discontinuities	60mm to 200mm	8
Condition of discontinuities	Separation 1-5mm	10
Groundwater	Completely dry	15
Adjustment for discontinuity orientation	Favourable	-2
Total		59

Q-rating		
RQD	50% to 75%	50
Jn (joint number)	3 joints and random	12
Jr (joint roughness)	smooth planar	1
Ja (joint alteration number)	Unaltered joint walls	1
RSF (Joint water reduction factor)	Dry conditions	1
SRF (Stress reduction factor)		1
Total		6

Table 11-10. Rock mass rating and Q-rating for pillar N3_25.

Pillar N3_25		
Rock mass rating		**Rating**
Strength of intact rock material	>250MPa	15
Drill core quality (RQD)	25%	3
Spacing of discontinuities	<60mm	3
Condition of discontinuities	Separation 1-5mm	10
Groundwater	Completely dry	15
Adjustment for discontinuity orientation	Favourable	-2
Total		44

Q-rating		
RQD	25%	25
Jn (joint number)	3 joints and random	12
Jr (joint roughness)	smooth planar	1
Ja (joint alteration number)	Unaltered joint walls	1
RSF (Joint water reduction factor)	Dry conditions	1
SRF (Stress reduction factor)		1
Total		2

Table 11-11. Rock mass rating and Q-rating for pillar N3_28.

Pillar N3_28		
Rock mass rating		**Rating**
Strength of intact rock material	>250MPa	15
Drill core quality (RQD)	90% to 100%	20
Spacing of discontinuities	200mm to 600mm	10
Condition of discontinuities	Separation less than 1mm, slightly weathered	25
Groundwater	Completely dry	15
Adjustment for discontinuity orientation	Favourable	-2
Total		83

Q-rating		
RQD	90%	90
Jn (joint number)	2 joints	4
Jr (joint roughness)	smooth planar	1
Ja (joint alteration number)	Unaltered joint walls	1
RSF (Joint water reduction factor)	Dry conditions	1
SRF (Stress reduction factor)		1
Total		23

Table 11-12. Rock mass rating and Q-rating for pillar N3_33.

Pillar N3_33		
Rock mass rating		**Rating**
Strength of intact rock material	>250MPa	15
Drill core quality (RQD)	90% to 100%	20
Spacing of discontinuities	200mm to 600mm	10
Condition of discontinuities	Separation less than 1mm, slightly weathered	25
Groundwater	Completely dry	15
Adjustment for discontinuity orientation	Favourable	-2
Total		83

Q-rating		
RQD	90%	90
Jn (joint number)	3 joints	9
Jr (joint roughness)	smooth planar	1
Ja (joint alteration number)	Unaltered joint walls	1
RSF (Joint water reduction factor)	Dry conditions	1
SRF (Stress reduction factor)		1
Total		10

Table 11-13. Rock mass rating and Q-rating for pillar N3_38.

Pillar N3_38		
Rock mass rating		**Rating**
Strength of intact rock material	>250MPa	15
Drill core quality (RQD)	75% to 90%	17
Spacing of discontinuities	60mm to 200mm	8
Condition of discontinuities	Separation 1-5mm	10
Groundwater	Completely dry	15
Adjustment for discontinuity orientation	Favourable	-2
Total		63

Q-rating		
RQD	75%	75
Jn (joint number)	3 joints	9
Jr (joint roughness)	smooth planar	1
Ja (joint alteration number)	Unaltered joint walls	1
RSF (Joint water reduction factor)	Dry conditions	1
SRF (Stress reduction factor)		1
Total		8

APPENDIX B

PHOTOGRAPHS OF SELECTED PILLARS

The following additional photographs illustrate the conditions of the pillars monitored for this study.

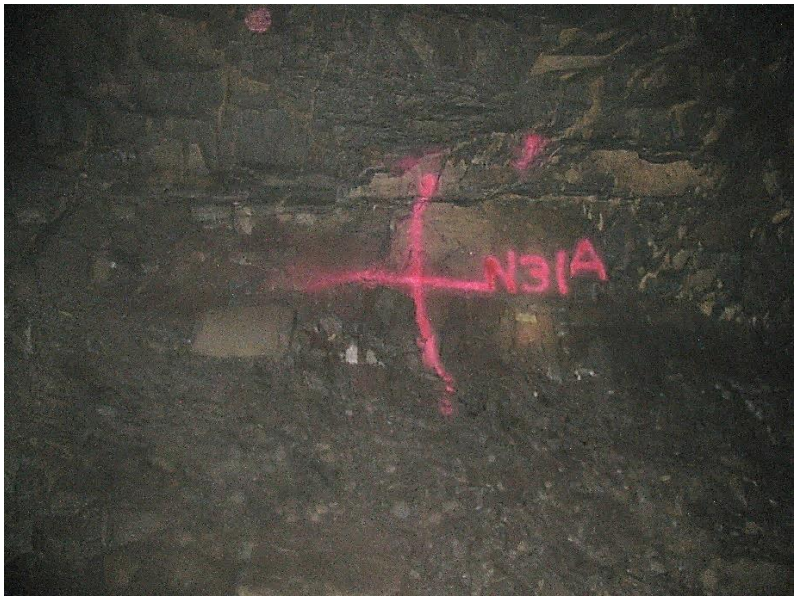

Figure 12-1. Side A of pillar N3_1 at Nchwaning III shaft as observed on the 4th of May 2021.

Figure 12-2. Side A of pillar N3_1 at Nchwaning III shaft as observed on the 18th of August 2021.

Figure 12-3. The left corner of side A of pillar N3_1 at Nchwaning III shaft as observed on the 4th of May 2021.

Figure 12-4. The left corner of side A of pillar N3_1 at Nchwaning III shaft as observed on the 18th of August 2021.

Figure 12-5. Side B of pillar N3_1 at Nchwaning III shaft illustrating buckling of the corner as observed on the 4th of May 2021.

Figure 12-6. Side B of pillar N3_1 at Nchwaning III shaft illustrating buckling of the corner as observed on the 18th of August 2021. No time-dependent scaling took place over this period.

Figure 12-7. Side C of pillar N3_1 at Nchwaning III shaft as observed on the 4th of May 2021.

Figure 12-8. Side C of pillar N3_1 at Nchwaning III shaft illustrating the scaling that has taken place since the pillar was cut.

Figure 12-9. Side C of pillar N3_1 illustrating the size of some of the blocks that scaled from the pillar.

Figure 12-10. Side D of pillar N3_1 at Nchwaning III shaft illustrating the vertical joints on the right-hand corner of the pillar.

Figure 12-11. Side A of pillar N3_2 at Nchwaning III shaft as observed on the 4th of May 2021.

Figure 12-12. Side A of pillar N3_2 at Nchwaning III shaft as observed on the 18th of August 2021.

Figure 12-13. Side A of pillar N3_2 at Nchwaning III shaft illustrating the vertical joint sets on the left-hand corner of the pillar.

Figure 12-14. Side B of pillar N3_2 at Nchwaning III shaft as observed on the 4th of May 2021.

Figure 12-15. Side B of pillar N3_2 at Nchwaning III shaft as observed on the 18th of August 2021.

Figure 12-16. Side B of pillar N3_2 at Nchwaning III shaft illustrating the vertical joint sets on the left-hand corner of the pillar.

Figure 12-17. Side B of pillar N3_2 illustrating the right corner.

Figure 12-18. Side C of pillar N3_2 at Nchwaning III shaft as observed on the 4th of May 2021, the red triangle was used as a reference point to measure the scaling distance as the pillar was too dangerous to mark

Figure 12-19. Side C of pillar N3_2 at Nchwaning III shaft, the red triangle was used as a reference point to measure the scaling distance as the pillar was too dangerous to mark. This photograph was taken on the 18th of August 2021.

Figure 12-20. Side C of pillar N3_2 at Nchwaning III shaft illustrating the right-hand corner of the pillar as observed on the 4th of May 2021.

Figure 12-21. Side C of pillar N3_2 at Nchwaning III shaft illustrating the right-hand corner of the pillar as observed on the 18th of August 2021.

Figure 12-22. Side D of pillar N3_2 at Nchwaning III shaft, illustrating the vertical joint sets on the left-hand corner of the pillar.

Figure 12-23. Side D of pillar N3_2 at Nchwaning III shaft, illustrating the vertical joint sets on the right-hand corner of the pillar as observed on the 4th of May 2021.

Figure 12-24. Side D of pillar N3_2 at Nchwaning III shaft, illustrating the vertical joint sets on the right-hand corner of the pillar as observed on the 18th of August 2021.

Figure 12-25. Side A of pillar N3_9 at Nchwaning III shaft as observed on the 4th of May 2021.

Figure 12-26. Side A of pillar N3_9 at Nchwaning III shaft, illustrating the vertical joint sets and the size of the block that are scaling off the pillar on the left-hand side.

Figure 12-27. Side B of pillar N3_9 at Nchwaning III shaft as observed on the 4th of May 2021.

Figure 12-28. Side B of pillar N3_9 at Nchwaning III shaft as observed on the 18th of August 2021. A small amount of scaling took place.

Figure 12-29. Side B of pillar N3_9 at Nchwaning III shaft, illustrating the vertical joint sets as observed on the 4th of May 2021.

Figure 12-30. Side B of pillar N3_9 at Nchwaning III shaft, illustrating the vertical joint sets on the left-hand corner as observed on the 4th of May 2021.

Figure 12-31. Side B of pillar N3_9 at Nchwaning III shaft, illustrating the vertical joint sets on the left-hand corner as observed on the 18th of August 2021.

Figure 12-32. Side C of pillar N3_9 at Nchwaning III shaft as observed on the 4th of May 2021.

Figure 12-33. Side C of pillar N3_9 at Nchwaning III shaft as observed on the 18th of August 2021.

Figure 12-34. Side C of pillar N3_9 at Nchwaning III shaft, illustrating the vertical joint spacing on the left-hand side.

Figure 12-35. Side D of pillar N3_9 at Nchwaning III shaft as observed on the 4th of May 2021.

Figure 12-36. Side D of pillar N3_9 at Nchwaning III shaft as observed on the 18th of August 2021.

Figure 12-37. Side A of pillar N3_15 at Nchwaning III shaft as observed on the 6th of May 2021.

Figure 12-38. Side A of pillar N3_15 at Nchwaning III shaft, illustrating slight weathering on the corner.

Figure 12-39. Side B of pillar N3_15 at Nchwaning III shaft, illustrating the vertical joint spacing.

Figure 12-40. Side B of pillar N3_15 at Nchwaning III shaft, illustrating the horizontal joint spacing.

Figure 12-41. Side C of pillar N3_15 at Nchwaning III shaft as observed on the 6th of May 2021.

Figure 12-42. Side C of pillar N3_15 at Nchwaning III shaft, illustrating the condition of the right-hand corner of the pillar.

Figure 12-43. Side C of pillar N3_15 at Nchwaning III shaft, illustrating the random joint terminating on Side C.

Figure 12-44. Side D of pillar N3_15 at Nchwaning III shaft as observed on the 6th of May 2021.

Figure 12-45. Side D of pillar N3_15 at Nchwaning III shaft, illustrating the condition of the left-hand corner of the pillar.

Figure 12-46. Side A of pillar N3_20 at Nchwaning III shaft, illustrating the left-hand corner of the pillar as observed on the 6th of May 2021.

Figure 12-47. Side A of pillar N3_20 at Nchwaning III shaft, illustrating the left-hand corner of the pillar as observed on the 18th of August 2021.

Figure 12-48. Side B of pillar N3_20 at Nchwaning III shaft as observed on the 6th of May 2021.

Figure 12-49. Side B of pillar N3_20 at Nchwaning III shaft as observed on the 18th of August 2021.

Figure 12-50. Side B of pillar N3_20 at Nchwaning III shaft, illustrating the right-hand corner of the pillar.

Figure 12-51. Side C of pillar N3_20 at Nchwaning III shaft as observed on the 6th of May 2021.

Figure 12-52. Side C of pillar N3_20 at Nchwaning III shaft, illustrating the hourglass shape of the corner of the pillar.

Figure 12-53. Side D of pillar N3_20 at Nchwaning III shaft as observed on the 6th of May 2021.

Figure 12-54. Side D of pillar N3_20 at Nchwaning III shaft as observed on the 18th of August 2021.

Figure 12-55. Side D of pillar N3_20 at Nchwaning III shaft, illustrating the two joint sets.

Figure 12-56. Side D of pillar N3_20 at Nchwaning III shaft, illustrating the vertical joint opening on the side.

Figure 12-57. Side A of pillar N3_25 at Nchwaning III shaft as observed on the 6th of May 2021.

Figure 12-58. Side A of pillar N3_25 at Nchwaning III shaft, illustrating the condition of the right-hand corner of the pillar.

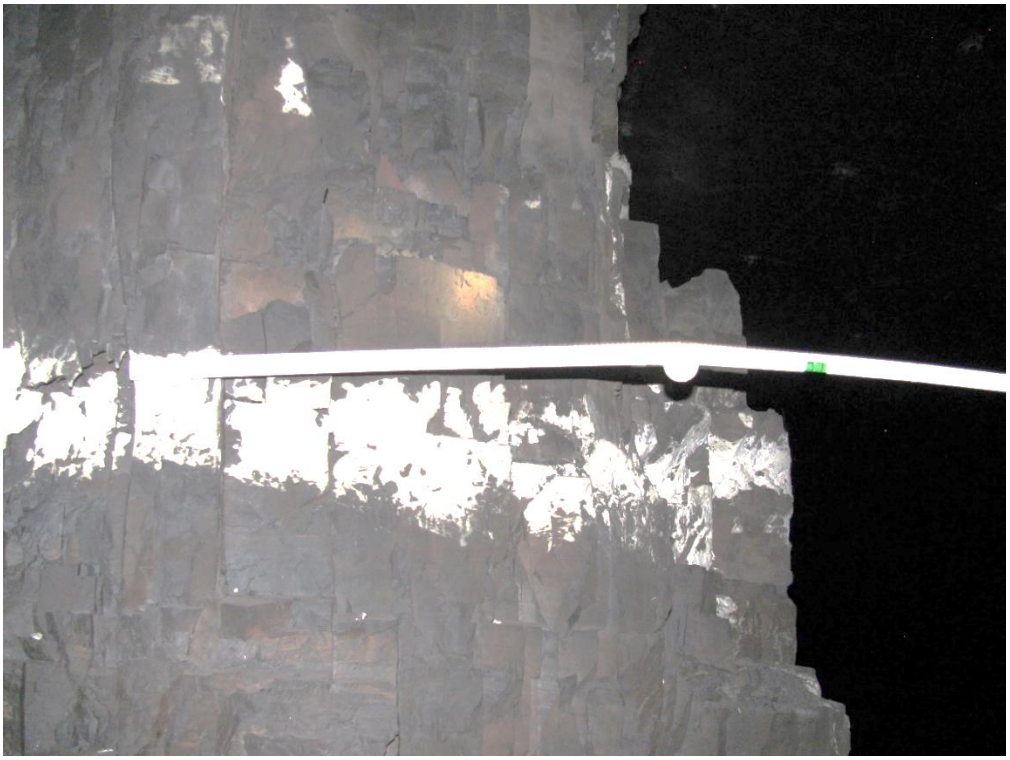

Figure 12-59. Side A of pillar N3_25 at Nchwaning III shaft, illustrating the vertical joint spacing of the right-hand corner of the pillar.

Figure 12-60. Side B of pillar N3_25 at Nchwaning III shaft as observed on the 6th of May 2021.

Figure 12-61. Side B of pillar N3_25 at Nchwaning III shaft as observed on the 18th of August 2021.

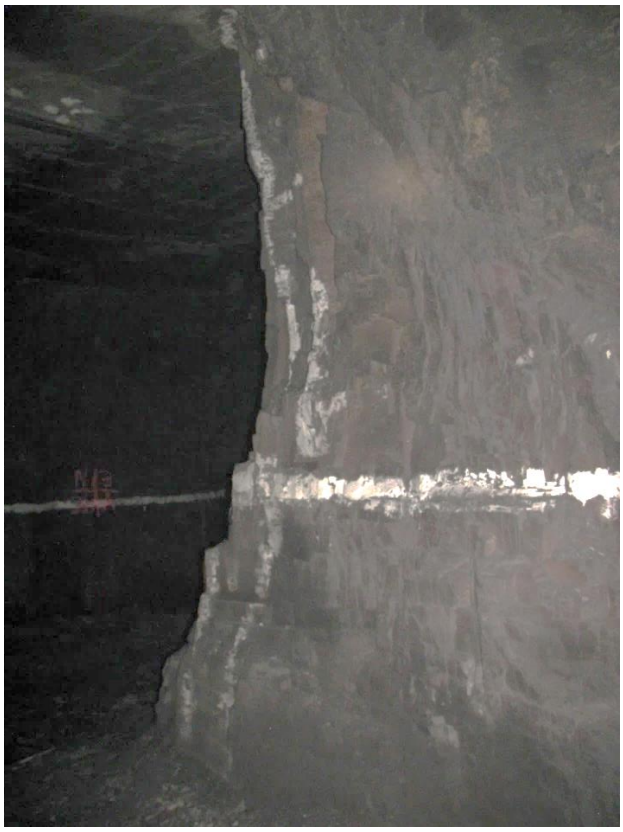

Figure 12-62. Side B of pillar N3_25 at Nchwaning III shaft, illustrating the hourglass shape on the left-hand corner of the pillar.

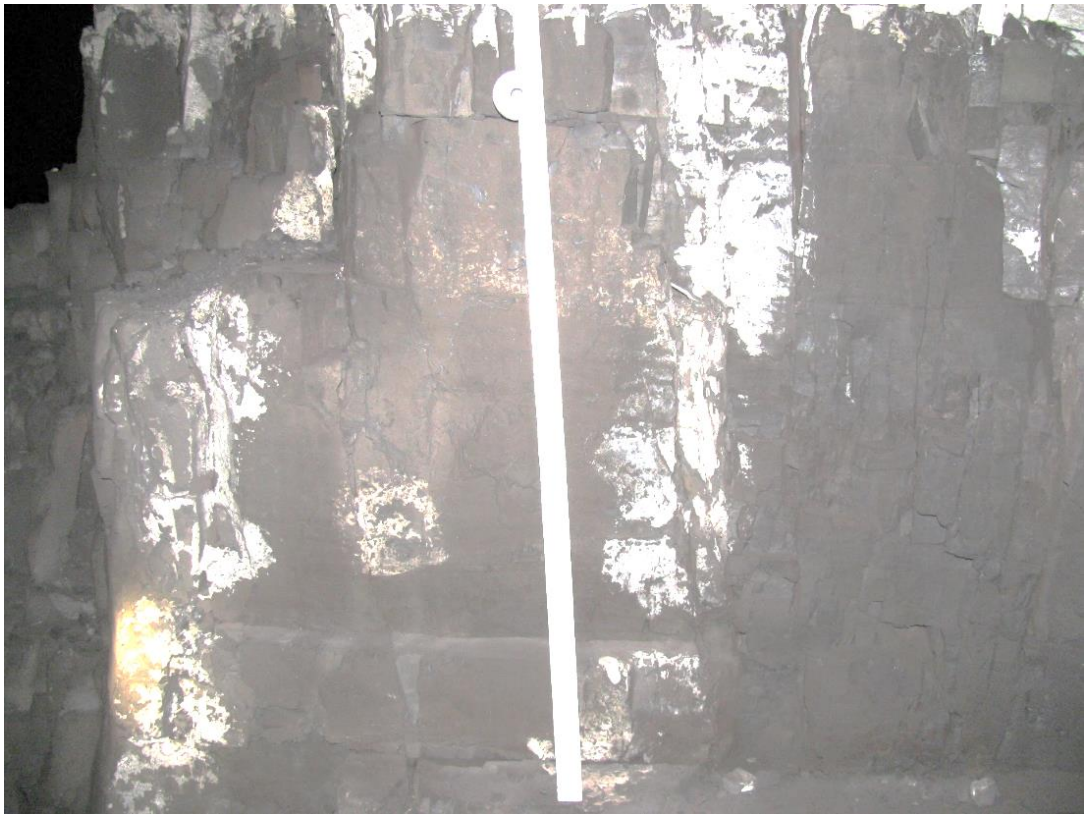

Figure 12-63. Side B of pillar N3_25 at Nchwaning III shaft, illustrating the horizontal joint spacing.

Figure 12-64. Side C of pillar N3_25 at Nchwaning III shaft as observed on the 6th of May 2021.

Figure 12-65. Side D of pillar N3_25 at Nchwaning III shaft, illustrating the left-hand corner of the pillar and no additional scaling of the corners was observed.

Figure 12-66. Side D of pillar N3_25 at Nchwaning III shaft, illustrating the right-hand corner of the pillar and no additional scaling of the corners was observed on the 18th of August 2021.

Figure 12-67. Side A of pillar N3_28 at Nchwaning III shaft as observed on the 17th of May 2021.

Figure 12-68. Side A of pillar N3_28 at Nchwaning III shaft, illustrating the contact between the sidewall and the hanging wall.

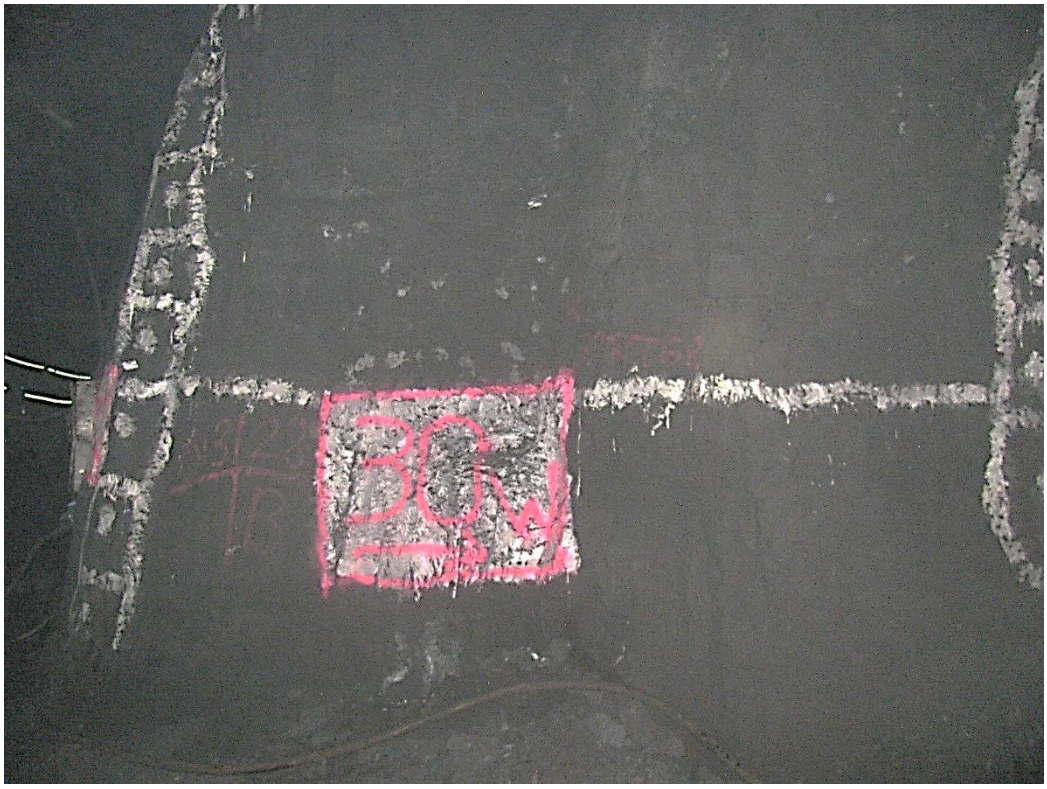

Figure 12-69. Side B of pillar N3_28 at Nchwaning III shaft as observed on the 18th of August 2021.

Figure 12-70. Side B of pillar N3_28 at Nchwaning III shaft, illustrating the left-hand side of the pillar as observed on the 17th of May 2021.

Figure 12-71. Side B of pillar N3_28 at Nchwaning III shaft, illustrating the left-hand side of the pillar as observed on the 18th of August 2021.

Figure 12-72. Side C of pillar N3_28 at Nchwaning III shaft as observed on the 17th of May 2021.

Figure 12-73. Side C of pillar N3_28 at Nchwaning III shaft as observed on the 18th of August 2021.

Figure 12-74. Side C of pillar N3_28 at Nchwaning III shaft, illustrating the vertical and horizontal joint sets.

Figure 12-75. Side D of pillar N3_28 at Nchwaning III shaft, illustrating the left-hand corner of the pillar as observed on the 18th of August 2021.

Figure 12-76. Side A of pillar N3_33 at Nchwaning III shaft as observed on the 17th of May 2021.

Figure 12-77. Side A of pillar N3_33 at Nchwaning III shaft as observed on the 18th of August 2021.

Figure 12-78. Side A of pillar N3_33 at Nchwaning III shaft, illustrating the left-hand corner of the pillar still in very good condition.

Figure 12-79. Side B of pillar N3_33 at Nchwaning III shaft, illustrating the horizontal joint set.

Figure 12-80. Side C of pillar N3_33 at Nchwaning III shaft as observed on the 17th of May 2021.

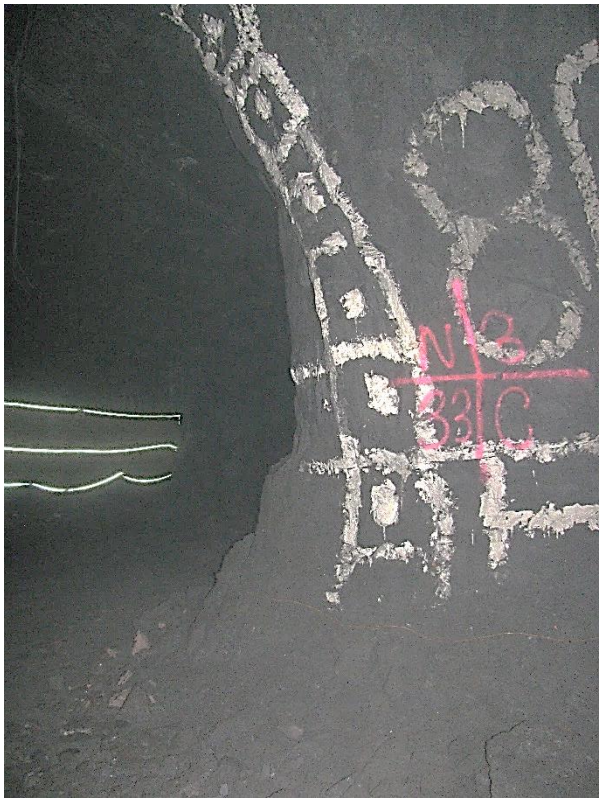

Figure 12-81. Side C of pillar N3_33 at Nchwaning III shaft as observed on the 18th of August 2021.

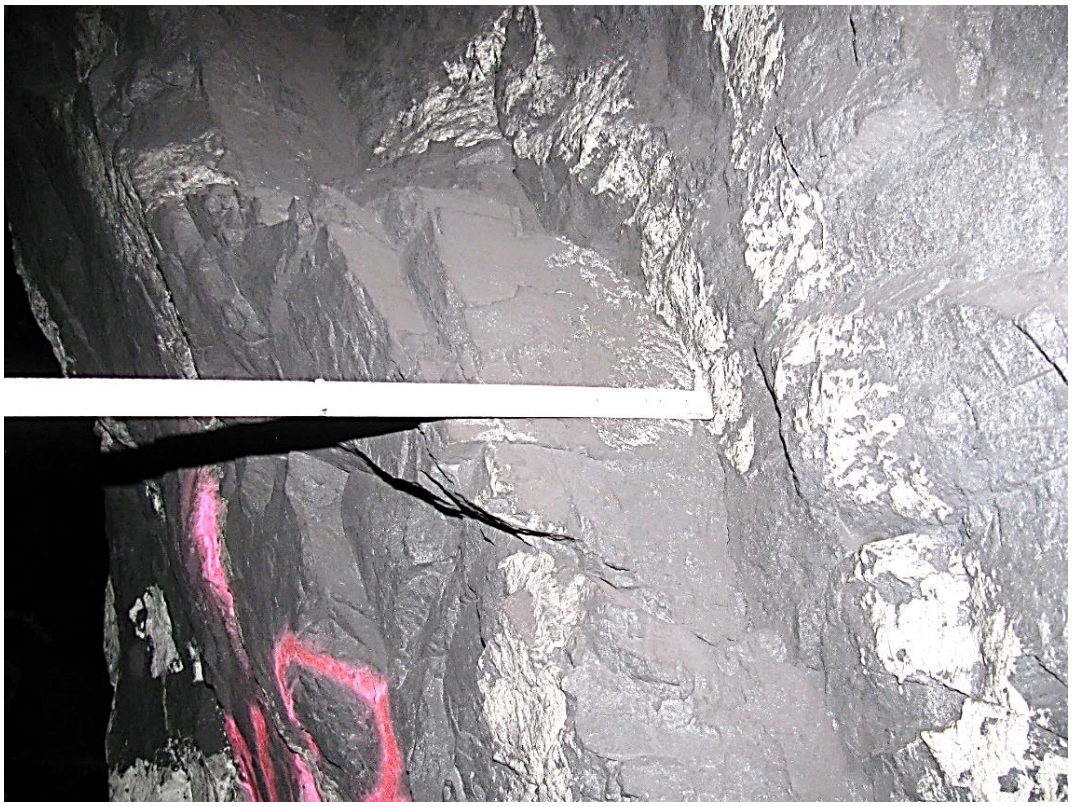

Figure 12-82. Side C of pillar N3_33 at Nchwaning III shaft, illustrating the vertical

Figure 12-83. Side D of pillar N3_33 at Nchwaning III shaft, illustrating the right-hand corner of the pillar as observed on the 17th of May 2021.

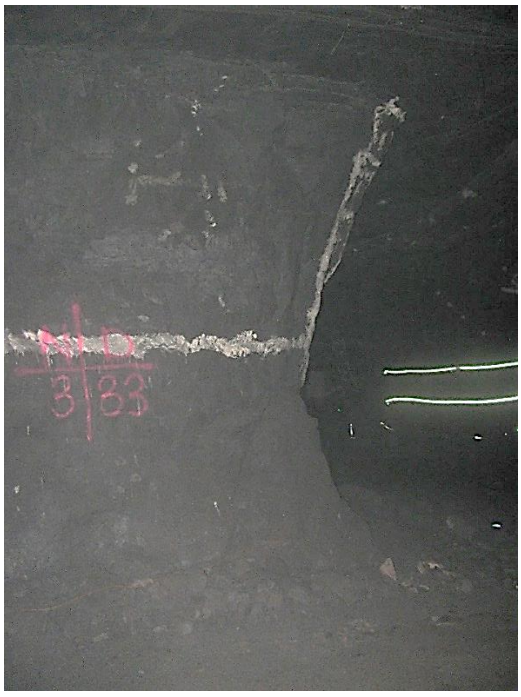

Figure 12-84. Side D of pillar N3_33 at Nchwaning III shaft, illustrating the right-hand corner of the pillar as observed on the 18th of August 2021.

Figure 12-85. Side A of pillar N3_38 at Nchwaning III shaft as observed on the 18th of May 2021.

Figure 12-86. Side A of pillar N3_38 at Nchwaning III shaft as observed on the 18th of August 2021.

Figure 12-87. Side A of pillar N3_38 at Nchwaning III shaft, illustrating the vertical joint spacing of the pillar.

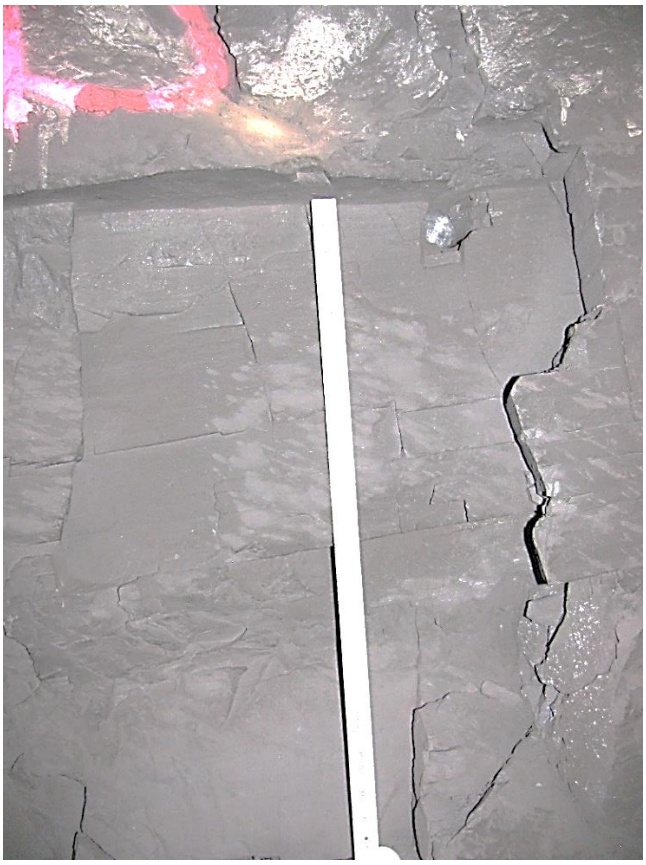

Figure 12-88. Side B of pillar N3_38 at Nchwaning III shaft, illustrating the horizontal joint spacing and the size of the blocks.

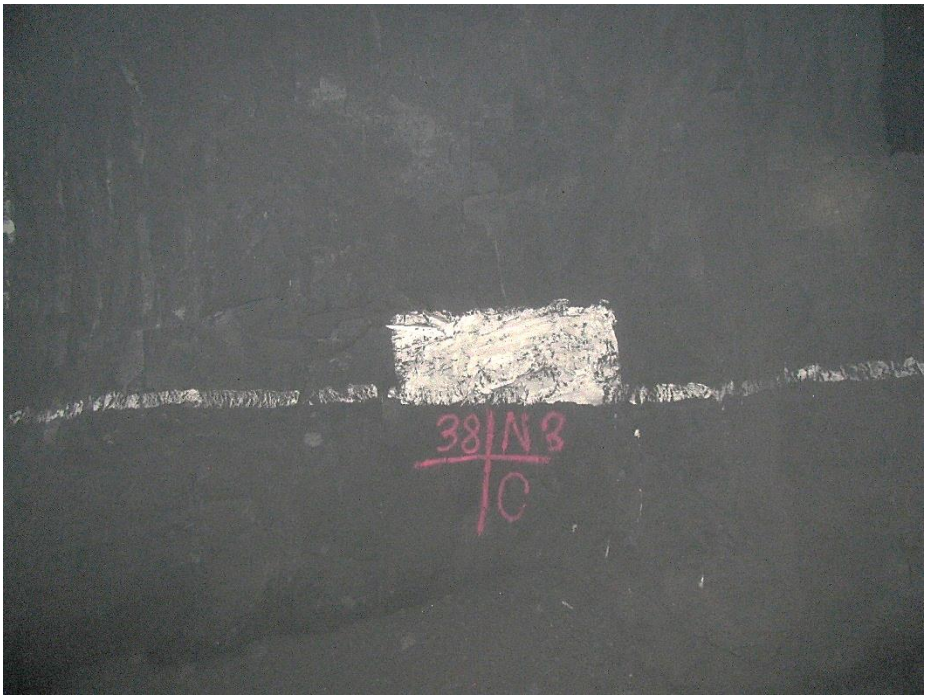

Figure 12-89. Side C of pillar N3_38 at Nchwaning III shaft as observed on the 18th of August 2021.

Figure 12-90. Side C of pillar N3_38 at Nchwaning III shaft, illustrating the vertical joint spacing on the edge of the pillar.

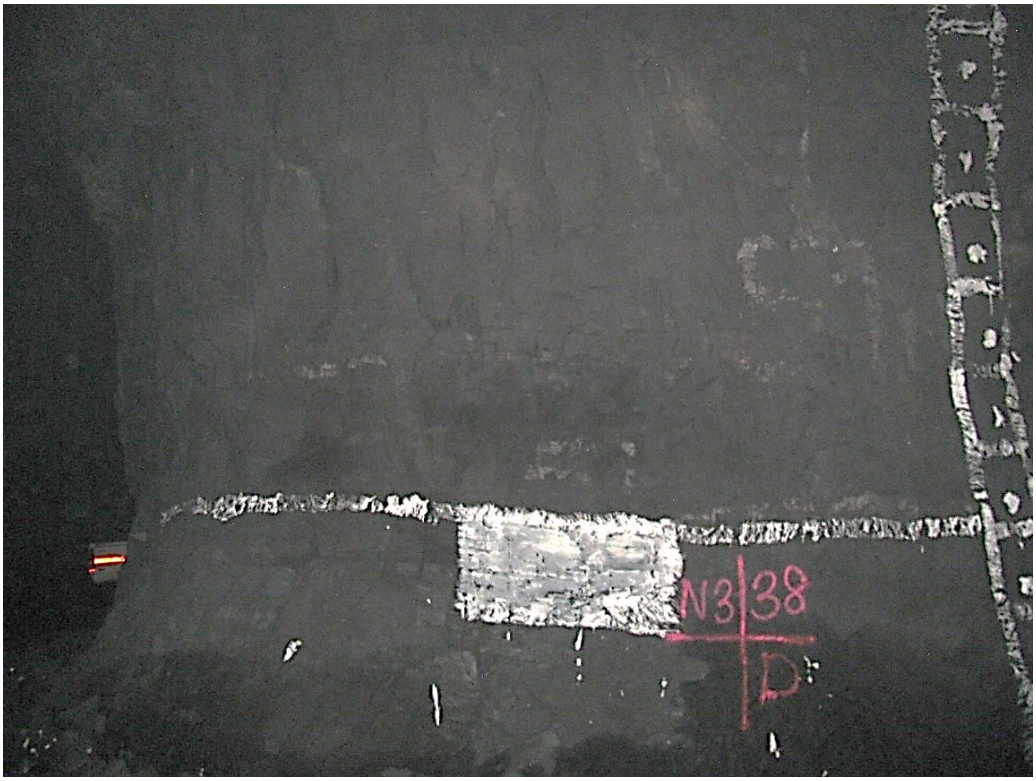

Figure 12-91. Side D of pillar N3_38 at Nchwaning III shaft as observed on the 18th of May 2021.

Figure 12-92. Side D of pillar N3_38 at Nchwaning III shaft as observed on the 18th of August 2021.

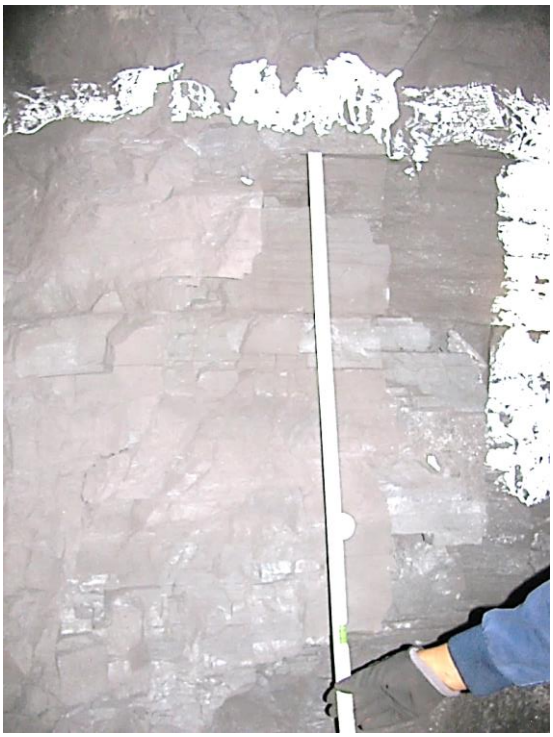

Figure 12-93. Side D of pillar N3_38 at Nchwaning III shaft, illustrating the horizontal joint spacing.

APPENDIX C

SIMULATED APS VALUES

The following tables illustrates the APS values obtained for the rigid pillar model and the limit equilibrium model described in Chapters 4 and 5. The pillars numbered in red are the ones studied in detail.

Table 13-1. Simulated APS values for the elastic model and the limit equilibrium model for Area 1.

Area 1		
Pillar number	**Elastic model (APS)**	**Limit equilibrium model (APS)**
P96	76	34
P97	69	35
P98	61	39
P99	68	33
P125	56	40
P126	47	39
P149	69	38
P150	73	39
P151 (N3_2)	71	36
P171	75	38
P172	84	28
P173 (N3_1)	68	41
P174	70	36
P192	86	30
P193 (N3_9)	76	38
P194	73	37
P195	65	34
P212	71	33
P213	53	39

Table 13-2. Simulated APS values for the elastic model and the limit equilibrium model for Area 2.

Area 2		
Pillar number	**Elastic model (APS)**	**Limit equilibrium model (APS)**
P3	53	42
P5 (N3_15)	47	41
P6	48	39
P11	58	44
P12	53	43
P13	59	45
P25	59	44
P26	65	35
P27	65	33
P33 (N3_20)	69	33
P34	61	36
P38	57	41

Table 13-3. Simulated APS values for the elastic model and the limit equilibrium model for Area 3.

Area 3		
Pillar number	**Elastic model (APS)**	**Limit equilibrium model (APS)**
P61	50	41
P62	59	37
P67	52	39
P68 (N3_25)	70	35
P73	64	36
P74	60	38
P78	64	35
P79	67	37
P85	62	37
P86	72	34

Table 13-4. Simulated APS values for the elastic model and the limit equilibrium model for Area 4.

Area 4		
Pillar number	**Elastic model (APS)**	**Limit equilibrium model (APS)**
P266	50	39
P268	51	42
P269 (N3_28)	56	38
P270	47	39
P278	53	44
P279	56	47
P280	42	37
P298	63	50
P299 (N3_33)	60	49
P300	47	40
P317	63	49
P318	61	48
P319	54	43

Table 13-5. Simulated APS values for the elastic model and the limit equilibrium model for Area 5.

Area 5		
Pillar number	**Elastic model (APS)**	**Limit equilibrium model (APS)**
P28	64	52
P29	74	59
P35	66	55
P36 (N3_38)	73	61
P37	65	53
P57	66	54
P58	67	56
P59	72	58